Precision cross-sections for advancing cosmic-ray physics and other applications: a comprehensive programme for the next decade

D. Maurin[a,*], L. Audouin[b], E. Berti[c], P. Coppin[d], M. Di Mauro[e], P. von Doetinchem[f], F. Donato[e,g,h], C. Evoli[i,j], Y. Génolini[k], P. Ghosh[l], I. Leya[m], M. J. Losekamm[n,o], S. Mariani[h], J. W. Norbury[p], L. Orusa[q,r], M. Paniccia[d], T. Poeschl[h], P. D. Serpico[k], A. Tykhonov[d], M. Unger[s], M. Vanstalle[t], M.-J. Zhao[u,v], D. Boncioli[w,j], M. Chiosso[e,g], D. Giordano[e], D. M. Gomez Coral[x], G. Graziani[c], C. Lucarelli[h], P. Maestro[y,z], M. Mahlein[n], L. Morejon[aa], J. Ocampo-Peleteiro[ab], A. Oliva[ab], T. Pierog[t], L. Šerkšnytė[h]

[a] *LPSC, Université Grenoble-Alpes, CNRS/IN2P3, 38026, Grenoble, France*
[b] *Université Paris-Saclay, IJC Lab, CNRS/IN2P3, 91405, Orsay, France*
[c] *INFN, Sezione di Firenze, I-50019 Sesto Fiorentino, Florence, Italy,*
[d] *DPNC, Université de Genève, 1211 Genève 4, Geneva, Switzerland*
[e] *INFN Sezione di Torino Via P. Giuria 1 10125 Torino Italy*
[f] *University of Hawaii at Manoa, HI, Honolulu, USA*
[g] *Università degli Studi di Torino, Torino, Italy*
[h] *European Organization for Nuclear Research (CERN), Geneva, Switzerland*
[i] *Gran Sasso Science Institute (GSSI), Viale Francesco Crispi 7, 67100, L'Aquila, Italy*
[j] *INFN-Laboratori Nazionali del Gran Sasso (LNGS), via G. Acitelli 22, 67100, Assergi (AQ), Italy*
[k] *LAPTh, CNRS, Université Savoie Mont Blanc, F-74940, Annecy, France*
[l] *NASA Goddard Space Flight Center, Greenbelt, Maryland, 20771, USA,*
[m] *University of Bern, Space Sciences and Planetology, CH-3012, Bern, Switzerland*
[n] *Technical University of Munich, School of Natural Sciences, Garching, Germany*
[o] *Excellence Cluster ORIGINS, Garching, Germany*
[p] *NASA Langley Research Center, Hampton, Virginia, 23666, USA,*
[q] *Department of Astrophysical Sciences, Princeton University, NJ 08544, Princeton, USA*
[r] *Department of Physics and Columbia Astrophysics Laboratory, Columbia University, NY 10027, New York, USA*
[s] *IAP, KIT, Karlsruhe, Germany*
[t] *Université de Strasbourg, CNRS, IPHC-UMR7178, F-67000 Strasbourg, France,*
[u] *Key Laboratory of Particle Astrophysics, Institute of High Energy Physics, Chinese Academy of Sciences, 100049, Beijing, China*
[v] *China Center of Advanced Science and Technology, 100190, Beijing, China*
[w] *Università degli Studi dell'Aquila, Dipartimento di Scienze Fisiche e Chimiche, Via Vetoio, 67100, L'Aquila, Italy,*
[x] *Instituto de Física, Universidad Nacional Autónoma de México, Circuito de la Investigación Científica, Ciudad de México, México,*
[y] *Department of Physical Sciences, Earth and Environment, University of Siena, via Roma 56, 53100 Siena, Italy,*
[z] *INFN, Sezione di Pisa, Polo Fibonacci, Largo B. Pontecorvo 3, 56127 Pisa, Italy,*
[aa] *Bergische Universität Wuppertal, Gausstrasse 20, 42117 Wuppertal, Germany,*
[ab] *INFN, Sezione di Bologna, 40126 Bologna, Italy,*

Abstract

Cosmic-ray physics in the GeV-to-TeV energy range has entered a precision era thanks to recent data from space-based experiments. However, the poor knowledge of nuclear reactions, in particular for the production of antimatter and secondary nuclei, limits the information that can be extracted from these data, such as source properties, transport in the Galaxy and indirect searches for particle dark matter. The *Cross-Section for Cosmic Rays at CERN* workshop series has addressed the challenges encountered in the interpretation of high-precision cosmic-ray data, with the goal of strengthening emergent synergies and taking advantage of the complementarity and know-how in different communities, from theoretical and experimental astroparticle physics to high-energy and nuclear physics. In this paper, we present the outcomes of the third edition of the workshop that took place in 2024. We present the current state of cosmic-ray experiments and their perspectives, and provide a detailed road map to close the most urgent gaps in cross-section data, in order to efficiently progress on many open physics cases, which are motivated in the paper. Finally, with the aim of being as exhaustive as possible, this report touches several other fields – such as cosmogenic studies, space

radiation protection and hadrontherapy – where overlapping and specific new cross-section measurements, as well as nuclear code improvement and benchmarking efforts, are also needed. We also briefly highlight further synergies between astroparticle and high-energy physics on the question of cross-sections.

Contents

*Corresponding author
Email addresses: david.maurin@lpsc.in2p3.fr (D. Maurin), fiorenza.donato@unito.it (F. Donato), saverio.mariani@cern.ch (S. Mariani)

1. Introduction

Charged particles arriving at the Earth from space with energies[1] above 100 MeV – the so-called cosmic rays (CRs) – are dominated by protons and helium nuclei (He in the following, mostly ^{4}He), with some traces of heavier nuclei, electrons, and antiparticles. Up to energies of about 100 TeV, it is now feasible to detect these particles *directly* using balloon-borne and space-based instruments, which can precisely determine their charge. At higher energies, the flux becomes exceedingly low, and CRs can only be detected *indirectly* through the extensive air showers they produce upon interacting with the atmosphere. A striking and well-known characteristic of the CR spectrum is its nearly featureless, power-law behaviour, spanning roughly 12 orders of magnitude in energy and 33 orders of magnitude in flux, as illustrated in Fig. 1. Beyond the overall energy range and the typical power-law index $\gamma \simeq 2.5$–3, considerable attention has been devoted to explaining specific spectral features. These include the *Knee* at a few PeV, where the spectral slope steepens by $\Delta\gamma \sim 0.5$, the *Ankle* at several EeV, where the spectrum flattens again, and a flux suppression at $E \sim 10^{20}$ eV. The *Knee* and *Ankle* are commonly interpreted as signatures of a transition from Galactic to extragalactic CR components. Meanwhile, the flux suppression at ultra-high energies may indicate either a maximum acceleration limit in extragalactic sources and/or reflect significant energy losses of CRs travelling through the cosmic background radiation field.

CRs in the GeV–PeV range are typically referred to as Galactic Cosmic Rays (GCRs), whereas those exceeding 10^{18} eV, dubbed ultra-high-energy cosmic rays (UHECRs), are generally considered to be of extragalactic origin. Within our Galaxy, μG-scale turbulent magnetic fields cause the trajectories of charged GCRs to lose any directional memory, yielding a highly isotropic flux at the level of 10^{-4}–10^{-3}. Above 3×10^{18} eV, however, the moderate strength and direction of the detected anisotropy (pointing toward the Galactic anti-centre) strengthens the case for an extragalactic nature of UHECRs, even further so if combined with the chemical composition indicators [1]. The Sun, for its part, can accelerate particles up to a few GeV during solar flares, and the heliosphere modulates GCR fluxes up to several tens of GeV. This solar modulation is reflected in an increased suppression of the observed GCR intensity with decreasing energy (at GeV energy, this suppression is $\gtrsim 10$).

The physics of GCR, which is the main focus of this paper, has entered a precision era. Thanks to satellite-borne and space-based experiments, data on many CR species reach a precision below 10% in the GeV–TeV energy range (e.g., [2, 3]). A major motivation to investigate messengers such as CRs, as well as understanding their sources and our Galactic environment, is the indirect search for particle dark matter (DM) signatures. These relics from the early universe could annihilate or decay in the halo of our Galaxy, leaving a feeble footprint in charged GCRs and/or in photons. The disentanglement of a possible hint from these particles in the observed CR fluxes must rely on a robust theoretical framework for GCRs as a whole. However, the poor knowledge of nuclear reactions, in particular for the production of antimatter and secondary nuclei, limits the information that can be extracted from the CR data about the source properties, the transport in the Galaxy, and the eventual presence of a signal from DM annihilation or decay.

The huge array of cross-sections needed for a precise prediction of CR data can actually be determined only by experiments at accelerators. While some of these data has already been collected in ongoing CERN experiments, significantly larger and more precise datasets are still required. The issue of determining the cross-sections necessary for a precise modelling of GCRs has been the topic of a series of workshops held at CERN [4–6]. This *review* is one of the outcomes of the last edition held in October 2024, XSCRC 2024

[1] To avoid any ambiguity in the notations and units, throughout this review, the total and kinetic energy are denoted E and $E_{\rm k}$, respectively, and are expressed in GeV (or other multiple of eV). The other energy variables and units employed are the momentum p in GeV/c, the rigidity $R = pc/Ze$ in GV and the kinetic energy per nucleon $E_{\rm k/n}$ in GeV/n. Different communities use different units in the literature for the latter, and the meaning of GeV/n is the same as, for instance, A GeV or GeV/u.

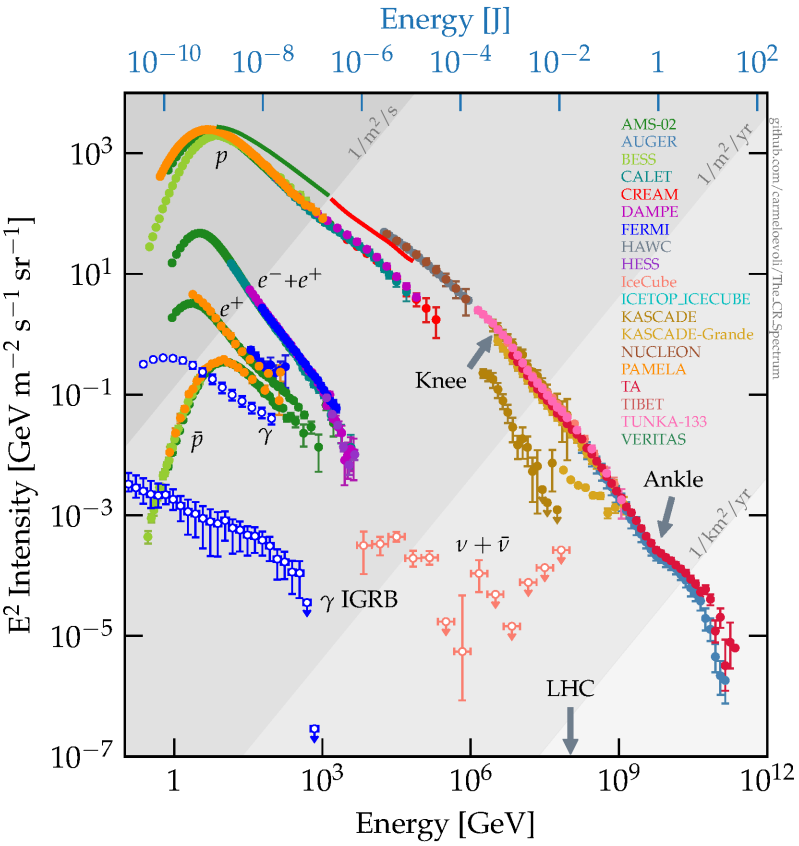

Figure 1: Compilation of the CR energy spectrum, scaled by E^2 to highlight spectral features (notably the *Knee* at $\sim 10^6$ GeV and the *Ankle* at $\sim 10^9$ GeV). Coloured markers and lines show measurements of the total (all-particle) spectrum and individual components (e.g., protons, electrons, positrons, antiprotons (=$\overline{\text{p}}$)), while open symbols indicate neutral particles (diffuse γ rays from the Galactic plane and from the isotropic γ-ray background, and diffuse neutrinos). Diagonal lines represent integral flux levels for reference. The charged-CR data are taken from the cosmic-ray database (CRDB) [7–9], with additional γ-ray and ν data from Fermi-LAT (Large Area Telescope) [10, 11] and IceCube [12], respectively. The energy reached at the LHC (Large Hadron Collider) at CERN is also indicated.

(Cross-Sections for Cosmic Rays at CERN) [6]. It aims at providing a road map to the most urgent cross-sections to (re-)evaluate, in order to progress on many physics cases, mostly related to GCRs, but not only.

The paper is organised as follows. In Sec. 2, we review the most important physics cases related to GCRs, highlighting specific situations where current cross-sections uncertainties prevent further progress. Improved cross-section measurements are also mandatory in several transverse topics, including cosmogenic studies, space exploration protection and hadron therapy. With the goal of building synergies between our communities (owing to overlapping or complementary needs), we also highlight their science cases. In Sec. 3, we review the current precision and energy reach of charged CR data, their most striking features, and some recent advances they brought to the field. These data are the primary drive for improving cross-sections, so we also present the ongoing and future CR experiments. The latter illustrate the existing long term and long-lasting programmes to get even more precise CR data, which will further drive the need for even more precise nuclear data (than the ones already needed now). In Sec. 4, we discuss the status and limitations of nuclear data, in the context of GCR data interpretation. We provide an actionable list of reactions and energies to measure, and their required precision, sorting the highest priority ones. We cover nuclear fragmentation but also anti-particle and γ-ray production, illustrating how these new nuclear data would be a game changer for GCRs. To be complete, we also discuss the status and impact of other cross-sections involved in the

modelling of GCRs (inelastic, annihilation, etc.). In Sec. 5, we move to the facilities and experiments where some of these nuclear measurements are taking or could take place. For the highest energies, we detail how strong synergies between the GCR and high-energy physics (HEP) communities have been recently built, highlighting recent successful results and ongoing measurements at CERN experiments. In the multi-GeV regime, we present ongoing experiments and forthcoming facilities (at the 2026–2027 horizon) where strong synergies with the nuclear physics community could be built. We also show that CR experiments are themselves excellent apparatus for measuring important cross-sections, in an energy range not accessible elsewhere. In Sec. 6, we come back to the cross-sections needs from transverse communities. We present their specific requirements, in terms of reactions, energies and precision, along with their priority list. We also briefly touch some other topics, where promising HEP and astroparticle physics synergies take place. Throughout this review, we provide summary tables and figures, to give an as clear and straightforward view as possible of: (i) the CR experiment panorama and projects; (ii) the nuclear data status and needs; and (iii) the beam capabilities and opportunities at various facilities. Although we do not have a dedicated section on nuclear and Monte Carlo (MC) codes in this review, we highlight and discuss at many points the importance, uses, and associated benefits and difficulties of these tools.

2. Physics cases in a high-precision era

This first section presents the physics cases and key questions in several topics where limitations appear because of cross-sections uncertainties. The main focus is on GCR physics questions and related cross-sections (Sec. 2.1), but we also present transverse fields where similar cross-sections are involved (Sec. 2.2), and other astroparticle physics cases where different cross-sections, but similar needs for better measurements, arise (Sec. 2.3).

2.1. Astrophysics and beyond SM physics cases for GCRs

In Fig. 2, the composition in the GCR flux is compared against the inferred one from photospheric measurements and chondrites in the Solar system (SS) [13], which is representative of the environment around a typical (population I) Galactic star. The overall similarity comforts the idea that GCRs are accelerated from an environment resembling the interstellar medium (ISM). Yet, intriguing differences stand out: elements like lithium, beryllium, and boron are only one order of magnitude less abundant than carbon or oxygen in the GCR flux, while merely present in traces in the ISM. Similar trends appear elsewhere, notably in fluorine and elements slightly lighter than iron (Sub-iron elements: Sc, Ti and V). These "over-represented" species are interpreted as formed (almost) exclusively during propagation (hence they are dubbed secondary) from the fragmentation of heavier GCR nuclei into lighter ones during interactions with the ISM targets. This secondary component provides relevant insights into the travel history of parent nuclei as they propagate through the ISM before reaching the Earth. For instance, they are one of the most solid evidences for some kind of diffusive propagation, since the amount of material crossed compatible with the measurements is orders of magnitude larger than what expected from a ballistic propagation.

2.1.1. Can we reveal DM with CRs?

Anomalous energy spectra, anisotropy, and composition patterns of the cosmic particle fluxes provide one of the main strategies (the so-called *indirect* one) in the searches for signals beyond the standard model (SM) of particle physics (see, e.g., [22, 23] for reviews). In particular, the rarest cosmic particles, such as antimatter (positrons, $\overline{\mathrm{p}}$ and antinuclei) and stable neutral messengers, are privileged channels for indirect searches of byproducts of DM particle decays or annihilations [24]. The current consensus is that the fluxes of all firmly detected energetic cosmic particles are dominated by established astrophysical processes, not all of them however precisely known. In particular, the bulk of CR antimatter and diffuse γ photons are related to interactions of GCRs with the atoms of the ISM in the Milky Way. This implies that any exotic contribution coming for instance from DM represents a subdominant contribution, with the possible exception of poorly probed energy ranges. To fully exploit the precision of current data, one should make sure that theoretical uncertainties are under control at least at a level comparable to the observational one, which is hardly the case today. Which directions appear as the most promising ones to tackle this challenge?

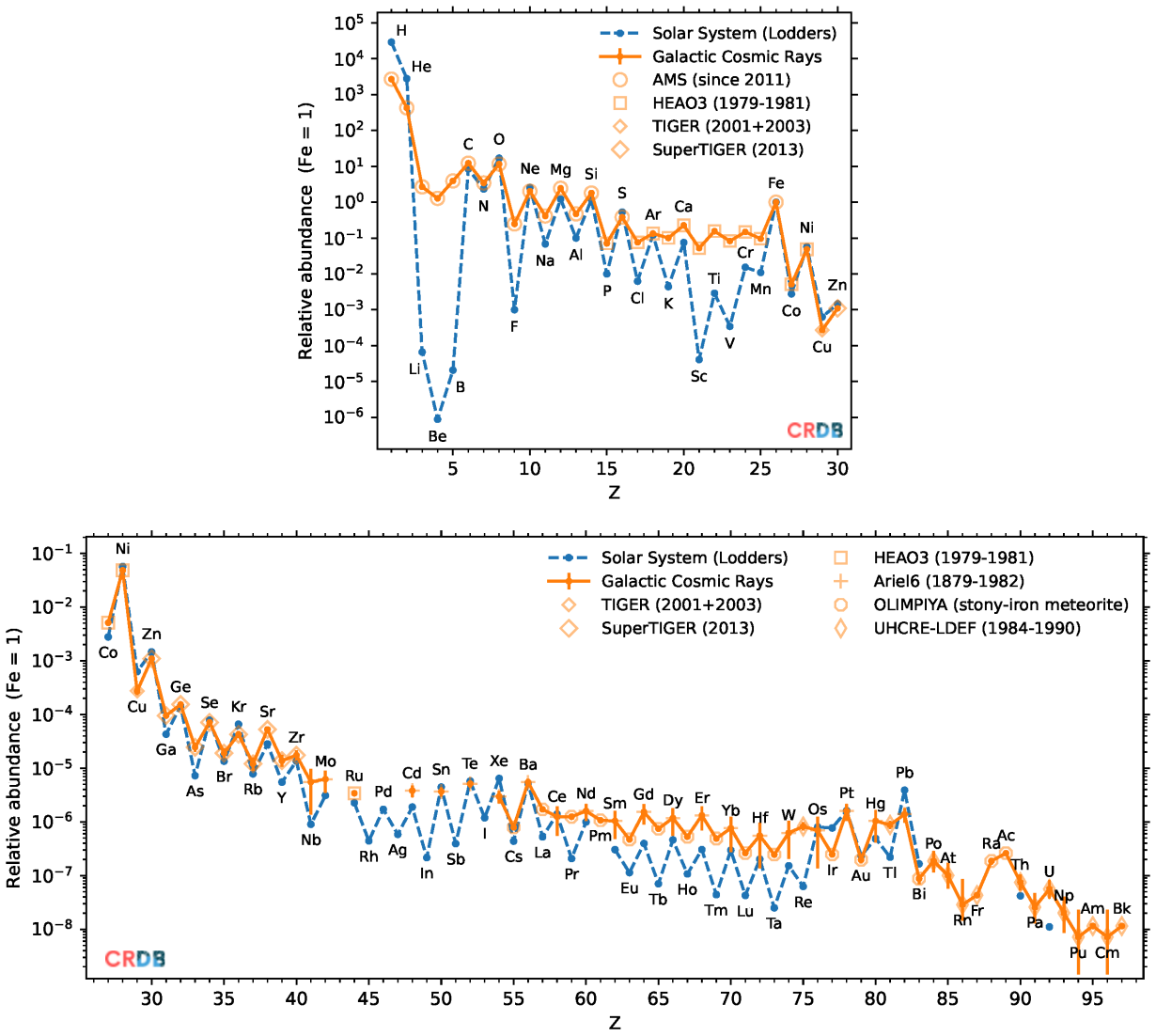

Figure 2: Relative abundance of elements in the SS (dashed blue line) [13] and in GCRs (solid orange line), arbitrarily normalised to Fe $\equiv$ 1. The even-odd pattern in the abundances is related to the even-odd nuclear stability effect. In the top panel, beside H and He, elements with near-matching abundances (names above the orange line) are mostly of primary origin, while SS/GCR $\ll 1$ (names below the blue line) are of secondary origin. In the lower panel, the pattern of GCR/SS abundances is less clear, owing to more uncertain data. GCR data were extracted and selected from CRDB [7–9], at $R = 5$ GV for $Z \leq 28$ and mostly at $E_{\rm k/n} \sim 1.5$ GeV/n ($\sim$3.82 GV) for the rest, rescaled to AMS flux ratio Fe(3.82 GV)/Fe(5 GV). Also, above $Z = 30$, only ratio x/y are measured with, for instance, y the flux of Fe, of all elements $Z \geq 55$, $Z \geq 70$, or some other charge ranges. These ratios were multiplied by Fe (AMS) and combinations of (Yb+W+Pt+Pb)/y flux data ratios to recover x. Data are AMS [3, 14, 15], HEAO3 [16], TIGER [17], SuperTIGER, [18], Ariel6 [19], OLIMPIYA [20] and UHCRE-LDEF [21].

The Galactic environment for GCR propagation is typically modelled as a cylinder with a radius of about 20 kpc and a vertical size or thickness, labelled Galactic halo (half-)height L, whose value is only poorly constrained between 2 and 10 kpc [25–27]. The value of L is especially relevant for the prediction of the flux of cosmic particles from DM annihilation, since it controls how much of the injected flux is retained in the diffusive environment [28–30]. In fact, the flux of positrons and $\overline{\mathrm{p}}$ from DM annihilation is directly related to the uncertainty on L (e.g., [30]). This halo size is determined from ratios of radioactive to stable secondary GCR species (e.g., [31]). The β-unstable species ^{10}Be, ^{26}Al, ^{36}Cl and ^{54}Mn, with half-live in the Myr range, of the order of the residence time in the Galaxy, are the considered species to constrain L [31–33]. Recent studies have focused on the $^{10}\mathrm{Be}/^{9}\mathrm{Be}$ ratio [25, 26, 34], and it was shown that nuclear cross-sections uncertainties on the production of Be isotopes were already limiting the interpretation of current data, and would similarly plague forthcoming CR measurements.

GCR $\overline{\mathrm{p}}$ are expected to be produced mainly as secondaries. The AMS experiment has measured the flux of $\overline{\mathrm{p}}$ between 0.5 GeV and 500 GeV, which is globally consistent with the expectations for a secondary origin [35, 36]. However, different groups have found a mild excess at around 10 GeV that could be explained by DM particles annihilating with a thermal cross-section into quarks [37, 38]. Nonetheless, the current uncertainties on the $\overline{\mathrm{p}}$ production cross-sections, as well as propagation and the correlations in the experimental data [39, 35], make these claims shaky and dependent on the data analysis approximations adopted [39, 40]. The NA49 experiment has released a preliminary measurement of antineutron ($\overline{\mathrm{n}}$) production from proton–proton (pp) collisions that is about 20% larger than the cross-section for $\overline{\mathrm{p}}$ production, corroborating earlier indications [41]. This data suggests an isospin asymmetry between the $\overline{\mathrm{p}}$ and $\overline{\mathrm{n}}$ production that is indeed relevant for the interpretation of the AMS $\overline{\mathrm{p}}$ flux, see e.g., [42]. The presence of an isospin asymmetry is expected considering the different production yields between the positive, negative, and neutral charged pions at low energies. However, regarding the $\overline{\mathrm{n}}/\overline{\mathrm{p}}$ asymmetry, no published and precise measurements have been performed so far, and no theoretical predictions have been calculated from fundamental assumptions. Currently, the magnitude of the isospin effect is the main theoretical uncertainty for the AMS data interpretation.

The search for antideuteron ($\overline{\mathrm{d}}$) and antihelium ($\overline{\mathrm{He}}$) nuclei in GCRs is one of the most promising indirect search strategies for DM [43]. The reason is that at kinetic energies below a few GeV/n, the secondary production is expected to be at least one order of magnitude smaller than the most optimistic yields associated to viable thermal relic DM models. However, theoretical predictions are not fully under control. Until recent years, CR antinuclei have been evaluated by considering simple coalescence models of antinucleons, whose free parameters are fitted to available antinuclei data from accelerator experiments. Currently, two data points from ARGUS (A Russian-German-United States-Swedish collaboration) at the Upsilon mass resonances [44], one data point from ALEPH (Apparatus for LEP PHysics) [45] at the Z resonance, and data from pp collisions with centre-of-mass energy $\sqrt{s}$ from 900 GeV to 13 TeV from ALICE (A Large Ion Collider Experiment) [46–51] are available. In a recent analysis, Ref. [52] reported that the main current theoretical uncertainties of the coalescence model resides in the $\overline{\mathrm{d}}$ production data from accelerator experiments. In fact, once different coalescence models are tuned using the same data point, e.g., the one from ALEPH, the theoretical predictions vary at most by 10–15% in the relevant energy range. Very precise measurements of the antinuclei production at centre-of-mass energies between 10 and 100 GeV are required to tune the coalescence parameters at the energies relevant for astroparticle physics. Alternatively, significant efforts have been made to develop a parameter-independent coalescence model, based on the Wigner function formalism. However, the nucleon yields and the nucleon emission source describing the relative distances at which nucleons are produced must be constrained by the data. This model has been applied successfully to predict $\overline{\mathrm{d}}$ spectra measured by ALICE in pp collisions at 13 TeV [53] and other collision energies [54].

On top of the rather uncertain production cross-sections of antinuclei, another uncertainty in their flux predictions is related to inelastic cross-sections, leading to antinuclei destruction during their propagation. Only recently a first measurement of such a quantity has been performed [55], but further progress is required to validate currently used parametrisations [56].

Another indirect mean to probe particle DM, albeit not strictly concerning charged GCRs, is through γ rays. The search for photons is not hampered by the diffusion on magnetic fields, and regions expected to exhibit high DM densities can be targeted by telescopes. So far, the deepest and most sensitive searches

have been conducted by Fermi-LAT [57]. Strong bounds have been obtained by targeting a number of dwarf spheroidal galaxies, whose mass is largely dominated by DM [58, 59]. A Galactic center excess (GCE) in Fermi-LAT data at GeV energies has been extensively investigated over the past two decades [60, 61]. Its angular and spectral features make it intriguingly similar to expectations from simple particle DM models, although alternative explanations invoking an unresolved millisecond pulsar population in the bulge have gained momentum over the years [62, 63]. For a DM origin of the GCE, a γ-ray signal is also expected from dwarf spheroidal galaxies: depending on the data analysis technique and the assumption on the DM abundance in these systems, they put weak or strong constraints on the DM hypothesis for the GCE, at a level comparable to $\overline{\mathrm{p}}$ constraints (see, e.g., Fig. 3b in [40]). One major issue for DM observations via γ rays is the modelling of the diffuse Galactic emission, typically produced by GCR nuclei scattering off the ISM and electrons interacting with the interstellar radiation fields. This emission, which unavoidably fills any line of sight, is dependent also on the nuclear production cross-sections.

2.1.2. Where are GCRs synthesised, accelerated, and how?

Both based on energetic considerations and multi-wavelength observations of their non-thermal spectra [64, 65], the main sources of GCRs have long been speculated to be supernova remnants (and, for leptons, also pulsar wind nebulae), with the role of star clusters, X-ray binaries or mergers of compact objects raised from time to time. The exact mechanisms that accelerate particles from these Galactic sources are not known, although variants of diffuse shock acceleration or magnetic reconnection are typically invoked (see, e.g., Ref. [66, 67]). The observation of fine spectral features in the proton, electron, and photon spectra are required to identify signatures of subtle non-linear effects in the acceleration process, or the relative weight of hadronic and leptonic components in the accelerated yields [68, 69]. The goal of identifying these signals is only meaningful, however, if uncertainties related to collisional physics, recently subject to re-evaluation [70, 71], are well under control.

Isotopic anomalies, such as the measured overabundance of the ^{22}Ne isotope over ^{20}Ne, may point to a prominent role of star clusters and superbubbles [72]. The detection of ^{60}Fe in GCRs, a short-lived radionuclide with a half-life of 2.6 Myr synthesised in core-collapse supernovae, further constrains the history and source location of the GCRs measured at Earth [73]. These topics are entangled with the understanding of the site of the r-process for the nucleosynthesis of ^{60}Fe, a transverse argument that links together the searches of ultra-heavy nuclei in GCRs with geophysical methods, our theoretical and experimental understanding of cross-sections in nuclear astrophysics, and the astrophysics of binary neutron star mergers and core-collapse supernovae (as revealed by the electromagnetic counterpart [74, 75] of the binary neutron star merger LIGO/Virgo GW170817 [76]).

2.1.3. GCR transport: refining the model or going beyond it?

Galactic energetic particles propagate in the Milky Way environment in their journey from the sources to the Earth. As detailed in Sec. 4.1, these particles are affected by both non-collisional processes and energy loss mechanisms, the latter being particularly relevant for electrons and positrons [77]. By a careful study of the energy spectra of these particles, notably the ratios of fluxes mostly produced by spallation in the ISM to fluxes mostly affected by source acceleration, one infers information on the rigidity and spatial dependence of the diffusion coefficient, which is ultimately informing on the physics of the Galactic magnetic turbulence [78, 79, 36]. The standard scenario assumes that GCRs propagate onto externally assigned magnetic field turbulence, onto which they do not backreact. Features of the CR data uncovered in the past decade (see Ref. [80] for an early review), such as the different slope of proton and He GCRs at energies below/above 100 GeV, may hint at a change of regime [81], where lower-energy GCRs would rather scatter onto the turbulence that they self-generate [82, 83]. However, non-factorisable spatial vs. power-spectrum properties of the turbulence may also accommodate the data [84]. It is not yet clear if the transport is close to quasi-homogeneous, rather than being localised in small volumes of the ISM [85–87]. Disentangling these possibilities is an extremely challenging effort, which may be completely hampered by cross-section uncertainties.

2.1.4. Going beyond the standard paradigm for the sources?

The source terms are typically factorised in a continuum function of $(t, \mathbf{x})$[2] in the Galaxy, times an often universal power-law energy spectrum. With respect to the chemical composition, normalised abundances tracing the ISM composition are often assumed, though the data seem to point at a preferential acceleration of refractory elements contained in interstellar dust [17, 88]. These various approximations can be questioned.

The stochastic distribution of astrophysical sources in space and time leads to spectral deviations from the average, see, e.g., [89–91]. Uncovering these effects at a statistical level requires however to keep errors associated to collisional effects at a percent-level or lower. This is especially true above 1–10 TeV, where specific spectral features may hint at a predominant contribution of one or few local sources.

Some isotopes and elements, such as deuteron [92] and lithium [93], seem to indicate some departure from the standard secondary origin [94, 95]. The robustness of these hints is however plagued by the significant uncertainties affecting their predicted yields from spallation cross-sections, so that the predictions are currently still consistent with the expectations thanks to the large uncertainties [96, 97].

One component that was supposed to be absent from primary sources until $\sim$15 years ago, but whose existence is now robustly accepted, is the positron flux [98–102]. Yet, its interpretation is still unclear. While DM could in principle contribute to the observed flux above 10 GeV, which provoked a significant early excitement for this measurement, the needed annihilation intensity is nowadays in conflict with other bounds. The two most physically motivated interpretations are related to the acceleration of electron and positron pairs from pulsar wind nebulae [103–107], or positrons produced and accelerated in supernova shocks sweeping the circumstellar medium [108, 109]. In order to infer as precisely as possible a primary component in the positron flux, a very precise estimate of the positron production cross-sections, which are used for calculating the secondary production, is mandatory [27].

To check the extent to which the GCR injection spectrum and the propagation properties are homogeneous over the Galaxy, one may want to probe GCR properties away from the location of Earth. This goal can be indirectly attained by studying the angular and spectral properties of the interstellar γ-ray emission (e.g., Ref. [110, 111]), probed by Fermi-LAT and, to lesser extent, by imaging Cherenkov telescopes. Its main contribution is due to the fragmentation of GCRs interacting with ISM atoms and their follow-up production of π^0, which subsequently decay into two photons (γ rays). Currently, data for the Lorentz invariant cross-section for the production of neutral pions are not sufficient to obtain a precise estimate of γ ray spectrum originating from π^0 production [70].

2.2. Transverse physics cases with overlapping nuclear cross-sections needs

Beyond the purely astrophysical and cosmological topics of interest summarised above, nuclear cross-sections also play a key role in other topics related to CRs. The key questions related to the time variation of GCRs are introduced below, and then some links to societal aspects, namely space exploration and medicine, are given.

2.2.1. Cosmogenic studies, impact on climate and life on Earth

For most cosmogenic nuclide studies, constant GCR fluences are assumed. There are, however, reasons why GCR fluences in the SS should vary over timescales of millions of years. *First*, the periodic passage of the SS through Galactic spiral arms might cause periodic GCR variations. In spiral arms, star formation and supernova rates are higher, leading to an increased GCR flux. *Second*, the SS periodically moves up and down the Galactic plane, which can affect the GCR flux. There are some arguments that such periodic GCR fluency variations can affect Earth's climate. At times of higher GCR fluences, there are higher ionisation rates in the upper atmosphere, which can produce higher cloud coverage. This finally could produce a cooling effect and even start an ice age. This would most likely affect the origin and evolution of life. *Third*, as the SS occasionally moves through dense molecular clouds, the heliosphere can shrink and, as a consequence, GCR modulation is diminished or disappears completely. Such an episode, in which the Earth might have been even outside the heliosphere and directly exposed to the ISM of the dense molecular cloud, would

[2] Usually, stationary conditions are considered and no time-dependence is assumed.

significantly affect the evolution of life on our planet. It has been proposed that the SS might have passed such a dense molecular cloud ~ 2 Myr ago (e.g., [112]). There are some arguments that cosmogenic nuclide studies in iron meteorites provide evidence for periodic GCR fluency variations (e.g., [113–115]). While some studies were supportive, many subsequent investigations have questioned the original hypothesis [116, 117] and/or the interpretation of the database [118]. In addition to periodic GCR intensity variations, there are also indications for a onetime and sudden increase in the GCR intensity with a higher flux in the past several million years, relative to the long-term average over the past 500–1000 Myr [119–121, 118].

To prove or reject GCR fluency variations, cosmogenic nuclides stored in terrestrial archives and produced in meteorites or planetary surfaces provide a powerful tool or even can be considered as the only diagnostics. The half-lives of the different radionuclides then correspond to the different time intervals the dating system is sensitive to. For example, the ^{14}C activity concentration is sensitive to the last $\sim$20 kyr, ^{53}Mn to the last $\sim$15 Myr, and ^{40}K to the entire age of the SS. For all these studies, a precise knowledge of the cosmogenic production rates is mandatory, and such production rates can only be determined based on an accurate, reliable, and consistent cross-section database for the relevant nuclear reactions [122].

2.2.2. Space exploration

Uncertainties in predicting radiation-related health effects due to exposure to the space radiation environment are one of the major challenges for human spaceflight beyond Earth orbit [123–125]. In shielded environments, light ions (i.e., isotopes of H and He) and neutrons make the largest contributions to the dose equivalent received by astronauts. The largest uncertainties in predicting radiation doses and the associated health risks stem from a limited understanding of radiation biology and from disagreements in transport codes [126–128]. The latter is primarily due to inadequate knowledge about the light-ion production cross-sections [129, 130], which also constitute the largest gap in currently available nuclear data [131]. It is therefore imperative that these cross-sections be measured to place space radiation protection on a solid foundation.

2.2.3. Hadrontherapy

Hadrontherapy treats deep-seated tumours using charged particle beams, such as protons and ^{12}C. Indeed, these particles exhibit a favourable depth-dose distribution in tissue, characterised by a peak in energy deposition (the Bragg peak) near their end range, which coincides with the tumour's location. Additionally, C and O ions demonstrate enhanced biological effectiveness, making them suitable for treating radio-resistant tumours. However, nuclear interactions between the ion beam and patient tissues can result in the fragmentation of projectiles and/or target nuclei. These interactions must be carefully considered when designing treatment planning systems (TPS). Currently, there is a significant lack of experimental data on nuclear fragmentation involving light fragments ($Z < 10$) within the energy range commonly used in hadrontherapy of 80 MeV/n to 400 MeV/n. Such data would be invaluable for further optimisation of TPS in hadron therapy [132].

2.3. Further astroparticle physics cases affected by cross-section uncertainties

Two additional examples where cross-sections data bridge the astrophysics and high-energy physics communities are presented in this section. Indeed, not only better cross-section data enhance our ability to interpret CR data, but also to deepen our understanding of dense and compact astrophysical objects and environments.

2.3.1. Origin of ultra-high energy cosmic-rays

Unveiling the composition and spectrum of UHECRs would reveal the most energetic accelerators in the Universe and the nucleosynthesis processes in the most hostile environments (e.g., the active galactic nucleus (AGN), compact binary mergers, collapsars). Mostly nuclei up to $A = 56$ are considered for the interpretation of current data, but heavier nuclei could play a role for the observed trend of the mass composition at the highest energies [133]. The results from the Pierre Auger Observatory and TA (Telescope Array) have stimulated several studies focusing on the nuleosynthesis [134], acceleration and multi-messenger

secondary emissions [135, 136]. Recent multi-messenger observations [137, 138] strongly indicate that the discovery of the sources is imminent, but the cross-sections are still one of the limiting factors [139]. UHECRs generate extensive air showers, whose precise modelling hinges on accurate hadronic cross-sections, well beyond energies accessible at current accelerators. Uncertainties in these cross-sections propagate directly into the interpretation of shower development, energy spectra and composition. Improved data are therefore crucial to refining theoretical frameworks and reducing systematic uncertainties in UHECR observations at facilities like the Pierre Auger Observatory and TA.

2.3.2. The equation-of-state of neutron stars and femtoscopy

Neutron stars are the most compact material objects in the Universe, with extreme conditions of pressure and density, possibly undergoing phase transitions during their evolution. These extreme properties can be probed by astronomical observations [140]. The outer core of neutron stars consists of matter composed by nucleons, electrons and muons, in a strongly interacting regime, where sophisticated models describing the correlations among two and three nucleons are necessary. The inner core is the least understood, and there could be charged mesons, such as pions or kaons in a Bose condensate, or other heavier baryons with strangeness (e.g., hyperons). At the highest densities, quarks might be deconfined. The recent NICER (Neutron Star Interior Composition Explorer) observations of pulsed X-ray emission from millisecond pulsars [141–144] provide the first data to constrain the equation-of-state from the reconstructed radius–mass diagrams. While the exact matter content and interactions in the neutron star are not the only ingredients of the modelling, they are one of the limiting factors. Femtoscopy probes hadron–hadron interactions, including multi-body forces, at distance scales unresolvable by direct scattering experiments. Precise cross-section measurements for particles containing strange quarks are particularly relevant for modelling the composition and equation-of-state of neutron stars, where strangeness and multi-body forces can drastically alter matter at high densities.

3. Direct detection CR experiments in a high-precision era: highlights and frontiers

Direct detection CR experiments – as opposed to indirect detection via air-showers arising from interactions of CRs in the Earth atmosphere, or other techniques (not covered here) – have probed the tens of MeV to hundreds of TeV energy range. Almost all CR data collected so far are from the Earth neighbourhood and are thus affected by the solar modulation cycle [145–148]. The modulation of fluxes is a few percents above hundreds of GeV/n, but critical at low energy, where the tens of MeV/n top of atmosphere (TOA) energies measured by balloons or satellites correspond to $\lesssim$GeV/n interstellar (IS) energies. The only IS data, and very significant ones, are those of the Voyager 1 and 2 detectors, launched in 1977, which crossed the heliopause in August 2012 and November 2018 respectively, providing for the first time (and probably for a long time) the only direct measurements outside the solar cavity. These tiny detectors (hundreds of cm^3) provided fluxes of elements in the range of a few tens to a few hundreds of MeV/n (IS energies) with a precision ranging from 5% for H up to 10% for Fe. The data for $e^- + e^+$ are at even lower energies and with a precision of 10% [149–151].

In the last two decades, large-acceptance sophisticated particle detectors have been launched onboard satellites and space stations for long-duration missions, allowing precision measurements of species-resolved CR spectra in the energy range from GeV to hundreds of TeV (TOA energies). Some of these detectors have run over 10 years or more – e.g., PAMELA (Payload for Antimatter Matter Exploration and Light-nuclei Astrophysics) and AMS (Alpha Magnetic Spectrometer) – and provided measurements of specie-resolved monthly and daily fluxes of particles and nuclei [152–159] crucial for space weather, space radiation and solar modulation studies.

To measure CRs above GeV energies, two experimental approaches can be distinguished: magnetic spectrometers, as BESS (Balloon-borne Experiment with Superconducting Spectrometer) on 9 balloon flights from 1993 to 2002 [160], BESS-Polar-I (flown on a balloon in 2004) and BESS-Polar-II (flown on a balloon in 2007) [161], PAMELA (satellite mission 2006–2016) [162, 163], AMS (operating on the International Space Station (ISS) since 2011) [3], HELIX [164] (High Energy Light Isotope Experiment, first balloon

flight in May 2024 for ∼6 days); and calorimeters, as *Fermi*-LAT (Large Area Telescope, satellite operating since 2008) [57], DAMPE (DArk Matter Particle Explorer, satellite operating since 2015) [165], CALET (CALorimetric Electron Telescope, operating on the ISS since 2015) [166], NUCLEON (satellite operated between 2014 and 2017) [167] and ISS-CREAM (Cosmic Ray Energetics And Mass, operated on the ISS between 2017 and 2019) [168]. Magnetic spectrometers can distinguish particles from antiparticles, and hence they can measure the spectra of positrons, $\overline{\mathrm{p}}$, and search for antinuclei in CRs. They measure the rigidity, i.e., the ratio between momentum and charge, of the incoming CR particle. Their maximum detectable rigidity (MDR), defined as the rigidity at which the relative rigidity resolution is equal to 1, is set by the intensity of the magnetic field provided by the magnet and the lever arm of the instrument. The largest magnetic spectrometer ever deployed, AMS, reaches an MDR of 2 TV for protons, 3.2 TV for He nuclei, and 3.5 TV for heavier nuclei [3].

Magnetic spectrometers combined with detectors able to measure the velocity, such as time-of-flight (TOF) systems or ring-imaging Cherenkov (RICH) counters, have the ability to measure isotopic compositions of nuclei by reconstructing the mass from the rigidity and the velocity measurements. Current experiments employing this technique, AMS and HELIX, can measure isotopic fluxes with accuracies of $\sim 10\%$, up to a kinetic energy per nucleon of about 10 GeV/n [169, 170, 164]. Both PAMELA and AMS have been equipped with an electromagnetic calorimeter to accurately determine the energy of electrons and positrons, with a resolution of a few percent over the entire energy range of their measurements. In the AMS experiment, the energy of electrons and positrons is determined with accuracies $\lesssim 2\%$ from 30 GeV to 500 GeV and $<4\%$ above, up to 3 TeV [171]. The maximum energy that can be measured by electromagnetic calorimeters is mainly determined by their depth. The depth of the AMS calorimeter is 17 radiation lengths, allowing measurements of energies of electrons and positrons up to 3 TeV [171]. Because of the rapid decrease with increasing energy of CR fluxes (see Fig. 1), flux measurements at the highest energies require, in addition to an extended upper energy, larger acceptance detectors operated over long-duration missions.

The past decade marked the era of active deployment of large-area calorimetric CR experiments in space. In 2015, the DAMPE [165] satellite was launched into orbit and the CALET [172] detector was delivered to the ISS. Both instruments feature deep total-absorption calorimeters, with an integrated detector thickness of $\gtrsim 30$ radiation lengths. The acceptance for electron detection with DAMPE and CALET is $\sim 0.3\,\mathrm{m}^2 \cdot \mathrm{sr}$ and $\sim 0.12\,\mathrm{m}^2 \cdot \mathrm{sr}$, respectively. Due to their thick fine-segmented calorimeters, the two detectors have excellent energy resolutions of about 1.2% and 2%, respectively, at >100 GeV energies. With their relatively large acceptance, this allows the combined electron and positron spectrum to be probed up to ~ 10 TeV energies. Next, the ISS-CREAM [168] detector – legacy of the balloon-flight CREAM [173] – is another calorimetric experiment that was deployed on the ISS in 2017. Unlike DAMPE and CALET, it utilises a sampling calorimeter alike the one of AMS, with scintillating fibres interleaved with passive tungsten layers, having a total thickness of 21 radiation lengths, and a geometric factor of $\sim 0.27\,\mathrm{m}^2 \cdot \mathrm{sr}$, close to the one of DAMPE. Thanks to their relatively large acceptance, calorimetric experiments like DAMPE, CALET and ISS-CREAM are capable of measuring individual CR nuclei spectra up to hundreds of TeV.

In this section, the status in terms of energy range and precision, and the recent progresses made by CR experiments, are discussed for all GCR species (Sec. 3.1). Then, the near and far future projects are listed (Sec. 3.2). The discussion is accompanied by a timeline of all datasets available for these various species. Figures 3 to 7 illustrate the increase of precision and upper energy of the CR experiments and data over time. Figure 8 also provides a summary view of ongoing and future experiments.

3.1. Energy range and precision of current data

3.1.1. Proton and He fluxes

AMS has provided precision measurements of the proton spectrum as a function of rigidity from 0.5 GV to 1.8 TV, with accuracies of 1% at 100 GV and $< 5\%$ beyond 1 TV, and for the He spectrum from 1.92 to 3 TV with uncertainties of 1% at 100 GV and $< 4\%$ at 1 TV [3]. A progressive spectral hardening has been observed around 200 GV, with a different rigidity dependency between proton and He, confirming earlier observations by PAMELA [174] and CREAM [173, 175]. The proton-to-helium ratio decreases with increasing rigidity [3]. Results of CALET and DAMPE confirm the spectral hardening in both proton and

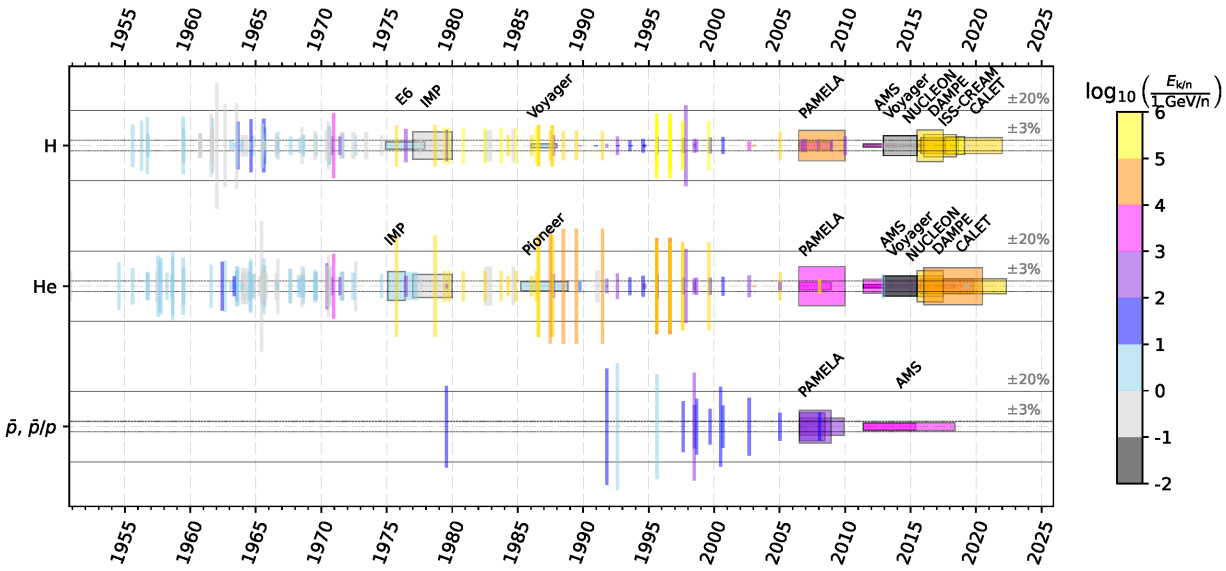

Figure 3: For H, He and $\overline{\text{p}}$ (top to bottom), timeline of the highest energy decade (colour-coded) and best precision reached (height of the bars) in CR experiments, based on the data compiled in the CRDB [7–9]. The width of the bars indicates the integration time of the CR experiments: very thin widths correspond to balloon flights (few days flights at most), and larger widths correspond to satellite or space (or more rarely ground-based) experiments. The best precision is always achieved at low energies, not at the highest (colour-coded) energy reached. The name of experiments for which datasets were collected over several months or years is indicated on top of the relevant period; some experiments like AMS have several datasets published with overlapping periods (same start date but longer integration time), but their name is indicated only once to avoid overlapping text. Note that the Voyager data after 2015 are the only datasets outside the solar cavity.

He CRs [176–179] and the decrease of the proton-to-helium ratio up to about 10 TeV/n. All experiments consistently show that the proton spectral index is about 0.1 softer than that of He, with no significant structures in the proton-to-helium flux ratio. While both calorimetric experiments demonstrate a higher value of the spectral break position, compared to AMS, at about 500 GeV for protons, the results for all the experiments are compatible within the uncertainties.

At higher energies, CALET, DAMPE and ISS-CREAM demonstrate a softening structure in proton and He spectra at about 10 TeV/n [176–179, 168], as previously indicated by CREAM [175, 173]. Recent updates from DAMPE and CALET indicate that the positions of both hardening and softening structures favour the charge (rigidity) dependence of the breaks, although mass (energy per nucleon) dependence is not ruled out [176, 180]. It has to be noted that while calorimetric experiments measure particle kinetic energy, the conversion to energy per nucleon requires knowledge of the isotopic composition, which is normally taken from available measurements at low-energy, below few GeV/n, and extrapolated to higher energies. The limited knowledge of isotopic compositions is considered as an additional source of systematic uncertainty in the interpretation of calorimetric data on nuclei. At even higher energies, a hint of a new structure – hardening at about 150 TeV – is seen in the recent data of DAMPE [180] and ISS-CREAM [168]. The DAMPE measurement of combined p+He spectrum, profiting from higher statistics and a cleaner event selection, reaches 0.5 PeV [181]. ISS-CREAM results reach even higher energy, 0.65 PeV for proton and $\sim$1 PeV for He, although with much larger uncertainties [182].

3.1.2. Antiprotons and searches for antinuclei

Antimatter is a tiny component in CRs. In the GeV–TeV energy range, there is only 1 antiproton per 10000 protons. The $\overline{\text{p}}$ spectrum has been measured by balloon-borne (e.g., BESS-Polar-I and II flights [183, 184]) and satellites experiments (e.g., PAMELA [185–187]). The most precise information is based on the 6.5 yr of AMS data, with accuracies $<4\%$ in the rigidity range 1 GV to 100 GV and $\sim$40% at 500 GV.

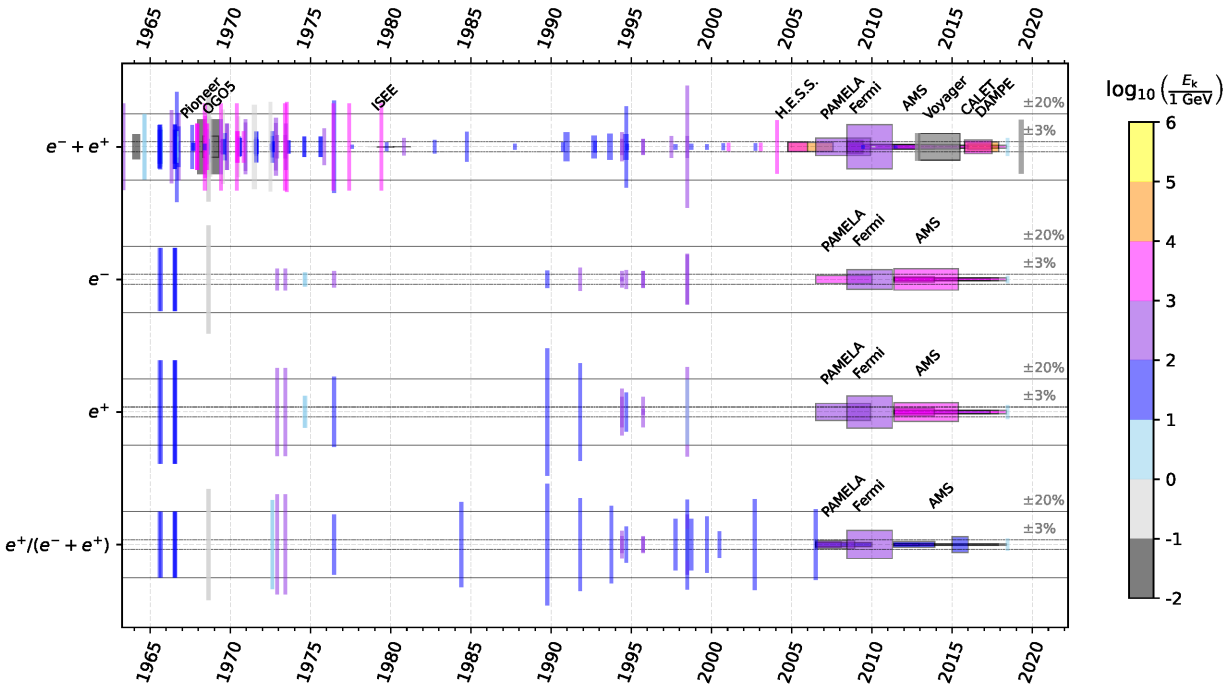

Figure 4: Same as Fig. 3 but for leptons (including the positron fraction, bottom row).

Statistical uncertainties still dominate above 125 GV [3]. The low-energy $\overline{\mathrm{p}}$ spectrum will soon be explored by the GAPS (General AntiParticle Spectrometer) experiment [188], see Sec. 3.2.4. GAPS will measure the $\overline{\mathrm{p}}$ flux in the kinetic energy per nucleon range from 0.07 to 0.21 GeV/n, where signals from hidden sector DM models are expected [189].

So far, no observation of antinuclei heavier than $\overline{\mathrm{p}}$ has been confirmed in CRs. The BESS, BESS-Polar-I and BESS-Polar-II magnetic spectrometer series of balloon flights, have extensively searched for $\overline{\mathrm{d}}$ in the kinetic energy per nucleon range from 0.163 to 1. GeV/n, setting the best upper limit on the $\overline{\mathrm{d}}$ flux in this energy range with the BESS-Polar-II flight at $6.7 \cdot 10^{-5}\,(\mathrm{m^2\,s\,sr\,GeV/n})^{-1}$ at 95% CL [190]. The BESS collaboration has also set the current best upper limit on the $\overline{\mathrm{He}}$ to He flux ratio, in the rigidity range from 1 to 14 GV, by combining the results from the BESS, BESS-Polar I and BESS-Polar-II flights. This limit is $6.9 \cdot 10^{-8}$ at 95% CL [161]. So far, AMS has reported few $\overline{\mathrm{d}}$ and $\overline{\mathrm{He}}$ candidates, both $^3\overline{\mathrm{He}}$ and $^4\overline{\mathrm{He}}$ [191], still needing further studies before an observation can be confirmed.

3.1.3. Electrons and positrons fluxes

To efficiently separate positrons from protons and $\overline{\mathrm{p}}$ from electrons, magnetic spectrometers are combined with electromagnetic calorimeters, as in PAMELA and AMS, and with transition radiation detectors, as in AMS. Electromagnetic calorimeters, beside distinguishing electron-like from proton-like particles, allow the determination of the energy of electrons and positrons with a resolution of a few percents. The measurements of the separate spectra of positron and electrons by magnetic spectrometers, PAMELA up to 300 GeV, and AMS up to 1 TeV, have ascertained that the rise of the positron fraction above $\sim$10 GeV observed by earlier experiments is due to an excess of high-energy positrons. The high-precision of the AMS measurements (4% at 100 GeV and $<10\%$ up to 500 GeV for the published results based on 6.5 years of data, still dominated by statistical uncertainties above 30 GeV) has also revealed a rapid decrease of the positron flux above $\sim$300 GeV compatible with an exponential energy cut-off in the TeV energy range [101, 3]. AMS has also released a high-precision measurement of the electron spectrum in the energy range from 0.5 GeV to 1.4 TeV ($\leq$2% up to 130 GeV and $<5\%$ up to 500 GeV), observing a hardening above $\sim$40 GeV but no high-energy

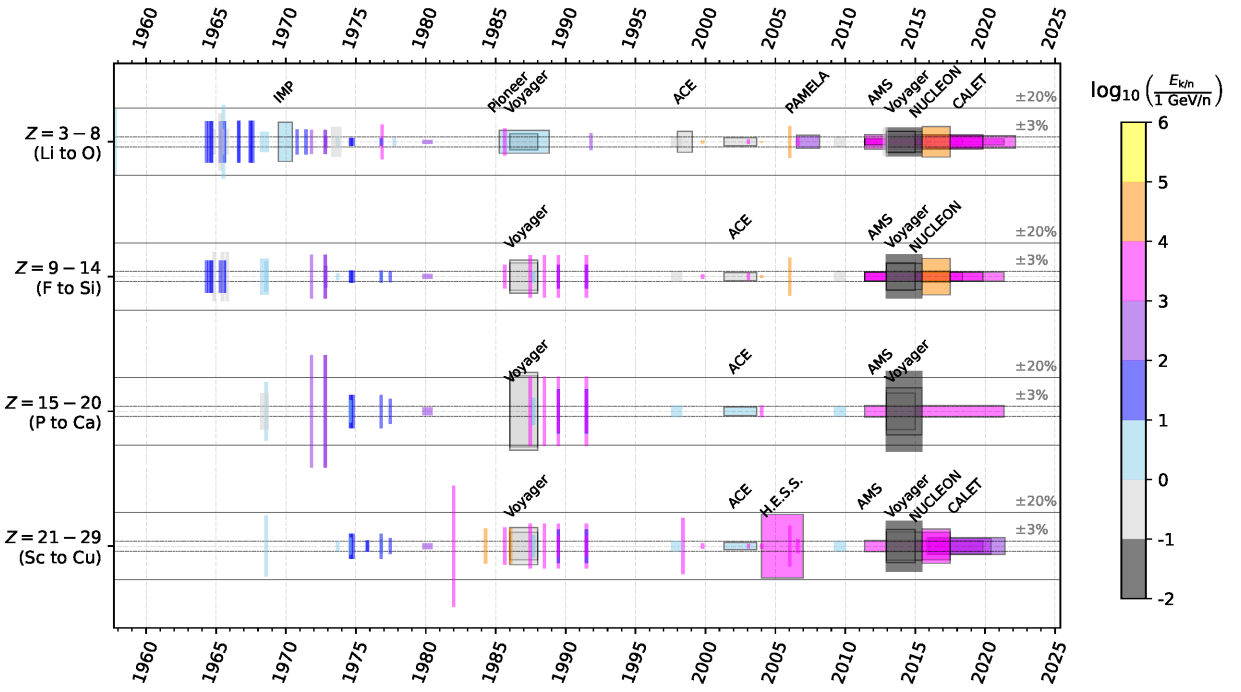

Figure 5: Same as Fig. 3, but for individual elements of broad groups (for the sake of compactness) of heavy nuclei with $Z < 30$. For each of these groups, the best precision and highest energy among the elements measured is reported: not all elements in these groups have been measured, and not all experiments have the capability to measure all elements of a given group, usually because of too low abundances.

cut-off [192, 3]. Analysis of the arrival directions of positrons and electrons with the AMS data has shown that both are compatible with the hypothesis of an isotropic flux, with upper limits on the amplitude of dipole anisotropy of 0.019 for positrons and 0.005 for electrons at 95% CL above 16 GeV [3, 193].

Results of the CR electron plus positron spectrum from CALET and DAMPE, reaching 4.6 and 7.5 TeV, respectively, reveal a remarkable softening at $\sim$1 TeV, consistent between the two experiments [194, 195]. While it is difficult to corroborate whether the observed spectral structure is due to the transition from a multiple source population to an individual GCR accelerator, further measurements towards 10 TeV and higher energies will be crucial to clarify the CR electron picture [196]. One of the key challenges in the realisation of such measurement with the existing experiments, such as DAMPE, is the rejection of the overwhelming proton background contamination, which increases with energy [197].

3.1.4. Heavy elemental fluxes (Z=3–30)

For $Z \leq 30$, ACE-CRIS (Advanced Composition Explorer Cosmic Ray Isotope Spectrometer) [198, 199] and Voyager have provided fluxes below hundreds of MeV/n at 3–5% precision, while AMS, CALET and DAMPE are measuring the individual spectra of nuclei in the hundreds of GeV to multi-TeV region. So far, AMS has published the rigidity spectra of all nuclei from He to Si, of S, and of Fe nuclei in the rigidity range from $\sim$2 GV to 3 TV [3, 200, 201, 14, 15], with typical accuracies at 100 GV of 3% to 4% for nuclei from Li to O, and 4% to 6% for heavier nuclei. Before AMS, the previous experiment which provided a comprehensive measurement of such a large range of nuclei was the HEAO3 satellite, flown between 1979 and 1980, with Be to Ni fluxes from 0.6 to 35 GeV/n at precision of $\sim$10% [16]). At 1 TV the AMS measurements of the primary nuclei, C, O, Ne, Mg and Si, have accuracies of 6% to 7%. For the less abundant Ne, Mg and Si nuclei, the statistical errors still dominate above 1.2 TV [15]. The AMS measurement of the Fe spectrum at 1 TV has an accuracy of 10%, but it is still dominated by statistical errors above 300 GV [14].

Slopes for primary and secondary species. AMS has found that above 60 GV the rigidity spectra of C and O are identical to He [202], and that the rigidity spectra of the heavier primaries Ne, Mg, and Si are distinctly different from the He spectrum [203]. Above 86.5 GV, Ne, Mg, and Si spectra have identical rigidity dependencies, they progressively harden above 200 GV, but less than the He, C and O spectra [203]. Instead, the Fe spectrum above 80.5 GV follows the same rigidity dependence as the light primary He, C and O [14]. AMS has found that light secondary nuclei, Li, Be and B, have identical rigidity dependencies above 30 GV, and that they harden above 200 GV with twice the hardening observed for C and O [204] hinting at a propagation origin (break in the diffusion coefficient) of the spectral hardenings. The accuracy of the latest AMS measurement of the F spectrum, recently updated with 10-year dataset, is 6% at 100 GV and 18% at $\sim$1 TV, dominated by statistical errors above $\sim$90 GV [15]. AMS has found that the rigidity spectrum of the heavier secondary F nuclei is different from the spectra of the light secondary Li, Be and B, and that the secondary-to-primary ratio F/Si is significantly different from the light secondary-to-primary ratios, B/O or B/C [200]. Alternative interpretations have been proposed for this observation, as the presence of a primary F component [205] or to spatially dependent diffusion [206]. However, model calculations of the expected secondary F spectrum with similar accuracy as the AMS measurement are currently out of reach because of uncertainties or lack of measurements of relevant nuclear fragmentation cross-sections [207].

Multi-TeV domain. The extension of B, C, O and Fe nuclei measurements to the multi-TeV domain has been recently advanced by CALET and DAMPE. The CALET results on B [208], C and O [209] reach about 3 TeV/n, indicating a spectral hardening in both CR primaries (C and O) and CR secondaries (B) at around 200 GeV/n, consistent with AMS. The CALET B/C and B/O ratios, similar to AMS, confirm that the break in secondaries is about twice as large as in primaries. Notably, while CALET B, C and O fluxes show an overall shape consistency with AMS, there is an apparent discrepancy in normalisation, with CALET fluxes being $\sim$20% lower than AMS fluxes. This difference is not accounted for by systematic uncertainties and, as was reported at this conference [6], is not attributed to the choice of the hadronic model (MC generator) used for the interpretation of CALET data (see also Sec. 4.4.4). At the same time, the normalisation errors cancel out in the B/C and B/O ratio calculations, resulting in very good normalisation match of CALET with AMS. Also, recent DAMPE results on the B/C and B/O flux ratios confirm the B/C and B/O breaks and find a hardening position at 100 ± 10 GeV/n [210]. This result is consistent with a hypothesis of a $\sim$200 GV universal CR hardening, and agrees well with the accurate measurements of spectral breaks in AMS data [211, 212, 204, 3]. For higher mass elements, CALET's Fe spectrum reaches 2 TeV/n and is consistent with a power law behaviour with coefficient $\gamma \sim 2.6$ and no indication of hardening [213]. CALET's Fe spectral shape is very similar to the AMS result, but is 20% lower in normalisation. The CALET Ni flux [214] measurement is still limited to below 240 GeV/n. It shows no structure in the spectrum along with a flat Ni/Fe ratio of about 0.06 in the entire energy range of the measurement, consistent with the expectation of similarity in acceleration mechanisms of primary GCRs.

3.1.5. Ultra-heavy elemental fluxes ($Z > 30$)

Fluxes above $Z = 30$ are about 10^4 to 10^5 lower than Fe [215], with the rarest actinides ($Z \geq 90$) about 10^7 times less abundant than Fe [216] – see the bottom panel of Fig. 2. Standard techniques used for measurements of $Z < 30$ CRs can still be pushed to cover the $30 \leq Z \leq 60$ region [215], but they are not able yet to provide fluxes, only ratios: the ACE-CRIS satellite (Si scintillators) collected data for more than 20 years to unveil the isotopic content of GCR elements $Z = 30$–38 at a few hundreds of MeV/n [217]; the SuperTIGER balloon-borne experiment is measuring elemental fractions up to $Z \leq 56$ [218]. For heavier species, passive detectors are exposed for long durations (several years), and chemical modifications made in a solid state nuclear track detector (by passing CRs) are etched in a chemical agent to reconstruct the charge and velocity of the CR. Very few datasets exist from $\lesssim$ 1990s experiments, with integrated measurements around GeV/n CR energies. These datasets are from Ariel 6 [19], HEAO3-HNE [219], UHCRE-LDEF [21], skylab [220] and Trek [221]. Some recent original data come from OLIMPIYA [20, 222], where olivine crystals contained in stony-iron meteorites (pallasites) are used as CR detectors. They give, however, only integral measurements over energies and irradiation time over up to hundreds of Myr.

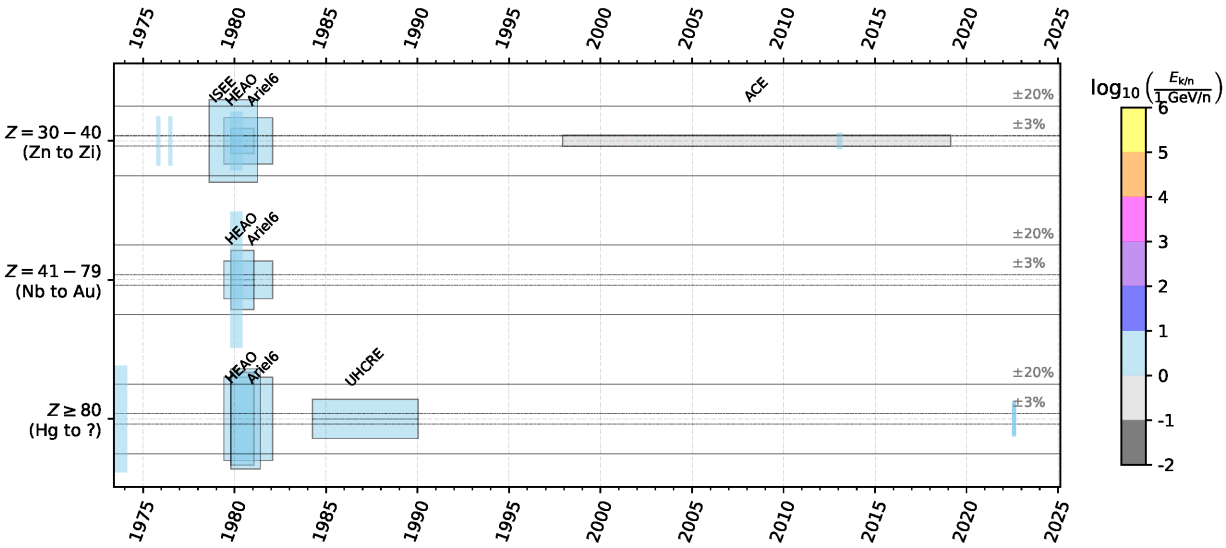

Figure 6: Same as Fig. 3 but for ultra-heavy nuclei. For the latter, only ratios are measured for individual elements below $Z = 40$, and pairs or range of elements for $Z > 40$. The question mark in the last group ($Z \geq 80$, Hg to ?) highlights the fact that the current situation is not completely clear regarding the heaviest CR species detected; the 2023 data points come from the OLIMPIYA stony-iron meteorites (see text for details).

3.1.6. Isotopic fluxes and ratios

Elements in GCRs are almost all mixtures of two or more isotopes. Isotopic composition measurements are still scarce and limited to low energies, below about 2 GeV/n in most cases.

Light isotopes. Recent measurements of H to Be isotopes have superseded all previous measurements in terms of precision and energy coverage (see Fig. 7). The so-called quartet isotopes include the dominant ^{1}H and ^{4}He species of primary origin, and ^{2}H and ^{3}He isotopes expected to be of secondary origin. PAMELA has measured them from a few hundreds of MeV/n to GeV/n at a precision of 10%, pushing their analysis to get ratios of some Li, Be, and B isotopes [223–227]. AMS has measured ^{2}H, ^{3}He and ^{4}He fluxes in the rigidity range 1.9 GV to 21 GV with accuracies of 3%, $\lesssim$ 3%, and $\lesssim$ 1%, respectively [92]. While the ^{3}He/^{4}He flux ratio exhibits a typical secondary-to-primary rigidity dependence, $\propto R^{-0.289\pm0.003}$, the ^{2}H/^{4}He ratio follows a distinct power law $\propto R^{-0.108\pm0.005}$. AMS has also presented preliminary measurements of ^{6}Li and ^{7}Li fluxes, roughly in equal amount in CRs, from 1.9 GV to 25 GV with accuracies $\sim$3% at 10 GV, which do not support the hypothesis of a primary component in ^{7}Li [228].

CR Be nuclei are secondaries, composed of three isotopes (^{7}Be, ^{9}Be and ^{10}Be), with ^{10}Be decaying to ^{10}B with a half-life of 1.39 Myr, probing the residence time in the Galaxy. Current measurements of the ^{10}Be/^{9}Be ratio include low-energy data at 100 MeV/n with a 20–30% uncertainty (ACE-CRIS [229], Ulysses [230] and Voyager [231]), and a couple of GeV/n data points from both PAMELA [225, 226] and the ISOMAX balloon-borne superconducting spectrometer [232], with a much poorer precision. AMS has presented at recent conferences preliminary measurements of the ^{7}Be, ^{9}Be and ^{10}Be fluxes as functions of kinetic energy per nucleon, ranging from 0.4 GeV/n to 12 GeV/n [228]. The accuracy of the AMS preliminary measurement of ^{10}Be/^{9}Be is $\sim$10%. Complementary results are also expected from HELIX [164] (see Sec. 3.2.3).

All these great and recent experimental achievements, however, cannot be exploited at full potential yet, as the interpretation of the light isotopes are particularly plagued by scarce nuclear data and large uncertainties [97, 233].

Heavier isotopes. For isotopes in $Z = 6$–30, only ratios are measured, and only at a very low energy below a few hundreds of MeV/n, with a precision of 10–20%. These measurements are all from pre-1980's balloon flights and pre-2000's space experiments (ACE-CRIS, CRRES, ISEE, Ulysses, Trek, Voyager) integrating

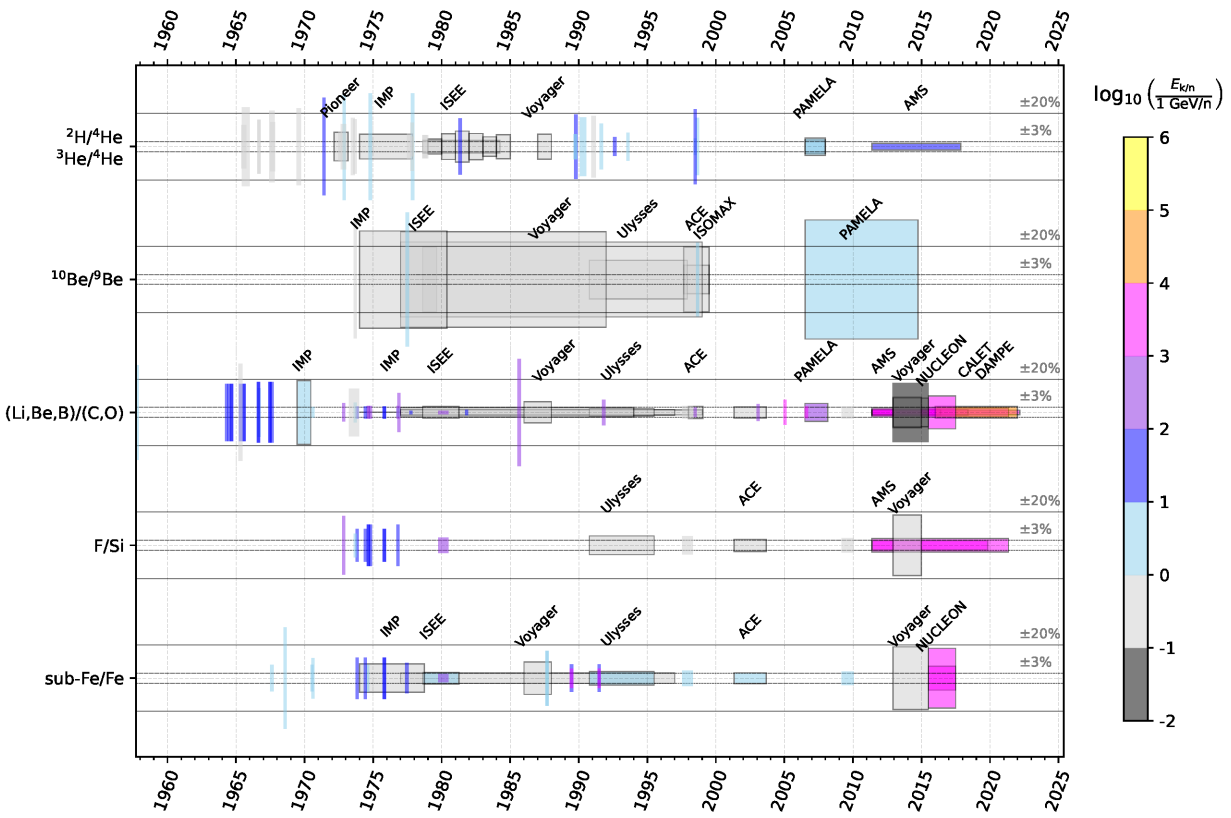

Figure 7: Same as Fig. 3 but for secondary-to-primary ratios currently used for GCR analyses. For compactness, we grouped together d/^{4}He and ^{3}He/^{4}He (top panel) and ratios of Li, Be, and B to C or O (third panel), but the precision and datasets are not exactly the same for these individual ratios (e.g., d is particularly difficult to separate from the dominant p, while a good charge separation is needed to isolate Li from the much more abundant He); sub-Fe (in the sub-Fe/Fe ratio, bottom panel) corresponds to Z = 21–23 (or sometimes Z = 21–25) and was used in almost all past experiments because of their limited charge resolution/statistics, but AMS will provide individual fluxes and ratios for this charge range. The GCR clock ratio ^{10}Be/^{9}Be (second panel) is the best measured ratio to date compared to other GCR clocks and other relevant radioactive GCR species (see text for details).

the signal over many years. A systematic survey of these isotopes is hence missing, with the main efforts concentrated on key isotopic ratios: GCR clocks (i.e., β-unstable species similar to ^{10}Be) via the ratios ^{10}Be/^{9}Be (see above), ^{26}Al/^{27}Al [234–236, 229], ^{36}Cl/Cl [237, 238, 229] and ^{54}Mn/Mn [239–243, 229]; nucleosynthesis clocks (i.e., unstable species constraining the time elapsed between their nucleosynthesis and acceleration, expected to be ∼Myr) with electron-capture unstable species (^{55}Fe, ^{57}Co, ^{59}Ni, and their daughter) [244, 239, 245, 243, 246] or the β-unstable ^{60}Fe recently detected by ACE-CRIS (cumulating ~ 17 yrs of data) [247]; electron-capture decay species sensitive to GCR re-acceleration (ratios of ^{49}V and ^{51}Cr and their daughters) [244, 243, 248]; source abundance anomalies (i.e., isotopes whose GCR abundance departs from SS ratios) with the striking ^{22}Ne/^{20}Ne anomaly [249–255] and possibly ^{58}Fe/^{56}Fe [245, 256].

For elements beyond Ni, the only datasets are $Z \leq 38$ ratios of isotopes to their elements provided by the ACE-CRIS experiment at a few hundreds of MeV/n with a precision ∼50%, from data cumulated over more than 20 years [217]. While the number of unstable isotopes grows steadily with mass, and could help to shed further light to the processes discussed above, the difficulties of pursuing such measurements due to the very low abundances and the limitation of cross-section models in this range leaves this region as uncharted territories for now.

3.2. Ongoing and future projects: energy, mass, isotopes, antinuclei and precision frontiers

In this section, a quick overview of operational experiments and future projects is presented. ACE-CRIS and Voyager satellites, that have recently provided very useful data sets (see previous section), are not covered: these detectors have outlasted their initial programmes by far, and although they are still taking data, it is not clear if their recent relevant results (IS spectra for Voyager and $Z = 30$–40 data for ACE-CRIS) could be surpassed, extended or reveal new surprises. In the coming years, space experiments will mostly target the energy frontier, thanks to upgrades (AMS), longer data taking periods (DAMPE and CALET) or larger acceptance detectors like HERD (High Energy cosmic-Radiation Detection) and HERO (High-Energy Ray Observatory). The mass frontier will be explored by TIGER-ISS and NUCLEON-2. Balloon-borne experiments are targeting the isotope (HELIX) and antinuclei (GAPS and others) frontiers. For the next decades, the sub-percent precision, energy, isotope and anti-matter frontiers will all be targeted at once, with the ambitious but very uncertain projects ALADInO (Antimatter Large Acceptance Detector In Orbit) and AMS-100. The reach in terms of species, energy, and precision of these current and future experiments is discussed below and summarised in Fig. 8. We do not report or discuss interstellar probe projects to measure very-low energy IS spectra by the end of the century [257].

3.2.1. AMS (2011–2030): prospects and upgrade

AMS will operate for the entire ISS lifetime, through at least 2030. By the end of the mission, AMS will provide the rigidity spectra for nuclei up to Ni and up to TV energies at least (to 3.7 TV rigidities), and measure the isotope fluxes in the 0.4–12 GeV/n range for light nuclei. An upgrade of the detector is foreseen in early 2026 by adding a double-layer of silicon micro-strip detectors at the top of the instrument. This will increase the geometrical acceptance by a factor 3 and add two charge measurement points with almost no material above. This allows measuring the fluxes of nuclei between S and Fe with similar accuracies as lighter nuclei, by collecting more statistics (3 times faster with the upgrade), and by improving the rejection of background originating from interactions of material above the first charge measurement point. The upgrade will also allow extending the measurements of the positron flux up to 2 TeV, that of the electron flux up to 3 TeV, and to improve the accuracy of the $\overline{\mathrm{p}}$ flux [193].

3.2.2. DAMPE and CALET (2015–2030): sub-PeV energy frontier

All sub-systems of DAMPE remain in excellent condition and the satellite is expected to continue data-taking for at least a few more years. With more accumulated data, it will be able to reach a few hundred TeV for individual hadronic CR spectral measurements and at least 10 TeV for electrons. Similarly, the CALET mission demonstrated stable performance, leading to the extension of its lifetime on ISS until 2030, with no special operations or interventions scheduled.

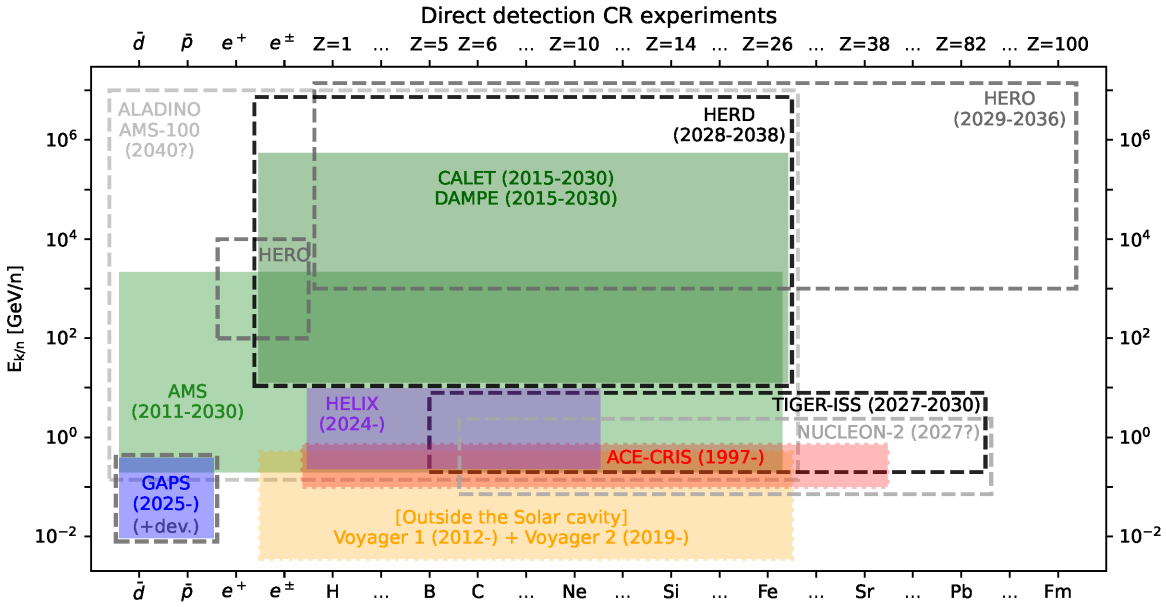

Figure 8: Species (x-axis) and energy (y-axis) reach of direct detection CR experiments. Shown are (i) experiments that have outlasted by far their initial physics programme but are still functioning (orange and red dotted line boxes), (ii) ongoing experiments (solid line filled boxes), and (iii) forthcoming or future projects (dashed line empty boxes). See Sec. 3.2 for details.

3.2.3. HELIX (first balloon flight in 2024): $^{10}Be/^{9}Be$

HELIX is aimed at measuring spectra and composition of light isotopes from He to Ne nuclei, thanks to a combination of a 1 T superconducting magnet, a high-resolution TOF system, and a RICH detector [164]. The first balloon flight was successfully conducted from Kiruna, Sweden to northern Canada, for 6 days from May 28 to June 3, 2024[3]. An anticipated longer flight in Antarctica will yield measurements up to 10 GeV/n. Compared to previous ISOMAX (ISOtope Magnet eXperiment) measurements [232], HELIX will enable, in particular, sampling the secondary production of the GCR clock ^{10}Be from a larger volume of the Galaxy, to provide more stringent constraints on the halo size of the Galaxy (crucial for DM searches).

3.2.4. GAPS (balloon-flight ready) and other future designs (GRAMS, PHeSCAMI): low-energy antinuclei

General AntiParticle Spectrometer (GAPS). The GAPS experiment is optimised for CR antinuclei [258] at low-energy (< 0.25 GeV/n). The experiment consists of ten planes of semiconducting Si(Li) strip detectors surrounded by a plastic scintillator TOF system. GAPS will undertake a series of Antarctic long-duration balloon flights, and is ready for its first flight during the 2025/26 balloon season. GAPS relies on a novel particle identification technique based on exotic atom formation and decay [258], in which antinuclei slow down and eventually annihilate within the detector. The identification of antinuclei uses the simultaneous occurrence in a narrow time window of X-rays of characteristic energy and nuclear annihilation products, providing high rejection power to suppress non-antiparticle background and identify the antinucleus species. This exotic atom detector design yields a large grasp compared to typical magnetic spectrometers, and allows for identifying $\overline{\mathrm{p}}$, $\overline{\mathrm{d}}$ and $\overline{\mathrm{He}}$ CRs. GAPS will provide a precision $\overline{\mathrm{p}}$ spectrum for the first time in the low-energy range below 0.25 GeV/n [189], and has a sensitivity to $\overline{\mathrm{d}}$ that is about two orders of magnitude better than the current BESS limits. Though the instrument is optimised for $\overline{\mathrm{d}}$, the exotic atom detection technique is also sensitive to $\overline{\mathrm{He}}$ signatures [259]. Due to the higher charge, the $\overline{\mathrm{He}}$ analysis is even less affected by $\overline{\mathrm{p}}$ backgrounds than the $\overline{\mathrm{d}}$ analysis, which allows for a competitive $\overline{\mathrm{He}}$ sensitivity in the low-velocity range.

[3] https://stratocat.com.ar/fichas-e/2024/KRN-20240528.htm

Gamma-Ray and AntiMatter Survey (GRAMS). The GRAMS experiment is a novel instrument designed to simultaneously target both astrophysical γ rays with MeV energies and antimatter signatures of DM [260]. The GRAMS instrument consists of a liquid argon time-projection chamber (LArTPC) surrounded by plastic scintillators. The LArTPC is segmented into cells to localise the signal, an advanced approach to minimise coincident background events in the large-scale LArTPC detector. The GRAMS concept potentially allows for a larger instrument since argon is naturally abundant and low-cost, compared to current experiments that rely on semiconductors or scintillation detectors. GRAMS is proposed to begin as a balloon-based experiment, as a step forward to a satellite mission. GRAMS has been developed to become a next-generation search for antimatter signatures of DM. The detection concept resembles GAPS's, relying on exotic atom capture and decay. However, as the LArTPC detector can provide an excellent 3-dimensional particle tracking capability, with nearly no dead volume inside the detector, the detection efficiency can be significantly improved while reducing the ambiguity of antimatter measurements, which is crucial for discovering rare events. A prototype flight called MiniGRAMS is planned for 2025/26.

Pressurised Helium Scintillating Calorimeter for AntiMatter Investigation (PHeSCAMI). The goal of the PHeSCAMI project is to study the signatures offered by a high-pressure He target for the identification of $\overline{\mathrm{d}}$ in space. Exotic atoms are produced by stopping $\overline{\mathrm{p}}/\overline{\mathrm{d}}$ in He gas. The identification uses the delayed annihilation of antinuclei in He to identify cosmic antimatter species. The typical lifetime for stopped $\overline{\mathrm{d}}$ in matter is of the order of picoseconds, similar to that of stopped $\overline{\mathrm{p}}$. However, the existence of long-lived (of the order of microseconds) metastable states for stopped $\overline{\mathrm{p}}$ in He targets has been measured [261]. These metastable states in He have also been measured for other heavy negative particles, such as pions and kaons [262, 263]. The theoretical description of this effect predicts that the lifetimes of these metastable states increase quadratically with the reduced mass of the system, i.e., a larger delay of the annihilation signature is expected for $\overline{\mathrm{d}}$ than for $\overline{\mathrm{p}}$ capture in He [264–268]. The project is still at the development stage [269], but a prototype could be flown as a payload for an Antarctic stratospheric balloon in the coming years.

3.2.5. TIGER-ISS (2027–2030) and NUCLEON-2 (2027?): ultra-heavy nuclei

TIGER-ISS, scheduled for launch in 2027 [270], is the next step of the TIGER and SuperTIGER project, whose dataset from the second flight, 32 days in 2019–2020, is still being analysed [271, 272]. It is designed to measure the abundances of rare ultra-heavy nuclei of energies above 350 MeV/n from B ($Z = 5$) up to Pb ($Z = 82$). The key instrumental difference of TIGER-ISS, compared to SuperTIGER, is the replacement of scintillator-based detectors by Si strip detectors, to avoid scintillator saturation effects, improving the charge resolution capability [270]. The instrument will have a geometrical factor of $1.3\,\mathrm{m}^2\cdot\mathrm{sr}$. In less than one year of operation, TIGER-ISS will collect as many events as the 55-day SuperTIGER-1 balloon flight [270]. One of the main advantages of an ISS-based configuration, compared to balloon flights, is that the results will be free of systematic effects related to nuclear interactions in the atmosphere.

The NUCLEON-2 satellite mission, to measure nuclei from C ($Z = 6$) to Pb and isotopes from $Z = 6$ to $Z = 66$ in the energy range from 100 MeV/n to 3 GeV/n, is currently under development [273, 274]. The detector design achieves a geometric factor of $0.8\,\mathrm{m}^2\cdot\mathrm{sr}$ with 48 hexagonal modules made of stacks of 40 silicon detectors, composed of 4 double layers of micro-strip tracking devices interleaved by 3 stacks of 10 calorimetric sensors each. NUCLEON-2 will determine nuclei charge and mass by multiple measurements of $E - dE$ along the nucleus trajectory inside the detector, until it stops. The isotope identification performance has been studied on a prototype detector, using test beams of $^{40}_{18}$Ar at the JINR (Joint Institute for Nuclear Research) Nuclotron and $^{159}_{18}$Xe at the CERN SPS. To accurately calibrate the isotope mass measurement method, further tests are foreseen in the framework of the DPS project [275, 276] at the NICA (Nuclotron-based Ion Collider Facility accelerator complex [277] in Dubna. NUCLEON-2 is expected to operate on a russian commercial satellite at 400 km altitude for at least five years.

3.2.6. HERD (2028–2038) and HERO (2029–2036): going to the Knee

Extension of direct CR measurements towards the *Knee* requires a significant enhancement of the instruments' geometric acceptance.

The HERD mission, expected to be deployed on the Chinese Space Station by 2028, is a leap forward for calorimetric experiments [278]. It will feature the first 3-D imaging cubic calorimeter, which allows accepting particles from 5 sides. This enables achieving the geometric acceptance of about $2\,\mathrm{m}^2\cdot\mathrm{sr}$ – nearly one order of magnitude more than the current largest calorimeters (DAMPE and ISS-CREAM). With a thickness of about 55 radiation lengths and 3 nuclear interaction lengths, HERD will probe CR protons and ions up to 10 PeV, and CR electrons up to 100 TeV. Among the scientific goals of HERD are the measurement of the CR elemental composition and spectra up to the *Knee*, and the search for indirect DM signatures in CR electrons and γ-ray spectra. The response to hadrons of a large-scale CaloCube, similar to HERD, has been recently investigated using data collected at the CERN SPS accelerator, at energies of a few hundreds of GeV [279].

Similarly, the HERO project will employ a heavy ionisation calorimeter in a 4π acceptance design to reach a geometric acceptance of at least $12\,\mathrm{m}^2\cdot\mathrm{sr}$ for protons, and at least $16\,\mathrm{m}^2\cdot\mathrm{sr}$ for nuclei and electrons [280, 281]. The calorimeter will be surrounded by multi-layer silicon detectors, able to measure absolute charges up to $Z\sim100$. HERO will measure the spectra of proton and nuclei in the energy range from 1 TeV to 10 PeV, and electron plus positron and γ-ray energy spectra from 100 GeV to 10 TeV [280]. The HERO mission will operate for at least 5 years on a Russian satellite. Designs with heavier calorimeters, reaching geometric acceptances up to $60\,\mathrm{m}^2\cdot\mathrm{sr}$, are being considered to match the payload capability of the Russian heavy and super-heavy launch vehicles, currently under development and expected to be ready not earlier than 2029 [282].

3.2.7. ALADInO and AMS-100 (beyond 2040): sub-percent precision and energies up to the Knee

The qualitative leap forward on direct CR measurements in space is expected with the deployment of large high-temperature superconducting magnets. Currently, two conceptual designs based on large-acceptance magnetic spectrometers equipped with deep 3D imaging cubic calorimeters are being developed, ALADInO [283, 284] and AMS-100 [285]. The combination of a magnetic spectrometer with a calorimeter allows their cross-calibration and precise determination of rigidity and energy scales as in AMS. Both ALADInO and AMS-100 are designed to be placed at the Earth Lagrange Point 2, to maintain a stable cold environment for the magnet operation. Either of the two instruments is anticipated to start science operation not earlier than 2040 [285, 284].

The AMS-100 instrument has a solenoidal magnetic field configuration with a magnetic spectrometer acceptance of $100\,\mathrm{m}^2\cdot\mathrm{sr}$, reaching an MDR of 100 TV, and a calorimeter of 70 radiation lengths and 4 interaction lengths with an acceptance of at least $30\,\mathrm{m}^2\cdot\mathrm{sr}$. AMS-100 is expected to measure the energy spectrum of electrons and positrons up to 20 TeV and 10 TeV, respectively, the rigidity spectrum of $\overline{\mathrm{p}}$ up to 10 TV, and the energy spectra of nuclei (up to at least Ni) up to 10 PeV. AMS-100 features also a TOF system with a 20 ps time resolution, allowing to search for $\overline{\mathrm{He}}$ and to measure $\overline{\mathrm{d}}$ in the energy range from 0.1 GeV/n to 8 GeV/n, with a sensitivity of $3\times10^{-11}(\,\mathrm{m}^2\,\mathrm{s\ sr\ GeV/n})^{-1}$ in 10 years of data taking. AMS-100 will also be able to perform detailed studies of diffuse γ-ray emission and γ-ray sources up to 10 TeV, with the ability of resolving structures with angular resolution comparable to modern X-ray telescopes.

With a much smaller payload mass (6.5 tons compared to the 40 tons of AMS-100), ALADInO has a magnetic spectrometer acceptance larger than $10\,\mathrm{m}^2\cdot\mathrm{sr}$, with a toroidal magnetic field setup and a calorimeter of similar acceptance, with 61 radiation lengths and 3.5 interaction lengths. ALADInO reaches a MDR better than 20|,TV, and will measure the energy of electrons and positrons up to 10 TeV with 2% resolution. It is expected to measure the rigidity spectrum of $\overline{\mathrm{p}}$ up to 10 TV, the energy spectra of proton and He nuclei up to 10 PeV, and those of heavier nuclei (up to at least Ni) up to 1 PeV [283]. The ALADInO setup will also include a TOF with time resolution better than 100 ps, allowing to measure the $\overline{\mathrm{d}}$ flux up to 4 GeV/n and to search for $\overline{\mathrm{He}}$ with a sensitivity better than $10^{-10}(\,\mathrm{m}^2\,\mathrm{s\ sr\ GeV/n})^{-1}$ in the first 5 years of operation.

4. Cross-section needs for GCRs: current *vs.* sought precision and energies

In this section, the reactions in terms of projectiles, targets and products, energy coverage, and the cross-section precision needed to be able to fully take advantage of current high-precision CR data are detailed.

These desired precisions are not the same for all reactions and all energies, as CR fluxes in which these reactions are involved are not measured with the same precisions, as discussed in Sec. 3.

Technically, the propagation of uncertainties goes through the GCR transport equation, and propagating them back to an observed GCR flux precision – to finally derive a desired nuclear data precision – is not completely straightforward. These questions have been investigated recently in depth for the production cross-sections of GCR nuclei and antinuclei. Indeed, both are pivotal to take full advantage of current CR data, e.g., for the DM searches discussed in Sec. 2. After introducing the transport equation and several definitions (Sec. 4.1), the reactions needed for the two above cases, i.e., nuclei and antinuclei production, are detailed (Sects 4.2 and 4.3). Many other reactions (inelastic, annihilation, etc.), relevant for GCR studies or by CR experiments themselves to deliver their promised precision, are also reviewed (Sec. 4.4), in particular with respect to their status and their contribution to the error budget.

4.1. The key transport equation for GCRs: definitions and relevant cross-sections

For a GCR species j, the central object of interest is the time, space and momentum-dependent function $\psi^j(t, \mathbf{x}, p)$, which is the ensemble and angle average (over realisations of magnetic inhomogeneities and momentum direction $\Omega_\mathbf{p}$, respectively) of the single-particle distribution function $f^j(t, \mathbf{x}, \mathbf{p})$ entering the Vlasov–Boltzmann equation. The function ψ^j is connected to the flux by $\Phi^j = (v/(4\pi))\psi^j$, where v is the particle's speed. It obeys the transport equation (see, e.g., [286]):

$$\frac{\partial \psi^j}{\partial t} - \nabla \cdot \left(\overline{\overline{D}} \nabla \psi^j \right) + \vec{u} \cdot \nabla \psi^j - \frac{1}{3} \nabla \cdot \vec{u} \left(p \frac{\partial \psi^j}{\partial p} \right) - \frac{1}{p^2} \frac{\partial}{\partial p} \left(p^2 D_{pp} \frac{\partial \psi^j}{\partial p} \right) = \tag{1}$$
$$q^j + \frac{1}{p^2} \frac{\partial}{\partial p} \left[p^2 \left(\frac{\mathrm{d}p}{\mathrm{d}t} \right) \psi^j \right] - \Gamma^j_{\rm tot}\, \psi^j + \sum_i \psi^i \otimes \Gamma^{i \to j} \,.$$

The left-hand side of Eq. (1) contains transport terms of collisionless origin, i.e., from the scattering onto the electromagnetic field irregularities. The second to the fifth term correspond to the spatial diffusion with diffusion tensor $\overline{\overline{D}}(\vec{\mathbf{x}}, E)$, a convective term associated to the ISM plasma velocity field $\vec{u}(\mathbf{x})$, adiabatic energy changes, and reacceleration (i.e., magnetic inhomogeneity diffusion in momentum space) controlled by D_{pp}. The latter two terms are notably involved in the so-called *first* and *second order Fermi acceleration*, respectively. The right-hand side, besides a possible primary source term q^j (first term), accounts for *collisional effects*, described by terms representing continuous losses (second term), catastrophic sinks (third term) and possible secondary sources (last term). Catastrophic sinks include both decays, if the species is unstable with lifetime at rest $\tau^j_{\rm dec}$, and inelastic interactions over all possible targets t of the ISM with density $n^t_{\rm ISM}$, quantified by the cross-section $\sigma^{j+t}_{\rm inel}$, so that

$$\Gamma^j_{\rm tot} = \frac{1}{\gamma\, \tau^j_{\rm dec}} + \sum_t n^t_{\rm ISM}\, v\, \sigma^{j+t}_{\rm inel} \,. \tag{2}$$

In practice, only H and He have significant densities in the ISM to be targets relevant above the percent level. The last term in Eq. (1) represents a generic integral operator acting on ψ^i, which is more easily expressed in terms of the kinetic energy $E_{\rm k} = E - m$, rather than momentum variables[4], so that

$$\psi^i \otimes \Gamma^{i \to j} = \sum_t n^t_{\rm ISM} \int \mathrm{d}E^i_{\rm k}\, v\, \frac{\mathrm{d}\sigma^{i+t \to j}_{\rm prod}}{\mathrm{d}E^j_{\rm k}}(E^i_{\rm k}, E^j_{\rm k}) \psi^i(E^i_{\rm k}) \,, \tag{3}$$

where we introduced the differential cross-sections to produce the secondary particle j, in the collision of the primary i with the target t. They can be written as a function of the kinetic energy of the primary parent, $E^i_{\rm k}$, and of the secondary daughter, $E^j_{\rm k}$, as

$$\frac{\mathrm{d}\sigma^{i+t \to j+\mathrm{X}}_{\rm prod}}{\mathrm{d}E^j_{\rm k}}(E^i_{\rm k}, E^j_{\rm k}) = \sigma^{i+t}_{\rm inel}(E^i_{\rm k})\, \frac{\mathrm{d}\mathcal{N}^{i+t \to j+\mathrm{X}}}{\mathrm{d}E^j_{\rm k}}(E^i_{\rm k}, E^j_{\rm k}) \,, \tag{4}$$

[4]Note that $\psi(E_{\rm k}) = \psi(p(E_{\rm k})) \cdot \mathrm{d}p/\mathrm{d}E_{\rm k} = \beta^{-1} \cdot \psi(p(E_{\rm k}))$, since $p^2 = (m + E_{\rm k})^2 - m^2 = 2mE_{\rm k} + E^2_{\rm k}$.

with $\mathrm{d}\mathcal{N}/\mathrm{d}E_\mathrm{k}^j$ the multiplicity spectrum of the species j in the collision of i with t. Since data are typically scarce, regularities motivating semi-empirical formulae turn out to be useful in interpolating between and extrapolating beyond measurements, or to estimate cross-sections involving nuclei for which no measurement exists.

As an example of some of these regularities, away from the thresholds, $\mathrm{d}\mathcal{N}/\mathrm{d}E_\mathrm{k}^j$ is only weakly dependent on E_k^i and depends on i and t mostly via a normalisation. To a good approximation, in spallation reactions, the kinetic energy per nucleon $E_{\mathrm{k/n}} = E_\mathrm{k}/A$, where A is the mass number, is conserved (we come back to this in Sec. 4.4), so that

$$\frac{\mathrm{d}\mathcal{N}^{i+t\to j+\mathrm{X}}}{\mathrm{d}E_\mathrm{k}^j}(E_\mathrm{k}^i, E_\mathrm{k}^j) \simeq \kappa^{i+t\to j+\mathrm{X}}\delta\left(\frac{E_\mathrm{k}}{A_j} - \frac{E_\mathrm{k}^i}{A_i}\right) . \tag{5}$$

Fragmentation and spallation cross-sections are hence strategic ingredients in numerous astroparticle physics processes related to the acceleration, propagation and detection of cosmic particles, both charged and neutrals (photons, neutrinos). In astrophysical settings, they limit for instance the maximum acceleration energy attainable in a source, and for the propagation from the source to the detector, they enter both as energy-loss channels and, above all, as source channels of the so-called *secondary* species [287]. In order to isolate these effects from other interesting and poorly known astrophysical aspects, however, one should reduce the current cross-section uncertainties below the differences spanned by several viable astrophysical scenarios.

4.2. Isotopic production cross-sections

The history of cross-sections and GCRs goes a very long way. Indeed, nuclear/particle and CR topics were one and the same until the 1950s, before becoming two communities going their separate ways and addressing different questions. With the flight of many balloons and space experiments from the 1950s to the 1970s, it was realised that the poor accuracy of the nuclear cross-sections was a limitation for the interpretation of their data (e.g., [288]). The situation back then had strong similarities with the current one, with dedicated studies to identify the needed reactions and then the set-up of long term programs for these new measurements (that started in the 1980s). Most of these data are still of use and remain the most accurate for many reactions.

Below, the procedure devised in Refs. [289, 207] is recalled to provide a priority list of nuclear production cross-sections to be measured and improved, in order to profit from the current CR data precision. Throughout this section, the straight-ahead approximation Eq. (5) is used, in which the kinetic energy per nucleon $E_{\mathrm{k/n}}$ is conserved in nuclear reactions. As a result, the quantities of interest are the total (and not the differential) production cross-section $\sigma_\mathrm{prod}^{i+j\to k}$ and their uncertainties, with i the GCR projectile, j the ISM target and k the fragment. Actually, for GCR propagation studies, cumulative cross-sections are used, i.e.,

$$\sigma_\mathrm{cumul}^{i+j\to k} = \sigma_\mathrm{prod}^{i+j\to k} + \sum_{g\in\mathrm{ghosts}} \sigma_\mathrm{prod}^{i+j\to g}\cdot\mathcal{B}r(g\to k) . \tag{6}$$

In this cumulative, the so-called *ghosts* are short-lived nuclei with half-live $\lesssim 100\,\mathrm{kyr}$, i.e., decay times much shorter than the propagation time, ending their decay chain into fragment k with a branching ratio $\mathcal{B}r(g\to k)$.

In practice, a network of more than a thousand reactions is involved for $Z < 30$, and many more for ultra-heavy nuclei. Nuclear data and codes need to provide both the direct and ghost production of any GCR fragment. To illustrate the severity of the situation and of the needs, a brief summary of the existing nuclear data and models and their limitation is provided.

4.2.1. Status of nuclear data and models

The ISM is made of $\sim 90\%$ of H and $\sim 10\%$ of He in number, with only traces of heavier elements. With the few percent precision of CR data, the need to include the interactions with C and O in the ISM is getting closer and should be re-evaluated in the future. But for current data, the requirements on the production cross-section precision is typically the percent level on H and tens of percents on He (see next

section). Actually, for the latter, very few data exist, and all GCR studies rely on the scaling proposed more than 35 years ago in Ref. [290], which has limitations, e.g., for the production of light elements from heavy projectiles [97].

Reference nuclear data in GCR studies. Nuclear data are obtained from two main techniques: (i) heavy ion beams on H effective targets, i.e., liquid hydrogen or CH_2 and C subtraction, and outgoing fragments identified by a spectrometer; (ii) targets of heavy elements irradiated by a proton beam with the cross-sections determined either by γ-spectrometry, whenever fragments are radioactive isotopes, or after chemical processing by mass spectroscopy for the long-lived and stable isotopes produced.

The current body of data and models (based on these data) used for contemporary GCR studies is a combination of a patchy collection of reactions measured by the nuclear and particle physics community, with some data dating back to the 1950s, and systematic measurements led by different groups over the last 40 years. One figurehead of the CR community, Bill Webber, led and coordinated many efforts over two decades, 1980s to 2000s, using mostly $Z < 26$ beams, to measure isotopic production cross-sections on liquid hydrogen, carbon and methylene CH_2 targets, in the energy range $\sim$400–800 MeV/n [291, 290, 292–303]. Extensive efforts were also driven by the study of space-flight radiation shielding applications (see Sec. 6.2) and the study of cosmogenic isotopes [304, 305] (see Sec. 6.1): for the former, a large body of data, using beams of light to heavy species, were obtained in the 2000s by Zeitlin's group [306–310], but for charge-changing cross-sections only (not directly of interest for GCR studies); for the latter, extensive measurements using proton [311] and neutron [312] beams were carried out from the 1990s, and over two decades, by R. Michel's group [313–322], and also by J. Sisterson's group [323–329]. To this list, a relatively recent and very useful body of high-precision Fe fragmentation cross-sections can also be added, down to Li fragments [330, 331]. However, it is fair to say the reactions of interest for the nuclear physics community nowadays involve ultra-heavy species, highly deformed nuclei, and/or short-lived radioactive beams, which is not providing further data for GCR science.

Nuclear codes status and perspectives. To account for the lack of data for many reactions and energies, dedicated formulae were developed as early as the 1960s [332]. Parametric codes soon followed to describe both the inelastic (see Sec. 4.4.2) and production cross-sections, with the semi-empirical parametrisation in the `YIELDX` code of Silberberg and Tsao's group [333–341] and in the `WNEW` code of Webber and coworkers [296, 302, 303, 301, 342] and other efforts (e.g., [343] – we refer the reader to Sec. 5 of Ref. [344] for a recent detailed review of nuclear models and the various interaction mechanisms). Both were developed in the 1980s and updated till the 2000s, and by comparing the prediction of these codes (fit on older data) to new nuclear data, the former was found to be better (resp. worse) than the latter for reactions without (resp. with) data [345, 340]. These codes remain the underlying models (original `FORTRAN` code) of the widely used numerical `GALPROP` package [346] for the propagation of relativistic $Z \leq 30$ GCRs. However, to improve on these models, `GALPROP` combines several parametric formulae re-normalised to data and direct fits [347, 32, 348–350] and also uses the parametrisation of Ref. [351] for light isotopes. The overall accuracy of these codes is difficult to assess, but is estimated to be in the 10%-20% range. Recent works have also shown the importance of continuously importing more recent nuclear data and sometimes less important GCR production channels to keep improving these nuclear predictions [352, 353, 97, 233]. It is also worth noticing that these parametrisations need further improvements, as they assume energy-independent cross-sections above a few GeV/n, whereas inelastic cross-sections are known to rise [354, 355].

Outside the GCR community, other parametric codes exist (`EPACS` [356–358], `SPACS` [359, 360], `FRACS` [361], `NUCFRAG` [362–365], `TALYS` [366]) as well as MC simulation codes and event generators (`FLUKA` [367], `MCNP6` with `CEM` and `LAQGSM` [368–370], `PHITS` [371–373], `SHIELD-HIT` [374], etc.). These models are benchmarked and compared with overall fair agreement (see also Sec. 6.2.1). The `Geant4` framework [375] also provides many options, including specific cascade models in the above list, that can be used, combined or compared. In terms of accuracy, these transport codes cannot replace the above-discussed ones tailored for GCR studies, but they could probably bridge some gaps in the data for specific regimes, despite this requiring dedicated studies and careful evaluations.

Overall, there is no free lunch with nuclear cross-section data and codes. Without new data, the margin of progress is probably thin, and will be based on painful compilations of missed data in the literature and possible updates and systematic benchmarking of existing codes. Machine learning techniques could possibly bring some improvements, but this remains to be proven. Gathering new high-precision nuclear data seems to be the only path to go forward.

4.2.2. From GCR data precision to desired cross-section precision

The impact of the production cross-section $\sigma_{abc} \equiv \sigma_{\rm prod}^{a+b\to c}$, on the flux ψ^j of a given GCR isotope or element j, is quantified in terms of the relative difference between the standard or reference flux calculation, $\psi^j_{\rm ref}$, and the calculation where this cross-section is set to zero, $\psi^j_{\sigma_{abc}=0}$. We thus define the coefficients

$$f^j_{abc}(E_{\rm k/n}) \equiv 1 - \frac{\psi^j_{\sigma_{abc}=0}(E_{\rm k/n})}{\psi^j_{\rm ref}(E_{\rm k/n})} \,, \tag{7}$$

whose ranking is equivalent to rank the most important production cross-sections [289]. These coefficients vary with energy, because the various GCR progenitors contributing to j have different energy dependence, owing to the energy-dependent solution of the transport equation and, obviously, to the energy dependence of σ_{abc} itself. Moreover, if we decompose $\psi^j_{\rm tot}$ into a primary and secondary origin, i.e., $\psi^j_{\rm tot} \equiv \psi^j_{\rm prim} + \psi^j_{\rm sec}$, then by definition $\psi^j_{\rm prim}$ does not depend on the production cross-sections, and f_{abc} is roughly the contributing fraction of the reaction $a+b\to c$ to $\psi^j_{\rm sec}$ [289].

As shown in Ref. [289, 207], the f^j_{abc} coefficients enable to link the cross-section uncertainties to the predicted flux uncertainties. Different plausible assumptions on the presence or absence of correlations between these cross-section datasets (i.e., in practice, on the modelling of the cross-sections based on these data) lead to different error propagation formulae. We report two noteworthy cases below, dropping the energy dependence for simplicity:

$$\left(\frac{\Delta\psi^j_{\rm tot}}{\psi_{\rm tot}}\right)^{\rm mix} \approx f^j_{\rm sec} \sum_a \sqrt{\sum_{b,c}\left(f^j_{abc}\frac{\Delta\sigma_{abc}}{\sigma_{abc}}\right)^2} \,, \tag{8}$$

$$\left(\frac{\Delta\psi^j_{\rm tot}}{\psi^j_{\rm tot}}\right)^{\rm multi} \approx f^j_{\rm sec} \sqrt{\sum_{a,b}\frac{(\mathcal{C}^j_{ab})^2}{N_{ab}}} \quad \text{with} \quad (C^j_{ab})^2 \equiv \sum_k (f^j_{abc})^2 \frac{\sigma_{ab}}{\sigma_{abc}} \,, \tag{9}$$

where $f^j_{\rm sec} = \psi^j_{\rm sec}/\psi^j_{\rm tot}$ is the secondary fraction of the flux j considered, $\Delta\sigma_{abc}/\sigma_{abc}$ the relative uncertainty of the nuclear cross-section, N_{ab} is the number of $a+b$ reactions considered in a new measurement campaign, and $\sigma_{ab} = \sigma^{a+b}_{\rm inel}$ is the inelastic cross-section of reaction $a+b$ (discussed in Sec. 4.4.2). These formulae can be used to decide which reactions need to be measured in order to reach a relative precision on the modelled flux, ψ^j, better than ϵ. The two cases are useful in the following situations:

- *Eq. (8) for rough estimates of improvements brought by new measurements*: this case assumes that the data gathered so far – and nuclear models based on these data – have uncorrelated uncertainties for fragments of the same projectile, but correlated uncertainties for different projectiles. This formula can be used to illustrate how the flux uncertainties can be brought back below the sought precision ϵ, when a growing number of the most important reactions are perfectly measured (e.g., see Fig. 3 in [207]);
- *Eq. (9) to determine the number of reactions N_{ab} and beam time to reach $(\Delta\psi/\psi) < \epsilon$*: this case assumes a multinomial distribution of the measured fragments c in the $a+b$ reaction, an approximation that fails for light fragments because of the multiplicity. As shown in Ref. [207], demanding for all measured reaction that

$$N^j_{ab} \geq (f^j_{\rm sec}/\epsilon)^2 \cdot C^j_{ab} \cdot \left(\sum_{a,b} C^j_{ab}\right) \tag{10}$$

is the optimal scheme to minimise the beam time, as it minimises the number of $N_{\rm tot} = \sum_{a,b} N_{ab}$ reactions that must be measured. The use of this equation is illustrated below to determine a wish list of measurements.

4.2.3. A game-changing wish list for $Z \leq 30$

The above formulae can be used to set up a wish list for any GCR species, energy, and CR data precision. However, this is a tedious and incremental process, requiring a careful review and update of the best nuclear data available. So far, only GCR fluxes from Li to Si have been analysed in detail [289, 207], relying on the `USINE` propagation code [376], and production cross-section parametrisations from `GALPROP` [346] updated for Li, Be, B and F isotopic production as described in Ref. [97, 377]. The study of light nuclei ($Z < 3$) and heavier ones ($14 < Z < 30$) are not published yet, but preliminary results are shown in Table 1.

As discussed in Sec. 3.1.6 and shown in Fig. 2, the most informative GCR nuclei are the secondary species, namely d, ^{3}He, LiBeB (and their isotopes), F, sub-Fe $Z = 21$–25 and also some GCR clocks. The precision of their measurements in CRs is illustrated in Fig. 7. Actually, the consistency of a pure secondary origin of the d [378, 379, 96, 94], Li [93, 380–382, 97] and F [205, 206, 377] fluxes is particularly debated in the literature in the light of recent AMS data, respectively Refs. [92], [204] and [200]. The ^{10}Be case is also an issue [233, 383, 34, 384], and the production cross-sections for $Z = 21$–25 elements will become a new focal point as soon as AMS will release its data. As highlighted in Sec. 2, these species have a key role in determining the transport parameters, and also to calculate accurate backgrounds for DM searches: they are also maximally sensitive to the production cross-sections, as the relevant fluxes are directly proportional to them. Mixed species, like N, Na or Al, come second in terms of priority, and require fewer reactions to reach the same modelling precision; indeed, their secondary production, overall, is only a fraction of the total flux. Finally, purely primary species like H, He, O, Si and Fe are just not impacted at all by these production cross-section uncertainties and are irrelevant in this context. There are two extreme and complementary situations regarding how to carry out new nuclear data measurement campaigns, which are motivated by past measurements and existing experimental setups, impacting the choice of the wish list. In all cases, the energy range of interest is from a few hundreds of MeV/n up to a few GeV/n (same projectile and fragment energy) and ideally up to a few tens of GeV/n for a few reactions, in order to test the expected mild energy dependence of the cross-sections.

- *high-precision measurement ($\lesssim 1\%$) of a few specific production cross-sections* over the energy range ~ 0.1–$10\,$GeV/n: in that case, the goal is to determine the energy dependence of the most important reactions, as available in the ranked list shown in Table 1. In there, the reactions for Li, Be, B and F are taken from Ref. [207], and those for d and ^{3}He isotopes and $Z = 21$–25 elements from a preliminary analysis following the same steps. The cumulative weight of tens to hundreds of reactions with individual $f_{abc} \lesssim 1\%$ can reach $\lesssim 20\%$, with most of these reactions having no data. Moreover, even more important reactions sometimes have inconsistent data, or only one or two energy points below a few hundreds of MeV/n, still in the rising or resonance part of the cross-section (i.e., before having reached their asymptotic high-energy value).

- *high-precision measurement of all fragments of many reactions at once* at a unique energy: in that case, the recommendation is to evaluate the number of each reaction to be measured in order to reach a desired flux precision of ϵ. This is done by using Eq. (9) and the f^j_{abc} coefficients (reported for Li to Si fragments in Ref. [207]). As an illustration, Table 2 reports the number of reactions required to reach a $\approx$1% uncertainty (i.e., below the best AMS $\sim 3\%$ accuracy) on Li, Be, B and F GCR data. These numbers were prepared for the test case of measurements at NA61/SHINE (a SPS Heavy Ion and Neutrino Experiment), where systematic uncertainties are $\lesssim 0.5\%$ [385]; see Sec. 5.2.2 and Refs. [386, 387] for more detais on the pilot run.

In Tables 1 and 2, the most abundant GCR isotopes (^{4}He, ^{12}C, ^{16}O, ^{20}Ne, ^{24}Mg, ^{28}Si, ^{56}Fe) are recognised as the most important progenitors of the ranked reactions. The key target is H, but reactions on He contribute to $\sim$10–15% of the GCR fluxes overall. Concerning the fragments, as seen in Table 1, the main channels always involve direct production of the isotopes, as well as unstable short-lived parents of the

Table 1: Wish list of individual reactions sorted according to their flux impact f^j_{abc}, Eq. (7), in percent, at 10.6 GeV/n, for CR secondary fluxes (only $f^j_{abc} > 1\%$ are shown). We highlight reactions with short-lived fragments (**bold**), reactions without nuclear data (†), and the ranking after which the cumulative is $> 50\%$ (*). Adapted from Tables V, VI, VII, and XI of Ref. [207] for j equals Li, Be, B, and F respectively, and preliminary analysis for the rest.

Deuterium	
^{4}He+H$\to^2$H	38.
^{16}O+H$\to^2$H	9.0
^{3}He+H$\to^2$H	7.9*
^{4}He+He$\to^2$H	6.5
^{12}C+H$\to^2$H	5.8
^{4}He+H$\to^3$He	5.2
^{1}H+He$\to^2$H	4.7
^{56}Fe+H$\to^2$H	4.0†
^{28}Si+H$\to^2$H	2.6†
^{24}Mg+H$\to^2$H	2.1†
^{16}O+He$\to^2$H	1.5
^{20}Ne+H$\to^2$H	1.2†
^{16}O+H$\to^{15}$N	1.1

^{3}He	
^{4}He+H$\to^3$He	32.
^{4}He+H$\to^3$H	32.*
^{4}He+He$\to^3$He	5.5
^{4}He+He$\to^3$H	5.5
^{16}O+H$\to^3$He	2.6
^{16}O+H$\to^3$H	2.6
^{12}C+H$\to^3$He	2.1
^{12}C+H$\to^3$H	2.1
^{56}Fe+H$\to^3$He	1.0
^{56}Fe+H$\to^3$H	1.0

Scandium	
^{56}Fe+H$\to^{45}$Sc	43.9
^{56}Fe+H$\to^{45}$Ti	6.35*
^{56}Fe+He$\to^{45}$Sc	4.95†
^{56}Fe+H$\to^{45}$Ca	3.27
^{47}Ti+H$\to^{45}$Sc	3.24†
^{54}Fe+H$\to^{45}$Sc	3.07†
^{56}Fe+H$\to^{55}$Fe	2.76
^{56}Fe+H$\to^{47}$Ti	2.63
^{46}Ti+H$\to^{45}$Sc	2.51†
^{48}Ti+H$\to^{45}$Sc	2.45†
^{46}Ti+H$\to^{45}$Ti	2.24†
^{52}Cr+H$\to^{45}$Sc	2.02
^{56}Fe+H$\to^{49}$V	2.02
^{56}Fe+H$\to^{46}$Ti	1.98
^{56}Fe+H$\to^{52}$Cr	1.93
^{56}Fe+H$\to^{51}$Cr	1.93
^{56}Fe+H$\to^{54}$Mn	1.91
^{49}V+H$\to^{45}$Sc	1.90†
^{54}Fe+H$\to^{45}$Ti	1.84†
^{56}Fe+H$\to^{53}$Mn	1.79
^{56}Fe+H$\to^{55}$Mn	1.53
^{51}Cr+H$\to^{45}$Sc	1.49†
^{55}Mn+H$\to^{45}$Sc	1.47
^{55}Fe+H$\to^{45}$Sc	1.40†
^{56}Fe+H$\to^{50}$V	1.32
^{56}Fe+H$\to^{50}$Cr	1.30
^{53}Mn+H$\to^{45}$Sc	1.25†
^{56}Fe+H$\to^{48}$Ti	1.22
^{50}V+H$\to^{45}$Sc	1.11†
^{50}Cr+H$\to^{45}$Sc	1.00

Lithium	
^{16}O+H$\to^6$Li	15.2
^{12}C+H$\to^6$Li	12.5
^{12}C+H$\to^7$Li	9.93
^{16}O+H$\to^7$Li	9.74
^{11}B+H$\to^7$Li	2.92
^{16}O+He$\to^6$Li	2.86†
^{12}C+He$\to^6$Li	2.14†
^{7}Li+H$\to^6$Li	2.11
^{13}C+H$\to^7$Li	2.05†
^{56}Fe+H$\to^7$Li	2.03
^{15}N+H$\to^7$Li	1.95
^{16}O+H$\to^{13}$N	1.88
^{16}O+He$\to^7$Li	1.82†
^{56}Fe+H$\to^6$Li	1.74
^{12}C+He$\to^7$Li	1.71†*
^{16}O+H$\to^{13}$O	1.70
^{24}Mg+H$\to^6$Li	1.69†
^{28}Si+H$\to^6$Li	1.69†
^{13}C+H$\to^6$Li	1.68†
^{16}O+H$\to^{15}$O	1.68
^{16}O+H$\to^{12}$C	1.51
^{24}Mg+H$\to^7$Li	1.50†
^{28}Si+H$\to^7$Li	1.50†
^{10}B+H$\to^6$Li	1.41†
^{14}N+H$\to^6$Li	1.39
^{15}N+H$\to^6$Li	1.37
^{16}O+H$\to^{14}$N	1.27
^{20}Ne+H$\to^6$Li	1.16†
^{12}C+H$\to^{11}$B	1.15
^{7}Be+H$\to^6$Li	1.14†
^{12}C+H$\to^{11}$C	1.11
^{16}O+H$\to^{13}$C	1.10
^{20}Ne+H$\to^7$Li	1.02†

Titanium	
^{56}Fe+H$\to^{47}$Ti	17.3
^{56}Fe+H$\to^{48}$Ti	11.1
^{56}Fe+H$\to^{46}$Ti	10.5
^{56}Fe+H$\to^{48}$V	8.71
^{56}Fe+H$\to^{46}$Sc	4.34*
^{56}Fe+H$\to^{49}$Ti	3.36
^{56}Fe+H$\to^{55}$Fe	2.80
^{56}Fe+H$\to^{49}$V	2.63
^{56}Fe+H$\to^{51}$Cr	2.08
^{56}Fe+H$\to^{54}$Mn	2.02
^{56}Fe+He$\to^{47}$Ti	1.94†
^{56}Fe+H$\to^{53}$Mn	1.93
^{56}Fe+H$\to^{47}$V	1.93
^{56}Fe+H$\to^{52}$Cr	1.86
^{56}Fe+H$\to^{47}$Sc	1.75
^{56}Fe+H$\to^{50}$V	1.70
^{56}Fe+H$\to^{55}$Mn	1.53
^{54}Fe+H$\to^{46}$Ti	1.36†
^{54}Fe+H$\to^{48}$V	1.33†
^{54}Fe+H$\to^{47}$Ti	1.29†
^{56}Fe+H$\to^{50}$Cr	1.25
^{56}Fe+He$\to^{48}$Ti	1.24†
^{48}Ti+H$\to^{47}$Ti	1.23†
^{56}Fe+He$\to^{46}$Ti	1.17†
^{47}Ti+H$\to^{46}$Ti	1.09†
^{56}Fe+He$\to^{48}$V	1.02†

Beryllium	
^{16}O+H$\to^7$Be	16.8
^{12}C+H$\to^7$Be	14.5
^{12}C+H$\to^9$Be	8.25
^{16}O+H$\to^9$Be	6.09
^{16}O+He$\to^7$Be	2.87†
^{28}Si+H$\to^7$Be	2.72
^{12}C+H$\to^{10}$Be	2.63
^{24}Mg+H$\to^7$Be	2.58
^{14}N+H$\to^7$Be	2.26
^{12}C+He$\to^7$Be	2.26†
^{11}B+H$\to^9$Be	2.22
^{16}O+H$\to^{10}$Be	1.69
^{20}Ne+H$\to^7$Be	1.67†
^{56}Fe+H$\to^7$Be	1.66*
^{16}O+H$\to^{12}$C	1.61
^{10}B+H$\to^9$Be	1.53†
^{24}Mg+H$\to^9$Be	1.52
^{16}O+H$\to^{15}$N	1.41
^{56}Fe+H$\to^9$Be	1.33
^{12}C+He$\to^9$Be	1.29†
^{12}C+H$\to^{11}$B	1.28
^{16}O+H$\to^{15}$O	1.26
^{12}C+H$\to^{11}$C	1.24
^{15}N+H$\to^9$Be	1.22
^{16}O+H$\to^{14}$N	1.20
^{11}B+H$\to^{10}$Be	1.10
^{15}N+H$\to^7$Be	1.08
^{16}O+H$\to^{13}$O	1.08
^{16}O+He$\to^9$Be	1.05†
^{11}B+H$\to^7$Be	1.04

Vanadium	
^{56}Fe+H$\to^{49}$V	30.7
^{56}Fe+H$\to^{50}$V	22.3*
^{56}Fe+H$\to^{51}$V	5.66
^{56}Fe+H$\to^{51}$Ti	3.93
^{56}Fe+He$\to^{49}$V	3.59†
^{56}Fe+H$\to^{49}$Cr	3.26
^{56}Fe+H$\to^{52}$Cr	2.77
^{56}Fe+He$\to^{50}$V	2.61†
^{54}Fe+H$\to^{49}$V	2.58†
^{56}Fe+H$\to^{55}$Fe	2.50
^{56}Fe+H$\to^{51}$Cr	2.17
^{52}Cr+H$\to^{49}$V	2.04
^{56}Fe+H$\to^{54}$Mn	1.79
^{56}Fe+H$\to^{53}$Mn	1.73
^{52}Cr+H$\to^{50}$V	1.72
^{52}Cr+H$\to^{51}$V	1.69
^{56}Fe+H$\to^{55}$Mn	1.59
^{55}Mn+H$\to^{49}$V	1.34
^{51}Cr+H$\to^{49}$V	1.30†
^{51}Cr+H$\to^{50}$V	1.23†
^{50}V+H$\to^{49}$V	1.18†
^{54}Fe+H$\to^{50}$V	1.14†
^{55}Fe+H$\to^{49}$V	1.07†
^{56}Fe+H$\to^{50}$Cr	1.03
^{53}Mn+H$\to^{49}$V	1.01†

Boron	
^{12}C+H$\to^{11}$B	17.2
^{12}C+H$\to^{11}$C	16.6
^{16}O+H$\to^{11}$B	10.8
^{12}C+H$\to^{10}$B	7.85
^{16}O+H$\to^{10}$B	7.05
^{16}O+H$\to^{11}$C	4.42
^{11}B+H$\to^{10}$B	4.12*
^{12}C+He$\to^{11}$B	2.46†
^{16}O+H$\to^{12}$C	2.45
^{15}N+H$\to^{11}$B	2.25
^{12}C+He$\to^{11}$C	2.20†
^{16}O+H$\to^{15}$N	1.84
^{16}O+He$\to^{11}$B	1.66†
^{16}O+H$\to^{15}$O	1.64
^{14}N+H$\to^{11}$B	1.64
^{13}C+H$\to^{11}$B	1.52†
^{12}C+H$\to^{10}$C	1.45
^{16}O+H$\to^{13}$O	1.32
^{16}O+H$\to^{14}$N	1.31
^{12}C+H$\to^{10}$Be	1.16
^{12}C+He$\to^{10}$B	1.12†
^{16}O+He$\to^{10}$B	1.10†
^{24}Mg+H$\to^{11}$B	1.01†

Chromium	
^{56}Fe+H$\to^{52}$Cr	22.7
^{56}Fe+H$\to^{51}$Cr	21.2
^{56}Fe+H$\to^{50}$Cr	12.9*
^{56}Fe+H$\to^{53}$Cr	5.96
^{56}Fe+H$\to^{52}$Mn	4.08
^{56}Fe+H$\to^{55}$Fe	3.11
^{56}Fe+He$\to^{52}$Cr	2.81†
^{56}Fe+He$\to^{51}$Cr	2.62†
^{56}Fe+H$\to^{53}$Mn	2.59
^{56}Fe+H$\to^{54}$Mn	2.31
^{54}Fe+H$\to^{52}$Mn	2.23
^{56}Fe+H$\to^{55}$Mn	1.96
^{54}Fe+H$\to^{51}$Cr	1.88
^{56}Fe+H$\to^{54}$Cr	1.86
^{52}Cr+H$\to^{51}$Cr	1.62
^{56}Fe+He$\to^{50}$Cr	1.59†
^{54}Fe+H$\to^{50}$Cr	1.21
^{55}Mn + H $\to$ ^{52}Cr	1.11

Fluorine	
^{20}Ne+H$\to^{19}$Ne	16.8
^{20}Ne+H$\to^{19}$F	13.9
^{24}Mg+H$\to^{19}$F	8.80
^{28}Si+H$\to^{19}$F	8.12
^{22}Ne+H$\to^{19}$F	6.13
^{24}Mg+H$\to^{19}$Ne	3.48
^{56}Fe+H$\to^{19}$F	3.25
^{21}Ne+H$\to^{19}$F	3.17
^{28}Si+H$\to^{19}$Ne	2.99
^{23}Na+H$\to^{19}$F	2.30
^{25}Mg+H$\to^{19}$F	2.24*
^{26}Mg+H$\to^{19}$F	2.19
^{20}Ne+He$\to^{19}$Ne	1.97†
^{20}Ne+He$\to^{19}$F	1.73†
^{27}Al+H$\to^{19}$F	1.65
^{24}Mg+H$\to^{20}$Ne	1.36
^{22}Ne+H$\to^{19}$O	1.29
^{28}Si+He$\to^{19}$F	1.21†
^{24}Mg+He$\to^{19}$F	1.19†
^{24}Mg+H$\to^{21}$Ne	1.08
^{24}Mg+H$\to^{23}$Na	1.08
^{28}Si+H$\to^{27}$Al	1.05
^{56}Fe+He$\to^{19}$F	1.03†
^{21}Ne+H$\to^{19}$Ne	1.03†

Manganese	
^{56}Fe+H$\to^{53}$Mn	30.2
^{56}Fe+H$\to^{55}$Mn	27.2*
^{56}Fe+H$\to^{54}$Mn	18.6
^{54}Fe+H$\to^{53}$Mn	4.78
^{56}Fe+He$\to^{53}$Mn	4.00†
^{56}Fe+He$\to^{55}$Mn	3.62†
^{54}Fe+H$\to^{53}$Fe	3.06
^{56}Fe+H$\to^{53}$Fe	2.64
^{56}Fe+He$\to^{54}$Mn	2.47†
^{56}Fe+H$\to^{55}$Fe	2.33
^{55}Fe+H$\to^{53}$Mn	1.30†
^{55}Mn+H$\to^{54}$Mn	1.03

Table 2: Required number of interactions to be recorded, oredered by increasing charge and mass of the projectiles, in order to reach a modelling precision $\lesssim 1\%$ on GCR fluxes Li, Be, B and F. Adapted from Table IV of Ref. [207].

Reaction	$N_{\rm int}$
^{7}Li+H	5k
^{10}B+H	5k
^{11}B+H	10k
^{12}C+H	50k
^{12}C+He	10k
^{13}C+H	5k
^{14}N+H	10k
^{15}N+H	10k
^{16}O+H	60k
^{16}O+He	20k

Reaction	$N_{\rm int}$
^{20}Ne+H	50k
^{20}Ne+He	10k
^{21}Ne+H	10k
^{22}Ne+H	20k
^{22}Ne+He	5k
^{23}Na+H	10k
^{24}Mg+H	50k
^{24}Mg+He	10k
^{25}Mg+H	10k
^{26}Mg+H	10k
^{27}Al+H	10k

Reaction	$N_{\rm int}$
^{28}Si+H	50k
^{28}Si+He	10k
^{29}Si+H	5k
^{32}S+H	5k
^{56}Fe+H	30k
^{56}Fe+He	10k

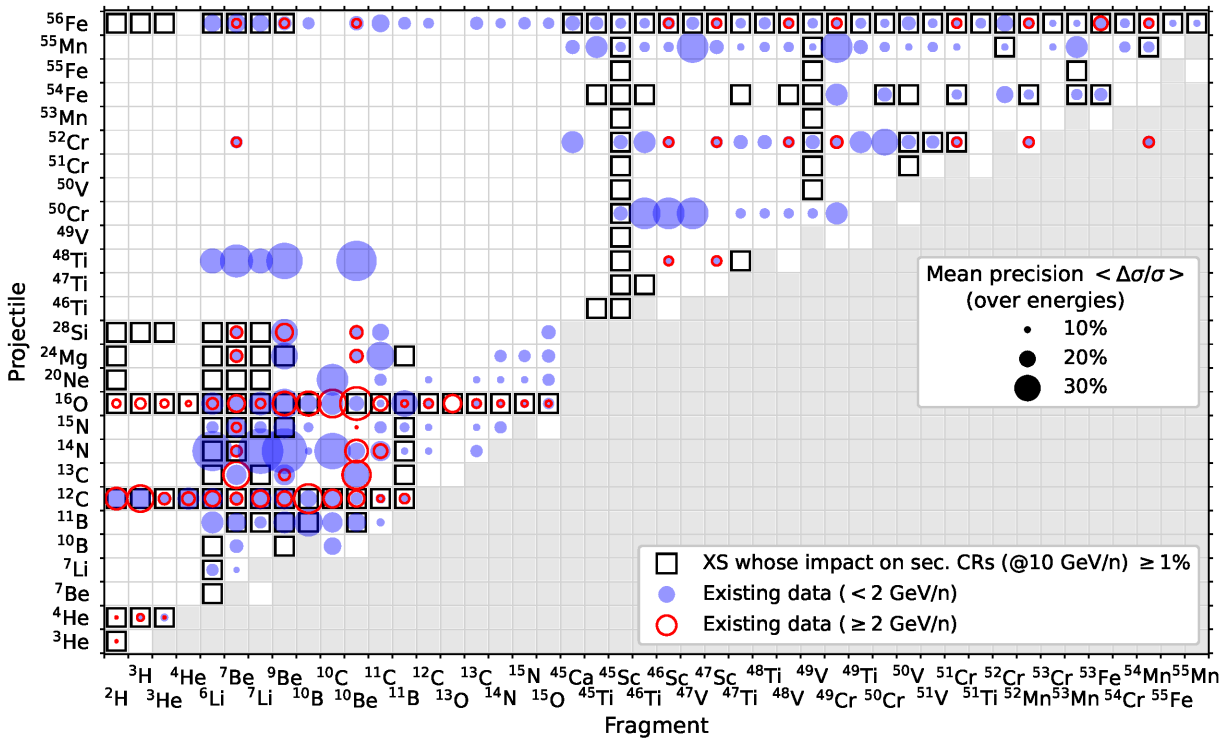

Figure 9: Illustration of the existing nuclear data below (blue disks) and above (red circles) 2 GeV/n, and their relative precision (size of the circles). We restrict ourselves to the matrix of projectiles (y-axis) and fragments (x-axis) formed from the reactions (black empty squares) contributing to at least 1% of the flux of GCR secondary species $Z < 30$, as listed in Table 1). The grey zone shows forbidden production regions ($A_f > A_p$): the fact that some nuclear data are reported for ^{52}Cr into ^{54}Mn, illustrates that some measured cross-sections come from projectiles in natural abundances (i.e., a mix of several isotopes, some heavier than the one reported) instead of single isotopes reported in this figure (for simplicity).

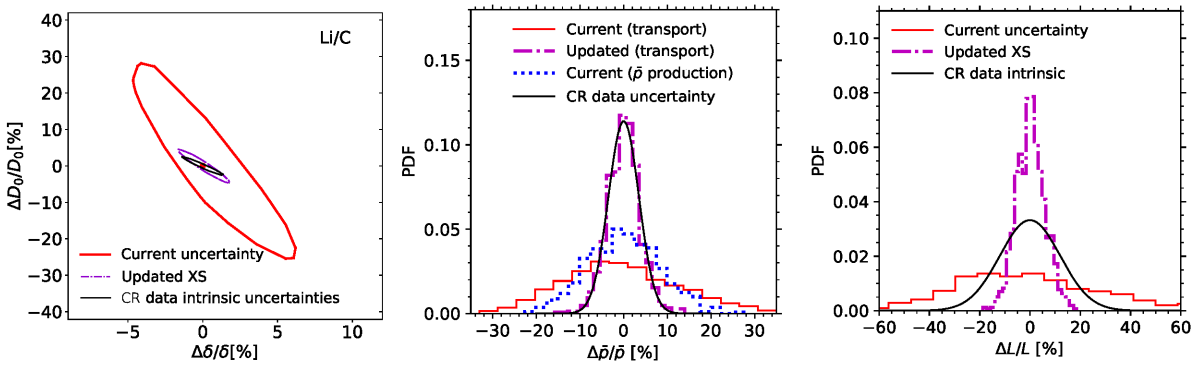

Figure 10: Forecast of the impact of new cross-section measurement campaigns on the normalisation and slope of the spatial diffusion coefficient entering the GCR transport Eq. (1), namely D_0–δ (left panel), $\overline{\text{p}}$ background calculation at 10 GV (middle panel) and diffusive halo size L determination (right panel). Each figure shows 1σ contours or distributions for current nuclear data uncertainties (red solid lines) and newly measured cross-sections according to Table 2 (magenta dashed lines), along with the irreducible/intrinsic uncertainty from current CR data (solid black line). For $\overline{\text{p}}$, we also show the uncertainties related to their direct production cross-section (blue dotted line), see Sec. 4.3. Adapted from [207].

GCR element under investigation. However, intermediate steps reactions, like the production of C and O isotopes from heavier nuclei always show up: this explains why the strategy of measuring all fragments for all reactions of interest (Table 2) is always the best option, if experimentally possible, to decrease the overall uncertainties on the modelled GCR fluxes. Figure 9 illustrates, for the most relevant reactions identified with black squares (matching those listed in Table 1), that (i) many reactions either have no data (empty squares) or data below 2 GeV/n only (blue disks and no red circles), and (ii) for the cases where data exist in the asymptotic regime above 2 GeV/n (red circles), their uncertainty is typically at the 20% level (as captured by the size of the circles).

To further prove that these measurements are worth doing, we can use the wish-list reactions given in Table 2 to sample the cross-sections before and after the new measurements. By repeating GCR analyses of secondary-to-primary ratios [26], the radioactive clock ratio ^{10}Be/^{9}Be [233] and $\overline{\text{p}}$ background calculations [35], we can forecast the impact of these new measurements [207]. Figure 10, adapted from [207], shows that the improvements on several key GCR parameters is drastic, and a sure game changer for the field.

4.2.4. Uncharted needs for $Z > 30$ reactions

The situation is far less clear for ultra-heavy nuclei. As illustrated in Fig. 6 and anticipated in Sec. 3.1.5, the GCR data in this mass range are very scarce and were mostly taken several decades ago. However, in the range $Z = 30$–40, the interpretation of the recent high-precision ACE-CRIS data [217], the forthcoming SuperTIGER [271, 272], and the future TIGER-ISS [270] and HERO [282] data (see Sec. 3.2.6), will also hit the cross-section uncertainties bottleneck. Besides, even the interpretation of the past $Z > 40$ data might also be limited by these uncertainties. The abundance pattern in Fig. 2 shows no dominant primary species (contrarily to C, O, Si and Fe for $Z \leq 30$), meaning that instead of a few dominant progenitors (as for $Z \leq 30$ species), many reactions from a broad range of elements will contribute equally in the modelled fluxes.

The efforts to perform new measurements have already started at Brookhaven, see Sec. 5.3.2. However, as for the lighter nuclei, a systematic analysis of the reactions to be measured with high priority must be carried out. The `YIELDX` code [340, 341], which gives the best results for unmeasured reactions, is appropriate for such study. But a systematic compilation of existing nuclear data is mandatory, to first renormalise the code before applying the predictions. Also, the number of short-live nuclei grows with A, so the decay branches of CRs, compiled more than four decades ago in Ref. [388], must first be updated from recent nuclear properties [389–391], in order to have the full list of ghost nuclei entering Eq. (6).

4.3. Production cross-sections relevant for indirect DM searches

As discussed in Sec. 3.1.2 and 3.1.3, the indirect search for DM in antimatter GCRs is pursued since decades. CR $\overline{\mathrm{p}}$, as well as antinuclei, positrons and γ rays, are very sensitive probes for DM annihilation or decay in our Galaxy, as discussed in Sec. 2. The first data on antimatter were collected by balloon-borne detectors [160, 190], then followed by satellite [162, 186, 99], and space-based experiments, especially by AMS on the ISS [3, 101, 392]. In particular, the discovery of the rise of the positron fraction data above 10 GeV, found by PAMELA [99] and Fermi-LAT [102], and confirmed with unprecedented precision by AMS [100], have been the subject of a broad theoretical debate. In fact, these very high-energy positrons cannot be explained with the secondary production alone, but may originate from primary sources, such as pulsar wind nebulae [103, 393, 105], supernova remnants [394] and DM annihilation or decay [395].

The modelling of all the above fluxes suffer from several uncertainties, including propagation uncertainties driven by nuclear cross-section uncertainties (see previous section). The calculation of exotic (primary) fluxes suffer in particular from the diffusive halo size uncertainty (see Section 4.1), while the calculation of background (secondary) fluxes are dominated by the production cross-sections uncertainties. The cross-sections entering the computations of the secondary flux, which acts as a background when searching for an exotic component, are the singly differential production cross-sections, $\mathrm{d}\sigma^{i+j\to k+X}(E^i, E^k)/\mathrm{d}E^k$, of a GCR projectile i (with energy E^i) interacting on the ISM target j to produce a GCR species k with energy E^k. In the Galaxy, the set-up is that of a fixed-target (ISM-like) experiment, and the secondary source spectrum is computed from an integration of the inclusive cross-section, $\mathrm{d}\sigma^{i+j\to k+X}(E^i, E^k)/\mathrm{d}E^k$, over all the GCR spectrum energies E^i, as seen in Eq. (3). However, the above cross-section derives from the measured, more fundamental and convenient, double differential Lorentz invariant cross-section:

$$\sigma_{\mathrm{inv}} = E\frac{\mathrm{d}^3\sigma}{\mathrm{d}p^3} = \frac{E}{\pi}\frac{\mathrm{d}^2\sigma}{\mathrm{d}p_{\mathrm{L}}\mathrm{d}p_{\mathrm{T}}^2}\,, \tag{11}$$

with E, p_{L} and p_{T} the energy, longitudinal and transverse momentum of the outgoing species f. The radial and Feynman scaling variables $x_R = E^*/E^*_{\mathrm{max}}$ and $x_{\mathrm{F}} = 2p^*_{\mathrm{L}}/\sqrt{s}$, where E^* and p^*_{L} are the energy and longitudinal momentum in the centre-of-mass frame, are also used. The centre-of-mass energy and GCR projectile energies are linked by $\sqrt{s} = (m_i^2 + m_j^2 + 2E_i m_j)^{1/2}$, where m_i and E_i are the mass and total energy of the GCR projectile, and m_j the mass of the ISM target (at rest).

The production cross-sections involved in the calculation of secondary $\overline{\mathrm{p}}$ are discussed in Sec. 4.3.1, those for antinuclei in Sec. 4.3.2, and those for positrons and γ rays in Sec. 4.3.3. For each GCR species, the current status of nuclear data is presented, and then the reactions – in terms of projectiles and targets, the energy range, and the cross-section precision –, needed to fully exploit current and near future CR data for DM searches, are listed. The role of nuclear codes is commented in Sec. 4.3.4, along with a synthetic view of a wish list in Table 3.

4.3.1. Antiprotons: status and game-changing measurements

Concerning $\overline{\mathrm{p}}$, the pp channel dominates the secondary production, alongside the contributions from Hep, pHe and HeHe, either in the GCR projectile or as ISM target, the rest coming mostly from interactions of heavier abundant GCR species (CNO, NeMgSi, and Fe) on H [396, 397, 35, 398, 35]. Data on the pp channel have been collected by the fixed-target NA49 experiment [399] at $\sqrt{s} = 17.3$ GeV, and by the NA61 experiment at $\sqrt{s}$=7.7, 8.8, 12.3 and 17.3 GeV, corresponding to beam proton energies $E_{\mathrm{k}} = 31$, 40, 80 and 158 GeV, respectively [400]. Lower-energy data are available at $\sqrt{s} = 6.1$ and 6.7 GeV [401], and at $\sqrt{s} = 6.15$ GeV [402]. Data from the BRAHMS (Broad RAnge Hadron Magnetic Spectrometers) experiment have been taken in pp collisions at $\sqrt{s} = 200$ GeV [403]. Data on p^{4}He have been recorded by the LHCb (LHC beauty) collaboration at CERN in fixed-target mode, using the SMOG (System for Measuring Overlap with Gas) device [404] with a proton beam momentum of 6.5 TeV/c (corresponding to $\sqrt{s} = 110$ GeV). More recently the AMBER (Apparatus for Meson and Baryon Experimental Research) collaboration, at the CERN SPS M2 beam line, has collected data with a proton beam impinging on a liquid ^{4}He target at six different momenta, from 60 GeV/c to 250 GeV/c (corresponding to $\sqrt{s} = 10.7$ GeV and 21.7 GeV). Data on pC have

also been collected by NA49 [405] at $\sqrt{s} = 17.3\,\mathrm{GeV}$. A full discussion on all the $\overline{\mathrm{p}}$ cross-section data and their role in the context of cosmic source spectra can be found in Ref. [398].

The current modelling of reactions on He of heavier GCR projectiles is based on a rescaling of the models derived on the pp reaction channels, and denoted $\sigma_{\mathrm{inv}}^{\overline{\mathrm{p}}}$ hereafter. The latter is separated in a prompt and a delayed emission originating from the decay of strange hadrons, labelled Λ in the following. Assuming $\sigma_{\mathrm{inv}}^{\overline{\mathrm{p}}\ \mathrm{delayed}} = \sigma_{\mathrm{inv}}^{\overline{\mathrm{n}}\ \mathrm{delayed}}$ [42], one can write:

$$\sigma_{\mathrm{inv}}^{\overline{\mathrm{p}}} = \sigma_{\mathrm{inv}}^{\overline{\mathrm{p}},\overline{\mathrm{n}}\ \mathrm{prompt}} + \sigma_{\mathrm{inv}}^{\overline{\mathrm{p}},\overline{\mathrm{n}}\ \mathrm{delayed}} = \sigma_{\mathrm{inv}}^{\overline{\mathrm{p}}\ \mathrm{prompt}}(2 + \Delta_{\mathrm{IS}} + 2\Delta_{\Lambda})\,, \tag{12}$$

with the isospin enhancement and the hyperon factors defined as:

$$\Delta_{\mathrm{IS}} = \frac{\sigma_{\mathrm{inv}}^{\overline{\mathrm{n}}\ \mathrm{prompt}}}{\sigma_{\mathrm{inv}}^{\overline{\mathrm{p}}\ \mathrm{prompt}}} - 1 \quad \text{and} \quad \Delta_{\Lambda} = \frac{\sigma_{\mathrm{inv}}^{\overline{\mathrm{p}}\ \mathrm{delayed}}}{\sigma_{\mathrm{inv}}^{\overline{\mathrm{p}}\ \mathrm{prompt}}}\,. \tag{13}$$

The currently available data are insufficient to establish distinct parametrisations for the above individual cross-sections. The parametrisations are therefore rescaled to the prompt emission and to the enhancement terms Δ_{IS} and Δ_{Λ}. The dominant production comes from the prompt emission, with significant additional contributions from hyperon-induced channels like $\overline{\Lambda}$ and $\overline{\Sigma}$. The $\overline{\mathrm{n}}$ contribution requires the knowledge of a possible isospin asymmetry, that could induce a possible enhancement Δ_{IS} of $\overline{\mathrm{n}}$ over $\overline{\mathrm{p}}$ production.

The total secondary GCR $\overline{\mathrm{p}}$ production uncertainty ranges about 15–20% [42, 398, 35]. It is primarily driven by the $\mathrm{p} + \mathrm{p} \to \overline{\mathrm{p}} + \mathrm{X}$ cross-section and receives contributions from all nuclei channels, dominated by the ones involving He. To enhance the accuracy of current models – to be on par with CR data precision (see Sec. 3.1.2 and Fig. 10) –, a set of key $\overline{\mathrm{p}}$ production measurements of the Lorentz-invariant fully differential cross-section (σ_{inv}) is essential for:

- *Prompt emission from pp at better than 3% precision*: first and foremost, new measurements should focus on reducing uncertainties of $\mathrm{p} + \mathrm{p} \to \overline{\mathrm{p}} + \mathrm{X}$ across the $\sqrt{s} = 5$–$100\,\mathrm{GeV}$ range, and cover regions with $p_{\mathrm{T}} \lesssim 1\,\mathrm{GeV/c}$ and $|x_{\mathrm{F}}| \leq 0.3$;
- *Production on He target with uncertainties below 5%:* additionally, measurements in pHe reactions are needed. The first-ever data on the inclusive cross-section $\mathrm{p} + \mathrm{He} \to \overline{\mathrm{p}} + \mathrm{X}$ were collected by the LHCb collaboration at CERN, using proton beams with $E_{\mathrm{k}} = 6.5\,\mathrm{TeV}$ and a fixed He target (see Sec. 5.1.1). These data were analysed in [398], although the centre-of-mass energy of the provided data is higher than the energy of the $\overline{\mathrm{p}}$ measured by AMS [392]. An extensive coverage of σ_{inv} in the $\sqrt{s} = 5$–$100\,\mathrm{GeV}$ range for pHe would allow an independent parametrisation for this channel.
- *Isospin enhancement Δ_{IS} with uncertainties below 5%*: an improved determination of the isospin asymmetry, affecting the contributions of $\overline{\mathrm{n}}$, is needed. The potential isospin asymmetry is particularly significant, as approximately half of the $\overline{\mathrm{p}}$ in GCRs originate from the decay of long-lived $\overline{\mathrm{n}}$. However, due to the limited experimental data on $\overline{\mathrm{n}}$ production, this contribution can only be inferred using symmetry arguments. Preliminary results from the NA49 experiment [41] suggest that $\overline{\mathrm{n}}$ production in pp collisions exceeds $\overline{\mathrm{p}}$ production, indicating the presence of an asymmetry; see also Sec. 5.2.1 and Fig. 17 for future measurements from AMBER and LHCb. To evaluate this asymmetry accurately, data on σ_{inv} for $\overline{\mathrm{n}}$ production in pp collisions, or for $\overline{\mathrm{p}}$ production in pp and pn collisions in the $\sqrt{s} = 5$–$100\,\mathrm{GeV}$ range, are critically needed.
- *Strange hadrons factor Δ_{Λ} with uncertainties below 10%*: the contributions from strange hadron decays, in particular the total $\overline{\Lambda}$ production in both pp and pHe reactions in the $\sqrt{s} = 5$–$100\,\mathrm{GeV}$ range, should be measured, with uncertainties at the 10% level [42].

For all these reactions, pushing the lower limit of $\sqrt{s}$ to values close to the $\overline{\mathrm{p}}$ production threshold ($\sim 3.8\,\mathrm{GeV}$) will be also extremely helpful for interpreting upcoming low-energy CR data from GAPS [258]. In order to get the GCR $\overline{\mathrm{p}}$ modelling uncertainties below a few percent, two conditions are required: first, the above quoted $\overline{\mathrm{p}}$ production precisions must be achieved for all production channels; second, significant improvement must be made on the nuclear production cross-sections, also responsible for dominant uncertainties on the GCR $\overline{\mathrm{p}}$ flux modelling (see Sec. 4.2.3).

4.3.2. Antideuterons and $\overline{\text{He}}$: coalescence-driven uncertainties

While not detected in CRs yet, $\overline{\text{d}}$ are expected to be even more sensitive probes than $\overline{\text{p}}$ for DM searches. Compared to possible DM production with a thermal cross-section, the secondary contribution of $\overline{\text{d}}$ is suppressed by a factor 10 or more at kinetic energy per nucleon below 1 GeV/n [406–408]. This is due to the fact that the secondary production has to satisfy the baryonic number conservation, and thus GCR p must have a total energy in the lab frame of at least $17m_{\text{p}}$ to produce an $\overline{\text{d}}$ (the corresponding value for $\overline{\text{p}}$ is $7m_{\text{p}}$).

Formation of antinuclei. The GCR spectra of $\overline{\text{d}}$ and $\overline{\text{He}}$ are typically calculated using the so-called coalescence models [409–411] both for secondary production and DM contributions. These models assume that individual $\overline{\text{p}}$ and $\overline{\text{n}}$ form antinuclei when their relative momentum falls below a certain threshold, referred to as the coalescence momentum. A first consequence is that the model describing $\overline{\text{d}}$ and $\overline{\text{He}}$ astrophysical production is directly impacted by the $\overline{\text{p}}$ production cross-section uncertainties described in the previous section. This coalescence parameter cannot be derived from first principles and varies depending on the production mechanism of the nucleus, such as whether it originates from different final states in DM annihilation or hadronic interactions. Alternative coalescence models, employing a quantum-mechanical Wigner function formalism [412–416, 53, 54], form the basis of recent advancements in calculating (anti)nuclei production from hadronic interactions, using MC simulations. We also stress that, the coalescence models are not the only approach to produce light nuclei in hadronic interactions. They can be produced by the statistical hadronisation of hot quark matter [409] which can be produced even in light systems [417]. This should be taken into account in particular in the description of pp data. Further studies and data are needed to understand if this could replace the coalescence model, or if both mechanisms play a role at the same time.

Existing nuclear data. The dataset for $\overline{\text{d}}$ production from pp collisions, which is relevant for the secondary flux, is quite rich thanks to the ALICE experiment, which provided data between 900 GeV and 13 TeV [51, 46–50], as described in Sec. 5.1.2. However, near the production threshold, only the Serpukov data at $p_{\text{lab}} = 70\,\text{GeV/c}$ [418] are available. For the production relevant for $\overline{\text{d}}$ primary flux, there are currently two data points from ARGUS at the Upsilon mass resonances 1S, 2S, 4S and continuum $\sim$10 GeV [44], and one data point from ALEPH at the Z boson resonance [45]. The latter is typically used to tune the DM production of $\overline{\text{d}}$, because the Z boson production from e^+e^- annihilation is assumed to be similar to the DM particle annihilation process.

Antideuteron and $\overline{\text{He}}$ flux modelling uncertainty. For primary antinuclei fluxes, Ref. [52] showed that once the coalescence models are tuned on the ALEPH data, the predictions for the $\overline{\text{d}}$ yield agree within 10% for high mass DM, despite the very different assumptions used in the simple coalescence and the Wigner function approach. For low mass DM, only the assumption of a decay into W^+W^- pairs gives a comparable prediction. In contrast, a decay of DM into $b\bar{b}$ pairs shows a significant enhancement of factor two for the Wigner function formalism using the Argonne v18 wave function. This indicates that the theoretical uncertainties in $\overline{\text{d}}$ production are no longer a major limitation, at least for high-mass DM and several channels for low-mass DM: the main limiting factor remains the error on the ALEPH data, of the order of 30%. While the Wigner function formalism is free of this parameter dependence, its dependence on the size of the emission source induces a similar constraint to its predictive power. The typical value of the coalescence momentum p_{coal} (see [419] for definitions) found when fitting ALEPH data is 0.15–0.21 GeV/c (see Refs. [407, 415, 419–421]). This leads to a conservative $\lesssim$ 60% uncertainty on the $\overline{\text{d}}$ primary flux prediction for most DM masses and channels, folding into a factor of a few for the flux of primary antinuclei.

For secondary antinuclei fluxes, values $p_{\text{coal}} > 0.2\,\text{GeV/c}$ are found when using ALICE data for pp collisions. Changing the coalescence momentum from the above 0.15 to 0.21 GeV/c would introduce uncertainties in the $\overline{\text{d}}$ spectra of approximately a factor of 3. However, the scarcity of current data on $\overline{\text{d}}$ from e^+e^- and the lack of reliable data at low energy for pp collisions (we recall that only the Serpukov data are available), makes difficult to study a possible dependence of the coalescence momentum value according to the physical process and the centre-of-mass energy: considering these Serpukov data leads to a strong decrease in the $\overline{\text{d}}$ production, which can be interpreted as an energy dependence of p_{coal} [422]. As a result,

coalescence-related uncertainties for the secondary flux are a factor of a few for $\overline{\mathrm{d}}$, and up to an order of magnitude for antinuclei [423].

Desired nuclear data. Collecting data on the production of $\overline{\mathrm{d}}$ and $\overline{\mathrm{He}}$ in pp collisions at $\sqrt{s} < 100\,\mathrm{GeV}$ would greatly improve the theoretical predictions for their secondary production. This could be achieved by measuring σ_{inv} over a large kinematic range in p_{T} and x_{F} or, at least, the integrated multiplicity in the energy range $\sqrt{s} \in [10, 100]\,\mathrm{GeV}$. Owing to a lower threshold, production from $\mathrm{p\overline{p}}$ collisions is also of interest: its contribution amounts to a few percents only at a few GV (see the pink dashed line in Fig. 15), but any data would be useful to check that the correct magnitude is used for this cross-section, i.e., to check that this production channel is not underestimated. In addition to this, more precise measurements for the antinuclei production from e^+e^- collisions are mandatory to verify whether the coalescence models and their parameters change according to the underlying physical process. In the light of the recent AMS claims on possible observation of several $\overline{\mathrm{He}}$ candidates, new scenarios for the enhanced production of $\overline{\mathrm{He}}$ have been proposed, including the decay of $\overline{\Lambda}_b$ baryons produced by the DM annihilation into $b\bar{b}$ pairs [424], though it is disputed [425, 426]. Preliminary results from LHCb seem to disfavour these models [427], but further measurements of the $\overline{\mathrm{He}}$ production from antibaryons decay could help better constrain the expected $\overline{\mathrm{He}}$ flux.

4.3.3. Positrons and γ-rays: improvement needed

The production cross-sections of positrons above 1 GeV in the pp channel, the primary channel for secondary positron production, were recently derived in an accurate model presented in Ref. [71]. This parametrisation was directly tuned using available measurements at various $\sqrt{s}$ values, from 3 GeV to 10 TeV, specifically from NA49 [428, 429], NA61 [400, 430], ALICE [431], CMS [432, 433] and a collection of older data [434]. While the empirical framework for the pp production cross-section is provided with an uncertainty of about 5-7%, there is room for improvement in the treatment of other nuclear channels. Indeed, no data on reactions involving He have ever been taken. For reactions beyond pp, the cross-sections employed in Ref. [71] rely on rescaling of the pp reaction channels. This rescaling is tuned on data from pC collisions collected by NA49 [435] at $\sqrt{s} = 17.3\,\mathrm{GeV}$ and by NA61/SHINE [385] at $\sqrt{s} = 7.7\,\mathrm{GeV}$. Improvements could be achieved through precise measurements of the Lorentz invariant fully differential cross-sections of $\pi^{\pm}$ and $K^{\pm}$ from pHe collisions in the $\sqrt{s} = 5$–$100\,\mathrm{GeV}$ range, with a primary focus on $\sqrt{s} = 10$–$20\,\mathrm{GeV}$. These measurements should cover a broad kinematic range, with $p_{\mathrm{T}} \lesssim 1\,\mathrm{GeV/c}$ and extensive coverage in x_{F}, aiming for uncertainties at the 5% level. Such data would enable proper modelling of individual reaction channels involving He, eliminating the need for simple rescaling approaches. For positron energies $E_{\mathrm{k}} \lesssim 1\,\mathrm{GeV}$, the cross-section data are missing, and the computation of the e^+ source spectrum relies on extrapolations.

Most of the γ rays produced by hadronic interactions and detected by Fermi-LAT [436] originate from the $\pi^0 \to \gamma\gamma$ decay, which results from hadronic interactions, with pp being the main production channel. A new model for the Lorentz-invariant cross-section of π^0 production was proposed in [70], with uncertainties ranging between 10% and 20%. This model was developed using the limited available data on total cross-sections of π^0[437], LHCf (LHC forward) data in the high-energy regime [438], and is strongly based on the previous analyses of the $e^{\pm}$ cross-section from Ref. [71]. New data on the Lorentz-invariant cross-section of π^0 production are necessary to reduce the uncertainty in $\sigma(i + j \to \pi^0 + X)$ to 5%, aligning it with the statistical uncertainties of Fermi-LAT. Specifically, measurements of π^0 production in the $\sqrt{s} = 5$–$1000\,\mathrm{GeV}$ range, covering a broad kinematic range with $p_{\mathrm{T}} \lesssim 1\,\mathrm{GeV/c}$ and extensive coverage in x_{F}, for both pp and pHe collisions, would significantly reduce these uncertainties. Even for pp collisions, the model in [70] depends on results obtained for $\pi^{\pm}$ to describe the p_{T} and x_{F} dependencies of the cross-section. The larger $\sqrt{s}$ range with respect to e^+ and $\overline{\mathrm{p}}$ is required by the energy range at which γ rays are measured by experiments like MAGIC (Major Atmospheric Gamma Imaging Cherenkov telescope) [439], H.E.S.S. (High Energy Stereoscopic System) [440], HAWC (High Altitude Water Cherenkov experiment) [441], LHAASO (Large High Altitude Air Shower Observatory) [442] and the upcoming CTAO (Cherenkov Telescope Array Observatory) [443].

Table 3: Summary of the wish list of production cross-sections for GCRs that can be indirect probes of particle DM. Here, $n_{\rm tot}$ is the integrated multiplicity. The most pressing need is for $\overline{\rm p}$, whose interpretation is already limited by cross-section uncertainties, but forthcoming CR data for $\overline{\rm d}$, and possible $\overline{\rm He}$ events from AMS, call for new cross-section measurements for these species. See text for the detailed motivations.

Particle	**Reaction**	**Measurement**	$\sqrt{s}$	**Sought precision**
$\overline{\rm p}$	$\rm p + p \to \overline{p} + X$	$\sigma_{\rm inv}$	5 to 100 GeV	$< 3\%$
	$\rm p + He \to \overline{p} + X$			$< 5\%$
	$\rm p + p \to \overline{\Lambda} + X$			$< 10\%$
	$\rm p + He \to \overline{\Lambda} + X$			$< 10\%$
	$\rm p + p \to \overline{n} + X$			$< 5\%$
	$\rm p + n \to \overline{p} + X$			$< 5\%$
$\overline{\rm d}$	$\rm p + p \to \overline{d} + X$	$\sigma_{\rm inv}/n_{\rm tot}$	5 to 100 GeV	(any data)
	$\rm p + He \to \overline{d} + X$	$\sigma_{\rm inv}/n_{\rm tot}$	5 to 100 GeV	(any data)
	$\overline{\rm p} + \rm p \to \overline{d} + X$	$\sigma_{\rm inv}$	2 to 10 GeV	(any data)
$\overline{\rm He}$	$\rm p + p \to \overline{He} + X$	$\sigma_{\rm inv}/n_{\rm tot}$	5 to 100 GeV	(any data)
$e^{\pm}$	$\rm p + He \to \pi^{\pm} + X$	$\sigma_{\rm inv}$	5 to 100 GeV	$< 5\%$
	$\rm p + He \to K^{\pm} + X$			$< 5\%$
γ	$\rm p + p \to \pi^0 + X$	$\sigma_{\rm inv}$	5 to 1000 GeV	$< 5\%$
	$\rm p + He \to \pi^0 + X$			$< 5\%$

4.3.4. Summary and wish list

In Table 3, the wish list of the measurements discussed throughout this section is reported. The needs and precision are not the same for various GCR species. The most pressing physics case is for $\overline{\rm p}$, where new nuclear data are needed now. Figure 11 illustrates the fraction of the source term, as defined in Eq. (3), covered by current and forthcoming data. As the source spectrum implies an integration of the cross-section over the kinematic phase-space of the produced $\overline{\rm p}$ and a convolution with the projectile, i.e., incident GCR, energy, a plethora of data with different $\sqrt{s}$ is needed for a very precise determination of the source spectrum. From left to right, we report the contribution to the pp, pHe and Hep source terms covered by available data (NA49 [399], NA61/SHINE [400] and LHCb [444, 445]), assuming the cross-sections are constant in a $\sqrt{s}$ interval around the provided results or the foreseen campaigns. The contributions are normalised to the total source term of each channel. Possible extensions brought by data that have been collected but are not yet publicly accessible (AMBER, dashed lines), or by potential data-taking campaigns (LHCb, dotted lines), are also indicated (see Sec. 5.1 for more details). It is worth underlining that, while data at lower $\sqrt{s}$ cover a larger fraction of the total produced $\overline{\rm p}$, following the power-spectrum decrease of the incident GCR fluxes (see Fig. 1), data at higher $\sqrt{s}$ allow the violation of the Feynman scaling to be constrained. For example, in Ref. [398], it was shown how the pioneering measurement by LHCb for antiprotons produced in pHe collisions [404] was able to discriminate between two different parametrisations for the invariant antiproton production cross-section. The pp channel is satisfactorily covered only for $\overline{\rm p}$ kinetic energies in the 5–30 GeV, corresponding to the low-energy range of AMS CR data; there are no high-precision CR data for $\overline{\rm p}$ below a few GeV, in a range where the future GAPS data will take data. For the He channels, the situation is far from optimal, and campaigns undertaken by AMBER and by LHCb would be very desirable. Second, improving the coalescence factor for $\overline{\rm d}$ is a necessity for the coming years, where one could expect their detection by ongoing and future CR experiments. Third, the impact of nuclear data uncertainties is less critical for the physics cases associated to e^+ and γ rays, but bringing nuclear data precision at the level of the current and forthcoming CR data precision remains desired.

These potential new measurements, encompassing various reactions and elements, are instrumental in refining and validating MC [446–452], the latter being crucial in simulating particle interactions and secondary production processes. By tuning MCs against experimental data, it is possible to improve their predictive

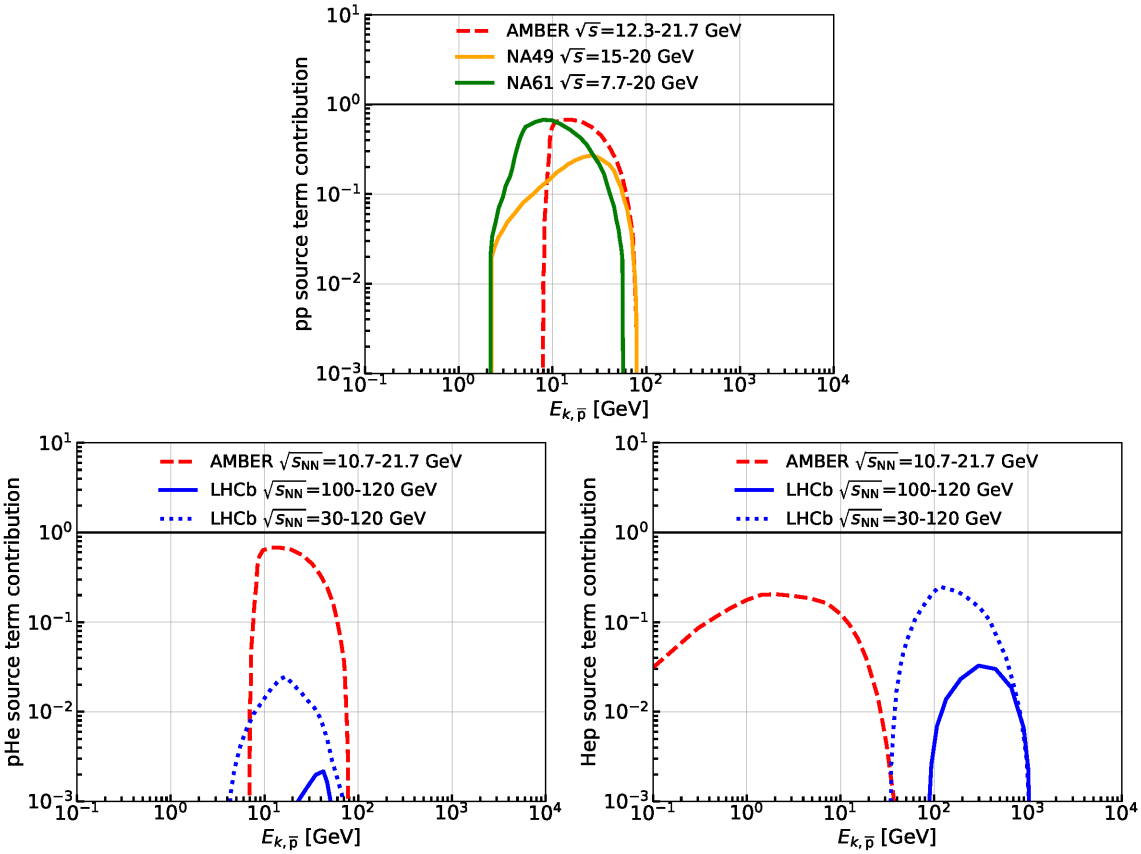

Figure 11: Fraction of the pp (top), pHe (bottom left) and Hep (bottom right) source terms originating from the kinematic parameter space of the cross-sections covered by different experiments. The contributions are normalised to the total source term of each channel. Solid lines represent experiments with data already collected and publicly available (NA49 [399], NA61/SHINE [400] and LHCb [444, 445]). Dashed lines indicate predictions for data that have been collected but are not yet publicly accessible (AMBER). Dotted lines correspond to future predictions for potential data-taking campaigns (LHCb).

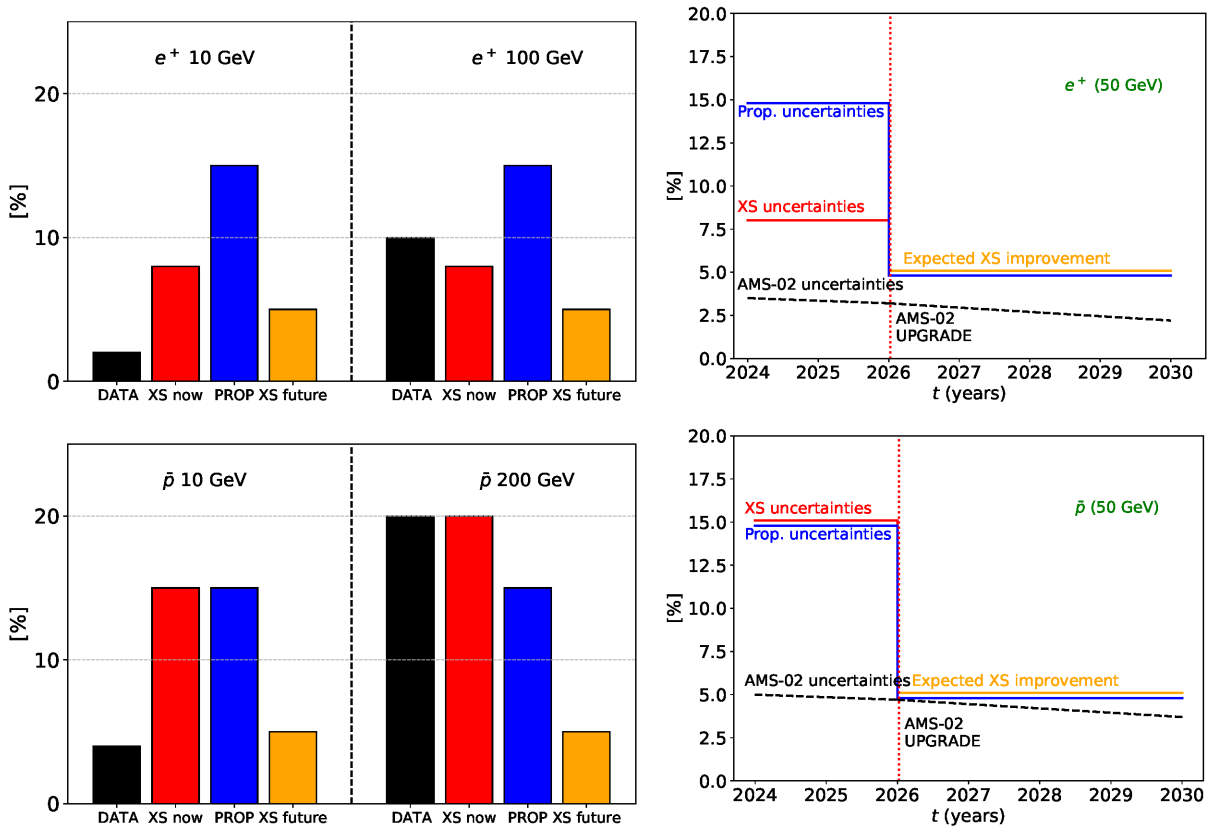

Figure 12: Left: the current AMS experimental $\overline{\mathrm{p}}$ errors at 10 and 200 GeV, alongside cross-section and propagation uncertainties. Right: prospects for the future, showing when and how cross-section uncertainties might reach levels comparable to AMS data.

accuracy, particularly for key observables such as cross-sections, particle multiplicities and energy spectra.

To conclude this section, as illustrative cases, Fig. 12 presents the current and future experimental errors for the AMS flux data and cross-sections for $\overline{\mathrm{p}}$ and electrons, together with the theoretical errors related to propagation. Current cross-section data uncertainties are 15% for $\overline{\mathrm{p}}$ and 8% for positrons, while the current AMS data errors are taken from [3]. The propagation uncertainties are taken to be about 15% across all the energies [52, 30]. Currently, the propagation and cross-section uncertainties are much larger than the AMS flux errors. This is true for both positrons and $\overline{\mathrm{p}}$ and for the most relevant energies for propagation and new physics studies. In the future, with the AMS upgrade, the CR flux errors could reach about 4% for $\overline{\mathrm{p}}$ and 2% for positrons at 50 GeV. The envisioned improvements in the e^+ and $\overline{\mathrm{p}}$ production cross-sections could reduce significantly the theoretical errors, at a level close to the AMS ones. Moreover, as explained in Sec. 4.2.3, the envisioned improvements in the nuclear cross-sections will bring to a significant reduction of the propagation uncertainties.

4.4. Other relevant cross-sections for data interpretation and experiments

Accurately modelling the propagation of GCR (anti-)nuclei from their source to their detection site requires precise knowledge of all cross-sections governing their interaction with the matter they encounter. Furthermore, and for antinuclei in particular, annihilation cross-sections are important not only to propagation but also to experiments. Some instruments purposely built for the detection of antinuclei, such as GAPS [188], rely on the characteristic patterns of secondary particles, mostly pions and γ rays, created upon annihilation, and therefore require knowledge of the multiplicities and energy spectra of these secondaries.

4.4.1. Contributions to $\sigma_{\rm tot}$ (inelastic, quasi-elastic, etc.) for nuclei and antinuclei

The total cross-section for the interaction of (anti-)nuclei with matter is given by the sum of the cross-sections for the different physical processes that can occur. In the following, we present decompositions of the cross-sections for nuclei and antinuclei that are consistent with each other, and briefly discuss the inconsistent use of nomenclature in the literature.

Contributions for nuclei. Following the notation used in Ref. [453], we decompose the total cross-section into

$$\sigma_{\rm tot} = \sigma_{\rm el} + (\sigma_{\rm quasi\text{-}el} + \sigma_{\rm prod}) = \sigma_{\rm el} + \sigma_{\rm inel}, \ . \tag{14}$$

Considering a generic reaction for a projectile i on a target j, the various subscripts in the above equation correspond to total (i.e., $i+j \to X$), elastic ($i+j \to i+j$), the sum of the quasi-elastic ($i+j \to i+j+X$) and production ($i+j \to X$ not i) reactions, combined into the total inelastic cross-section, $\sigma_{\rm inel}$. Other notations are also used in the literature, namely $\sigma_{\rm R}$ (reaction) for $\sigma_{\rm inel}$ and $\sigma_{\rm abs}$ (absorption) for $\sigma_{\rm prod}$. However, as stressed in Ref. [453], not all measurements and experiments use the same terminology for these processes (e.g., $\sigma_{\rm abs}$ has been used for $\sigma_{\rm prod}$ and $\sigma_{\rm inel}$), leading to some confusion. In the GCR community, the modelling for propagation studies relies on $\sigma_{\rm inel}$, but the different roles of $\sigma_{\rm quasi\text{-}el}$ and $\sigma_{\rm prod}$ is probably overlooked – as illustrated in Fig. 6 of Ref. [289] for C projectiles, where $\sigma_{\rm inel}$ and $\sigma_{\rm prod}$ data are treated on the same footing.

Contributions for antinuclei. As for nuclei, the total antinuclei interaction cross-section can be decomposed into

$$\sigma_{\rm tot} = \sigma_{\rm el} + (\sigma_{\rm quasi\text{-}el} + [\sigma_{\rm ann} + \sigma_{\rm prod}]) = \sigma_{\rm el} + (\sigma_{\rm quasi\text{-}el} + \sigma_{\rm abs}) = \sigma_{\rm el} + \sigma_{\rm inel}, \tag{15}$$

where the subscripts stand for total, quasi-elastic, annihilating, production, absorption and inelastic cross-sections, respectively. Compared to the total cross-section for nuclei, Eq. (14), annihilation is a third inelastic contribution to take into account: at high energy (above a few tens of GeV), $\sigma_{\rm ann} \approx 0$, so that $\sigma_{\rm inel} \approx \sigma_{\rm quasi\text{-}el} + \sigma_{\rm prod}$. In GCR publications, $\sigma_{\rm abs}$ is often denoted $\sigma_{\rm ann}$, while $\sigma_{\rm quasi\text{-}el}$ is denoted $\sigma_{\rm non-ann}$ or $\sigma_{\rm NAR}$ (for non-annihilating rescattering).

4.4.2. Inelastic and other relevant cross-sections for interpreting GCR nuclear data

The low-energy part of the GCR spectrum is shaped by energy losses, dominant below a few hundred MeV/n, and by inelastic interactions – the second term in Eq. (2). The latter is the second most important ingredient, after production cross-sections, required to model GCR fluxes with percent-level precision.

Relevance of elastic, quasi-elastic and production contributions in Eq. (14). First, in all GCR propagation codes, elastic interactions are neglected. However, a recent analysis pointed out that their impact is $\sim$1% for protons below GeV energies [454]. For consistency, this effect should thus be taken into account in the modelling, given the percent-level precision of measured proton fluxes.

Second, the correct way to model GCR transport should be to use $\sigma_{\rm inel}$ (i.e., including $\sigma_{\rm quasi\text{-}el}$) *and* consider the energy redistribution of the surviving projectile toward lower energies. The latter effect is modelled via the differential cross-section $\mathrm{d}\sigma_{\rm quasi\text{-}el}(E_{\rm in}, E_{\rm out})/\mathrm{d}E_{\rm out}$, which is non-zero for $E_{\rm out} \lesssim E_{\rm in}$ only, and which satisfies $\int_0^\infty (\mathrm{d}\sigma_{\rm quasi\text{-}el}/\mathrm{d}E_{\rm out})\ \mathrm{d}E_{\rm out} = \sigma_{\rm quasi\text{-}el}(E_{\rm in})$. This redistribution is important for antinuclei (see next section), but is expected to be sub-dominant for nuclei: indeed, GCR nuclei shifted to lower energies add up to a larger flux (at these lower energies), owing to a power-law behaviour observed down to $\sim$100 MeV/n [149, 150]. This energy redistribution is not considered in current propagation codes and should be quantified, as it may impact the flux, in the GeV/n regime, at the few-percent level.

Parametrisations and codes for $\sigma_{\rm inel}$ (often denoted $\sigma_{\rm R}$ in the literature). The simplest approximation for this cross-section considers the total surface of the projectile i and the target j, i.e., $\sigma_{\rm inel} \propto (A_i^{1/3} + A_j^{1/3})^2$. A first correction was proposed in the 1950s in Ref. [455],

$$\sigma_{\rm inel} = \pi r_0 \left(A_i^{1/3} + A_j^{1/3} - b_0 \right)^2 , \tag{16}$$

with r_0 the effective radius of the nucleus and b_0 the overlapping or transparency parameter. To account for the energy dependence of $\sigma_{\rm inel}$ at low energy, several improvements and refinements have been proposed since [335, 338, 456–467], based on the inclusion of more nuclear effects (Coulomb barrier, Pauli blocking, etc.), and thanks to growing nuclear data sets. Several of the above parametrisations are tailored for interactions on protons, scaled to He targets following Ref. [290], while others provide full parametrisations for nucleon–nucleon interactions. For light projectile–target systems, whose nuclear structure is quite different, specific modifications of the above formulae were proposed [459, 460, 462] (see, in particular, Ref. [346] for comparisons of these predictions). Some of the above cases are available in general-purpose tools (e.g., `Geant4` and `PHITS`). Alternative approaches are also being developed, for instance based on the Glauber theory (see, e.g., Refs. [468–471]), and in nuclear and MC codes (`FLUKA` [472], `CEM` event generator in `MCNP6` [370], the `Liège intranuclear-cascade model` [473]) – the modelling of the elastic and differential cross-sections is included in some of these codes.

Over the years, systematic comparisons between the proposed cross-sections have been carried out [340, 474, 467, 370, 475]; see, in particular, Ref. [475] for the most recent comparison of a variety of parametrisations. Overall, the nucleon–nucleon NASA parametrisations [461], with special cases for light systems [462], are always among the most successful to match all data sets: they are thus the ones used below for estimating the error budget in GCR fluxes. It is worth stressing that many nuclear data reach a $\lesssim 5\%$ precision, but as their coverage is not complete in terms of reaction (see Fig. 13), the precision of the models is unclear, because their spread in the asymptotic high-energy region can be as large as 20% (e.g., [476]).

From GCR data precision to desired $\Delta\sigma_{\rm inel}/\sigma_{\rm inel}$ precision. To estimate the precision needed on $\sigma_{\rm inel}$ for propagation modelling, we first quantify their impact on fluxes and flux ratios. We define the impact on the isotopic flux ψ^j to be

$$I^j_{\rm inel} = 1 - \frac{\psi^j}{\psi^j_{\sigma^{j+({\rm H,He})}_{\rm inel}=0}}, \tag{17}$$

i.e., the relative difference between the modelled flux with and without $\sigma_{\rm inel}$. For simplicity, the ISM targets are not considered separately. This relative difference is calculated with `USINE`, and is shown in the left panel of Fig. 13 for several energies and elements with $Z \leq 30$ (fluxes are not directly measured for heavier elements, see Sec. 3.1.5, so they are not shown). The flux of individual isotopes (also not shown) have similar $\sigma_{\rm inel}$, hence exhibit similar impacts (only isotopic fluxes for$Z < 6$ have been reported so far, see Sect. 3.1.6). Overall, the impact of $\sigma_{\rm inel}$ on fluxes decreases with energy (from black squares to pink crosses) – as the timescale of escape from the Galaxy becomes much shorter than the inelastic cross-section timescale ($t_{\rm diff}/t_{\rm inel} \propto 1/R^\delta$, with δ the diffusion slope) –, and increases with the GCR mass (as $\sigma_{\rm inel} \propto A^{2/3}$).

It is also useful to show the impact of destruction on elemental and isotopic flux ratios, the latter being often published in experiments (as they minimise the systematics) and also used in GCR phenomenology analyses. The thin lines (disk symbols) in the right panel of Fig. 13 show the impact of $\sigma_{\rm inel}$ on elemental ratios: the best way to mitigate this impact (and that of $\Delta\sigma_{\rm inel}$) is to consider adjacent charges, i.e., $\psi^Z/\psi^{Z_{\rm ref}}$ with $|Z - Z_{\rm ref}| \lesssim 3$. For isotopes, most of the CR data consists of ratios at low energy, and the solid black line (square symbols) shows that these ratios strongly mitigate the impact of $\sigma_{\rm inel}$, and thus of $\Delta\sigma_{\rm inel}$. The only, but very important, exception is for ratios involving a β-unstable isotope (e.g., ^{10}Be in ^{10}Be/^{9}Be). In that case, $\sigma_{\rm inel}$ does not impact the flux of the radioactive species (whose transport is dominated by its decay time), while the stable isotope is fully impacted (no mitigation). As a result, the impact of $\sigma_{\rm inel}$ on this ratio is directly that of the stable isotope.

The precision needed for $\sigma_{\rm inel}$ to reach a desired flux modelling precision is given by

$$\left(\frac{\Delta\psi^Z}{\psi^Z}\right)^{\rm modelled}(E_{\rm k/n}) = \left(\frac{\Delta\sigma^Z_{\rm inel}}{\sigma^Z_{\rm inel}}\right) \times \left|I_{\rm inel}(Z, E_{\rm k/n})\right| . \tag{18}$$

With the best CR data precision at the few-percent level for many elements and some very light isotopes, a modelling precision of 1% should be targeted, i.e., nuclear data with $\Delta\sigma_{\rm inel}/\sigma_{\rm inel} \lesssim 1/|I_{\rm inel}|$ are needed. To

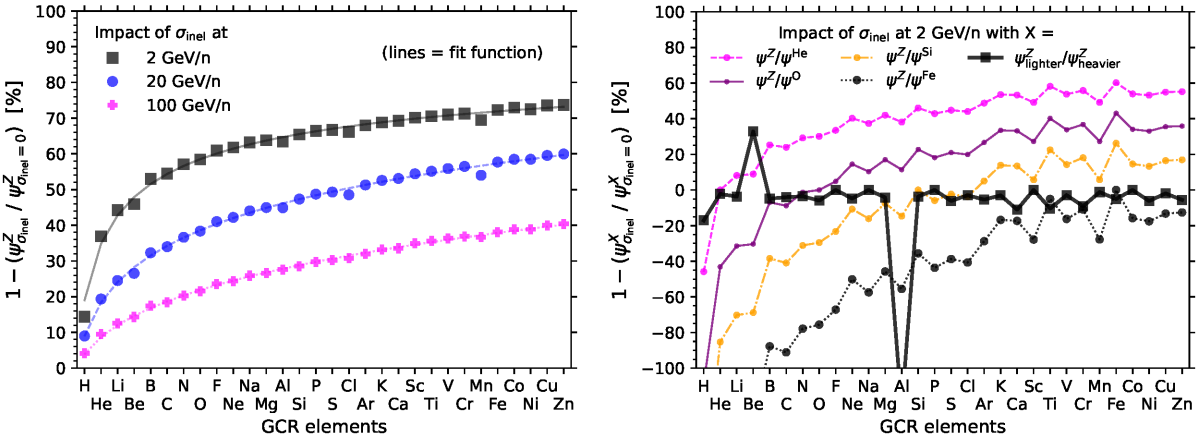

Figure 13: Impact of destructive interactions, Eq. (17), on the flux of GCR with $Z \leq 30$. Left: impact on elemental fluxes at 2 GeV/n (black squares), 20 GeV/n (blue disks) and 100 GeV/n (magenta crosses). The lines correspond to the fit function given in Eq. (19). Right: impact on the ratio of two elemental fluxes (coloured lines with disks) or the lighter-to-heavier isotopic flux ratio of the corresponding element (solid black line and squares). For the latter, the spikes for Be and Al are related to the presence of a β-unstable isotope in the ratios $X = (^7\mathrm{Be}/^{10}\mathrm{Be})$ and $X = (^{26}\mathrm{Al}/^{27}\mathrm{Al})$ because the fluxes of radioactive isotopes are insensitive to destruction at low energy. In this plot, the impact of inelastic interactions on flux ratios is shown at 2 GeV/n only. See text for discussion.

calculate this number for any species and energy, $I_{\rm inel}$ can be parametrised as

$$I_{\rm inel}^{Z+({\rm H,He})}(E_{\rm k/n}) = \left[\left(a_0 + a_1 E_{\rm k/n} + a_2 \log_{10}\left(E_{\rm k/n}\right)\right) \times \log_{10}(Z+0.45) \times Z^{b_0+b_1 E_{\rm k/n}+b_2 \log_{10}\left(E_{\rm k/n}\right)}\right] , \quad (19)$$

with $a_{(0,1,2)} = (0.49565, 0.00069, -0.104312)$, $b_{(0,1,2)} = (-0.254173, 0.000252, 0.070613)$ and $E_{\rm k/n}$ in GeV/n, as shown by the thin lines in the left panel of Fig. 13. Finally, to get the elemental flux at the desired precision, the uncertainty on the isotopic inelastic cross-sections is further weighted by the contribution of each isotope j to the flux of the element Z:

$$\left(\frac{\Delta\sigma^j_{\rm inel}}{\sigma^j_{\rm inel}}\right) = \left(\frac{\Delta\sigma^Z_{\rm inel}}{\sigma^Z_{\rm inel}}\right) \times \left(\frac{\psi^Z}{\psi^j}\right)^{\rm GCRdata} . \quad (20)$$

These values are shown in Fig. 14, where the needs are compared to the current precision of (or merely whether there exists) nuclear data for all relevant isotopes. The y-axis shows the GCR relative abundance of relevant isotopes, averaged over all data found in CRDB. The desired nuclear data precision calculation is weighted by the above isotopic fraction, Eq (20). Some inelastic cross-section data used in Fig. 14 were extracted from the EXFOR database [477, 478, 476]: pN scattering measurements below 1 GeV/n, as compiled in Refs. [479, 480] and, above 2 GeV/n, very few data points for pd [481, 482], p on He, Be, Al and Cu [483, 484]. The rest of the data above 2 GeV/n were retrieved from the largest set of Ref. [485], complemented by Refs. [486–494], and more recent measurements from 50 to 900 GeV [495–497], including the very recent NA61/SHINE data points [453].

Overall, the existing nuclear data points exhibit precisions below a few percent, but it is somehow difficult to believe that data taken from the 1960s to the 1980s are as precise as the data reported very recently from NA61/SHINE [453]. Moreover, most data come from interaction with elements in natural abundances, not always dominated by a single isotope. Also, the most abundant natural and GCR isotopes are not always the same. The main conclusion from this plot is that the data for $\sigma_{\rm inel}$ above a few GeV/n (i.e., in the asymptotic regime) remain scarce for many important isotopes/elements (e.g., Be, N, O and heavier species) while, for the modelling, a precision of $\lesssim 3\%$ is needed for all leading-order GCR isotopes.

Beyond the straight-ahead approximation for nuclear production. For secondary production, all propagation calculations rely on the straight-ahead approximation, Eq. (5), where the kinetic energy per nucleon of the

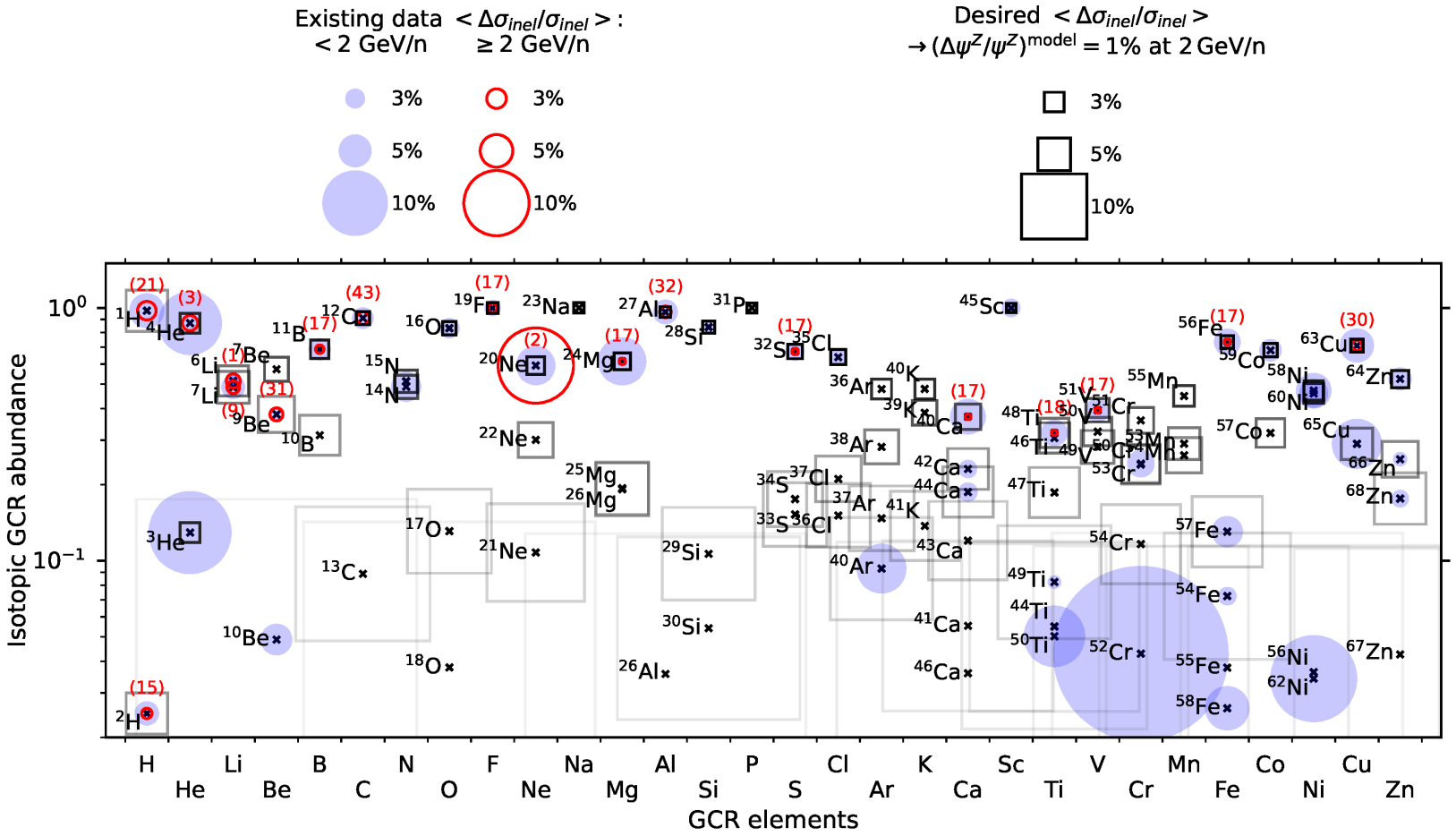

Figure 14: For all meta-stable isotopes in GCRs (sorted by increasing Z on the x-axis), the plot shows: (i) the relative abundance of each isotope in GCRs ($\times$ symbol), calculated from the weighted average over all data extracted from CRDB; (ii) the currently existing nuclear data and their average precision below (blue disks) and above 2 GeV/n (red circles); (iii) the cross-section precision needed to get a 1% modelling precision (black/grey squares) on $Z \leq 2$ isotopic fluxes and $Z \leq 30$ elemental fluxes, as obtained from Eqs. (18), (19) and (20). To illustrate the scarcity of data in the high-energy asymptotic regime, the number of available data sets is indicated in red in parentheses. Higher-precision (or any) data are needed for each isotope for which the red or blue circles are larger than the black/grey squares, or if there are no red circles at all. See text for discussion.

fragment is conserved. However, non-zero recoil velocities of the fragments [330] lead to a broadening of their energy distributions. Besides the intrinsic interest of connecting this velocity to reaction mechanisms and to the internal nucleonic motion (e.g., [498, 499]), this broadening, if not taken into account, affects the precision of the modelled fluxes. As studied in Ref. [500], it can be parameterised by a Gaussian distribution of the momentum transfer, with a parabolic dependence on the fragment mass. For the B/C ratio, the impact of relaxing the straight-ahead assumption was found to be $\lesssim 6\%$, peaking at $\sim 1\,\mathrm{GeV/n}$; similar conclusions were reached using an improved modelling of the recoil-velocity distributions [501]. This implies that the effect must be incorporated when comparing modelled secondary fluxes to AMS data. In particular, it should also be re-investigated and assessed for different secondary elements. A priori, the precision of current data should be sufficient for modelling this effect, given its small impact on the calculated fluxes. This hypothesis, however, must be confirmed with a dedicated study.

Electron attachment and stripping cross-sections for electron capture decay. Beside spontaneous β-decay, electronic capture (EC) decay – whereby an orbital electron is captured by a proton in the nucleus and the latter is transformed into a neutron – is another catastrophic loss to consider in the GCR transport equation. It involves a competition between three timescales [388, 502]: $t_{\mathrm{attachment}}$, $t_{\mathrm{stripping}}$ and t_{EC}, which refer to the timing of the attachment and stripping of electrons in the ISM, and to the EC decay, respectively. Precise EC-decay time can be challenging to disentangle from β^+ decay experimentally, as the daughter nucleus is the same in both decays, and fully ionised species (in the laboratory) are needed to disentangle the two channels. According to available data [503, 504], the attachment and stripping cross-sections vary roughly as $(Z^5, E^{1.5})$ and (Z^{-2}, E^0), respectively. This explains why, above a few hundred MeV/n, GCR species are fully ionised and why heavy species at low energy are the most likely to pick up electrons. For this reason, the latter have, among others, been used as (re-)acceleration clocks (see the discussion and references in Sec. 3.1.6, and see also, e.g., Ref. [505]). It is worth stressing that the current attachment and stripping cross-sections are based on parametrisations from the 1980s [388, 502] fit on data from the 1970s [503, 504]. So, in principle, they should be updated and their uncertainties re-estimated. However, in Ref. [506], the impact of EC in the associated fluxes and flux ratios – which is maximal at $\lesssim 1\,\mathrm{GeV/n}$ – was estimated to be at most at the precision of the current data (AMS and SuperTIGER). Therefore, there seems to be no urgency for new measurements of these cross-sections, unless one can assess that they are not known at better than a 50% precision.

4.4.3. Inelastic and non-annihilating cross-sections for interpreting GCR antinuclei data

The precision of available data and required improvements for the three inelastic processes of Eq. (15) are discussed below. As underlined in Sec. 4.4.2, we do not discuss elastic scattering, as it peaks in the forward direction (and hence results in negligible energy losses) and has a $\lesssim 1\%$ impact on antinuclei fluxes.

Desired precision on inelastic and quasi-elastic cross-sections for GCR antinuclei. Figure 15 shows the impact of the above cross-sections on the flux of $\overline{\mathrm{p}}$ and $\overline{\mathrm{d}}$ calculated with the `USINE` code. It does so in the form of the relative difference,

$$I_{\sigma}^{\overline{\mathrm{p}},\overline{\mathrm{d}}} = \psi_{\sigma=0}^{\overline{\mathrm{p}},\overline{\mathrm{d}}}/\psi_{\mathrm{ref}}^{\overline{\mathrm{p}},\overline{\mathrm{d}}} - 1\,, \tag{21}$$

for the reaction cross-section, σ_{inel} (solid lines), and for quasi-elastic scattering, $\sigma_{\mathrm{quasi\text{-}el}}$ (dashed lines), using the parametrisations of Refs. [507–510, 407] and assuming that $\mathrm{d}\sigma_{\mathrm{quasi\text{-}el}}/\mathrm{d}E = \sigma_{\mathrm{quasi\text{-}el}}/E_{\mathrm{k/n}}$. The impact of σ_{abs} on $\overline{\mathrm{p}}$ and $\overline{\mathrm{d}}$ is similar to its effect on p and d shown in Fig. 13: it is highest at low rigidities and increases with the atomic number, A. Actually, the impact of σ_{abs} (resp. $\sigma_{\mathrm{quasi\text{-}el}}$) increases (resp. decreases) with A, so that σ_{abs} is the dominant source of uncertainty for $A \geq 2$. To model the $\overline{\mathrm{p}}$ flux at the precision of AMS data, we thus need the uncertainty of both $\Delta\sigma_{\mathrm{abs}}/\sigma_{\mathrm{abs}}$ and $\Delta\sigma_{\mathrm{quasi\text{-}el}}/\sigma_{\mathrm{quasi\text{-}el}}$ to be much better than $(\Delta\psi/\psi)^{\mathrm{data}}/I_{\sigma}$, i.e., much smaller than 20%. For $(\Delta\psi/\psi)^{\mathrm{modelled}} \lesssim 1\%$, this translates into $\Delta\sigma/\sigma \lesssim 5\%$. For some forthcoming CR experiments, and as part of a long-term effort toward the detection of antinuclei (e.g., for DM searches), validating and improving the existing [511, 512] inelastic cross-section parametrisations (e.g., used in `Geant4`) for antinuclei–p and antinuclei–antinuclei, is already important now. While not critical for current GCR modelling, new data for the differential cross-section $\mathrm{d}\sigma_{\mathrm{non-ann}}/\mathrm{d}E$ and

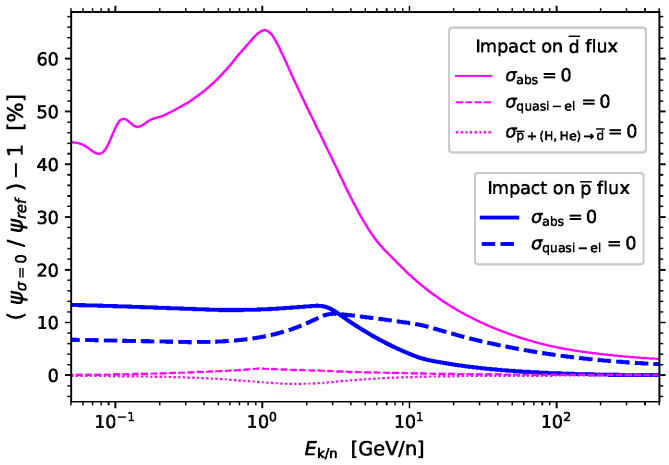

Figure 15: Impact of $\sigma_{\rm abs}$ (solid lines)and $\sigma_{\rm quasi\text{-}el}$ (dashed lines) on $\overline{\rm d}$ (thin magenta) and $\overline{\rm p}$ (thick blue) fluxes as a function of $E_{\rm k/n}$. For $\overline{\rm d}$, the specific contribution to the flux of the production via $\overline{\rm p}$ is also shown, as discussed in Sec. 4.3.1.

any data for $\sigma_{\rm non-ann}$ for $\overline{\rm d}$ (none exist at the moment) should prove very useful as well in the coming years.

Status of total and elastic scattering data. Total-reaction ($\sigma_{\rm tot}$) and elastic ($\sigma_{\rm el}$) cross-sections for $\overline{\rm p}$–p scattering were measured at CERN's LEAR (Low Energy Antiproton Ring) [513, 514], ISR (Intersecting Storage Rings) [515, 516], PS (Proton Synchrotron) [517] and SPS (Super Proton Synchrotron) [518, 516, 519, 520], at Fermilab [521–524], at LBNL (Lawrence Berkeley National Laboratory) [525–528], at BNL (Brookhaven National Laboratory) [529–531] and at IHEP (Institute of High Energy Physics) [532, 533], over a wide range of energies. Most early fixed-target experiments were performed at $\overline{\rm p}$ beam momenta between 200 MeV/c and 900 MeV/c, and between 4 GeV/c and 370 GeV/c. Only one experiment covered the range from 575 MeV/c to 5.35 GeV/c. For a compilation of all these data, see Ref. [534]. Many of the older measurements suffer from poorly understood (or reported) systematic uncertainties, and few have statistical uncertainties better than 5%. Later experiments at colliders were more precise but focused on much higher energies (31 GeV $\leq \sqrt{s} \leq$ 1.8 V, corresponding to fixed-target projectile momenta between 512 GeV/c and 1727 TeV/c), where the difference between $\overline{\rm p}$–p and p–p scattering is negligible.

Status of inelastic scattering data. Less data is available on inelastic $\overline{\rm p}$–nucleus scattering ($\sigma_{\rm non-ann}$). Measurements were performed on deuterons (deuterium) for projectile momenta between 1 GeV/c and 370 GeV/c at LBNL [528], at BNL [530, 531] and at Fermilab [521, 522]. Total-reaction cross-sections have also been published at a few selected energies (i.e., usually not more than two or three per experiment) for He [535, 536], Li [491], Be [537, 491], C [537, 491, 538], O [539], Al [491, 538], Cu [491, 538, 539], Ag [539], Sn [491], Pb [537, 491, 539] and U [491]. These, however, often suffer from poorly understood uncertainties and limited statistical significance. Comprehensive measurements are therefore needed to improve the ability to model the interaction of $\overline{\rm p}$ with, for example, detectors and the shielding surrounding them.

Besides $\overline{\rm p}$, the first measurement of the inelastic cross-section for $\overline{\rm d}$–nucleus interactions at low energies was performed by the ALICE experiment at momenta between 300 MeV/c and 4 GeV/c [540]. The only previously published measurements were those of the $\overline{\rm d}$ absorption cross-sections in Li, C, Al, Cu, and Pb at fixed momenta of 25 GeV/c [541] and 13.3 GeV/c [542]. In a unique experimental approach, the ALICE collaboration used their detector as interaction target for $\overline{\rm d}$ created in pPb collisions at $\sqrt{s_{\rm NN}} = 5.02$ TeV.[5]

[5]In collisions involving nuclei a and b with four-momenta p_a and p_b, respectively, it is conventional to introduce another variable in addition to the centre-of-mass energy $\sqrt{s} = \sqrt{(p_a + p_b)^2}$, denoted the *centre-of-mass energy per nucleon pair*

This approach, however, did not allow them to determine the cross-section for the interaction with a specific material. Instead, they measured $\sigma_{\rm inel}(\overline{\rm d} + \langle A \rangle)$, where $\langle A \rangle$ is the average mass number, with corresponding average nuclear charge, $\langle Z \rangle$, of the material seen by the particles; $\langle A \rangle$ and $\langle Z \rangle$ come from simulations with an accurate model of the detector. They benchmarked their method with $\overline{\rm p}$, achieving good agreement with the `Geant4` parametrisation of antinucleus–nucleus interactions. For $\overline{\rm d}$, they observed reasonable agreement above 1 GeV/c but discrepancies of up to a factor 2.1 at lower momenta.

This near complete lack of experimental data must therefore be addressed. The ALICE measurements have only hinted at a discrepancy between experimental data and theoretical models at lower momenta. They are unfortunately of limited use for improving the latter, because they do not allow to extract element-specific values. Using the same experimental technique, ALICE also performed the first ever measurements of the inelastic interaction cross-sections for $\overline{\rm t}$ [543] and $^3\overline{\rm He}$ [55], though with larger uncertainties than for $\overline{\rm d}$. So far, there are no other measurements for these isotopes, and none at all for $^4\overline{\rm He}$. While conclusively detecting $\overline{\rm d}$ and $\overline{\rm He}$ in GCR will probably only be achieved with the next generation of experiments, the $\overline{\rm d}$ and $\overline{\rm He}$ event candidates observed by AMS [191] show that cross-section measurements related to these species will be needed.

4.4.4. Nuclear cross-section needs for CR detectors

Apparent discrepancies exist among CR nuclei flux measurements from different experiments. The recent precision measurement of B, C, O and Fe from AMS [202, 204, 14] and CALET [209, 208, 213] exhibit an overall normalisation discrepancy of about 20% (as discussed in Sec. 3.1.4). In contrast, preliminary B flux measurements by DAMPE [544] show no such discrepancy relative to AMS. Earlier measurements from HEAO3 [16], PAMELA [545], CRN (Cosmic Ray Nuclei detector) [546] and CREAM [547] seemingly show a similar $\sim 20\%$ offset with respect to the B, C, O and Fe data of AMS. Disagreements are also observed between AMS and HEAO3, CREAM and CRN regarding Ne, Mg and Si fluxes [203]. Interestingly, no evident normalisation difference is observed among the H and He fluxes measured by AMS [202, 211], CALET [177, 176] and DAMPE [179, 178]. The existing discrepancies, particularly in the recent high-precision datasets from AMS, DAMPE and CALET, pose a challenge to the understanding of CR propagation.

While it is difficult to conclude what could be the origin of such discrepancies – given the large differences in the employed experimental and data-analysis techniques in different experiments –, an important and often predominant source of systematic error is due to the limited understanding of nuclear interactions in the detector materials. In general, the CR flux estimation relies on the knowledge of the experiment's geometric factor and fragmentation probabilities of the traversing CR nuclei, which are calculated using simulation codes such as `Geant4` [548] or `FLUKA` [549, 550]. These codes model the transport of nuclei through the detection volumes, simulating their interactions with detector materials and the subsequent production of secondary particles. However, in such codes, the interaction of heavy CR nuclei ($Z > 2$) with detector materials (such as C, Al, Si, and others) is modelled with a sparse and scattered dataset of nucleus–nucleus cross-section measurements. Often, nuclear models are extrapolated in regions where no experimental data exists. The lack of such nuclear data translates into a systematic uncertainty in the CR measurements. As described in Sec. 5.4, important efforts have been made by the AMS [551] and DAMPE [552] experiments to determine the interaction of CR nuclear species in their detectors, though additional measurements are still required.

Current (AMS, CALET and DAMPE), and future experiments (HERD, HERO, TIGER-ISS, etc.), can significantly benefit from precision measurements of the nucleus–nucleus inelastic cross-sections. The knowledge of the cross-sections of materials used in calorimeters is of particular importance, because they make

$\sqrt{s_{\rm NN}} \equiv \sqrt{(p_a/A_a + p_b/A_b)^2}$, A_a and A_b being the respective nuclear mass numbers. For collisions involving equal nuclei, one has $\sqrt{s_{\rm NN}} = \sqrt{s}/A$, so that this new variable coincides with $\sqrt{s}$ for nucleon–nucleon collisions. In the relativistic limit $E \approx p \gg m$,

$$\sqrt{s_{\rm NN}} \approx 2\sqrt{\frac{E_a E_b}{A_a A_b}} = \sqrt{s_{\rm pp}}\sqrt{\frac{Z_a Z_b}{A_a A_b}}\,, \tag{22}$$

where the latter equality assumes that the energy of a nucleus of atomic number Z_a is $E_a = Z_a E_p$, E_p being the energy that a proton reaches in the same accelerator; the expression thus relates $\sqrt{s_{\rm NN}}$ to $\sqrt{s_{\rm pp}}$, the centre-of-mass energy for two colliding protons in the same machine.

up most of the mass (and thus radiation length) of experiments. For instance, BGO (bismuth germanium oxide) and LYSO (lutetium–yttrium oxyorthosilicate) scintillating crystals are the major constituents of the DAMPE and HERD calorimeters, respectively, with other materials (mostly scintillators and absorbers) used in the calorimeters of some other experiments.

4.4.5. Annihilation cross-section needs for antinuclei CR detectors

The annihilation cross-section ($\sigma_{\rm ann}$) is particularly relevant to experiments that rely on the detection of annihilation products for identifying antinuclei, like GAPS [188]. Such experiments do not only require precise knowledge of $\sigma_{\rm ann}$ to calculate fluxes but also of the multiplicities and energy distributions of the created secondary particles. Some data exists for $\overline{\rm p}$ annihilation in H at rest [553, 554] and in flight [539, 555–559] but much of the energy range of interest to CR experiments remains uncovered and many older experiments have large (between about 5% and >20%) and sometimes unknown uncertainties. Only some newer measurements for in-flight annihilation reach precisions < 5% (e.g., [559]). Limited experimental data for other targets are available [560, 555, 561–567], suffering from a similarly limited precision, and agreement with theoretical models varies. For $\overline{\rm p}$ annihilation in C, for example, significant deviations from model expectations were observed below 500 MeV/c, which led to renewed interest in theoretical calculations [568, 569]. In addition to the problem of poorly known cross-sections, the multiplicities and energy distributions of secondaries emerging from the annihilation were only measured for a selection of targets and energies. The available data do not agree well with model predictions: see, for example, `Geant4` and `FLUKA`, which deviate from each other by as much as 25% [554].

Due to the complexity of such experiments, even fewer measurements were performed for $\overline{\rm d}$ [570] and none at all for $\overline{\rm He}$. While the recent measurements by ALICE (see Section 4.4.2) have shown that inelastic and absorption cross-sections for $\overline{\rm d}$ and $\overline{\rm He}$ can in principle be measured above a certain threshold energy using unconventional techniques, the feasibility of performing experiments at the low energies required to probe the annihilation process currently remains questionable. With the availability of facilities like CERN's Antiproton Decelerator and LEAR, the situation is much better for $\overline{\rm p}$, for which comprehensive measurements of the most relevant $\sigma_{\rm ann}$ and of the secondary particles created during annihilation, including multiplicities and energy distributions, should be conducted. Better data on the $\overline{\rm n}$–p [571–573] and $\overline{\rm n}$–nucleus [574] annihilation cross-sections and secondaries would allow improving theoretical models of the annihilation process. Finally, if the annihilation of $\overline{\rm d}$ and $\overline{\rm He}$ could be probed in ways similar to the ALICE approach, even data with relatively large uncertainties would be useful for model validation.

4.4.6. Summary and wish list

In this section, all cross-sections (not production) relevant for GCR data interpretation, and also for CR experiment analyses, were carefully reviewed. The most pressing needs are gathered in Table 4.

Related to the first item, i.e., to better constrain GCR propagation models, inelastic cross-sections for nuclei on H are needed at the few percent level – for energies from a few hundreds of MeV/n to several tens of GeV/n – for all leading isotopes in GCRs; measurements on He targets are also needed, but at a lesser precision ($\lesssim$ 10%). Figure 14 provides the current status of the nuclear data on H along with the desired precision for all the CR isotopes. For the interpretation of $\overline{\rm p}$ data, absorption and quasi-elastic cross-sections for $\overline{\rm p}$–p scattering need to be precise at the $\sim$ 5% level for energies between 1 and 10 GeV; slightly less accurate measurements for $\overline{\rm p}$–He are also desired. While data at this level of precision exists for the total and elastic cross-sections (with some caveats), direct measurements of the absorption cross-sections would be highly useful because of their large impact on the $\overline{\rm p}$ flux (see Figure 15). If the quest for $\overline{\rm d}$ detection in forthcoming CR experiments succeeds, having data on the absorption cross-sections for $\overline{\rm d}$ + p and $\overline{\rm d}$ + He at energies between 100 MeV/n and 50 GeV/n will no longer be optional; the required precision will depend on how precisely these future experiments will be able to measure fluxes. In light of the potential detection of $\overline{\rm He}$ nuclei by AMS, experiments should also be devised to measure cross-sections for $\overline{\rm He}$–p and $\overline{\rm He}$–He scattering at similar projectile kinetic energies.

A second item on the wish list is the extension of cross-sections to target materials relevant to instrumentation. First, new nuclear data are needed for inelastic interactions of GCR nuclei above GeV/n energies on C, Al, Si and Cu targets, and also on elements constituting BGO and LYSO crystals (because their

Table 4: Summary of highest-priority measurements for inelastic nucleus–nucleus and antinucleus–nucleus interactions (see definitions in Eq. (14) and Eq. (15), respectively): (i) interactions of GCR isotopes (for $Z \leq 30$ species only, summarised from Fig. 13) and antinuclei with H and He targets are required for propagation modelling, and thus for the interpretation of data gathered by CR experiments – the needed precision decreases with energy; (ii) interactions of GCR elements and $\overline{\text{p}}$ with heavier targets are needed for modelling the interaction with the detector material (C, Al, Si, Fe, and Cu) and with Earth's atmosphere (N and O) for the specific case of balloon-borne experiments; (iii) σ_{ann} and the total multiplicity, n_{tot}, are required for experiments relying on annihilation signatures for identifying antinuclei (e.g., GAPS), with σ_{ann} measured at rest up to 500 MeV (with a stronger emphasis on lower energies), and n_{tot} and the energy spectra of the emerging secondaries measured particularly for ^{1,2,3}H, ^{3,4}He, γ and $\pi^{\pm}$. In this table, the projectile kinetic energies per nucleon, $\text{E}_{\text{k/n}}$, for a (hypothetical) fixed-target experiment are quoted.

Reaction	**Measurements**	**Projectile** $\text{E}_{\text{k/n}}$	**Precision**
$(\text{p}, \text{d}) + \text{H}$	σ_{inel}, σ_{prod}	1 to 10 GeV/n	$< 10\%$
$(\text{p}, \text{d}) + \text{He}$			$\lesssim 50\%$
$(^3\text{He}, ^4\text{He}) + \text{H}$			$< 5\%$
$(^3\text{He}, ^4\text{He}) + \text{He}$			$\lesssim 50\%$
$(^6\text{Li}, ^7\text{Be}, ^{11}\text{B} \ldots ^{56}\text{Fe} \ldots ^{64}\text{Zn}) + \text{H}$			$< 1\%$
$(^6\text{Li}, ^7\text{Be}, ^{11}\text{B} \ldots ^{56}\text{Fe} \ldots ^{64}\text{Zn}) + \text{He}$			$\lesssim 10\%$
$\overline{\text{p}} + \text{p}$	σ_{abs}, $\sigma_{\text{quasi-el}}$	0.1 to 50 GeV/n	$< 5\%$
$\overline{\text{p}} + \text{He}$	σ_{abs}, $\sigma_{\text{quasi-el}}$		$< 50\%$
$\overline{\text{d}} + (\text{p}, \text{He})$	σ_{abs}, $\sigma_{\text{quasi-el}}$		(any data)
$\overline{\text{He}} + (\text{p}, \text{He})$	σ_{abs}		(any data)
$(\text{p}, \text{He}, \text{C} \ldots \text{Fe}) + (\text{C}, \text{N}, \text{O}, \text{Al}, \text{Si}, \text{Fe}, \text{Cu})$	σ_{inel}	0.1 to 1000 GeV/n	$\lesssim 10\%$
$\overline{\text{p}} + (\text{C}, \text{N}, \text{O}, \text{Al}, \text{Si}, \text{Fe}, \text{Cu})$	σ_{abs}	0.1 to 50 GeV/n	10%
$\overline{\text{p}} + \text{p}$	σ_{ann}, n_{tot}	< 500 MeV/n	<5%
$\overline{\text{p}} + (\text{C}, \text{Al}, \text{Si}, \text{Fe}, \text{Cu})$			<10%
$\overline{\text{p}} + \text{n}$			(any data)
$\overline{\text{n}} + \text{any}$	σ_{ann}, n_{tot}	< 500 MeV/n	(any data)
$\overline{\text{d}} + \text{any}$			
$\overline{\text{He}} + \text{any}$			

composition is variable) and other commonly used calorimeter materials. Dedicated studies are required to assess the possible mass-dependence of the cross-section uncertainty impact on the CR data precision. This impact is detector-dependent, but roughly, a better than 10% precision is needed. Second, cross-sections of $\overline{\text{p}}$ and antinuclei annihilating on C, Al, Si, Fe, and Cu for GAPS-like experiments, or inelastically scattering on N and O (prevalent in Earth's atmosphere), to aid the interpretation of data gathered by balloon-borne experiments, are required. The energy ranges and desired precisions are provided in Table 4. For experiments relying on annihilation signatures, the precision to which σ_{ann} is known directly drives the uncertainty of the measured flux; a precision of <5% for H and <10% for other targets is therefore desirable. Since σ_{ann} is largest for annihilation at rest, experiments should probe energies below 10 MeV/n and, if possible, extend to about 500 MeV/n, above which the cross-section becomes small enough for its uncertainty to not significantly impact flux calculations. Realistically, these measurements can only be performed comprehensively for $\overline{\text{p}}$. Data for $\overline{\text{n}}$, $\overline{\text{d}}$ and $\overline{\text{He}}$ are not a priority for the next ten years, but any measurements would certainly be crucial to GAPS-like next-generation experiments. Any data for $\overline{\text{d}}$ and $\overline{\text{He}}$ on p and He targets would also help to validate and improve interaction models and, therefore, reduce uncertainties compared to the scenario where only $\overline{\text{p}}$ data is available and extrapolated to heavier projectiles.

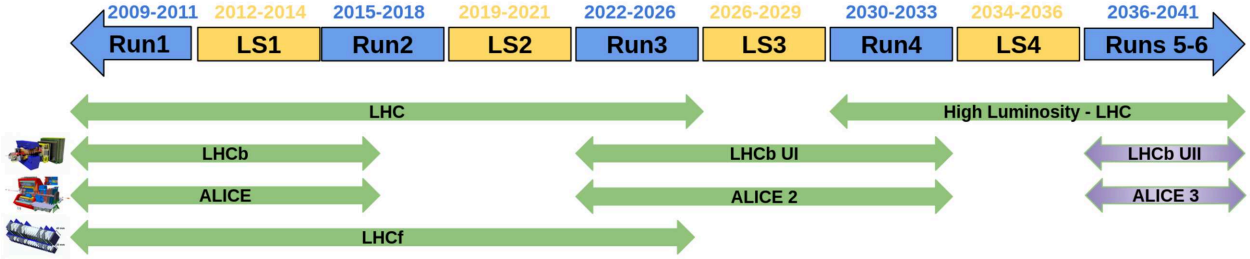

Figure 16: Timeline of the data acquisition (Run) and shutdown (LS) periods for the CERN LHC accelerator operations. The main phases of the ALICE, LHCb and LHCf experiments (discussed in the main text) are also overlaid. Upgrades currently under review and hence not yet officially approved, LHCbUII and ALICE3, are indicated in light purple.

5. Main facilities and experiments for ongoing and future cross-section measurements

In this section, the ongoing and future efforts carried out by the HEP and nuclear physics communities to provide some cross-sections listed in Sec. 4 (nuclear fragmentation, anti-matter production and interactions) are presented. The variety of required reactions and energy ranges calls for a variety of facilities and experiments, whose properties and specifics define in turn the measurements they are/will be able to do. These facilities include high-energy beams available at CERN from the LHC (Sec. 5.1), the SPS and the PS accelerators (Sec. 5.2), current and future nuclear physics multi-GeV accelerators (Sec. 5.3), and space CR experiments themselves (Sec. 5.4). Other facilities, where in principle relevant measurements can be carried out, such as the KEK or Fermilab [575] accelerators, are not covered here (see also Ref. [576] for a road map of the next generation accelerator facilities in the next decade). In the following, the most important characteristics of these facilities and experiments are highlighted, together with some recent results and planned measurements. The results obtained in the last years illustrate the successful emergence and growth of synergies between our communities, which need to be further strengthened in order to tackle the physics cases presented in Sec. 2.

5.1. CERN LHC experiments

Measurements of the $\overline{\mathrm{p}}$ production cross-sections have been performed at various facilities and different collision energies. While historical experiments [401, 434, 577, 578] laid the groundwork for these studies, the precision of their results falls short of current requirements, about 5%, as summarised in Table 3. In addition, the interpretation of their systematic effects, such as the subtraction of the $\overline{\mathrm{p}}$ feed-down contribution, is not always clear. High-statistics collision samples are also needed for $\overline{\mathrm{d}}$ and $\overline{\mathrm{He}}$ production measurements, as their production is rare and suppressed by at least a factor of 1000 for each additional antinucleon with respect to antiprotons [47]. For light collision systems and collision energies below 100 GeV, which are relevant for models of GCR antinuclei production, only sparse data are available. Precise measurements of their production mechanisms have only been achieved at colliders with very large collision energy [422, 579, 580]. Finally, as discussed in Sec. 4.3.3, measurements of neutral particle production cross-sections are crucial to better constrain the γ-ray case.

At CERN, the LHC particle accelerator provides collisions of protons at multi-TeV energies, up to the value of 13.6 TeV (recently achieved in 2022), and also of lead and lighter ions. As summarised in Fig. 16, the accelerator has operated since 2009, with several Long Shutdown (LS) periods, i.e., interruptions necessary to increase the achievable energy or luminosity. During those periods, experiments also have been significantly improved, as separately discussed in more details in the sections below.

5.1.1. The LHCb experiment

The LHCb experiment [581] at CERN LHC is a fully instrumented single-arm spectrometer, covering a pseudorapidity[6] region, $2 < \eta < 5$, not accessible by other LHC experiments. In addition, LHCb has the unique possibility to operate in fixed-target mode, leveraging on the injection of gases in the LHC beam pipe through the SMOG [582]. The energies covered by LHCb-SMOG, between 27 and 113 GeV in the nucleon–nucleon centre-of-mass frame for LHC beam energies ranging between 450 GeV and 7 TeV, bridge the gap between previous fixed-target experiments and the higher values by RHIC (Relativistic Heavy Ion Collider) or LHC. Starting from the LHC Run 3, simultaneous operation of the upgraded experiment [583] in collider and fixed-target mode has been proven [444, 445], allowing the negative to central Feynman-x values to be probed with very high-precision at a poorly explored energy scale. The SMOG upgrade, SMOG2, is equipped with a direct measurement of the gas flux, which reflects into a measurement of the collected luminosity with a 1–2% expected uncertainty, and also non-noble gases, such as H and D, can be used. In all collision systems, $\overline{\mathrm{p}}$ identification is ensured by RICH detectors, for momenta above 10 GeV/c. First measurements in pHe collisions for the prompt [404] and feed-down from strange [584] $\overline{\mathrm{p}}$ production have been published with data collected in 2016 at $\sqrt{s_{\mathrm{NN}}} = 110.5$ GeV, constraining for the first time – at the relevant energy scales – the extrapolation from H to He as a target. Another pHe dataset at $\sqrt{s_{\mathrm{NN}}} = 87$ GeV was collected in 2016 with SMOG, while with SMOG2 high-statistics samples with injected H, D and He have been acquired at $\sqrt{s_{\mathrm{NN}}} = 70.9$ GeV and $\sqrt{s_{\mathrm{NN}}} = 113$ GeV in 2024. With these datasets, as summarised in Fig. 17, the isospin-violating difference between $\overline{\mathrm{p}}$ and $\overline{\mathrm{n}}$ production will be constrained with expected uncertainties below 5%, filling the gap between the expected AMBER results and measurements at collider energies. Absolute cross-section measurements with similar precisions will also be repeated with all these gases. Finally, discussions are ongoing to explore the opportunity to develop machine optics such as to squeeze a 1 TeV beam sufficiently, in order to close the LHCb innermost detector and acquire data close to the lowest possible energy scale at LHC [585]. This would provide a larger coverage of the $\overline{\mathrm{p}}$ production phase space, and would allow comparing with results from lower-energy fixed-target experiments.

Although heavier antinuclei identification was initially not planned at LHCb, methods have been recently developed to identify $\overline{\mathrm{d}}$ and $\overline{\mathrm{He}}$ in the recorded Run 2 data. For $\overline{\mathrm{d}}$, the TOF capabilities of the tracking detectors downstream of the LHCb magnet are exploited, leading to identification of low-momentum (anti)deuterons [586, 587]. Based on this new technique, measurements of the deuteron production cross-section, both absolute and relative to $\overline{\mathrm{p}}$, are ongoing. For $\overline{\mathrm{He}}$, the detector responses are used to build discriminators quantifying the energy loss. Despite initially only applied to pp collision data [588, 589, 427], measurements are ongoing to constrain $\overline{\mathrm{He}}$ production in pNe fixed-target data as well. The absolute cross-sections at 13.6 TeV pp collision data, albeit at higher energy scales with respect to those needed for CR experiments interpretation, will also be finalised soon. In the long-term future, a further upgrade of the LHCb experiment is planned [590, 591], starting from the LHC Run5. This will include a dedicated TOF detector, TORCH (Time Of internally Reflected CHerenkov light) [590], allowing direct identification of nuclei in a large momentum range.

5.1.2. The ALICE experiment

The ALICE experiment at CERN LHC is a mid-rapidity experiment dedicated to nuclear physics in pp and heavy-ion collisions. The detector consists of several subdetectors that allow particle tracking in the pseudorapidity range of $|\eta| \leq 0.9$. Particle identification is mainly based on energy-loss measurements in a large time-projection chamber, and is completed with a TOF measurement system for higher momenta [592].

Antiproton production has been measured in pp, pPb, PbPb and XeXe collisions at several collision energies and particle multiplicities [431, 593–597]. Different antinuclei species and their ratios have also been measured, including $\overline{\mathrm{d}}$, $\overline{\mathrm{t}}$, $^3\overline{\mathrm{He}}$ and $^4\overline{\mathrm{He}}$ [597–600]. Additionally, (anti)hypernuclei – nuclei including a nucleon with strangeness – productions have been measured [601]. The variety of measurements allows detailed studies of the formation process of light nuclei, often described by the so-called coalescence model [409]. Parameters related to the coalescence probability of nuclei, with two and three nucleons, have been measured, and the experimental results have triggered studies beyond the classical coalescence model [50, 53].

[6] Being θ a particle polar angle with respect to the beam axis, its pseudorapidity is defined as $\eta = -\ln[\tan(\theta/2)]$.

ALICE has also performed momentum correlation studies [602–604], known as femtoscopy technique, of several hadron pairs. This allowed to constrain the size of the particle-emitting source in pp collisions, which is a necessary input for the coalescence model based on the Wigner function formalism. These results, together with the above-mentioned precise measurements of $\overline{\mathrm{p}}$ and $\overline{\mathrm{d}}$ production spectra, showed that $\overline{\mathrm{d}}$ yields can be successfully predicted by this model [54]. Moreover, ALICE also used femtoscopy to study the residual strong interaction between hadron pairs and triplets, including hyperons. This provides essential inputs for astrophysics, for instance to constrain the equation of state of dense matter, and to understand better the composition of such dense systems, in particular the inner core of neutron stars [605–607]. Further details on this technique are given in Sec. 6.4.2.

Besides the formation process of antinuclei, ALICE also measured the absorption of $\overline{\mathrm{d}}$ and $\overline{\mathrm{He}}$ in matter [540, 55]. These processes have been experimentally mostly unexplored, while they impact the survival probability of antinuclei produced in our Galaxy during their propagation from their sources to the Earth (see Sec. 4.4.3).

An upgrade of the experiment, ALICE3, is expected to start by the LHC Run 5. This will include a more extensive rapidity coverage, allowing to probe antinuclei production out of the central rapidity regime [608].

5.1.3. The LHCf experiment

The LHCf experiment [609] at CERN LHC is made of two imaging and sampling calorimeters, located at a distance of 141.05 m from Interaction Point 1, and covering a pseudorapidity region $\eta > 8.4$. The experiment is dedicated to the precise measurement of forward neutral particle production in pp and p–ion collisions, in order to provide calibration data to tune the hadronic interaction models used to simulate extensive air showers. These data provide indirect information on the event inelasticity, and on the fraction of the primary energy that goes into the electromagnetic and the hadronic channels. By changing the collision energy and the colliding ion, it is also possible to test the reliability of different scaling laws, and study the impact of mass number on forward production. Finally, the LHCf–ATLAS (A Toroidal LHC Apparatus) joint analysis gives access to an even higher level of information, for example by separating different mechanisms responsible for forward production (e.g., diffractive and non-diffractive), and by studying central-forward correlation or exclusive production mechanisms (like one-pion exchange or Δ resonance).

So far, the experiment has acquired data in pp collisions between $\sqrt{s} = 0.9$ and 13.6 TeV and pPb collisions at $\sqrt{s_{\mathrm{NN}}} = 5.02$ and 8.16 TeV. The published results indicate a tension between models and data, which is particularly strong in the case of neutron production [610, 611], and not negligible in the case of γ [612], π^0 [438] and η [613] production. Thanks to an ongoing improvement of the reconstruction algorithm, it will be possible to measure K^0_s and possibly Λ^0 forward production, from the data acquired in pp collisions at $\sqrt{s} = 13.6$ TeV. In parallel, the LHCf–ATLAS joint analysis will give a better insight in the understanding of production mechanisms, leading to greater constraints for the calibration of hadronic interaction models. The LHCf measurements can be used to constrain the production cross-sections entering the calculation of the astrophysical γ-ray background (from GCRs on the ISM), as shown in Ref. [70]. Indeed, π^0 and η are the main contributions to the γ-ray flux, and the inclusive γ production measured by the experiment can be used as a benchmark.

5.2. CERN SPS and PS experiments

Before circulating in LHC, particles are accelerated at CERN by lower-energy machines. The PS accelerator is one of the first acceleration stages, and can reach a maximum energy of 26 GeV. It delivers particles to the SPS, which has a maximum energy of 450 GeV for nuclei, and also provides secondary beams of nuclei to experiments from 10 to 158 GeV energy per nucleon. To this purpose, a primary beam of ^{208}Pb is extracted onto a beryllium target, and nuclear fragments are guided to the experimental area. The rigidity acceptance of the beam line can be adjusted to select the specific mass-to-charge ratio of the desired nuclei [614–616]. The SPS also delivers secondary hadrons at momenta up to 400 GeV/c, depending on the beam line[7]: on the H2 beam line (for NA61/SHINE), secondary hadron beams up to 400 GeV/c can be produced; on the M2 beam line (for AMBER), 280 GeV/c is the maximum hadron beam momentum.

[7] https://sba.web.cern.ch/sba/BeamsAndAreas/H2/H2_presentation.html

5.2.1. The AMBER experiment

The AMBER experiment at the M2 secondary beam line of CERN SPS is a fixed-target experiment that started data-taking in 2023 as the successor of the long-standing COMPASS (Common Muon and Proton Apparatus for Structure and Spectroscopy) experiment. Within the first approved phase of the experiment, from 2023 to around 2031, AMBER reuses and upgrades the 2-stage magnetic spectrometer from COMPASS, to perform measurements of the $\overline{\mathrm{p}}$ production cross-section, of the charge radius of the proton, and of parton-distribution functions of pions and kaons via the Drell-Yan process [617]. Measurements of $\overline{\mathrm{p}}$ production in collisions of protons on H, D and He targets took place in 2023 and 2024. The experimental setup includes two differential Cherenkov counters with achromatic ring focus to identify protons in the mixed hadron beam, a cryogenic target filled with the target gas, and the AMBER spectrometer to characterise the secondary particles created in the interaction. In order to measure the momentum of the secondary particles, the AMBER spectrometer consists of around 300 tracking detector planes that measure the tracks of charged particles traversing the two spectrometer magnets, with a bending strength of up to 1 Tm and 4 Tm, respectively. Additionally, a RICH detector and muon detectors allow particle identification over an extensive momentum range. Antiprotons with a total momentum between 10 GeV/c and 60 GeV/c, and transverse momentum up to 2 GeV/c, are identified. In 2023, a cryogenic target filled with He was used to performing the $\overline{\mathrm{p}}$ production measurement in pHe collisions. Data were recorded at six different collision energies between $\sqrt{s_{\mathrm{NN}}} = 10.7\,\mathrm{GeV}$ and $\sqrt{s_{\mathrm{NN}}} = 21.7\,\mathrm{GeV}$. In 2024, a new cryogenic target was built to allow the usage of flammable gases, such as H and D. For both targets, collisions at 12.3 GeV, 17.3 GeV, and 21.7 GeV were recorded with an identical spectrometer setup.

Besides providing $\overline{\mathrm{p}}$ production cross-sections for the different targets on the level of 5% relative uncertainty, one dedicated goal of the measurements is to investigate the possible isospin asymmetry of $\overline{\mathrm{p}}$ in pp and pn collisions (see Sec. 4.3.1), as suggested by data from NA49 [41], by comparison of the $\overline{\mathrm{p}}$ production in proton–hydrogen and proton–deuterium. The expected uncertainties on the individual cross-sections should allow a measurement of the isospin asymmetry, $\Delta_{\mathrm{IS}} = f_0^{\overline{\mathrm{n}}}/f_0^{\overline{\mathrm{p}}} - 1$, at the 10% level for the three collision energies. In the case of a measurable asymmetry, the measurement of the different collision energies would additionally constrain the collision-energy dependence of the effect. Figure 17 illustrates the impact of the AMBER and LHCb measurements on the isospin asymmetry in $\overline{\mathrm{p}}$ production, given an arbitrary asymmetry (based on the parametrisation of M. Winkler [42]).

In the future, the AMBER spectrometer will undergo several upgrades and improvements to operate the spectrometer at around 10–100 times higher read-out rates [618]. This improvement would allow the measurement of rare particles, such as $\overline{\mathrm{d}}$ and $\overline{\mathrm{He}}$. However, dedicated nuclei identification is needed for these studies, and is currently under investigation.

5.2.2. The NA61/SHINE experiment

The fixed-target experiment NA61/SHINE at the CERN SPS is a hadron spectrometer capable of studying collisions of hadrons with different targets, over a wide range of incident beam momenta [619]. It is the successor to the NA49 experiment, which pioneered $\overline{\mathrm{p}}$ production cross-section measurements at $\sqrt{s_{\mathrm{NN}}} = 17.3\,\mathrm{GeV}$ in pp and pC collisions, covering nearly the full phase space of created $\overline{\mathrm{p}}$. Using a deuterium beam, NA49 also provided a first measurement of a potential isospin asymmetric production of $\overline{\mathrm{p}}$ and $\overline{\mathrm{n}}$, by comparing the flipped reaction of $\overline{\mathrm{p}}$ in pp and pn collisions. The recorded data hints at an isospin asymmetry of up to 50% in central production ($x_{\mathrm{F}} = 0$).

NA61/SHINE consists of different subdetectors for particle identification. It has already recorded pp interactions with beam momenta from 13 to 400 GeV/c, and also collected data for other hadron interactions, including pC, $\pi^{\pm}$C, ArSc, pPb, BeBe, XeLa and PbPb at different energies. During the CERN LS2, upgrades to the time projection chamber backend electronics resulted in improvements in the specific energy loss ($\mathrm{d}E/\mathrm{d}x$) resolution. Essential for future $\overline{\mathrm{d}}$ production measurements is the new data acquisition system, with about 20 times faster rate and new TOF detectors with improved time resolution [620, 621]. NA49 and NA61/SHINE have published several relevant data [405, 400] for tuning models of the production of GCR species, and also for models describing CR-induced air showers [622, 623].

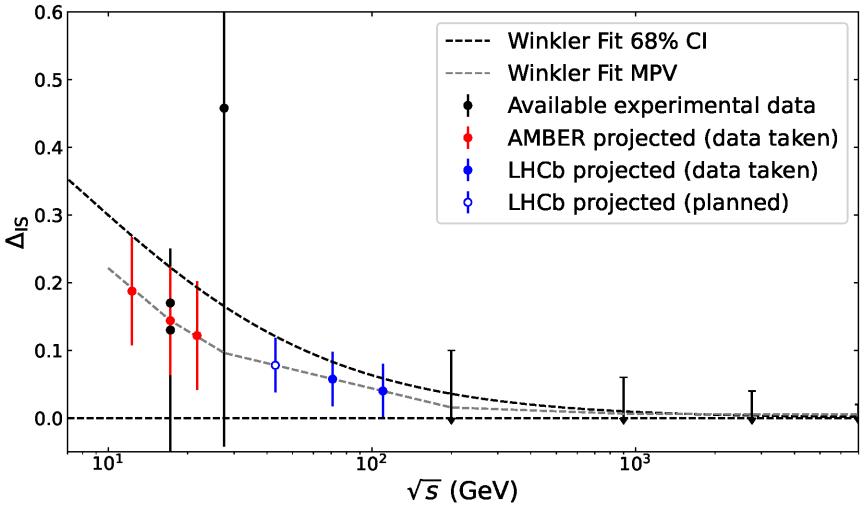

Figure 17: Impact of the AMBER and LHCb measurements on the uncertainties of a potential isospin asymmetric production of $\overline{\mathrm{p}}$ and $\overline{\mathrm{n}}$; see Eqs. (12) and (13). Data points are filled in case of data already taken and empty in case of planned for the upcoming years. The black dashed line indicates the current uncertainty on Δ_{IS} given the current data and model of the isospin asymmetry by M. Winkler [42]. The projected uncertainties for the individual measurement points from LHCb and AMBER are estimated based on assumed measurement uncertainties of 1% and 2% for the ratio of $\overline{\mathrm{p}}$ production cross-sections in p–D and p–H, respectively. Additionally, the limited phase-space coverage of both experiments reduces the sensitivity to the isospin asymmetry, which is primarily located in the target-fragmentation region (negative Feynman-x values, x_{F}). As a conservative estimate, the given uncertainties account for sensitivities of the experiments only down to $x_{\mathrm{F}} = 0$. Other potential modelling uncertainties, such as an explicit x_{F} dependence of the isospin asymmetry, are not considered in this estimate.

Antiproton cross-sections and coalescence for antinuclei. The published measurements of light nuclei in pp and various nucleus–nucleus data sets can be used to study the production of light ions at the threshold. These measurements will complement the NA49 [624, 625] and ALICE results, and allow testing coalescence and thermal models in a different regime. Extended data-taking with an upgraded NA61/SHINE experiment, relevant to understanding cosmic antinuclei, is already planned before 2026. A pp dataset of approximately 600 M events, collected with a beam energy of 300 GeV, will provide new measurements of pp correlations, $\overline{\mathrm{p}}$ and deuterons. This proposed dataset will feature significantly reduced systematic and statistical uncertainties, enhancing the ability to discriminate between different nuclear formation models. It is also anticipated that, for the first time, $\overline{\mathrm{d}}$ will be identified in this range, crucial for the cosmic antideuteron interpretation. Combining these new measurements will enable building, testing and validating data-driven d and $\overline{\mathrm{d}}$ production models in the energy range most relevant to GCRs. This will reduce uncertainties in the modelling of the astrophysical background of $\overline{\mathrm{d}}$.

Nuclear fragmentation. A first pilot run of carbon fragmentation measurement at 13.5 A GeV was conducted at NA61/SHINE in 2018, demonstrating that the measurements are possible [616]. For this type of measurement, the primary ^{208}Pb is extracted from the SPS and fragmented in collisions with a 160 mm-long beryllium plate in the H2 beam line. The resulting nuclear fragments of a chosen rigidity are guided to the NA61/SHINE experiment, where the projectile isotopes are identified via a measurement of the particle charge and TOF over a length of approximately 240 m. Moreover, data of the fragmentation of nuclei from Li to Si at 12.5 GeV/n were collected at the end of 2024, and are currently being analysed. The collected data were inspired by the interactions listed in Tab. 2, and they will provide a comprehensive set of cross-sections in the lower triangular region of Fig. 9. High-precision measurements of σ_{inel} and σ_{prod}, as defined in Eq. (14), necessary for GCR data interpretation (see Sec. 4.4.2), is also possible, as illustrated in Ref. [453]. In the future, these measurements of nuclear fragmentation (and inelastic cross-sections) with NA61/SHINE can potentially be extended up to Fe and performed at different energies.

Table 5: Overview of maximum beam energies (in GeV/n), for a few selected nuclei of interest for GCR fragmentation measurements (see Sec. 4.2), at the facilities described in Sect. 5. See the text for more details and discussions about possible measurements. The next-to-last column (secondary beams) indicates whether any of the above beams can be fragmented and filtered, thus offering a high-purity secondary beam with an energy close to the primary beam; for NA61, except for p, all species listed are from a primary beam of ^{208}Pb (see Sec. 5.2), but other primary nuclear beams (e.g., O) are possible. The last column (experiment type) corresponds to the detection system used at the date of this paper – it might evolve in the future: *spectrometry* refers to the identification in mass and charge of each heavy fragments; *activation* refers to the determination of concentrations of elements from γ-ray emitters.

Facility	**Selected beams and maximum $E_{k/n}$ (GeV/n)**								**Secondary beams**	**Experiment type**
	p	^{4}He	^{7}Li	^{12}C	^{16}O	^{20}Ne	^{28}Si	^{56}Fe		
CNAO	0.25			0.4					no	Spectrometry
NSRL	2.5	1.5		1.0	1.0	1.0	1.0	1.0	no	Activation
FAIR	4.5	2.0	1.55	2.0	2.0	2.0	2.0	1.75	yes	Spectrometry
HIAF	6.5	2.9	2.4	2.9	2.9	2.9	2.9	2.7	yes	Spectrometry
SPS	400	158	158	158	158	158	158	158	yes	Spectrometry

5.2.3. CERN n_TOF for neutron-related cross-sections

The n_TOF neutron time-of-flight facility [626] is located at CERN. A 20 GeV/c proton beam from the PS accelerator is shot on a thick lead target, generating neutron beams covering kinetic energies ranging from the thermal region to several GeV. The facility was optimised for high-precision measurements on radioactive materials, due to a very low duty cycle (repetition rate less than 0.5 Hz) and very long flight-paths, from 20 to 180 m. In recent years, developments have been made to measure cross-sections of reactions leading to the emission of charged particles, often abbreviated in (n,cp) channels, using silicon detectors. Preliminary results were obtained for neutron energies up to a few MeV [627]. A limitation to reach higher energies can be ascribed to the very strong γ flash that comes with every neutron pulse and blinds most detectors for a short time. A development has started to use gaseous detectors PPACs (Parallel Plate Avalanche Counter) for such measurements, since these detectors are much less sensitive to the γ flash.

This facility could be taken advantage of to carry out measurements on various targets (C, O, etc.), crucial for cosmogenic studies. Indeed, neutron-induced reactions are the dominant contributors to the formation, for instance, of ^{10}Be (see Fig. 19 in Sec. 6.1).

5.3. Multi-GeV facilities for nuclear cross-sections

Nuclear fragmentation cross-sections are critical down to energies of a few hundreds of MeV/n, hence high-precision measurements are also needed in this energy range. Below the energies of the CERN complex (covered in sections 5.1 and 5.2), many facilities exist. However, the requirement of energy beams above $\sim$100 MeV/n drastically limits the list of facilities where direct relevant measurements may be conducted: the CNAO (Centro Nazionale di Adroterapia Oncologica) reaches a few hundreds of MeV/n for proton and carbon beams (Sec. 5.3.1), the NSRL at BNL offers a variety of beams in the GeV/n range (Sec. 5.3.2), the GSI/FAIR (Facility for Antiproton and Ion Research at GSI Helmholtz Centre for Heavy Ion Research) offers various beams in the 1–2 GeV/n range [628] (Sec. 5.3.3), and the upcoming HIAF (Heavy-Ion Accelerator Facility) in China should deliver heavy beams up to 2.9 GeV/n (Sec. 5.3.4).

Below, the most salient features of these facilities are presented, including the detection systems adapted to high-precision fragmentation cross-section measurement. In Table 5, the maximum energy and most relevant beams that could be suitable to carry out the nuclear fragmentation programme of Sec. 4.2 are listed. Note that the NICA complex [277] in Dubna, designed to produce heavy ions with an energy of 1–3.9 GeV/n, is not discussed in this paper, since no appropriate detection system is known at the time of writing.

5.3.1. CNAO (Italy)

The CNAO facility, located in Pavia (Italy), is a hadrontherapy centre using a synchrotron accelerator. It is equipped with an experimental room that can provide clinical ion beams [629]. Currently, it can provide

protons and ^{12}C ions with energies between 60–250 MeV (protons) and 120–400 MeV/n for ^{12}C, and will soon be able to provide other ion types: ^{4}He, ^{7}Li, ^{16}O. The accelerator can deliver up to 10^{10} p per spill (equivalent to 2 nA) and 4.10^{8} C ions per spill (equivalent to 0.4 nA). The spills are delivered within 1 s, with a time of 2 s between each spill. The size of the pencil beam is around 10 mm (full width half-maximum), and thanks to the scanning magnets, it can irradiate a field up to 200×200 mm^2 at the isocenter.

This facility is being used to measure a variety of cross-sections relevant to hadrontherapy (see details in Sec. 6.3), and future measurements will take advantage of the additional ion beams available. No energy or intensity upgrades are planned for the next 5 years.

5.3.2. Brookhaven (USA)

The RHIC accelerator [630] at BNL, New York, is a high-energy collider (up to 100 GeV/n for gold and to 250 GeV/n for protons). However, RHIC is dedicated to the physics of quark and gluon plasma and no experimental hall is currently equipped or foreseen to host fixed-target experiments focused on the identification of heavy fragments.

Also part of BNL, the NSRL (NASA Space Radiation Laboratory) is an irradiation facility that takes advantage of the BNL AGS (Alternating Gradient Synchrotron) to provide protons and heavy ions at space-relevant energies [631] (see more in Sec. 6.2): protons up to 2.5 GeV, ^{4}He up to 1.5 GeV/n, and several heavy nuclei (^{12}C, ^{16}O, ^{20}Ne, ^{40}Ar, ^{56}Fe) up to 1 GeV/n. The maximum intensities are on the order of a few 10^{9} per second, except for protons, where the intensity can reach 2.2×10^{11}/s. A series of quadrupole magnets is available to shape the beam to cover large areas or to irradiate multiple targets at once. NSRL can provide measurements over the entire energy range with a single experimental setup, a feature which contributes to reduce systematic uncertainty. The NSRL proton beam flux is measured in situ with a precision of 3.6%.

After irradiation at NSRL, on-site activation measurements are made for short-lived daughter products using local high-purity Germanium detectors (HPGe), while for longer-lived isotopes the irradiated targets can be sent back to NASA GNTF (Gamma-ray Neutron Test Facility) at GSFC (Goddard Space Flight Center) for decay analysis using high-precision Ge-based γ-spectrometers. The detection efficiency is calibrated using NIST-traceable (National Institute of Standards and Technology) sources that have activities known with a precision of 3% or better. Cross-sections can be determined from the activated target measurements using basic nuclear physics coupled with the relevant nuclear decay parameters. Recent examples of such experiments are the measurement of spallation cross-sections of ^{nat}Cu [632], ^{nat}Cr and ^{nat}Mn, from 200 MeV to 2.5 GeV protons.

5.3.3. GSI (Germany): past measurements and FAIR in 2027

GSI offers a large variety of beams with a maximum energy defined by the magnetic rigidity of its synchrotron, 18 Tm presently. This corresponds to 2 GeV/n energies for light systems such as C and O. Currently, 28 different primary beams are available at GSI, from p to ^{238}U, covering the most abundant nuclei in the ISM. In addition to these primary beams, hundreds of radioactive species can be proposed as secondary beams using the FRS (FRagment Separator), a low-transmission, high-resolution recoil magnetic spectrometer [633].

The facility has a significant history with spallation cross-section measurements. Between 1996 and 2011, several such measurements were performed at GSI, based on the inverse kinematics technique and using liquid hydrogen targets: ^{56}Fe at 300, 500, 750, 1000 and 1500 MeV/n [330]; ^{136}Xe at 200 and 500 [634], and at 1000 MeV/n [635], ^{197}Au at 800 MeV/n [636], ^{208}Pb at 500 MeV/n [637] and at 1000 MeV/n [638], and ^{238}U at 1000 MeV/n [639]. Most of these measurements relied on the complete identification (mass and charge) of the heavy fragment by the aforementioned FRS. Cross-sections were obtained with a typical uncertainty of 4%, but it should be noted that the transmission of the spectrometer was estimated in a rather crude way (a sharp 15 mrad cut-off), so error bars for large mass variations and/or low energies were possibly underestimated at the time. Another pair of experiments, on ^{56}Fe [640] and ^{136}Xe [641], both at 1000 MeV/n, were conducted using the large-acceptance ALADIN (A Large Acceptance DIpole magNet) magnet, with the goal of simultaneously measuring the heavy residue and the light fragments and particles.

The FAIR facility is currently in the final stage of construction and is expected to host its first experiments in 2027. Its powerhouse will be a new synchrotron, the SIS100 [642], with a maximum magnetic rigidity of

100 Tm. Depending on the chosen element, beams are expected to have a maximum intensity of the order of 10^{11} per spill, the slow extraction mode making this roughly equivalent to a constant intensity of 10^{11} Hz. Taking over the role of the present FRS, the new recoil separator, the Super-FRS [643], will offer access to an even larger diversity of secondary beams, with increased intensities.

The first possibility to measure GCR cross-sections is to use the Super-FRS, in a way similar to the spallation campaign mentioned above. It is important to note that the Super-FRS itself was designed with a maximal magnetic rigidity of 18 Tm, the same as the FRS. However, the Super-FRS will offer improved transmission (cut-off of 40 mrad in the horizontal direction and 20 mrad in the vertical one) and, more importantly, better knowledge and flexibility of its optics. Therefore, Super-FRS could prove to be an excellent tool for measuring cross-sections with high accuracy, provided the efficiency can be assessed with sufficient precision. At the time of this writing, no liquid-hydrogen target is foreseen at the entrance of the Super-FRS, so early experiments should be conducted with CH_2 and C targets.

A second direction is to set up a measurement in the future HEC (High Energy Cave), where the new supraconducting, large-acceptance magnet GLAD (GSI Large Acceptance Dipole) will be installed to be the backbone of the R^3B (Reactions with Relativistic Radioaktiv Beams) setup. Exclusive experiments, similar to the SPALADIN (spallation at ALADIN) measurements mentioned above, can be foreseen there. A liquid-hydrogen target is already available for this setup. A possible downside of such an experiment is that only reduced beam intensities can be used, as the full beam goes through the detection chain. Since the beams will be delivered to the HEC through the Super-FRS, the rigidity limit of 18 Tm also applies.

A third, and much more hypothetic at the moment, possibility is the compressed baryonic matter (CBM) cave. There, the SIS100 beams will be delivered up to their maximal energy. However, CBM is a fixed setup, designed to study high-multiplicity events, and focused on the identification of light hadrons and baryons. A spallation measurement would require a large modification of the CBM setup.

5.3.4. HIAF (China) in 2026

For over half a century, the HIRFL (Heavy Ion Research Facility in Lanzhou) [644], designed and operated by the IMP (Institute of Modern Physics) of the Chinese Academy of Sciences, has played a pivotal role in advancing heavy-ion accelerator technology, heavy-ion physics, and their applications in China. To meet the increasing demands for higher beam intensity and beam energy in next-generation heavy-ion accelerators, IMP proposed the HIAF(Heavy-Ion Accelerator Facility) [645], which is expected to become operational by the end of 2025.

HIAF consists of a superconducting ion linear accelerator, a high-energy synchrotron booster, a high-energy radioactive isotope beam line, an experimental storage ring, and a few experimental setups. The BRing (Booster synchrotron Ring) is designed to achieve a maximum magnetic rigidity of 34 Tm, enabling the delivery of a typical ^{16}O beam with the energy of 2.6 GeV/n at an intensity of $6{\cdot}10^{11}$ particles per pulse (ppp) or a proton beam with the energy of 9.3 GeV/n at $2{\cdot}10^{12}$ ppp [645]. Beams extracted from the BRing are injected into the HFRS (High-energy FRagment Separator), a powerful high-energy radioactive beam line. At the entrance of the HFRS, the beams impinge on a target to produce RIBs (Radioactive Ion Beams) via projectile fragmentation or in-flight fission reactions. The HFRS is engineered to purify and separate RIBs with a maximum magnetic rigidity of 15 Tm through a two-stage separation process (pre-separator and main-separator). This setup achieves an excellent removal rate of primary beams and an effective separation for nuclides from hydrogen to uranium. Notably, the current design of 15 Tm magnetic rigidity is not the ultimate goal, as future upgrades aim to enhance the HFRS to a maximum magnetic rigidity of 25 Tm, which corresponds to the maximum energy of 2.9 GeV/n for light nuclei with a mass-to-charge ratio of two.

Several methods are available for cross-section measurements at HIAF. The first approach utilises the HFRS itself. Isotopes are separated and purified in the pre-separator and the initial half of the main separator before impinging on a target. The second half of the main separator acts as a zero-degree spectrometer, enabling the identification of fragments after the reaction using the Bρ–TOF–ΔE method, and fragmentation cross-section measurements. Recent design optimisations have increased the horizontal and longitudinal angular acceptances of the HFRS to $\pm$30 mrad and $\pm$25 mrad, respectively [646]. These enhancements allow the HFRS to collect fragments after the target more effectively, thereby yielding more precise cross-section

measurements. Similar to the Super-FRS in GSI, initial experiments with the HFRS do not support the hydrogen targets, and the C−CH_2 subtraction would be used instead.

The second method relies on the ETF (External Target Facility) of the HFRS. The HFRS can function as a complete beam separator, delivering RIBs to the ETF, where the beams impinge on a target. A detector array at the ETF can identify reaction products and facilitate fragmentation cross-section measurements. Currently, IMP operates a radioactive isotope beam line, the second RIBLL2 (Radioactive Ion Beam Line in Lanzhou) at HIRFL, which has successfully conducted fragmentation cross-section measurements at its external target facility [647]. With the enhanced magnetic rigidity of the HFRS compared to RIBLL2, future operations are expected to enable cross-section measurements in higher energy regions.

5.4. GeV-to-TeV measurements from CR experiments

CR experiments, as particle physics detectors in space, possess the capability to perform cross-section measurements. Although not primarily designed for this purpose, the need to understand and constrain challenging systematic uncertainties in their data provides a strong motivation for such measurements (see Sec. 4.4.4). A key advantage of CR experiments is their natural access to a diverse range of beam species and energies (although the GCR "beam luminosity" rapidly declines with energy). Recent results have demonstrated their potential to deliver important contributions to cross-section measurements, as described below.

Spectroscopic. Accurate measurements of the individual spectra of nuclei require knowledge of nuclear fragmentation cross-sections with the detector material to reject background from fragmentation of heavier nuclei within the upper part of the detector. The modularity of modern experiments, such as AMS, allows to directly measure nuclei survival probabilities within the detector and rescale the MC simulation accordingly to overcome the lack of measurements of nuclear fragmentation cross-sections. From the measured survival probabilities and the knowledge of the material within the AMS detector, the AMS collaboration has derived measurements of charge-changing inelastic cross-sections on a C target for projectile nuclei: He, Li, Be, B, C, N, O, Ne, Mg, Si, and Fe in the rigidity range from 2 GV to 1 TV [551, 3, 14].

Calorimetric. For calorimetric experiments, uncertainties from fragmentation cross-sections are secondary to those of the total inelastic cross-sections, which determines the acceptance and energy response of the detector. More accurate parametrisations of inelastic nucleus–nucleus cross-sections in the GeV–PeV regime are one of the main requirements needed to improve the accuracy of CR nuclei fluxes at these energies. Due to a lack of measurements, models generally rely on the conversion of pp cross-sections to different primaries and target materials using, e.g., the Glauber-Gribov approach [648–651]. For heavy-target materials ($A \gtrsim 50$), often present in calorimetric detectors, such conversions come with typical uncertainties of 10–20%. Lowering these hadronic uncertainties would make CR flux measurements more constraining, significantly improving CR production and propagation models. The DAMPE collaboration recently published a measurement of the inelastic cross-section of H (mostly protons) and He (mostly ^{4}He) on a BGO ($Bi_4Ge_3O_{12}$) target [552], see Figure 18. In the case of He, these are the first measurements in the kinetic energies range of 20 GeV to 10 TeV (lab frame) on any heavy-target material. This pioneering measurement achieved three major objectives: it demonstrates the feasibility and potential of doing inelastic cross-section measurements with calorimetric space-based experiments; it enables improving the accuracy of CR flux measurements; and it provides a base measurement from which the cross-section of other heavy-target materials can be extracted with model dependencies of only a few percent. Efforts are currently planned to extend the DAMPE cross-section measurements to other nuclei, including C and O. On longer timescales, it is worth noting that the HERD mission [652], planned to launch in 2027, will significantly enhance the statistics of high-energy CR observations. With its calorimeters segmented in all three spatial dimensions, HERD data will enable to improve the accuracy of the current CR cross-section measurements, and to extend them to higher energies.

Caveats of these measurements. It is worth noting that for both the AMS and DAMPE cross-section measurements, the projectile nuclei are GCRs and therefore a mixture of two or more isotopes, with one dominating isotope in some cases. Moreover, only the charge of the projectile and of the final-state nuclei was

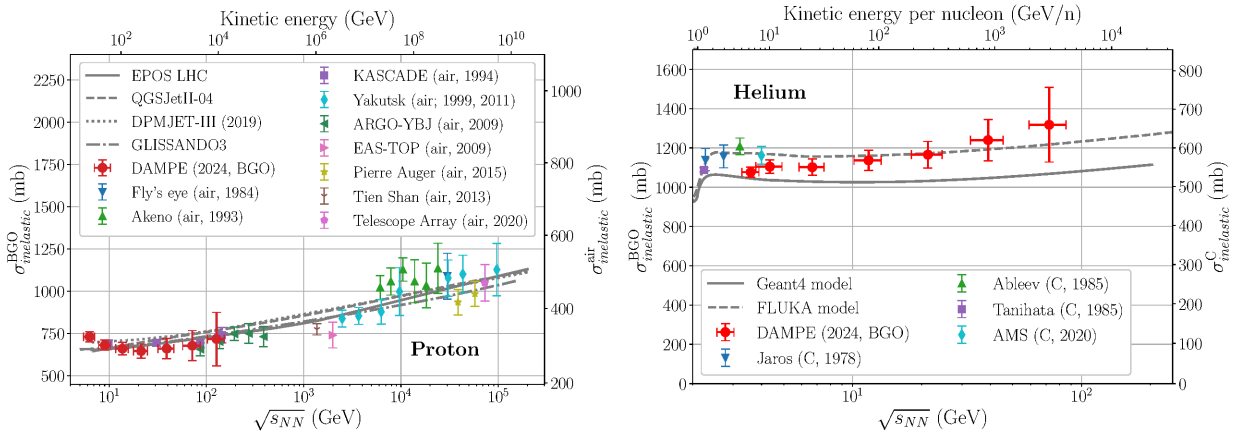

Figure 18: Left: measurements of the proton inelastic cross-section with calorimetric space-based experiments [552], respective to results by extensive air shower experiments [653–663] and model predictions [664–669]. Right: inelastic cross-section of He measured by DAMPE [552] and AMS [551], compared to results by accelerator experiments [483, 670, 671] and model predictions [664–669].

measured, but not the isotopic composition, though with the AMS detector it is possible to measure the isotopic composition of the daughter nuclei (see Section 3.1.6). In general, space detector have not been designed to perform cross-section measurements, and verifications with accelerator experiments where the same quantities can be measured in a more straightforward way are needed. This is illustrated with the discrepant charge-changing cross-section in C+C as inferred in AMS or recently measured in NA61/SHINE [616].

6. Overlapping cross-section needs from other communities, and further astro/HEP synergies

As briefly introduced in Sec. 2.2, GCR physics is an interdisciplinary domain, with connections to several adjacent fields of research. The long term evolution and stability of GCR fluxes over Gyr timescales comes with its specific wish list of reactions and priorities (Sec. 6.1). Other science cases, more related to applied physics and societal topics, have yet other cross-section needs and priorities. Among them, space radiation protection is a topic of growing interest (Sec. 6.2). Hadrontherapy is a curious example, where GCRs are completely absent, yet a significant overlap exists in terms of the cross-sections and energies of interest (Sec. 6.3). For these three topics, where some overlap exists with the reactions needed for GCR studies, the reactions involved, the status of nuclear data or codes, and the needs in terms of reactions, energy, and precision are detailed below.

To further illustrate the richness, similarities, and advantages of synergies between the HEP and astroparticle communities, the cases of ultra-high energy CRs and femtoscopy (related to the equation of state of neutron stars) – where even completely different cross-sections or regimes are explored –, are also briefly covered (Sec. 6.4).

6.1. Cosmogenic production in meteorites

As briefly introduced in Sec. 2.2.1, cosmogenic studies focus on the nuclides stored in meteorite and terrestrial archives. Long-lived radioactive nuclides, in particular, provide a powerful tool to assess GCR fluency variations over time.

Obtaining cosmogenic production rates is possible via physical model calculations, some type of empirical calibration using experimental meteorite data, or a combination of both. Here we focus on physical model calculations as they are widely used for cosmogenic nuclide studies. Though the following discussion is mainly focused on cosmogenic nuclide production in meteorites, most of the arguments are also applicable

to terrestrial cosmogenic nuclides. The production rate P^k (number of atoms per mass and time unit) of a cosmogenic nuclide of type k in a meteoroid of radius R at position $\vec{r}$ is given by:

$$P^k(\vec{r}, \vec{c}_{\text{sample}}, \vec{C}_{\text{meteoroid}}, R) = \sum_i \sum_j \vec{c}^j \int_E \sigma_{\text{prod}}^{i+j\rightarrow k}(E)\psi^i(\vec{r}, \vec{C}_{\text{meteoroid}}, R, E)dE, \tag{23}$$

with R the pre-atmospheric radius of the meteoroid, $\vec{c}_{\text{sample}}$ the chemical composition of the studied sample, and $\vec{C}_{\text{meteoroid}}$ the chemical composition of the meteoroid. Note that $\vec{c}_{\text{sample}}$ and $\vec{C}_{\text{meteoroid}}$ can be different if, for example, a metallic inclusion in a stony meteorite is studied. The differential flux density of primary and secondary particles of type i is $\psi^i(\vec{r}, \vec{C}_{\text{meteoroid}}, R, E)$ – particle per time, surface, and energy unit – and depends on the pre-atmospheric geometry, the depth of the sample within the pre-atmospheric meteoroid, and the bulk chemical composition of the meteoroid $\vec{C}_{\text{meteoroid}}$. The nuclear cross-section for the production of nuclide k from chemical element j by particles of type i is $\sigma_{\text{prod}}^{i+j\rightarrow k}(E)$, i.e., the same cross-section type as needed for GCRs, and $\vec{c}^j$ represents the concentration of element j in the meteoroid, assumed to be constant. For simplicity, it is usually assumed that the pre-atmospheric meteoroid was spherical and that the GCR flux was temporally constant. It can be shown that the calculated production rates are not very sensitive to the assumption of a spherical shape (e.g., [672]). In addition, there are earlier and still ongoing studies tackling the very important question of whether the GCR fluence was temporal constant (for a discussion, see [344]).

While the chemical composition of the studied sample $\vec{c}_{\text{sample}}$ and of the bulk meteoroid $\vec{C}_{\text{meteoroid}}$ can easily be measured, the particle spectra and the relevant cross-sections are more problematic input parameters. Since the particle spectra $\psi^i(\vec{r}, \vec{C}_{\text{meteoroid}}, R, E)$ – that are typically calculated using MC techniques – are not the subject of this paper, we focus the discussion on the current status of knowledge for the relevant cross-sections. Considering the possible target elements, the bulk composition of *chondrites* (common meteorite type) closely matches the bulk composition of the Sun, except for a few elements that usually occur in the gas phase, e.g., H, C, Ni and He. Consequently, almost 95% of a chondrite is made from only six elements. As an example, for a special chondrite type, called CI carbonaceous chondrite, the six major elements are (in percent by weight): C (3.22%), O (46.5%), Mg (9.61%), Si (10.68%), S (5.41%), Fe (18.43%) and Ni (1.08%). The other elements of the periodic table are all there but only in minor concentrations (e.g., [673]). Some of such minor elements, however, are major target elements for some cosmogenic nuclides. For example, cosmogenic Kr is produced from the minor amounts of Rb, Sr, Yr and Zr, cosmogenic Xe is produced from La and Ba, and cosmogenic ^{129}I is produced from Te.

6.1.1. Cross-sections for proton-induced reactions

Thanks to decades of experimental effort, most of the relevant cross-sections for proton-induced reactions are relatively well known and are compiled in various databases, e.g., [477]. However, some relevant published cross-sections need to be improved/adjusted due to the changed/adjusted standards used for the analysis by accelerator mass spectrometry (^{10}Be, ^{36}Cl, ^{41}Ca). For example, when the activity concentrations of the long-lived radionuclide ^{10}Be are measured by accelerator mass spectrometry, the ^{10}Be/^{9}Be ratio of the sample is measured against the ^{10}Be/^{9}Be ratio of a standard. If the ^{10}Be/^{9}Be ratio of the standard is not as assumed, all samples measured against these standards end with wrong ^{10}Be/^{9}Be ratios and therefore wrong cross-sections. Thanks to recent inter-laboratory comparisons, the differences among the different standards used in different laboratories are better resolved. Some standards, however, needed to be revised, and such data need either to be recalculated and/or to be remeasured. Such changes are sometimes in the range 10–15% and are therefore relevant (e.g., [674–677]). In addition, some relevant half-lives have recently been revised, e.g., for ^{10}Be, ^{41}Ca and ^{60}Fe (e.g., [678, 679]) and therefore also such cross-sections need to be recalculated and/or redetermined.

For some relevant target product combinations, the cross-section database is still scarce. Examples are the production of ^{41}Ca and ^{53}Mn from Fe and Ni, the production of Kr isotopes from Rb, Sr, Yr and Zr, and the production of Xe isotopes from Ba and La. Importantly, the cross-section database for the production of ^{14}C, which is a relevant target element for terrestrial and extraterrestrial applications, is still very scarce. This is probably due to the fact that extracting ^{14}C and measuring ^{14}C/^{12}C ratios via accelerator mass

spectroscopy was for a long time very challenging. However, new instruments making ^{14}C extractions and measurements more accurate and more precise have been developed (e.g., [680, 681], which would make revisiting the ^{14}C cross-sections worthwhile.

6.1.2. Cross-sections for neutron-induced reactions

For neutron-induced reactions the situation is different, as there are only very few experimental data in the energy range of interest, from the reaction threshold up to a few GeV. To overcome this problem, some relevant neutron-induced cross-sections have been inferred from various thick target irradiation experiments [682–687]. For details of the procedure, see [687, 688]. In addition, there are very few directly measured neutron-induced cross-sections relevant for the study of meteorites and planetary surfaces ([689, 690]). For some relevant target-product combinations, there are not enough data to perform the adjustment procedure, and the neutron excitation functions must be calculated using various nuclear model codes (e.g., `TALYS` or `INCL++6`). Though some of these models have significantly been improved over the decades, the quality of the calculated cross-sections is often still not sufficient for high-quality studies of cosmogenic nuclide production in meteorites and planetary surfaces. As a consequence, currently the most limiting factor for the quality of the model calculations is the ill-known and sometimes missing knowledge of the neutron cross-sections. Some major improvements can be expected, if at least some relevant cross-sections could be measured directly.

6.1.3. Cross-sections for ^{4}He-induced reactions

For ^{4}He-induced reactions, the situation is even worse: there are essentially no experimental data for the relevant reactions, namely the production of cosmogenic species on O, Si, Fe... targets, and in the energy range of interest, from threshold up to a few GeV/n. So far, this was of no major problem, because the MC codes used to calculate the differential particle spectra were not able to consider ^{4}He or other light charged particles reliably. Due to this shortcoming, there was no real effort in measuring the cross-sections for ^{4}He-induced reactions. Moreover, primary GCR ^{4}He ions and their secondary products were considered using a relatively crude approximation. However, this situation has just changed, and it is now possible, for the first time, to directly include the full interactions of these ^{4}He ions [677], and exciting new results are expected. However, the missing experimental cross-sections are a serious limitation.

6.1.4. Cross-sections for muon-induced reactions

Most studies of cosmogenic nuclides in extraterrestrial material assume that production is dominated by primary and secondary protons and secondary neutrons and that for some target–product combinations, secondary ^{4}He-particles also contribute. However, a recent study argues that secondary charged pions might contribute more than 20% to the measured activity concentration of ^{10}Be on the lunar surface [691]. This finding contrasts with the good results obtained by studies that describe depth profiles for a variety of cosmogenic nuclides on the lunar surface (including ^{10}Be) without it (e.g., [677, 692]). Therefore, confirming or rejecting the secondary pions hypothesis is crucial. This is especially true, considering that the study of muons (originating from the decay of pions) on planetary surfaces is just becoming an important tool, in space missions, to study the water-ice composition, and the density and chemical composition of lunar or asteroidal surfaces (e.g., [693]).

In contrast to cosmogenic nuclides in extraterrestrial matter, muon-induced reactions are very relevant for some terrestrial cosmogenic nuclide studies. Since muons are leptons – and therefore do not interact via the strong force –, they penetrate much deeper into the ground than neutrons. Therefore, despite their short lifetime and their relatively small contribution (<2%) to the total terrestrial nuclide production at the Earth surface, slow negative muons and fast muons are the dominant projectiles for nuclide production at depths larger than $\sim$4 m. This makes muon-induced production very important, whenever the sample was buried more than 1 m deep and/or whenever terrestrial cosmogenic nuclides are used to study burial histories (for more information see, e.g., [677]). Currently, there are no cross-sections for muon-induced production of cosmogenic nuclides and all estimates are based on theoretical nuclear model codes with unverifiable quality. Consequently, studying and quantifying muon-induced production in terrestrial and extraterrestrial samples is one of the next important steps in the field. Some data are already available [694, 695], but the database is far from complete.

6.1.5. Summary and wish list

The most important needs for modelling cosmogenic production are summarised in Table 6. The main target elements are C, O, Mg, Al, Si, S, Fe and Ni, although for some product nuclides, other (and heavier) target elements are also important. Cross-sections from the respective reaction thresholds up to ∼20 GeV are needed. Since most excitation functions show little energy dependencies above a few GeV, extrapolation towards higher energies is often possible and accurate enough. Figure 19 shows measured and modelled cosmogenic production rates for ^{10}Be (left panel) and ^{26}Al (right panel) for the L/LL6 chondrite Knyahinya. The experimental data are from Ref. [696], and for the model calculations, the contributions from protons, neutrons and ^{4}He are distinguished. The estimated uncertainties for the individual contributions, but also for the total production rates, are given by the grey areas. This plot helps to demonstrate the different priorities and precisions reported in Table 6.

- The highest priority and precision is for neutron-induced reactions, because their contributions often dominate the total production in extraterrestrial samples; they are also often the sole contributions for terrestrial applications. In that respect, the scarce (or very often lacking) cross-section database is the limiting factor for most cosmogenic nuclide studies. This situation must urgently been improved. This is clearly seen in Fig. 19, where the neutrons contribute to ∼70% and ∼50% of the total for ^{10}Be and ^{26}Al, respectively, and where the (so far large) uncertainties attributed to the neutron contributions clearly dominate the uncertainties for the total production rates.

- The second priority (and precision) is for protons-induced reactions, as illustrated in Fig. 19, although dominate the production of some nuclides (e.g., ^{36}Cl and ^{41}Ca from Fe and Ni). Most of the relevant data are relatively well known. However, some target-product combinations, highlighted in boldface in Table 6, need remeasurements, due to recent changes in standards and/or half-lives (as detailed in Sec. 6.1.1).

- The contribution of ^{4}He-induced reactions is small, and cross-sections calculated from nuclear models should be reliable enough not to significantly enlarge the uncertainties for the production rates (darker shade in Fig. 19). However, there are only very few experimental data, and new measurements (at mild precision) would more strongly support these conclusions.

- Finally, there is the open question about muon-induced reactions, whose contribution is not yet clear. Studying, for instance, ^{10}Be cross-sections for some relevant target elements (at a mild precision) is a necessary first step to assess the impact and importance of these interactions. Muon production and muon-induced reactions will also be very important for future space missions (collecting extraterrestrial samples), and it is also not clear, whether existing models are accurate enough or if experimental cross-sections will be needed.

6.2. Space radiation protection

An important safety priority for human spaceflight is the protection of astronauts from the harmful effects of the radiation environment in space [697–700]. The three main sources of radiation exposure are geomagnetically trapped particles (mostly protons and electrons [701]), solar energetic particles (mostly protons and light ions [702]), and GCRs. The GCR contribution is of primary importance for long-duration missions to the Moon, Mars, and other deep-space destinations, where little or no natural atmospheric and magnetospheric shielding is available [699, 703]. The relevant part of the GCR spectrum includes all nuclei up to Ni, with energies up to at least tens of GeV/n, or even up to TeV/n for some aspects. Nuclei of higher mass or energy are currently not considered in space radiation protection because of their much lower fluxes. This radiation field interacts with a spacecraft's hull and structures, and is significantly modified – via electronic energy loss, fragmentation, and nuclear interactions [704] – by the time it reaches an astronaut inside the vessel [705, 706]. It is then modified even further throughout the astronaut's body [707]. The most important particles that contribute to the radiation environment (inside a spacecraft or habitat) are neutrons [708–710], protons [711], light ions (i.e., isotopes of H and He), and pions [712]. All these particles

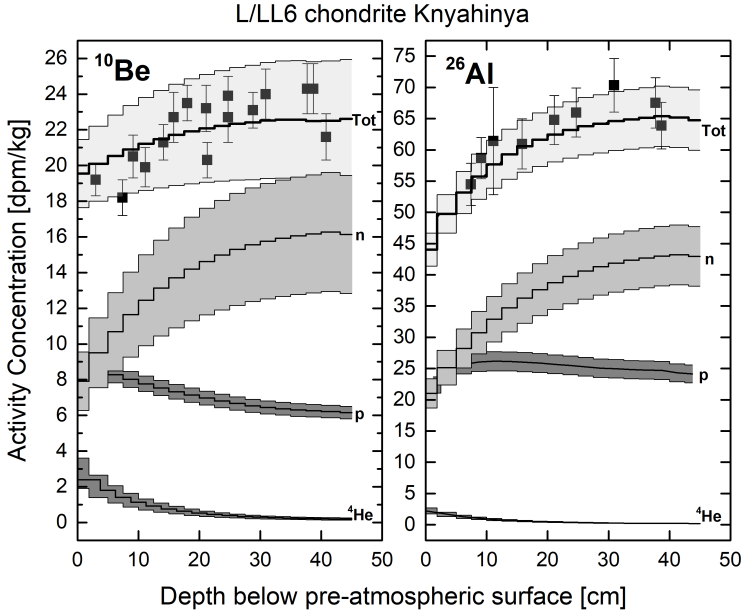

Figure 19: Production rates of ^{10}Be (left panel) and ^{26}Al (right panel) as a function of depth below the pre-atmospheric surface for the L/LL6 chondrite Knyahinya (solid symbols). The result of the physical model calculations are shown by the solid lines. The grey areas indicate the estimated uncertainties. For the model calculations, the contributions by protons, neutrons and ^{4}He projectiles are distinguished. The total production rate is the sum of the three individual contributions. The experimental data are from Ref. [696].

Table 6: Summary of the critical cross-section measurements for cosmogenic nuclide studies in terrestrial and extraterrestrial matter. The highest-priority measurements are for neutron-induced, then proton- and muon-induced, and then ^{4}He-induced reactions. The most important reactions within these priorities are highlighted in bold.

Particle	**Targets** j	**Products** k	**Measurements**	**Projectile** E_k	**Precision**
Neutrons	C, **O, Mg, Al, Si** Ca, Fe, Ni, Rb, Sr Yr, Zr, Nb, Ba, La	t, ^{3,4}He, ^{10}Be, ^{14}C, ^{i}Ne, ^{26}Al, ^{36}Cl, ^{i}Ar, ^{41}Ca, ^{53}Mn, ^{60}Fe, ^{i}Kr, ^{i}Xe	$\sigma^{\mathrm{n}+j\rightarrow k}_{\mathrm{prod}}$	Threshold up to a few 100 MeV	$< 5\%$
Protons	**O, Mg, Al, Si** Ca, Fe, Ni, Rb, Sr Yr, Zr, Nb, Ba, La	t, **^{3}He, ^{10}Be, ^{14}C** ^{53}Mn, ^{60}Fe ^{i}Kr, ^{i}Xe	$\sigma^{\mathrm{p}+j\rightarrow k}_{\mathrm{prod}}$	Threshold up to a few GeV	$< 10\%$
Muons	O, Mg, Al, Si Ca, Fe, Ni	t, ^{3,4}He, ^{10}Be, ^{14}C, ^{i}Ne, ^{26}Al, ^{36}Cl, ^{i}Ar, ^{41}Ca, ^{53}Mn, ^{60}Fe, ^{i}Kr, ^{i}Xe	$\sigma^{\mu+j\rightarrow k}_{\mathrm{prod}}$	Threshold up to a few GeV	$< 20\%$
^{4}He	O, Mg, Al, Si Ca, Fe, Ni	t, ^{3,4}He, ^{10}Be, ^{14}C, ^{i}Ne, ^{26}Al, ^{36}Cl, ^{i}Ar, ^{41}Ca, ^{53}Mn, ^{60}Fe, ^{i}Kr, ^{i}Xe	$\sigma^{^4\mathrm{He}+j\rightarrow k}_{\mathrm{prod}}$	Threshold up to a few GeV/n	$< 20\%$

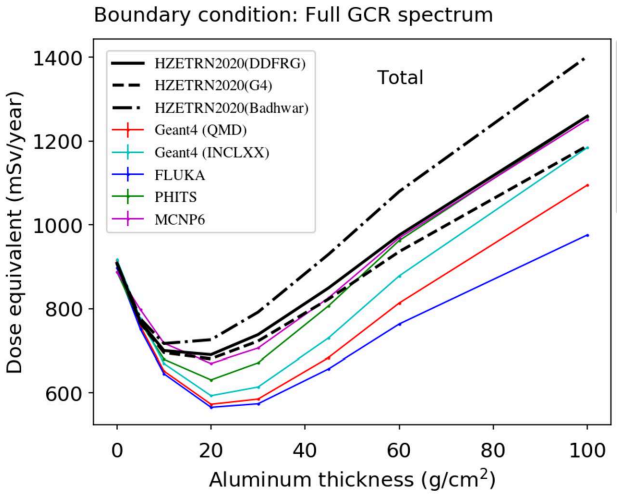

Figure 20: Simulated dose equivalent (total all particles) as a function of shielding depth for a detector exposed to the full GCR spectrum and located between two slab shields, *each* of them having the thickness indicated on the horizontal axis. The results of the `Geant4` MC code [548, 717] with the `QMD` and `INCLXX` nuclear models are shown in red and cyan, respectively. Those of the `HZETRN` [718–721] transport code with three different nuclear models (`DDFRG` [722, 723], Badhwar [724], and G4, where G4 refers to the `INCLXX` model from `Geant4`) are shown as solid and dashed black lines. The other evaluated MC codes are `FLUKA` (blue) [549, 550], `PHITS` (green) [725, 726] and `MCNP6` (purple) [727]. Updated version of Fig. 13 in Ref. [130], provided by Tony Slaba.

are light in mass and are therefore scattered at large angles. Thus, fully three-dimensional transport codes, which use double-differential cross-sections in solid angle and energy as input, are required to assess how spacecraft shielding alters the primary CR radiation field.

6.2.1. Transport code disagreements

To date, most spacecraft shielding has been relatively thin, with typical aerial thicknesses of about $20\,\mathrm{g/cm^2}$ (compared to $1000\,\mathrm{g/cm^2}$ and $20\,\mathrm{g/cm^2}$ for Earth's and Mars' atmospheres, respectively). The ISS shielding, for example, shows considerable variation, from less than $10\,\mathrm{g/cm^2}$ to about $100\,\mathrm{g/cm^2}$ or more [713]. Figure 20 shows the results of a variety of transport-code calculations that assess the dose equivalent produced by the full GCR spectrum, in a detector between two slab shields of varying thickness [130]. As the shielding increases, the dose equivalent drops steadily and reaches a minimum around $20\,\mathrm{g/cm^2}$, beyond which it starts to rise again due to the increased production of secondary particles. The existence of this minimum shows that there is an optimal shield thickness for radiation protection, if only GCR are taken into account [130]. Martian and lunar habitats for crewed long-duration missions will likely have shielding approaching or exceeding this optimal thickness [714, 715] and may, in extreme cases, reach several hundreds of $\mathrm{g/cm^2}$ [716]. Good radiation protection criteria will thus need to rely heavily on accurate and reliable estimates of the radiation environment inside these thick shields. Unfortunately, the transport-code calculations presented in Fig. 20 show disagreements on the order of 30% or more at large shielding depths.

The key question is: what is the source of this large variation, and what can be done about it? The main reason for the disagreement between the codes are the different nuclear-reaction models they use, which is nicely illustrated by Fig. 20. For example, two different nuclear models, `QMD` and `INCLXX`, are used as input to the otherwise identically configured `Geant4` MC framework [548, 717], showing variation of about 10% at large shielding depth. Another example is the deterministic transport code `HZETRN` [718–721] that was evaluated with three different nuclear models, producing even larger variations of about 40%. The other MC codes, `FLUKA` [549, 550], `PHITS` [725, 726] and `MCNP6` [727], did not allow changes to their underlying nuclear models, though it can be argued that they are among the primary differences between the otherwise similar codes [728]. Clearly, the key to resolving the observed disagreements hence lies in significantly improving

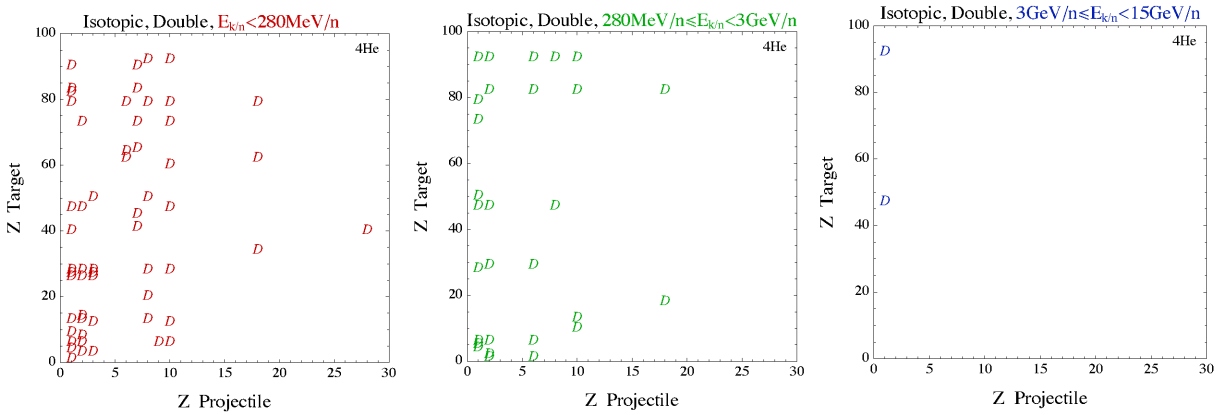

Figure 21: Example of available nuclear-reaction double-differential cross-section measurements (represented by the symbols "D") for the production of ^{4}He particles from nucleus–nucleus reactions with $E_{\mathrm{k/n}} < 280\,\mathrm{MeV/n}$ (left), $280\,\mathrm{MeV/n} \leq E_{\mathrm{k/n}} < 3\,\mathrm{GeV/n}$ (middle) and $3\,\mathrm{GeV/n} \leq E_{\mathrm{k/n}} < 15\,\mathrm{GeV/n}$ (right). There are no measurements available for $E_{\mathrm{k/n}} > 15\,\mathrm{GeV/n}$. Figure reproduced from Ref. [131].

the nuclear-reaction models. What, then, is the obstacle to doing so? It is not the shortage of models or the lack of nuclear theorists working on model development. Rather, it is the lack of sufficient experimental cross-section data that would allow validating the available models.

6.2.2. Nuclear data: availability and gaps

Norbury et al. [131] performed an exhaustive survey of the availability of nuclear-reaction cross-section data for charged-nuclei production relevant to space radiation protection. An example, highlighting the availability of double-differential cross-sections for nucleus–nucleus reactions producing ^{4}He particles, is shown in Fig. 21. The presence of the symbol "D" on the plots indicates that experimental data are available for a given projectile–target combination, while the quality of the data is not ascertained. Below the pion-production threshold, 280 MeV/n, there is an abundance of data available for a variety of targets and for projectile charges $Z \leq 10$. Above $Z = 10$, there is very little data. The same is true to a lesser extent for projectile energies, $E_{\mathrm{k/n}}$, between the pion threshold and 3 GeV/n; for $3\,\mathrm{GeV/n} < E_{\mathrm{k/n}} < 15\,\mathrm{GeV/n}$, there are only two data sets; for $E_{\mathrm{k/n}} > 15\,\mathrm{GeV/n}$, no data is available. Figure 21 only shows the production of ^{4}He particles, but Norbury et al. [131] compiled measurement data for a broad range of nuclear fragments and types[8] of cross-sections (total, charge-changing, single-differential, etc.).

The most important reference for neutron production data is that by Nakamura and Heilbronn [729]. They collected all the existing world data for both cross-sections and thick-target yields. Most data came from experiments at the RIKEN (Rikagaku Kenkyūsho, Institute of Physical and Chemical Research, Japan), HIMAC (Heavy Ion Medical Accelerator in Chiba, Japan) and Bevalac (at LBNL) accelerators. Subsequently, Satoh et al. [730] and Itashiki et al. [731] reported more data, some of which overlaps with that listed in Ref. [729], enabling comparisons between experiments. When one analyses all these data, some significant disagreements are found. Bevalac data (337 MeV/n) [729] show inconsistencies with HIMAC data, though the recent measurements by Satoh and Itashiki are broadly consistent with the latter. The low-energy (95 MeV/n and 135 MeV/n) RIKEN data [729] also show some inconsistencies. Overall, the complete neutron data set needs a re-evaluation and extensive new experimental data to resolve disagreements between the different available measurements.

6.2.3. Summary and wish list

As summarised in Table 7, the primary projectiles of interest for future measurements of light-ion production relevant to space radiation protection are Fe, Si, O and He. Energies of interest are between 100 MeV/n

[8] Yield distributions were not included because they cannot be used without prior conversion into cross-sections.

Table 7: Summary of highest-priority cross-section measurements for light-ion, neutron and pion production relevant to space radiation protection. Experiments should determine the multiplicities and energy spectra of the reaction products. If possible, neutron energies should be measured down to 1 MeV.

Projectile i	**Targets** j	**Products** k	**Measurements**	**Projectile** $E_{\mathrm{k/n}}$	**Precision**
He	p, C, Al, Fe	^{1,2,3}H, ^{3,4}He, n, $\pi^{\pm}$	$\frac{\mathrm{d}^2\sigma^{i+j\to k}}{\mathrm{d}\Omega\mathrm{d}E}$, $\sigma^{i+j}_{\mathrm{inel}}$	0.1 to 50 GeV/n	(any data) pref. $< 20\%$
O, Si, Fe	p, C, Al, Fe	^{1,2,3}H, ^{3,4}He, n, $\pi^{\pm}$	$\frac{\mathrm{d}^2\sigma^{i+j\to k}}{\mathrm{d}\Omega\mathrm{d}E}$, $\sigma^{i+j}_{\mathrm{inel}}$	0.1 to 50 GeV/n	(any data) pref. $< 20\%$

and 50 GeV/n, with an emphasis on data at higher energies, where there are significant data gaps. Other projectiles and energies above 10 GeV/n are also of interest for testing models and transport codes, if such data is all that is available. A variety of targets are of interest, including the major constituent elements of the most commonly used aerospace materials and the human body (e.g., H, C, Al and Fe). To be useful as input to nuclear-reaction models and hence transport codes, measurements must determine double-differential as a function of the solid angle and energy, and total inelastic cross-sections σ_{inel} – also denoted σ_{R}, see discussion of Eq. (14) –, and identify fragments and secondary particles over as broad an energy range as possible. For secondary particles, pions are of particular interest, for which production cross-sections should be measured with high precision. In principle, any data is helpful for improving nuclear models, though preferably measurements should reach a precision of 20% or better.

There is also a variety of other measurement needs, the most important being double-differential cross-sections for neutron production, especially above 1 GeV/n, where there is essentially no data, and for energies as low as 1 MeV, where the biological damage from neutrons is the largest [732]. Many measurements of yield distributions are already available in the literature (see, e.g., [733]), for which it would be very helpful if a methodology was developed to reliably convert them into cross-sections. Finally, extensive comparisons of the most important nuclear models used in transport codes are needed, including validations against currently available and future measurements.

6.3. Hadrontherapy

The study of nuclear processes involved in the interaction of protons and heavier ions is crucial for hadrontherapy, as well as for space radiation protection. In fact, the energies and ions of interest for clinical applications overlap the ion types and energies composing the GCR particle field. It was previously demonstrated that ion fragmentation processes in clinical treatments are a source of uncertainties in the calculation of the relative biological effectiveness, which is commonly used to calculate the dose delivered to the patient via the TPS [734].

It is also essential to correctly reproduce nuclear reactions during a particle-therapy treatment, as many dose monitoring techniques are based on the detection of secondary particles emitted by these reactions. For example, many research teams are developing monitoring systems based on prompt-gamma detection, these prompt-gamma being emitted during hadronic processes occurring in the patient [735, 736]. Other techniques suggest detecting the annihilation γ from ^{11}C, produced by the incoming beam interacting with the target [737, 738]. Finally, it was also suggested to develop monitoring techniques based on the detection of secondary protons that are produced by ion fragmentation in the patient (only if $Z > 1$) [739, 740]. Most of these studies rely on MC simulations, although it was demonstrated that important discrepancies exist between measured data and simulated output [741, 742]. An example of the differences in energy spectra simulated by different hadronic models of the `Geant4` MC code (`BIC`, `QMD` and `INCL`), compared to measured data, is presented in Fig. 22. The significant discrepancies, observed between the three models and the experimental results, mainly arise from the difficulties MC simulations encounter in accurately reproducing the hadronic processes undergone by the incoming carbon ion. Therefore, improving the accuracy of the nuclear cross-sections, that can occur during particle-therapy treatment, is essential.

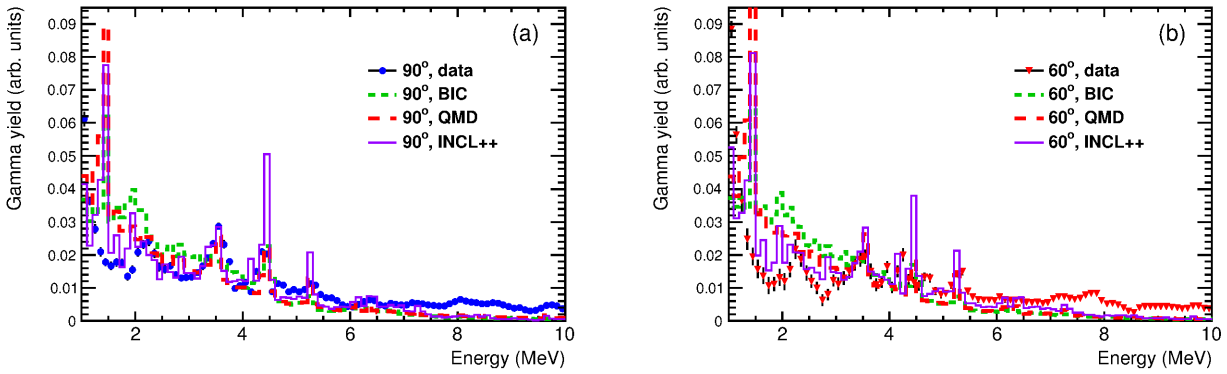

Figure 22: Measured and simulated energy spectra of prompt-gamma produced by 220 MeV/n ^{12}C interacting in a 20-cm thick target of PMMA, measured at 90 and 60^o. Reproduced from Ref. [742].

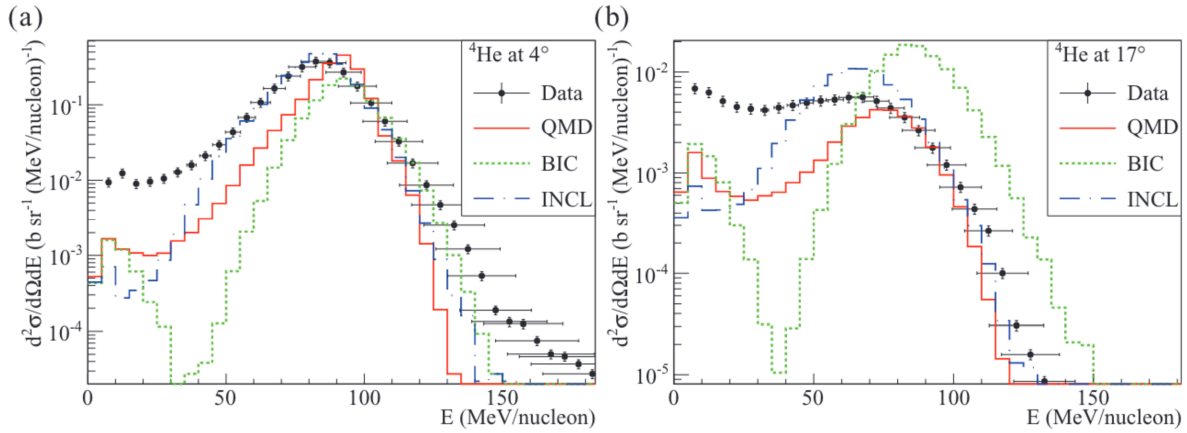

Figure 23: Double differential cross-sections of ^{4}He produced by 95 MeV/n ^{12}C ion on carbon target, measured at 4 and 17^o. Reproduced from [741].

6.3.1. Current status

Many studies have already been carried out to characterise the radiation fields of secondary particles produced by MeV to GeV ions [743, 741, 744–746]. For example, the GSI Biophysics Department made available a fragmentation cross-section database, providing useful and crucial data for GCR field characterisation [475]. Measurements on thin and thick targets were also carried out. Several experiments were performed at the GANIL (Grand Accélérateur National d'Ions Lourd, Caen, France) facility with 50 and 95 MeV/n ^{12}C ions, allowing to extract double-differential cross-sections on different targets (H, C, O, Al and ^{nat}Ti). For example, the measured d$^2\sigma$/(dΩdE) of ^{4}He produced by ^{12}C ions on carbon target at different angles can be seen in Fig. 23, compared to several hadronic models provided by `Geant4`. Different measurement strategies were investigated to characterise secondary particles, from TOF techniques with scintillating detectors to dose measurements, with thermoluminescent dosimeters-based [747] or Bonner sphere spectroscopy for neutron measurements, or *tissue equivalent proportional counter* that can provide a direct measurement of the linear energy transfer.

Currently, the international FOOT (FragmentatiOn Of Target) collaboration intends to perform systematic measurements of differential cross-sections of secondary particles produced by radiation on tissue-equivalent targets [748]. The first results produced by the collaboration were measurements of elemental

Table 8: Summary of highest-priority cross-section measurements and precision required for hadrontherapy. See text for the motivation.

Particle i	**Targets** j	**Products** k	**Measurements**	**Projectile** $E_{\mathrm{k/n}}$	**Precision**
^{4}He, ^{12}C, ^{16}O	H, C, O, Ca	All	$\sigma_{\Delta Z}^{i+j\to k}$ (charge changing)	$80 < E_{\mathrm{k/n}} < 400\,\mathrm{MeV/n}$	$< 2\%$
			$\sigma_{\Delta A}^{i+j\to k}$ (mass changing)		$< 5\%$
			$\mathrm{d}\sigma^{i+j\to k}/\mathrm{d}E$		$< 10\%$
			$\mathrm{d}^2\sigma^{i+j\to k}/(\mathrm{d}\Omega\mathrm{d}E)$		$< 5\%$

cross-sections in [749], performed at the GSI facility, from 400 MeV/n ^{16}O interacting with a carbon target. Another experiment at GSI with the same ion allowed the first measured differential cross-sections by the collaboration, available in [750].

6.3.2. Wish list

Several studies have already been carried out, but there is still an important lack of data on double-differential cross-sections in the energy range of hadrontherapy (i.e., between 80 and 400 MeV/n), as presented in Fig. 21. The needs of charge-changing, differential and double-differential cross-section measurements for ion therapy overlap some recommendations for space radiation protection (see previous section). The most important needs (reactions and precision) for the hadrontherapy community are summarised in Table 8.

For therapy, the most used ions are currently p and ^{12}C, but a renewed interest has recently emerged for ^{4}He and ^{16}O [751, 752]. Therefore, the priority in the hadrontherapy field is to measure double-differential cross-sections of ^{4}He, ^{12}C and ^{16}O-induced reactions on targets of interest for clinical applications: mainly H, C, O and Ca. The measurements of hadronic reactions on H targets will allow the evaluation of target fragmentation through an inverse kinematic approach, as proposed by the FOOT collaboration [749]. Nuclear reactions on Al can also be of interest to take into account the activation of accelerator materials. The precision required for the cross-sections measurements in hadrontherapy is based on compliance with requirements on delivered dose uncertainties in clinical practice. Indeed, the 62$^{\mathrm{nd}}$ report of the ICRU (International Committee for Radiological Units) recommends a maximal variation around the delivered dose of +7% and −5% [753]. The charge-changing cross-sections, owing to their large contribution to the target fragmentation, dominate the error budget of the delivered dose, and hence require the best precision. As secondary particles produced during hadrontherapy treatments are responsible for an additional dose delivered outside the tumour volume, the double-differential cross-sections accuracy will have a more important impact on the out-of-field dose.

6.4. Further synergies between astroparticle and high-energy physics

Despite not described in detail in this paper, other synergies between the astroparticle and high-energy physics communities exist, where experimental inputs on the cross-sections are also needed. A first example discusses how the current interpretation of the atmospheric shower data induced by UHECRs is limited by the knowledge of the hadronic cross-sections (Sec. 6.4.1). A second example explains how measurements of two-particle correlations is relevant to the understanding of the structure of neutron stars (Sec. 6.4.2).

6.4.1. Ultra-High-Energy Cosmic Rays

The physics case of UHECRs was discussed in Sec. 2.3.1. We highlight below two interaction meachanisms for which better nuclear data are needed, and how they impact the measurement or interpretation of UHECR data.

Hadronic interactions in the atmosphere. Knowledge of hadronic cross-sections is fundamental to understand the physics of air showers, namely cascades of secondary particles generated when UHECRs (see Fig. 1) interact with Earth's atmosphere [659]. These interactions, dominated by hadronic processes, govern the development, energy distribution, and particle composition of air showers. Precise measurements of hadronic

cross-sections are essential for interpreting air shower data, with profound implications for analysing the UHECRs spectrum and composition, as observed by facilities like the Pierre Auger Observatory and the TA. At the heart of air shower physics lies the challenge of modelling hadronic interactions across an enormous energy range, often surpassing the energies achievable in terrestrial accelerators such as the LHC. These high-energy interactions involve nuclei from primary CRs colliding with atmospheric atoms, resulting in a complex cascade of secondary particles, including pions, kaons, and baryons. Measuring hadronic cross-sections provides critical constraints on the theoretical models used to predict particle multiplicities, energy spectra and angular distributions within the shower. Accurate cross-section data enable more reliable extrapolations of hadronic interactions at ultra-high energies, where theoretical uncertainties and model dependencies become significant [754]. Reducing uncertainties in these measurements enhances our ability to distinguish between different CR composition models and deepens our understanding of the origins and acceleration mechanisms of these particles.

Photo-disintegration and giant dipole resonances. The observed UHECRs exhibit a predominantly heavy composition, suggesting that photo-disintegration processes play a crucial role in modifying their nuclear species as they travel from their sources to Earth. The dominant contribution to photo-disintegration arises from the excitation of the giant dipole resonance, a collective vibration of protons and neutrons within the nucleus. This resonance typically occurs at photon energies above $\sim$8 MeV (in the nucleus' rest frame) and leads to the emission of one or two nucleons. At higher energies, the quasi-deuteron process becomes significant, wherein the photon interacts with a nucleon pair, resulting in the ejection of nucleons or light fragments. For photon energies exceeding $\sim$150 MeV, even more energetic processes, such as baryonic resonances, begin to dominate. Given the average energy of today's photons from the cosmic microwave background (CMB), UHECR nuclei with Lorentz factors exceeding a few 10^9 experience interactions where CMB photons can reach tens of MeV in their rest frame. In the sources of UHECRs, intense photon fields from local structures (e.g., accretion disks) can even reach beyond 150 MeV in the UHECR's rest frame and lead to photopion production, with observable predictions of coincident neutrino and gamma-ray emissions [755], besides also producing photodisintegrations of these CR. Therefore, photonuclear interactions contribute significantly to the evolution of the UHECR composition during propagation [756, 757] and in the sources [758].

Despite extensive studies, photonuclear cross-section data remain incomplete and inconsistent. Systematic discrepancies persist among different experimental techniques at various accelerator facilities, and there is a lack of measurements for many nuclear species [759]. Several models have been developed to describe photonuclear reactions in UHECR propagation. The Puget–Stecker–Bredekamp model historically provided a simplified approach by implementing a single decay chain per nucleus. However, more advanced simulations, such as those in `TALYS` [366], allow for multiple decay chains and have been incorporated into modern propagation codes like `CRPropa` [760] and `SimProp` [761]. Nonetheless, discrepancies between model predictions and available cross-section data introduce systematic uncertainties in interpreting current UHECR observations [762]. In the case of photomeson interactions, the limited data available have been gathered to produce models beyond the prevalent simplistic *nucleon superposition* approach [139], but the description is still lacking, and the required precision in the cross-sections and secondary yields have not been attained.

Addressing these experimental and theoretical challenges is a key motivation for ongoing efforts, such as the PANDORA (Photo-Absorption of Nuclei and Decay Observation for Reactions in Astrophysics) project, which aims to refine our understanding of photonuclear interactions relevant to UHECR physics [763, 764]. Measurements of photomeson-related quantities are not currently under planning, but they could be carried out at CERN, where the necessary projectile energies are already available.

6.4.2. Femtoscopy for neutron-star research

Femtoscopy allows the study of residual strong interaction between hadrons, by measuring momentum correlations of hadron pairs produced in collisions at accelerator facilities. It is especially beneficial for the studies of more exotic particles, for which direct scattering experiments are limited or even impossible, due to their short-lived nature – for instance, hadrons containing strange quark(s) [605]. The residual strong interactions between nucleons and hyperons are of especial interest for astrophysics (as introduced in Sec. 2.3.2), as they are the necessary components to understand what are the constituents of neutron

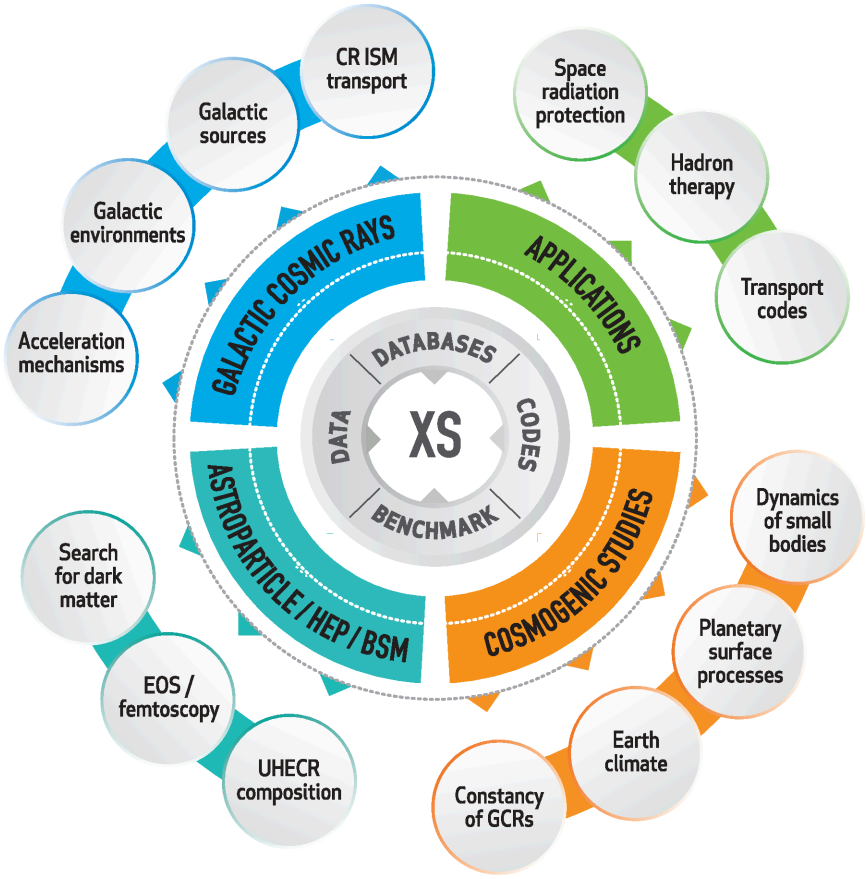

Figure 24: Sketch illustrating the central role of cross-sections (denoted XS) for many physics cases discussed in this review. At the core of all studies lie the cross-sections. The first layer includes the measurements of cross-section `DATA` in diverse facilities (Sec. 5), ideally curated and made available in public `DATABASES`, included and fitted in public nuclear `CODES`, ideally regularly `BENCHMARKED` (against the data and one another). The second layer consists in the physics topics, some having been deeply discussed in this review, with high-precision era of CR experiments (Sec. 3) motivating GCR studies (Sec. 4), but also others more briefly described, such as cosmogenic studies (Sec. 6.1), space and medicine applications (Secs. 6.2 and 6.3), and other astroparticle/HEP/BSM (Beyond Standard Model) synergies (Secs. 4 and 6.4). The last layer highlights some salient physics cases (Sec. 2) that can be advanced with high-precision cross-section measurements (and the use of nuclear codes, ideally for the less important unmeasured reactions only).

stars [765]. Whether and at which density hyperons appear in neutron stars depends on the equation of state of dense matter, and thus on the nucleon–hyperon interactions included in it. In the last decade, correlation functions were measured for p–Σ [766], p–Ξ hyperons [767] and p–Λ [768, 769], providing unprecedented precision data to constrain the relevant two-body strong interactions. Moreover, femtoscopy technique was recently extended to the three-body sector, allowing the study of three free hadron scattering process $3 \rightarrow 3$, which is not accessible with any other experimental setup [770, 771]. Hyperon–nucleon–nucleon three-body force is one of the most crucial components for the proper description of the equation of state of dense matter [772, 773].

The facilities and experiments capable of performing femtoscopy in high-energy collisions are shared laboratories for hadron and nuclear physics (e.g., ALICE, AMBER, LHCb, NA61/SHINE). They provide important input for different research questions in astrophysics. For more details, see, for instance, the recent JENAA 2024 workshop at CERN [774].

7. Conclusions and long-term plans

This paper is a call to start, support and develop long-term campaigns to measure a variety of cross-sections. High-precision cross-sections are mandatory to fully exploit recent high-precision GCR measurements, and of pivotal importance to address the associated physics puzzles. In the last decade, many studies were pursued to provide actionable lists of cross-sections to measure, and successful synergies were built between several communities to do some of these measurements. The most salient results presented in this review can be summarised as follows:

- *Physics and societal challenges.* The quest for difficult physics questions, relatively new (What is DM?) or much older (What are the sources of GCRs and the origin of life on terrestrial planets?), cannot go forward without new campaigns of high-precision cross-section measurements. Some of these cross-sections, and many others, are also needed for several societal and applied topics, ranging from human space exploration to cancer treatment. These synergies are summarised and highlighted in Fig. 24.

- *Ongoing and future CR experiments.* In the last decade, direct CR experiments broke several barriers in terms of precision (percent level), energy (hundreds of TeV) and variety (anti-matter, leptons, nuclei) – see Figs. 4 to 7. The next decade will see even more results (see Fig. 8), and despite a foggy horizon after 2030, the sub-percent-precision frontier is one of the many ambitious objectives of projects beyond 2040.

- *Cross-section needs for GCRs.* The methodology to establish and rank the list of cross-sections to improve is sound, and the desired reactions have been well-identified. Moreover, forecasts have shown that these measurements are guaranteed to be a game changer for the field. We refer readers and experimentalists to our summary tables and plots of cross-section needs (reactions, energy range and precision): production cross-sections (for GCR flux modelling) are presented in Tables 1, 2 and Fig. 9 for nuclei, and in Table 3 for antinuclei, positrons and γ rays; inelastic, annihilating and non-annihilating cross-sections – required for GCR propagation studies or the analysis of CR experiments – are presented for nuclei and antinuclei in Table 4 (and further detailed in Fig. 14 for nuclei).

- *Other cross-section needs.* A large variety of reactions (projectiles, targets, and products) and cross-sections (total, simply or doubly differential) are also required in adjacent fields, where some overlap exists with the GCR needs. Tables 6, 7 and 8 summarise the highest-priority cross-section needs for cosmogenic studies, space-radiation protection and hadrontherapy. We do not provide wish lists for UHECRs or neutron stars/femtoscopy physics, as these topics were presented mostly to illustrate further existing synergies between the astrophysics and HEP communities.

- *Key facilities and experiments.* Given the wide range of energies (hundreds of MeV to hundreds of TeV), projectiles (all nuclei, anti-matter, neutrons and muons), targets (H, He, C, O, etc.) and fragments to measure, not a single facility will provide all the needs. Luckily, facilities at PS, SPS and LHC at CERN (see Fig. 16) are already being taken advantage of, and several near-future nuclear physics facilities will have the capability to perform some desired measurements (see Table 5). In addition, CR experiments themselves have proven to be excellent detectors and complementary setups to measure cross-sections based on flight data. However, measurements of the cross-sections highlighted in this review remain marginally supported in current physics programs. We hope this paper will give more visibility to the current efforts and motivate experimentalists to join, in order to achieve at least the most urgent measurements in our wish lists.

- *Nuclear databases, transport codes and MC event generators.* The number and energy coverage of the cross-sections needed is huge. On the one-hand, easy-to-use and up-to-date databases of nuclear data, possibly specific to physics sub-topics, would be a huge boost to facilitate their comparison and use. On the other-hand, general-purpose parametrisations and codes will always play a critical role for filling the gaps. Several efforts and initiative already exist to provide public and verified data,

and to benchmark codes in the nuclear physics and HEP communities. Nevertheless, more synergies and coordinated efforts could only be more beneficial to all communities. This possibly calls for a dedicated road map.

Looking at the past often gives a good vantage point to prepare for the future. In that respect, it is worth stressing that in the 1980s, similar synergies, though at a smaller scale, and efforts were carried for over 20 years to provide the cross-section data needed to interpret GCR data of the time with a precision of tens of percent. These nuclear data and codes still have a legacy status. Today's and tomorrow's challenges are no less difficult than these past ones, but we are clearly embarked on the premises and promises of a long term programme that will secure legacy nuclear data for the next 20 years.

Besides pursuing the current data campaigns highlighted in this paper, there are straightforward and *relatively easy* directions to follow: on the modelling side, one need to provide more robust and comprehensive compilations of nuclear cross-sections, extend the wish list of desired cross-section to ultra-heavy GCR species, quantify in more detail the impact and needs for other cross-section types (inelastic, non-annihilating, ...), etc. There are also somehow *more difficult* or involved directions to follow: survey more closely the possibilities offered by current facilities and experiments, and prepare and plan for new opportunities and new detectors to make strong proposals for beam time for these cross-section measurements. On the CR experiment side, the next generation of detectors will bring even more challenging precisions in terms of cross-sections needed to analyse and interpret their data. As these particle physics detectors already rely on beam tests at CERN (integration and validation), it could be interesting to think about, and possibly plan as well for, dedicated cross-section measurements campaigns at this early stage.

The clear, long-term, challenging but rewarding programme ahead of us, however, faces the difficulties of limited human resources and funding, in a future constrained by a necessary decrease of our footprint in terms of greenhouse gas emissions. Its advantage is that it relies on existing facilities, taking a priori a very small fraction of the physics programmes for which they were conceived. In this respect, given the broad and interdisciplinary questions, we hope that the road map provided in this review will help convince and gather support from deciding committees and the many agencies financing research world-wide.

Contribution statements

F. Donato, S. Mariani and D. Maurin proposed the project and coordinated the discussions during XSCRC 2024 [6], then supervised the preparation of the article.

L. Audouin, E. Berti, P. Coppin, M. Di Mauro, P. von Doetinchem, F. Donato, C. Evoli, Y. Génolini, P. Ghosh, I. Leya, M. J. Losekamm, S. Mariani, D. Maurin, J. W. Norbury, L. Orusa, M. Paniccia, T. Poeschl, P. D. Serpico, A. Tykhonov, M. Unger, M. Vanstalle and M.-J. Zhao wrote the article, also contributing to its organisation and content.

The participants of XSCRC 2024 [6] who gave a talk or contributed to the discussions at the workshop were invited to participate in the paper: D. Boncioli, M. Chiosso, D. Giordano, D. M. Gomez Coral, G. Graziani, C. Lucarelli, P. Maestro, M. Mahlein, J. Ocampo-Peleteiro, A. Oliva, T. Pierog and L. Šerkšnytė, provided comments, additional text and references.

All authors read and commented on the manuscript to provide the final version.

Acknowledgements

We thank our colleagues of the XSCRC series for lively discussions over the years, which helped to crystallise and define the cross-section needs for various physics cases, leading to new cross-sections measurements, and many successful synergies between our communities. We thank CERN, and in particular the Theoretical Physics Department, for hosting and supporting all the editions of the XSCRC workshop. We thank R. Delorme and V. Tatischeff for their helpful suggestions regarding nuclear and medical physics experts for the XSCRC 2024 workshop.

F. Donato is supported by the Research grant *The Dark Universe: A Synergic Multimessenger Approach*, No. 2017X7X85K, funded by the MIUR. P. Coppin and A. Tykhonov acknowledge the support of the European Research Council (ERC) under the European Union's Horizon 2020 research and innovation programme (Grant No. 851103). P. Coppin is also supported by the Swiss National Science Foundation (SNSF). Philip von Doetinchem knowledges the support of the National Science Foundation grant PHY-2411633. F. Donato, C. Evoli and M. Di Mauro acknowledge support from the research grant *TAsP (Theoretical Astroparticle Physics)* funded by Istituto Nazionale di Fisica Nucleare (INFN). Y. Génolini et P. D. Serpico acknowledge support by the Université Savoie Mont Blanc via the research grant NoBaRaCo. P. Ghosh was supported by the Pioneers mission, the Trans-Iron Galactic Element Recorder for the International Space Station, TIGERISS, an Exceptional Nucleosynthesis Pioneer. The work of D. M. Gomez Coral is supported by UNAM-PAPIIT IA101624 and SECIHTI under grant CBF2023-2024-118. M. Mahlein is supported by the European Research Council (ERC) under the European Union's Horizon 2020 research and innovation programme (Grant Agreement No 950692) and the BMBF 05P24W04 ALICE. The work of I. Leya is funded by the Swiss National Science Foundation (200020_219357, 200020_196955). The work of M.J. Losekamm is funded by the Deutsche Forschungsgemeinschaft (DFG, German Research Foundation) via Germany's Excellence Initiative – EXC-2094 – 390783311. The work of D. Maurin was supported by the *Action thématique Phénomènes extrêmes et Multi-messagers (AT-PEM)* of CNRS/INSU PN Astro with INP and IN2P3, co-funded by CEA and CNES, and by the INTERCOS project funded by IN2P3. J.W. Norbury was supported by the RadWorks project within Exploration Capabilities of the Mars Campaign Development Division in the Exploration Systems Development Mission Directorate of NASA, United States. J. Ocampo-Peleteiro and A. Oliva are supported by INFN and ASI under ASI-INFN Agreements No. 2019-19-HH.0, No. 2021-43-HH.0, and their amendments. L. Orusa acknowledges the support of the Multimessenger Plasma Physics Center (MPPC), NSF grants PHY2206607. M. Unger acknowledges the support of the German Research Foundation DFG (Project No. 426579465). M.-J. Zhao acknowledges the support from the National Natural Science Foundation of China under Grants No. 12175248 and No. 12342502.

Acronyms

ACE-CRIS Advanced Composition Explorer Cosmic Ray Isotope Spectrometer. 16–18, 20, 31

AGN active galactic nucleus. 11

AGS Alternating Gradient Synchrotron. 54

ALADIN A Large Acceptance DIpole magNet. 54, 55

ALADInO Antimatter Large Acceptance Detector In Orbit. 2, 20, 23

ALEPH Apparatus for LEP PHysics. 8, 34

ALICE A Large Ion Collider Experiment. 8, 34, 35, 44–46, 48–50, 52, 68

AMBER Apparatus for Meson and Baryon Experimental Research. 32, 33, 36, 37, 49–52, 68

AMS Alpha Magnetic Spectrometer. 2, 7, 8, 12–20, 23, 28, 32, 33, 35, 36, 38, 43, 45, 46, 56, 57

ARGUS A Russian-German-United States-Swedish collaboration. 8, 34

ATLAS A Toroidal LHC Apparatus. 50

BESS Balloon-borne Experiment with Superconducting Spectrometer. 12, 14, 15, 21

BGO bismuth germanium oxide. 46, 56

BNL Brookhaven National Laboratory. 44, 53, 54

BRAHMS Broad RAnge Hadron Magnetic Spectrometers. 32

BRing Booster synchrotron Ring. 55

BSM Beyond Standard Model. 68

CALET CALorimetric Electron Telescope. 2, 13, 14, 16, 17, 20, 45

CBM compressed baryonic matter. 55

CERN Conseil européen pour la recherche nucléaire (European Organization for Nuclear Research). 3–6, 22, 23, 32, 33, 44, 46, 48–51, 53, 67–70

CMB cosmic microwave background. 67

CMS Compact Muon Solenoid. 35

CNAO Centro Nazionale di Adroterapia Oncologica. 3, 53

COMPASS Common Muon and Proton Apparatus for Structure and Spectroscopy. 51

CR cosmic ray. 2–6, 8–18, 20–26, 28, 29, 31–34, 36, 38, 40, 43, 45–49, 51, 56, 57, 62, 67–70

CRDB cosmic-ray database. 5, 7, 14, 41, 42

CREAM Cosmic Ray Energetics And Mass. 13, 14, 23, 45

CRN Cosmic Ray Nuclei detector. 45

CRRES Combined Release and Radiation Effects Satellite. 18

CTAO Cherenkov Telescope Array Observatory. 35

DAMPE DArk Matter Particle Explorer. 2, 13, 14, 16, 17, 20, 23, 45, 46, 56, 57

DM dark matter. 2, 4, 6, 8–10, 15, 21–24, 28, 32, 34, 36, 43, 69

EC electronic capture. 43

ETF External Target Facility. 56

FAIR Facility for Antiproton and Ion Research. 3, 53, 54

FOOT FragmentatiOn Of Target. 65, 66

FRS FRagment Separator. 54–56

GANIL Grand Accélérateur National d'Ions Lourd. 65

GAPS General AntiParticle Spectrometer. 2, 15, 20–22, 33, 36, 38, 46, 47

GCE Galactic center excess. 9

GCR Galactic cosmic ray. 2–11, 13, 16–21, 24–28, 30–34, 36, 38–43, 45–48, 50–53, 55–60, 62, 64, 65, 68–70

GLAD GSI Large Acceptance Dipole. 55

GNTF Gamma-ray Neutron Test Facility. 54

GRAMS Gamma-Ray and AntiMatter Survey. 2, 21, 22

GSFC Goddard Space Flight Center. 54

GSI GSI Helmholtz Centre for Heavy Ion Research. 3, 53, 54, 56, 65, 66

H.E.S.S. High Energy Stereoscopic System. 35

HAWC High Altitude Water Cherenkov experiment. 35

HEAO3 High Energy Astrophysical Observatory. 7, 16, 45

HEAO3-HNE Heavy Nuclei Experiment on HEAO3. 17

HEC High Energy Cave. 55

HELIX High Energy Light Isotope Experiment. 2, 12, 13, 18, 20, 21

HEP high-energy physics. 3, 6, 48, 57, 68–70

HERD High Energy cosmic-Radiation Detection. 2, 20, 22, 23, 45, 46, 56

HERO High-Energy Ray Observatory. 2, 20, 22, 23, 31, 45

HFRS High-energy FRagment Separator. 55, 56

HIAF Heavy-Ion Accelerator Facility. 3, 53, 55

HIMAC Heavy Ion Medical Accelerator in Chiba. 63

HIRFL Heavy Ion Research Facility in Lanzhou. 55, 56

HPGe high-purity Germanium detectors. 54

ICRU International Committee for Radiological Units. 66

IHEP Institute of High Energy Physics. 44

IMP Institute of Modern Physics. 55, 56

IS interstellar. 12, 20

ISEE International Sun-Earth Explorer. 18

ISM interstellar medium. 6, 9, 10, 24, 25, 32, 40, 43, 50, 54

ISOMAX ISOtope Magnet eXperiment. 18, 21

ISR Intersecting Storage Rings. 44

ISS International Space Station. 2, 12–14, 20, 22, 23, 31, 32, 45, 62

JENAA Joint ECFA-NuPECC-APPEC Activities. 68

JINR Joint Institute for Nuclear Research. 22

KEK Kō Enerugī Kasokuki Kenkyū Kikō (High Energy Accelerator Research Organization). 48

LArTPC liquid argon time-projection chamber. 22

LAT Large Area Telescope. 5, 9, 10, 13, 32, 35

LBNL Lawrence Berkeley National Laboratory. 44, 63

LEAR Low Energy Antiproton Ring. 44, 46

LHAASO Large High Altitude Air Shower Observatory. 35

LHC Large Hadron Collider. 3, 5, 48–50, 67, 69

LHCb LHC beauty. 32, 33, 35–37, 48, 49, 51, 52, 68

LHCf LHC forward. 35, 48, 50

LIGO Laser Interferometer Gravitational-wave Observatory. 9

LS Long Shutdown. 48, 51

LYSO lutetium–yttrium oxyorthosilicate. 46

MAGIC Major Atmospheric Gamma Imaging Cherenkov telescope. 35

MC Monte Carlo. 6, 17, 26, 34, 36, 40, 56, 58, 59, 62, 64, 69

MDR maximum detectable rigidity. 13, 23

NASA National Aeronautics and Space Administration. 40, 54

NICA Nuclotron-based Ion Collider Facility. 22, 53

NICER Neutron Star Interior Composition Explorer. 12

NIST National Institute of Standards and Technology. 54

NSRL NASA Space Radiation Laboratory. 53, 54

OLIMPIYA OLIvined from Meteorites—Poisk search for heavy I and superheavy YAder nuclei. 7, 17, 18

PAMELA Payload for Antimatter Matter Exploration and Light-nuclei Astrophysics. 12–15, 18, 32, 45

PANDORA Photo-Absorption of Nuclei and Decay Observation for Reactions in Astrophysics. 67

PHeSCAMI Pressurised Helium Scintillating Calorimeter for AntiMatter Investigation. 2, 21, 22

PPAC Parallel Plate Avalanche Counter. 53

PS Proton Synchrotron. 3, 44, 48, 50, 53, 69

R3B Reactions with Relativistic Radioaktiv Beams. 55

RHIC Relativistic Heavy Ion Collider. 49, 54

RIBLL2 Radioactive Ion Beam Line in Lanzhou. 56

RIBs Radioactive Ion Beams. 55, 56

RICH ring-imaging Cherenkov. 13, 21, 49, 51

RIKEN Rikagaku Kenkyūsho, Institute of Physical and Chemical Research. 63

SHINE a SPS Heavy Ion and Neutrino Experiment. 28, 35–37, 41, 50–52, 57, 68

SM standard model. 2, 6

SMOG System for Measuring Overlap with Gas. 32, 49

SPS Super Proton Synchrotron. 3, 22, 23, 32, 44, 48, 50–53, 69

SS Solar system. 6, 7, 10, 11, 20

TA Telescope Array. 11, 12, 67

TIGER Trans-Iron Galactic Element Recorder. 2, 7, 17, 20, 22, 31, 43, 45

TOA top of atmosphere. 12

TOF time-of-flight. 13, 21, 23, 49, 51–53, 55, 65

TORCH Time Of internally Reflected CHerenkov light. 49

TPS treatment planning systems. 11, 64

UHCRE-LDEF Ultra Heavy Cosmic Ray Experiment on the Long Duration Exposure Facility. 7, 17

UHECR ultra-high-energy cosmic ray. 4, 11, 12, 66, 67, 69

XSCRC Cross-Sections for Cosmic Rays at CERN. 4, 5, 70

References

[1] A. Aab, et al. (Pierre Auger collaboration), Observation of a Large-scale Anisotropy in the Arrival Directions of Cosmic Rays above 8×10^{18} eV, Science 357 (2017) 1266–1270. doi:10.1126/science.aan4338. arXiv:1709.07321.

[2] A. M. Galper, et al., The PAMELA experiment: a decade of Cosmic Ray Physics in space, J. Phys. Conf. Series 798 (2017) 012033. doi:10.1088/1742-6596/798/1/012033.

[3] M. Aguilar, et al. (AMS collaboration), The Alpha Magnetic Spectrometer on the international space station: Part II — Results from the first seven years, Phys. Rep. 894 (2021) 1–116. doi:10.1016/j.physrep.2020.09.003.

[4] B. Bertucci, F. Donato, G. Giudice, G. Passaleva, P. Serpico (organizing committee), XSCRC2017: Cross sections for Cosmic Rays @ CERN, https://indico.cern.ch/event/563277/, 2017.

[5] B. Bertucci, F. Donato, J. Kopp, D. Maurin, M. Unger (organizing committee), XSCRC2019: Cross sections for Cosmic Rays @ CERN, https://indico.cern.ch/event/820869/, 2019.

[6] F. Donato, S. Mariani, D. Maurin (organizing committee), XSCRC2024: Cross sections for Cosmic Rays @ CERN, https://indico.cern.ch/event/1377509/, 2024.

[7] D. Maurin, F. Melot, R. Taillet, A database of charged cosmic rays, A&A 569 (2014) A32. doi:10.1051/0004-6361/201321344. arXiv:1302.5525.

[8] D. Maurin, H. P. Dembinski, J. Gonzalez, I. C. Mariş, F. Melot, Cosmic-Ray Database Update: Ultra-High Energy, Ultra-Heavy, and Antinuclei Cosmic-Ray Data (CRDB v4.0), Universe 6 (2020) 102. doi:10.3390/universe6080102. arXiv:2005.14663.

[9] D. Maurin, M. Ahlers, H. Dembinski, A. Haungs, P.-S. Mangeard, F. Melot, P. Mertsch, D. Wochele, et al., A cosmic-ray database update: CRDB v4.1, Eur. Phys. J. C 83 (2023) 971. doi:10.1140/epjc/s10052-023-12092-8. arXiv:2306.08901.

[10] M. Ackermann, et al. (Fermi-LAT collaboration), Fermi-LAT Observations of the Diffuse Gamma-Ray Emission: Implications for Cosmic Rays and the Interstellar Medium, ApJ 750 (2012) 3. doi:10.1088/0004-637X/750/1/3. arXiv:1202.4039.

[11] M. Ackermann, et al. (Fermi-LAT collaboration), Resolving the Extragalactic γ-Ray Background above 50 GeV with the Fermi Large Area Telescope, Phys. Rev. Lett. 116 (2016) 151105. doi:10.1103/PhysRevLett.116.151105. arXiv:1511.00693.

[12] M. G. Aartsen, et al. (IceCube collaboration), Evidence for High-Energy Extraterrestrial Neutrinos at the IceCube Detector, Science 342 (2013) 1242856. doi:10.1126/science.1242856. arXiv:1311.5238.

[13] K. Lodders, Solar System Abundances and Condensation Temperatures of the Elements, ApJ 591 (2003) 1220–1247. doi:10.1086/375492.

[14] M. Aguilar, et al. (AMS collaboration), Properties of Iron Primary Cosmic Rays: Results from the Alpha Magnetic Spectrometer, Phys. Rev. Lett. 126 (2021) 041104. doi:10.1103/PhysRevLett.126.041104.

[15] M. Aguilar, et al. (AMS collaboration), Properties of Cosmic-Ray Sulfur and Determination of the Composition of Primary Cosmic-Ray Carbon, Neon, Magnesium, and Sulfur: Ten-Year Results from the Alpha Magnetic Spectrometer, Phys. Rev. Lett. 130 (2023) 211002. doi:10.1103/PhysRevLett.130.211002.

[16] J. J. Engelmann, P. Ferrando, A. Soutoul, P. Goret, E. Juliusson, L. Koch-Miramond, N. Lund, P. Masse, et al., Charge composition and energy spectra of cosmic-ray nuclei for elements from Be to Ni - Results from HEAO-3-C2., A&A 233 (1990) 96–111.
[17] B. F. Rauch, J. T. Link, K. Lodders, M. H. Israel, L. M. Barbier, W. R. Binns, E. R. Christian, J. R. Cummings, et al., Cosmic Ray origin in OB Associations and Preferential Acceleration of Refractory Elements: Evidence from Abundances of Elements $_{26}$Fe through $_{34}$Se, ApJ 697 (2009) 2083–2088. doi:10.1088/0004-637X/697/2/2083. arXiv:0906.2021.
[18] R. P. Murphy, M. Sasaki, W. R. Binns, T. J. Brandt, T. Hams, M. H. Israel, A. W. Labrador, J. T. Link, et al., Galactic Cosmic Ray Origins and OB Associations: Evidence from SuperTIGER Observations of Elements $_{26}$Fe through $_{40}$Zr, ApJ 831 (2016) 148. doi:10.3847/0004-637X/831/2/148. arXiv:1608.08183.
[19] P. H. Fowler, R. N. F. Walker, M. R. W. Masheder, R. T. Moses, A. Worley, A. M. Gay, Ariel 6 Measurements of the Fluxes of Ultra-heavy Cosmic Rays, ApJ 314 (1987) 739. doi:10.1086/165101.
[20] A. Alexandrov, P. Babaev, A. Bagulya, et al., History of heavy r-process elements in galactic cosmic rays from nuclei tracks in meteorite olivine, Adv. Space Res. 70 (2022) 2674–2684. doi:10.1016/j.asr.2022.06.055.
[21] J. Donnelly, A. Thompson, D. O'Sullivan, J. Daly, L. Drury, V. Domingo, K. P. Wenzel, Actinide and Ultra-Heavy Abundances in the Local Galactic Cosmic Rays: An Analysis of the Results from the LDEF Ultra-Heavy Cosmic-Ray Experiment, ApJ 747 (2012) 40. doi:10.1088/0004-637X/747/1/40.
[22] J. M. Gaskins, A review of indirect searches for particle dark matter, Contemp. Phys. 57 (2016) 496–525. doi:10.1080/00107514.2016.1175160. arXiv:1604.00014.
[23] M. Cirelli, A. Strumia, J. Zupan, Dark Matter (2024). arXiv:2406.01705.
[24] P. Salati, F. Donato, N. Fornengo, Indirect Dark Matter Detection with Cosmic Antimatter, Chapter 26 of Particle Dark Matter: Observations, Models and Searches, edited by Gianfranco Bertone (Cambridge University Press, 2010) (2010) 521–546. arXiv:1003.4124.
[25] C. Evoli, G. Morlino, P. Blasi, R. Aloisio, AMS-02 beryllium data and its implication for cosmic ray transport, Phys. Rev. D 101 (2020) 023013. doi:10.1103/PhysRevD.101.023013. arXiv:1910.04113.
[26] N. Weinrich, M. Boudaud, L. Derome, Y. Génolini, J. Lavalle, D. Maurin, P. Salati, P. Serpico, et al., Galactic halo size in the light of recent AMS-02 data, A&A 639 (2020) A74. doi:10.1051/0004-6361/202038064. arXiv:2004.00441.
[27] M. Di Mauro, F. Donato, M. Korsmeier, S. Manconi, L. Orusa, Novel prediction for secondary positrons and electrons in the Galaxy, Phys. Rev. D 108 (2023) 063024. doi:10.1103/PhysRevD.108.063024. arXiv:2304.01261.
[28] F. Donato, N. Fornengo, D. Maurin, P. Salati, Antiprotons in cosmic rays from neutralino annihilation, Phys. Rev. D 69 (2004) 063501. doi:10.1103/PhysRevD.69.063501. arXiv:astro-ph/0306207.
[29] C. Evoli, I. Cholis, D. Grasso, L. Maccione, P. Ullio, Antiprotons from dark matter annihilation in the Galaxy: astrophysical uncertainties, Phys. Rev. D 85 (2012) 123511. doi:10.1103/PhysRevD.85.123511. arXiv:1108.0664.
[30] Y. Génolini, M. Boudaud, M. Cirelli, L. Derome, J. Lavalle, D. Maurin, P. Salati, N. Weinrich, New minimal, median, and maximal propagation models for dark matter searches with Galactic cosmic rays, Phys. Rev. D 104 (2021) 083005. doi:10.1103/PhysRevD.104.083005. arXiv:2103.04108.
[31] F. Donato, D. Maurin, R. Taillet, β -radioactive cosmic rays in a diffusion model: Test for a local bubble?, A&A 381 (2002) 539–559. doi:10.1051/0004-6361:20011447. arXiv:astro-ph/0108079.
[32] I. V. Moskalenko, A. W. Strong, S. G. Mashnik, J. F. Ormes, Challenging Cosmic-Ray Propagation with Antiprotons: Evidence for a "Fresh" Nuclei Component?, ApJ 586 (2003) 1050–1066. doi:10.1086/367697. arXiv:astro-ph/0210480.
[33] A. Putze, L. Derome, D. Maurin, A Markov Chain Monte Carlo technique to sample transport and source parameters of Galactic cosmic rays. II. Results for the diffusion model combining B/C and radioactive nuclei, A&A 516 (2010) A66. doi:10.1051/0004-6361/201014010. arXiv:1001.0551.
[34] M.-J. Zhao, X.-J. Bi, K. Fang, P.-F. Yin, Interpretation of AMS-02 beryllium isotope fluxes using data-driven production cross sections, Phys. Rev. D 109 (2024) 083036. doi:10.1103/PhysRevD.109.083036. arXiv:2402.04659.
[35] M. Boudaud, Y. Génolini, L. Derome, J. Lavalle, D. Maurin, P. Salati, P. D. Serpico, AMS-02 antiprotons' consistency with a secondary astrophysical origin, Phys. Rev. Res. 2 (2020) 023022. doi:10.1103/PhysRevResearch.2.023022. arXiv:1906.07119.
[36] M. Di Mauro, M. Korsmeier, A. Cuoco, Data-driven constraints on cosmic-ray diffusion: Probing self-generated turbulence in the Milky Way, Phys. Rev. D 109 (2024) 123003. doi:10.1103/PhysRevD.109.123003. arXiv:2311.17150.
[37] A. Cuoco, M. Krämer, M. Korsmeier, Novel Dark Matter Constraints from Antiprotons in Light of AMS-02, Phys. Rev. Lett. 118 (2017) 191102. doi:10.1103/PhysRevLett.118.191102. arXiv:1610.03071.
[38] M.-Y. Cui, Q. Yuan, Y.-L. S. Tsai, Y.-Z. Fan, Possible dark matter annihilation signal in the AMS-02 antiproton data, Phys. Rev. Lett. 118 (2017) 191101. doi:10.1103/PhysRevLett.118.191101. arXiv:1610.03840.
[39] A. Cuoco, J. Heisig, L. Klamt, M. Korsmeier, M. Krämer, Scrutinizing the evidence for dark matter in cosmic-ray antiprotons, Phys. Rev. D 99 (2019). doi:10.1103/physrevd.99.103014.
[40] F. Calore, M. Cirelli, L. Derome, Y. Génolini, D. Maurin, P. Salati, P. D. Serpico, AMS-02 antiprotons and dark matter: Trimmed hints and robust bounds, SciPost Phys. 12 (2022) 163. doi:10.21468/SciPostPhys.12.5.163. arXiv:2202.03076.
[41] H. G. Fischer (NA49 collaboration), Baryon yields, isospin effects and strangeness production in elementary hadronic interactions, Acta Phys. Hung. A 17 (2003) 369–386. doi:10.1556/APH.17.2003.2-4.20.
[42] M. W. Winkler, Cosmic Ray Antiprotons at High Energies, J. Cosmology Astropart. Phys. 02 (2017) 048. doi:10.1088/1475-7516/2017/02/048. arXiv:1701.04866.
[43] P. von Doetinchem, et al., Cosmic-ray antinuclei as messengers of new physics: status and outlook for the new decade, J. Cosmology Astropart. Phys. 08 (2020) 035. doi:10.1088/1475-7516/2020/08/035. arXiv:2002.04163.
[44] H. Albrecht, et al. (ARGUS), Observation of Anti-deuteron Production in Electron - Positron Annihilation at 10-GeV Center-of-mass Energy, Phys. Lett. B 157 (1985) 326–332. doi:10.1016/0370-2693(85)90675-6.

[45] S. Schael, et al. (ALEPH collaboration), Deuteron and anti-deuteron production in e^+ e^- collisions at the Z resonance, Phys. Lett. B 639 (2006) 192–201. doi:10.1016/j.physletb.2006.06.043. arXiv:hep-ex/0604023.
[46] J. Adam, et al. (ALICE collaboration), Production of light nuclei and anti-nuclei in pp and Pb-Pb collisions at energies available at the CERN Large Hadron Collider, Phys. Rev. C 93 (2016) 024917. doi:10.1103/PhysRevC.93.024917. arXiv:1506.08951.
[47] S. Acharya, et al. (ALICE collaboration), Production of deuterons, tritons, ^{3}He nuclei and their antinuclei in pp collisions at $\sqrt{s}$ = 0.9, 2.76 and 7 TeV, Phys. Rev. C 97 (2018) 024615. doi:10.1103/PhysRevC.97.024615. arXiv:1709.08522.
[48] S. Acharya, et al. (ALICE collaboration), Multiplicity dependence of (anti-)deuteron production in pp collisions at $\sqrt{s}$ = 7 TeV, Phys. Lett. B 794 (2019) 50–63. doi:10.1016/j.physletb.2019.05.028. arXiv:1902.09290.
[49] S. Acharya, et al. (ALICE collaboration), (Anti-)deuteron production in pp collisions at $\sqrt{s} = 13$ TeV, Eur. Phys. J. C 80 (2020) 889. doi:10.1140/epjc/s10052-020-8256-4. arXiv:2003.03184.
[50] S. Acharya, et al. (ALICE collaboration), Production of light (anti)nuclei in pp collisions at $\sqrt{s} = 13$ TeV, J. High Energy Phys. 01 (2022) 106. doi:10.1007/JHEP01(2022)106. arXiv:2109.13026.
[51] S. Acharya, et al. (ALICE collaboration), Production of light (anti)nuclei in pp collisions at $\sqrt{s}$ = 5.02 TeV, Eur. Phys. J. C 82 (2022) 289. doi:10.1140/epjc/s10052-022-10241-z. arXiv:2112.00610.
[52] M. Di Mauro, N. Fornengo, A. Jueid, R. R. de Austri, F. Bellini, Nailing down the theoretical uncertainties of $\overline{\mathrm{D}}$ spectrum produced from dark matter (2024). arXiv:2411.04815.
[53] M. Mahlein, L. Barioglio, F. Bellini, L. Fabbietti, C. Pinto, B. Singh, S. Tripathy, A realistic coalescence model for deuteron production, Eur. Phys. J. C 83 (2023) 804. doi:10.1140/epjc/s10052-023-11972-3. arXiv:2302.12696.
[54] M. Mahlein, C. Pinto, L. Fabbietti, ToMCCA: a Toy Monte Carlo Coalescence Afterburner, European Physical Journal C 84 (2024) 1136. doi:10.1140/epjc/s10052-024-13486-y. arXiv:2404.03352.
[55] S. Acharya, et al. (ALICE collaboration), Measurement of anti-^{3}He nuclei absorption in matter and impact on their propagation in the Galaxy, Nat. Phys. 19 (2023) 61–71. doi:10.1038/s41567-022-01804-8. arXiv:2202.01549.
[56] F. D'Angelo, A. Oliva, N. Masi, Production of antiprotons in cosmic rays with new cross-sections, Nuovo Cimento C 47 (2024) 302. doi:10.1393/ncc/i2024-24302-x.
[57] W. B. Atwood, et al. (Fermi-LAT collaboration), The Large Area Telescope on the Fermi gamma-ray space telescope mission, ApJ 697 (2009) 1071. doi:10.1088/0004-637X/697/2/1071.
[58] M. Ackermann, et al. (Fermi-LAT collaboration), Searching for Dark Matter Annihilation from Milky Way Dwarf Spheroidal Galaxies with Six Years of Fermi Large Area Telescope Data, Phys. Rev. Lett. 115 (2015) 231301. doi:10.1103/PhysRevLett.115.231301.
[59] A. McDaniel, M. Ajello, C. M. Karwin, M. Di Mauro, A. Drlica-Wagner, M. A. Sánchez-Conde, Legacy analysis of dark matter annihilation from the Milky Way dwarf spheroidal galaxies with 14 years of Fermi-LAT data, Phys. Rev. D 109 (2024) 063024. doi:10.1103/PhysRevD.109.063024. arXiv:2311.04982.
[60] L. Goodenough, D. Hooper, Possible Evidence For Dark Matter Annihilation In The Inner Milky Way From The Fermi Gamma Ray Space Telescope (2009). arXiv:0910.2998.
[61] M. Ajello, et al. (Fermi-LAT collaboration), Fermi-LAT observation of high-energy γ-ray emission toward the Galactic centre, ApJ 819 (2016) 44. doi:10.3847/0004-637X/819/1/44.
[62] R. Bartels, S. Krishnamurthy, C. Weniger, Strong Support for the Millisecond Pulsar Origin of the Galactic Center GeV Excess, Phys. Rev. Lett. 116 (2016) 051102. doi:10.1103/PhysRevLett.116.051102.
[63] F. Calore, M. Di Mauro, F. Donato, J. W. T. Hessels, C. Weniger, Radio detection prospects for a bulge population of millisecond pulsars as suggested by Fermi-LAT observations of the inner Galaxy, ApJ 827 (2016) 143. doi:10.3847/0004-637X/827/2/143. arXiv:1512.06825.
[64] J. Becker Tjus, L. Merten, Closing in on the origin of Galactic cosmic rays using multimessenger information, Phys. Rep. 872 (2020) 1–98. doi:10.1016/j.physrep.2020.05.002. arXiv:2002.00964.
[65] A. M. Bykov, D. C. Ellison, A. Marcowith, S. M. Osipov, Cosmic ray production in supernovae, Space Sci. Rev. 214 (2018) 41. doi:10.1007/s11214-018-0479-4. arXiv:1801.08890.
[66] D. Caprioli, Particle acceleration at shocks: An introduction, Proc. Int. Sch. Phys. Fermi 208 (2024) 143–181. doi:10.3254/ENFI240005. arXiv:2307.00284.
[67] E. Amato, Particle acceleration in pulsars and pulsar wind nebulae, Proc. Int. Sch. Phys. Fermi 208 (2024) 183–221. doi:10.3254/ENFI240006. arXiv:2402.10912.
[68] G. Winner, C. Pfrommer, P. Girichidis, M. Werhahn, M. Pais, Evolution and observational signatures of the cosmic ray electron spectrum in SN 1006, MNRAS 499 (2020) 2785–2802. doi:10.1093/mnras/staa2989. arXiv:2006.06683.
[69] N. J. Corso, R. Diesing, D. Caprioli, Hadronic versus Leptonic Origin of Gamma-Ray Emission from Supernova Remnants, ApJ 954 (2023) 1. doi:10.3847/1538-4357/ace699. arXiv:2301.10257.
[70] L. Orusa, M. Di Mauro, F. Donato, M. Korsmeier, New determination of the production cross section for γ rays in the Galaxy, Phys. Rev. D 107 (2023) 083031. doi:10.1103/PhysRevD.107.083031. arXiv:2302.01943.
[71] L. Orusa, M. Di Mauro, F. Donato, M. Korsmeier, New determination of the production cross section for secondary positrons and electrons in the Galaxy, Phys. Rev. D 105 (2022) 123021. doi:10.1103/PhysRevD.105.123021. arXiv:2203.13143.
[72] S. Gabici, Cosmic rays from star clusters, Proc. Int. Sch. Phys. Fermi 208 (2024) 223–255. doi:10.3254/ENFI240007. arXiv:2307.01596.
[73] W. Binns, et al., Ultra-heavy cosmic-ray science: Are r-process nuclei in the cosmic rays produced in supernovae or binary neutron star mergers?, BAAS 51 (2019) 313. doi:10.48550/arXiv.1903.12228. arXiv:1903.12228.
[74] R. Chornock, E. Berger, D. Kasen, P. S. Cowperthwaite, M. Nicholl, V. A. Villar, K. D. Alexander, P. K. Blanchard, T. Eftekhari, W. Fong, et al., The Electromagnetic Counterpart of the Binary Neutron Star Merger LIGO/Virgo

GW170817. IV. Detection of Near-infrared Signatures of r-process Nucleosynthesis with Gemini-South, ApJ 848 (2017) L19. doi:10.3847/2041-8213/aa905c. arXiv:1710.05454.

[75] M. Nicholl, E. Berger, D. Kasen, B. D. Metzger, J. Elias, C. Briceño, K. D. Alexander, P. K. Blanchard, R. Chornock, P. S. Cowperthwaite, et al., The Electromagnetic Counterpart of the Binary Neutron Star Merger LIGO/Virgo GW170817. III. Optical and UV Spectra of a Blue Kilonova from Fast Polar Ejecta, ApJ 848 (2017) L18. doi:10.3847/2041-8213/aa9029. arXiv:1710.05456.

[76] B. P. Abbott, R. Abbott, T. D. Abbott, F. Acernese, K. Ackley, C. Adams, T. Adams, P. Addesso, R. X. Adhikari, V. B. Adya, et al., GW170817: Observation of Gravitational Waves from a Binary Neutron Star Inspiral, Phys. Rev. Lett. 119 (2017) 161101. doi:10.1103/PhysRevLett.119.161101. arXiv:1710.05832.

[77] C. Evoli, U. Dupletsa, Phenomenological models of cosmic ray transport in galaxies, Proc. Int. Sch. Phys. Fermi 208 (2024) 257–313. doi:10.3254/ENFI240008. arXiv:2309.00293.

[78] E. Amato, P. Blasi, Cosmic ray transport in the Galaxy: A review, Adv. in Space Res. 62 (2018) 2731–2749. doi:10.1016/j.asr.2017.04.019. arXiv:1704.05696.

[79] C. Evoli, R. Aloisio, P. Blasi, Galactic cosmic rays after the AMS-02 observations, Phys. Rev. D 99 (2019) 103023. doi:10.1103/PhysRevD.99.103023. arXiv:1904.10220.

[80] P. D. Serpico, Possible physics scenarios behind cosmic-ray "anomalies", in: 34th ICRC, 2016, p. 009. doi:10.22323/1.236.0009. arXiv:1509.04233.

[81] Y. Génolini, et al., Indications for a high-rigidity break in the cosmic-ray diffusion coefficient, Phys. Rev. Lett. 119 (2017) 241101. doi:10.1103/PhysRevLett.119.241101. arXiv:1706.09812.

[82] P. Blasi, E. Amato, P. D. Serpico, Spectral breaks as a signature of cosmic ray induced turbulence in the Galaxy, Phys. Rev. Lett. 109 (2012) 061101. doi:10.1103/PhysRevLett.109.061101. arXiv:1207.3706.

[83] C. Evoli, P. Blasi, G. Morlino, R. Aloisio, Origin of the Cosmic Ray Galactic Halo Driven by Advected Turbulence and Self-Generated Waves, Phys. Rev. Lett. 121 (2018) 021102. doi:10.1103/PhysRevLett.121.021102. arXiv:1806.04153.

[84] N. Tomassetti, Origin of the Cosmic-Ray Spectral Hardening, ApJ 752 (2012) L13. doi:10.1088/2041-8205/752/1/L13. arXiv:1204.4492.

[85] M. Lemoine, Particle transport through localized interactions with sharp magnetic field bends in MHD turbulence, J. Plasma Phys. 89 (2023) 175890501. doi:10.1017/S0022377823000946. arXiv:2304.03023.

[86] I. S. Butsky, P. F. Hopkins, P. Kempski, S. B. Ponnada, E. Quataert, J. Squire, Galactic cosmic-ray scattering due to intermittent structures, MNRAS 528 (2024) 4245–4254. doi:10.1093/mnras/stae276. arXiv:2308.06316.

[87] P. Kempski, D. Li, D. B. Fielding, E. Quataert, E. S. Phinney, M. W. Kunz, D. L. Jow, A. A. Philippov, A Unified Model of Cosmic Ray Propagation and Radio Extreme Scattering Events from Intermittent Interstellar Structures (2024). arXiv:2412.03649.

[88] V. Tatischeff, J. C. Raymond, J. Duprat, S. Gabici, S. Recchia, The origin of Galactic cosmic rays as revealed by their composition, MNRAS 508 (2021) 1321–1345. doi:10.1093/mnras/stab2533. arXiv:2106.15581.

[89] Y. Génolini, P. Salati, P. Serpico, R. Taillet, Stable laws and cosmic ray physics, A&A 600 (2017) A68. doi:10.1051/0004-6361/201629903. arXiv:1610.02010.

[90] P. Mertsch, Stochastic cosmic ray sources and the TeV break in the all-electron spectrum, J. Cosmology Astropart. Phys. 11 (2018) 045. doi:10.1088/1475-7516/2018/11/045. arXiv:1809.05104.

[91] C. Evoli, E. Amato, P. Blasi, R. Aloisio, Stochastic nature of Galactic cosmic-ray sources, Phys. Rev. D 104 (2021) 123029. doi:10.1103/PhysRevD.104.123029. arXiv:2111.01171.

[92] M. Aguilar, et al. (AMS collaboration), Properties of Cosmic Deuterons Measured by the Alpha Magnetic Spectrometer, Phys. Rev. Lett. 132 (2024) 261001. doi:10.1103/PhysRevLett.132.261001.

[93] M. J. Boschini, S. D. Torre, M. Gervasi, D. Grand i, G. Jøhannesson, G. L. Vacca, N. Masi, I. V. Moskalenko, et al., Deciphering the Local Interstellar Spectra of Secondary Nuclei with the Galprop/Helmod Framework and a Hint for Primary Lithium in Cosmic Rays, ApJ 889 (2020) 167. doi:10.3847/1538-4357/ab64f1.

[94] X.-J. Lv, X.-J. Bi, K. Fang, P.-F. Yin, M.-J. Zhao, Cosmic-ray deuteron excess from a primary component, Phys. Rev. D 110 (2024) 123030. doi:10.1103/PhysRevD.110.123030. arXiv:2409.07139.

[95] F. Dimiccoli, F. M. Follega, A novel experimental approach to uncover the nature of cosmic-ray Deuterium (2025). arXiv:2501.03966.

[96] Q. Yuan, Y.-Z. Fan, The AMS-02 Cosmic-Ray Deuteron Flux is Consistent with a Secondary Origin, ApJ 974 (2024) L14. doi:10.3847/2041-8213/ad7e2c. arXiv:2406.19315.

[97] D. Maurin, E. Ferronato Bueno, Y. Génolini, L. Derome, M. Vecchi, The importance of Fe fragmentation for LiBeB analyses. Is a Li primary source needed to explain AMS-02 data?, A&A 668 (2022) A7. doi:10.1051/0004-6361/202243446. arXiv:2203.00522.

[98] O. Adriani, et al. (PAMELA collaboration), An anomalous positron abundance in cosmic rays with energies 1.5-100 GeV, Nature 458 (2009) 607–609. doi:10.1038/nature07942. arXiv:0810.4995.

[99] O. Adriani, et al. (PAMELA collaboration), Cosmic-Ray Positron Energy Spectrum Measured by PAMELA, Phys. Rev. Lett. 111 (2013) 081102. doi:10.1103/PhysRevLett.111.081102. arXiv:1308.0133.

[100] L. Accardo, et al. (AMS collaboration), High Statistics Measurement of the Positron Fraction in Primary Cosmic Rays of 0.5–500 GeV with the Alpha Magnetic Spectrometer on the International Space Station, Phys. Rev. Lett. 113 (2014) 121101. doi:10.1103/PhysRevLett.113.121101.

[101] M. Aguilar, et al. (AMS collaboration), Towards Understanding the Origin of Cosmic-Ray Positrons, Phys. Rev. Lett. 122 (2019) 041102. doi:10.1103/PhysRevLett.122.041102.

[102] M. Ackermann, M. Ajello, A. Allafort, W. B. Atwood, L. Baldini, G. Barbiellini, D. Bastieri, K. Bechtol, et al., Measurement of Separate Cosmic-Ray Electron and Positron Spectra with the Fermi Large Area Telescope, Phys. Rev. Lett.

108 (2012) 011103. doi:10.1103/PhysRevLett.108.011103. arXiv:1109.0521.
[103] D. Hooper, P. Blasi, P. D. Serpico, Pulsars as the Sources of High Energy Cosmic Ray Positrons, J. Cosmology Astropart. Phys. 01 (2009) 025. doi:10.1088/1475-7516/2009/01/025. arXiv:0810.1527.
[104] P. Blasi, E. Amato, Positrons from pulsar winds, in: D. F. Torres, N. Rea (Eds.), High-Energy Emission from Pulsars and their Systems, volume 21 of *Astrophys. Space Sci. Proc.*, 2011, p. 624. doi:10.48550/arXiv.1007.4745. arXiv:1007.4745.
[105] L. Orusa, S. Manconi, F. Donato, M. Di Mauro, Constraining positron emission from pulsar populations with AMS-02 data, J. Cosmology Astropart. Phys. 12 (2021) 014. doi:10.1088/1475-7516/2021/12/014. arXiv:2107.06300.
[106] L. Orusa, S. Manconi, F. Donato, M. Di Mauro, Disclosing the catalog pulsars dominating the Galactic positron flux, JCAP 02 (2025) 029. doi:10.1088/1475-7516/2025/02/029. arXiv:2410.10951.
[107] C. Evoli, E. Amato, P. Blasi, R. Aloisio, Galactic factories of cosmic-ray electrons and positrons, Phys. Rev. D 103 (2021) 083010. doi:10.1103/PhysRevD.103.083010. arXiv:2010.11955.
[108] P. Blasi, P. D. Serpico, High-energy antiprotons from old supernova remnants, Phys. Rev. Lett. 103 (2009) 081103. doi:10.1103/PhysRevLett.103.081103. arXiv:0904.0871.
[109] P. Mertsch, S. Sarkar, AMS-02 data confront acceleration of cosmic ray secondaries in nearby sources, Phys. Rev. D 90 (2014) 061301. doi:10.1103/PhysRevD.90.061301. arXiv:1402.0855.
[110] M. Ackermann, et al. (Fermi-LAT collaboration), Constraints on the Cosmic-ray Density Gradient Beyond the Solar Circle from Fermi γ-ray Observations of the Third Galactic Quadrant, ApJ 726 (2011) 81. doi:10.1088/0004-637X/726/2/81. arXiv:1011.0816.
[111] C. Evoli, D. Gaggero, D. Grasso, L. Maccione, A common solution to the cosmic ray anisotropy and gradient problems, Phys. Rev. Lett. 108 (2012) 211102. doi:10.1103/PhysRevLett.108.211102. arXiv:1203.0570.
[112] M. Opher, A. Loeb, C. Zucker, A. Goodman, R. Konietzka, A. Z. Worden, E. P. Economo, J. A. Miller, et al., The Passage of the Solar System through the Edge of the Local Bubble, ApJ 972 (2024) 201. doi:10.3847/1538-4357/ad596e.
[113] N. J. Shaviv, Cosmic Ray Diffusion from the Galactic Spiral Arms, Iron Meteorites, and a Possible Climatic Connection, Phys. Rev. Lett. 89 (2002) 051102. doi:10.1103/PhysRevLett.89.051102. arXiv:astro-ph/0207637.
[114] N. J. Shaviv, The spiral structure of the Milky Way, cosmic rays, and ice age epochs on Earth, New A 8 (2003) 39–77. doi:10.1016/S1384-1076(02)00193-8. arXiv:astro-ph/0209252.
[115] K. Scherer, H. Fichtner, T. Borrmann, J. Beer, L. Desorgher, E. Flükiger, H. J. Fahr, S. E. S. Ferreira, et al., Interstellar-Terrestrial Relations: Variable Cosmic Environments, The Dynamic Heliosphere, and Their Imprints on Terrestrial Archives and Climate, Space Sci. Rev. 127 (2006) 327–465. doi:10.1007/s11214-006-9126-6.
[116] K. Wallmann, Impact of atmospheric CO_2 and galactic cosmic radiation on Phanerozoic climate change and the marine $\delta^{18}O$ record, Geochem. Geophys. Geosyst. 5 (2004) Q06004. doi:10.1029/2003GC000683.
[117] T. Sloan, A. W. Wolfendale, Cosmic rays and climate change over the past 1000 million years, New A 25 (2013) 45–49. doi:10.1016/j.newast.2013.03.008. arXiv:1303.7314.
[118] R. Wieler, J. Beer, I. Leya, The Galactic Cosmic Ray Intensity over the Past 10^6-10^9 Years as Recorded by Cosmogenic Nuclides in Meteorites and Terrestrial Samples, Space Sci. Rev. 176 (2013) 351–363. doi:10.1007/s11214-011-9769-9.
[119] W. Hampel, O. A. Schaeffer, ^{26}Al in iron meteorites and the constancy of cosmic ray intensity in the past, Earth Planet. Sci. Lett. 42 (1979) 348–358. doi:10.1016/0012-821X(79)90043-8.
[120] D. Aylmer, G. F. Herzog, J. Klein, R. Middleton, ^{10}Be and ^{26}Al contents of eucrites: Implications for production rates and exposure ages, Geochim. Cosmochim. Acta 52 (1988) 1691–1698. doi:10.1016/0016-7037(88)90237-2.
[121] B. Lavielle, K. Marti, J. P. Jeannot, K. Nishiizumi, M. Caffee, The ^{36}Cl- ^{36}Ar- ^{40}K- ^{41}K records and cosmic ray production rates in iron meteorites, Earth Planet. Sci. Lett. 170 (1999) 93–104. doi:10.1016/S0012-821X(99)00099-0.
[122] T. Smith, D. L. Cook, S. Merchel, S. Pavetich, G. Rugel, A. Scharf, I. Leya, The constancy of galactic cosmic rays as recorded by cosmogenic nuclides in iron meteorites, Meteorit. Planet. Sci. 54 (2019) 2951–2976. doi:10.1111/maps.13417.
[123] N. A. Schwadron, J. B. Blake, A. W. Case, C. J. Joyce, J. Kasper, J. Mazur, N. Petro, M. Quinn, et al., Does the worsening galactic cosmic radiation environment observed by CRaTER preclude future manned deep space exploration?, Space Weather 12 (2014) 622–632. doi:10.1002/2014SW001084.
[124] A. Rizzo, E. M. Borra, L. Ciciani, L. Di Fino, G. Romoli, G. Santi Amantini, L. Sperandio, I. Vilardi, et al., Foundations of radiological protection in space: the integrated multidisciplinary approach for next manned missions in deep space, Eur. Phys. J. Plus 138 (2023). doi:10.1140/epjp/s13360-023-04572-3.
[125] L. Sihver, S. M. J. Mortazavi, Biological Protection in Deep Space Missions, J. Biomed. Phys. Engineering 11 (2021) 663–674. doi:10.31661/jbpe.v0i0.1193.
[126] A. Fogtman, S. Baatout, B. Baselet, T. Berger, C. E. Hellweg, P. Jiggens, C. La Tessa, L. Narici, et al., Towards sustainable human space exploration—priorities for radiation research to quantify and mitigate radiation risks, Nat. Microgravity 9 (2023). doi:10.1038/s41526-023-00262-7.
[127] J. C. Chancellor, R. S. Blue, K. A. Cengel, S. M. Auñón-Chancellor, K. H. Rubins, H. G. Katzgraber, A. R. Kennedy, Limitations in predicting the space radiation health risk for exploration astronauts, Nat. Microgravity 4 (2018) 8. doi:10.1038/s41526-018-0043-2.
[128] M. Durante, F. A. Cucinotta, Physical basis of radiation protection in space travel, Rev. Mod. Phys. 83 (2011) 1245–1281. doi:10.1103/RevModPhys.83.1245.
[129] J. H. Heinbockel, J. W. Wilson, S. R. Blattnig, G. D. Qualls, F. F. Badavi, F. A. Cucinotta, HZE ion fragmentation cross-section sensitivity and propagated errors in HZE exposure estimates, Radiat. Meas. 41 (2006) 1103–1114. doi:10.1016/j.radmeas.2006.02.002.
[130] T. C. Slaba, A. A. Bahadori, B. D. Reddell, R. C. Singleterry, M. S. Clowdsley, S. R. Blattnig, Optimal shielding thickness for galactic cosmic ray environments, Life Sci. Space Res. 12 (2017). doi:10.1016/j.lssr.2016.12.003.
[131] J. W. Norbury, J. Miller, A. M. Adamczyk, L. H. Heilbronn, L. W. Townsend, S. R. Blattnig, R. B. Norman, S. B.

Guetersloh, et al., Nuclear data for space radiation, Radiat. Meas. 47 (2012) 315–363. doi:10.1016/j.radmeas.2012.03.004.
[132] G. Battistoni, et al. (FOOT collaboration), Measuring the impact of Nuclear Interaction in Particle Therapy and in Radio Protection in Space: the FOOT experiment., Front. Phys. 8 (2021) 555. doi:10.3389/fphy.2020.568242.
[133] B. T. Zhang, K. Murase, N. Ekanger, M. Bhattacharya, S. Horiuchi, Ultraheavy Ultrahigh-Energy Cosmic Rays (2024). arXiv:2405.17409.
[134] G. R. Farrar, Binary neutron star mergers as the source of the highest energy cosmic rays (2024). arXiv:2405.12004.
[135] V. Decoene, C. Guépin, K. Fang, K. Kotera, B. D. Metzger, High-energy neutrinos from fallback accretion of binary neutron star merger remnants, J. Cosmology Astropart. Phys. 2020 (2020) 045. doi:10.1088/1475-7516/2020/04/045. arXiv:1910.06578.
[136] A. A. Halim, et al. (Pierre Auger collaboration), Constraining the sources of ultra-high-energy cosmic rays across and above the ankle with the spectrum and composition data measured at the Pierre Auger Observatory, JCAP 05 (2023) 024. doi:10.1088/1475-7516/2023/05/024. arXiv:2211.02857.
[137] B. P. Abbott, et al., Multi-messenger Observations of a Binary Neutron Star Merger, ApJ 848 (2017) L12. doi:10.3847/2041-8213/aa91c9. arXiv:1710.05833.
[138] IceCube Collaboration, et al. (IceCube collaboration), Neutrino emission from the direction of the blazar TXS 0506+056 prior to the IceCube-170922A alert, Science 361 (2018) 147–151. doi:10.1126/science.aat2890. arXiv:1807.08794.
[139] L. Morejon, A. Fedynitch, D. Boncioli, D. Biehl, W. Winter, Improved photomeson model for interactions of cosmic ray nuclei, J. Cosmology Astropart. Phys. 2019 (2019) 007. doi:10.1088/1475-7516/2019/11/007. arXiv:1904.07999.
[140] K. Chatziioannou, H. T. Cromartie, S. Gandolfi, I. Tews, D. Radice, A. W. Steiner, A. L. Watts, Neutron stars and the dense matter equation of state: from microscopic theory to macroscopic observations (2024). arXiv:2407.11153.
[141] A. J. Dittmann, M. C. Miller, F. K. Lamb, I. M. Holt, C. Chirenti, M. T. Wolff, S. Bogdanov, S. Guillot, et al., A More Precise Measurement of the Radius of PSR J0740+6620 Using Updated NICER Data, ApJ 974 (2024) 295. doi:10.3847/1538-4357/ad5f1e. arXiv:2406.14467.
[142] T. Salmi, D. Choudhury, Y. Kini, T. E. Riley, S. Vinciguerra, A. L. Watts, M. T. Wolff, Z. Arzoumanian, et al., The Radius of the High-mass Pulsar PSR J0740+6620 with 3.6 yr of NICER Data, ApJ 974 (2024) 294. doi:10.3847/1538-4357/ad5f1f. arXiv:2406.14466.
[143] D. Choudhury, T. Salmi, S. Vinciguerra, T. E. Riley, Y. Kini, A. L. Watts, B. Dorsman, S. Bogdanov, et al., A NICER View of the Nearest and Brightest Millisecond Pulsar: PSR J0437–4715, ApJ 971 (2024) L20. doi:10.3847/2041-8213/ad5a6f. arXiv:2407.06789.
[144] S. Vinciguerra, T. Salmi, A. L. Watts, D. Choudhury, T. E. Riley, P. S. Ray, S. Bogdanov, Y. Kini, et al., An Updated Mass-Radius Analysis of the 2017-2018 NICER Data Set of PSR J0030+0451, ApJ 961 (2024) 62. doi:10.3847/1538-4357/acfb83. arXiv:2308.09469.
[145] M. S. Potgieter, Solar Modulation of Cosmic Rays, Living Rev. Sol. Phys. 10 (2013) 3. doi:10.12942/lrsp-2013-3. arXiv:1306.4421.
[146] D. H. Hathaway, The Solar Cycle, Living Rev. Sol. Phys. 12 (2015) 4. doi:10.1007/lrsp-2015-4. arXiv:1502.07020.
[147] K. Petrovay, Solar cycle prediction, Living Rev. Sol. Phys. 17 (2020) 2. doi:10.1007/s41116-020-0022-z. arXiv:1907.02107.
[148] I. G. Usoskin, A history of solar activity over millennia, Living Rev. Sol. Phys. 20 (2023) 2. doi:10.1007/s41116-023-00036-z.
[149] E. C. Stone, A. C. Cummings, F. B. McDonald, B. C. Heikkila, N. Lal, W. R. Webber, Voyager 1 Observes Low-Energy Galactic Cosmic Rays in a Region Depleted of Heliospheric Ions, Science 341 (2013) 150–153. doi:10.1126/science.1236408.
[150] A. C. Cummings, E. C. Stone, B. C. Heikkila, N. Lal, W. R. Webber, G. Jóhannesson, I. V. Moskalenko, E. Orlando, et al., Galactic Cosmic Rays in the Local Interstellar Medium: Voyager 1 Observations and Model Results, ApJ 831 (2016) 18. doi:10.3847/0004-637X/831/1/18.
[151] E. C. Stone, A. C. Cummings, B. C. Heikkila, N. Lal, Cosmic ray measurements from Voyager 2 as it crossed into interstellar space, Nat. Astron. 3 (2019) 1013–1018. doi:10.1038/s41550-019-0928-3.
[152] O. Adriani, et al. (PAMELA collaboration), Time Dependence of the Electron and Positron Components of the Cosmic Radiation Measured by the PAMELA Experiment between July 2006 and December 2015, Phys. Rev. Lett. 116 (2016) 241105. doi:10.1103/PhysRevLett.116.241105.
[153] M. Martucci, et al. (PAMELA collaboration), Proton Fluxes Measured by the PAMELA Experiment from the Minimum to the Maximum Solar Activity for Solar Cycle 24, ApJ 854 (2018) L2. doi:10.3847/2041-8213/aaa9b2.
[154] M. Aguilar, et al. (AMS collaboration), Periodicities in the Daily Proton Fluxes from 2011 to 2019 Measured by the Alpha Magnetic Spectrometer on the International Space Station from 1 to 100 GV, Phys. Rev. Lett. 127 (2021) 271102. doi:10.1103/PhysRevLett.127.271102.
[155] M. Aguilar, et al. (AMS collaboration), Properties of Daily Helium Fluxes, Phys. Rev. Lett. 128 (2022) 231102. doi:10.1103/PhysRevLett.128.231102.
[156] M. Aguilar, et al. (AMS collaboration), Temporal Structures in Electron Spectra and Charge Sign Effects in Galactic Cosmic Rays, Phys. Rev. Lett. 130 (2023) 161001. doi:10.1103/PhysRevLett.130.161001.
[157] M. Aguilar, et al. (AMS collaboration), Temporal Structures in Positron Spectra and Charge-Sign Effects in Galactic Cosmic Rays, Phys. Rev. Lett. 131 (2023) 151002. doi:10.1103/PhysRevLett.131.151002.
[158] M. Aguilar, et al. (AMS collaboration), Antiprotons and Elementary Particles over a Solar Cycle: Results from the Alpha Magnetic Spectrometer, Phys. Rev. Lett. 134 (2025) 051002. doi:10.1103/PhysRevLett.134.051002.
[159] M. Aguilar, et al. (AMS collaboration), Solar Modulation of Cosmic Nuclei over a Solar Cycle: Results from the Alpha

Magnetic Spectrometer, Phys. Rev. Lett. 134 (2025) 051001. doi:10.1103/PhysRevLett.134.051001.
[160] J. Mitchell, et al. (BESS collaboration), The BESS Program, Nucl. Phys. B- Proceedings Supplements 134 (2004) 31–38. doi:10.1016/j.nuclphysbps.2004.08.003, proceedings of the Second International Conference on Particle and Fundamental Physics in Space (SpacePart '03).
[161] K. Abe, et al. (BESS collaboration), The results from BESS-Polar experiment, Adv. in Space Res. 60 (2017) 806–814. doi:10.1016/j.asr.2016.11.004, solar Energetic Particles, Solar Modulation and Space Radiation: New Opportunities in the AMS-02 Era.
[162] O. Adriani, et al. (PAMELA collaboration), Ten years of PAMELA in space, Nuovo Cimento Rivista 40 (2017) 473–522. doi:10.1393/ncr/i2017-10140-x.
[163] A. Galper, P. Spillantini, Ten years of CR physics with PAMELA, Phys. Part. Nucl. 48 (2017) 710–719. doi:10.1134/S1063779617050185.
[164] S. Coutu, et al. (HELIX), The High Energy Light Isotope eXperiment program of direct cosmic-ray studies, JINST 19 (2024) C01025. doi:10.1088/1748-0221/19/01/C01025.
[165] J. Chang, et al. (DAMPE collaboration), The DArk Matter Particle Explorer mission, Astropart. Phys. 95 (2017) 6–24. doi:10.1016/j.astropartphys.2017.08.005.
[166] Y. Akaike, et al. (CALET collaboration), The Calorimetric Electron Telescope on the International Space Station: Results from the first eight years on orbit, Adv. in Space Res. 74 (2024) 4353–4367. doi:10.1016/j.asr.2024.04.035.
[167] A. N. Turundaevskiy, et al. (NUCLEON collaboration), Main Results from the NUCLEON Experiment, Bull. Russ. Acad. Sci. Phys 85 (2021) 353–356. doi:10.3103/S1062873821040377.
[168] G. H. Choi, et al. (ISS-CREAM collaboration), Measurement of High-energy Cosmic-Ray Proton Spectrum from the ISS-CREAM Experiment, ApJ 940 (2022) 107. doi:10.3847/1538-4357/ac9d2c.
[169] F. Giovacchini (AMS collaboration), The RICH detector of the AMS-02 experiment aboard the International Space Station, Nucl. Instr. Meth. Phys. Res. A 1055 (2023) 168434. doi:10.1016/j.nima.2023.168434.
[170] H. Jeon (HELIX), The Design and Status of the HELIX Ring Imaging Cherenkov Detector and Hodoscope Systems, in: 38th ICRC, 2024, p. 121. doi:10.22323/1.444.0121.
[171] A. Kounine, Z. Weng, W. Xu, C. Zhang, Precision measurement of 0.5 GeV–3 TeV electrons and positrons using the AMS Electromagnetic Calorimeter, Nucl. Instr. Meth. Phys. Res. A 869 (2017) 110–117. doi:https://doi.org/10.1016/j.nima.2017.07.013.
[172] S. Torii (CALET collaboration), Calorimetric electron telescope mission. Search for dark matter and nearby sources, Nucl. Instr. Meth. Phys. Res. A 630 (2011) 55–57. doi:10.1016/j.nima.2010.06.026.
[173] Y. S. Yoon, et al. (CREAM), Cosmic-ray Proton and Helium Spectra from the First CREAM Flight, ApJ 728 (2011) 122. doi:10.1088/0004-637X/728/2/122. arXiv:1102.2575.
[174] O. Adriani, et al. (PAMELA collaboration), PAMELA Measurements of Cosmic-Ray Proton and Helium Spectra, Science 332 (2011) 69. doi:10.1126/science.1199172. arXiv:1103.4055.
[175] Y. S. Yoon, et al. (CREAM), Proton and Helium Spectra from the CREAM-III Flight, ApJ 839 (2017) 5. doi:10.3847/1538-4357/aa68e4. arXiv:1704.02512.
[176] O. Adriani, et al. (CALET collaboration), Direct Measurement of the Cosmic-Ray Helium Spectrum from 40 GeV to 250 TeV with the Calorimetric Electron Telescope on the International Space Station, Phys. Rev. Lett. 130 (2023) 171002. doi:10.1103/PhysRevLett.130.171002. arXiv:2304.14699.
[177] O. Adriani, et al. (CALET collaboration), Observation of Spectral Structures in the Flux of Cosmic-Ray Protons from 50 GeV to 60 TeV with the Calorimetric Electron Telescope on the International Space Station, Phys. Rev. Lett. 129 (2022) 101102. doi:10.1103/PhysRevLett.129.101102. arXiv:2209.01302.
[178] F. Alemanno, et al. (DAMPE collaboration), Measurement of the cosmic ray helium energy spectrum from 70 GeV to 80 TeV with the DAMPE space mission, Phys. Rev. Lett. 126 (2021) 201102. doi:10.1103/PhysRevLett.126.201102. arXiv:2105.09073.
[179] Q. An, et al. (DAMPE collaboration), Measurement of the cosmic-ray proton spectrum from 40 GeV to 100 TeV with the DAMPE satellite, Sci. Adv. 5 (2019) eaax3793. doi:10.1126/sciadv.aax3793. arXiv:1909.12860.
[180] A. Ruina, et al. (DAMPE collaboration), Charge Loss Correction in the Silicon-Tungsten Tracker-Converter for Proton-Helium Charge Identification in the DAMPE Detector, in: 37th ICRC, 2022, p. 83. doi:10.22323/1.395.0083.
[181] F. Alemanno, et al. (DAMPE collaboration), Measurement of the cosmic p+He energy spectrum from 50 GeV to 0.5 PeV with the DAMPE space mission, Phys. Rev. D 109 (2024) L121101. doi:10.1103/PhysRevD.109.L121101. arXiv:2304.00137.
[182] G. Choi, E. S. Seo (ISS-CREAM collaboration), Measurement of cosmic-ray proton and helium spectra from the ISS-CREAM experiment, in: 38th ICRC, 2024, p. 108. doi:10.22323/1.444.0108.
[183] K. Abe, et al. (BESS collaboration), Measurement of the cosmic-ray low-energy antiproton spectrum with the first BESS-Polar Antarctic flight, Phys. Lett. B 670 (2008) 103–108. doi:10.1016/j.physletb.2008.10.053. arXiv:0805.1754.
[184] K. Abe, et al. (BESS collaboration), Measurement of the Cosmic-Ray Antiproton Spectrum at Solar Minimum with a Long-Duration Balloon Flight over Antarctica, Phys. Rev. Lett. 108 (2012) 051102. doi:10.1103/PhysRevLett.108.051102. arXiv:1107.6000.
[185] O. Adriani, et al. (PAMELA collaboration), New Measurement of the Antiproton-to-Proton Flux Ratio up to 100 GeV in the Cosmic Radiation, Phys. Rev. Lett. 102 (2009) 051101. doi:10.1103/PhysRevLett.102.051101. arXiv:0810.4994.
[186] O. Adriani, et al. (PAMELA collaboration), PAMELA results on the cosmic-ray antiproton flux from 60 MeV to 180 GeV in kinetic energy, Phys. Rev. Lett. 105 (2010) 121101. doi:10.1103/PhysRevLett.105.121101. arXiv:1007.0821.
[187] O. Adriani, et al. (PAMELA collaboration), Measurement of the flux of primary cosmic ray antiprotons with energies of 60 MeV to 350 GeV in the PAMELA experiment, JETP Lett. 96 (2013) 621–627. doi:10.1134/S002136401222002X.

[188] A. Stoessl, et al. (GAPS collaboration), The GAPS experiment - a search for light cosmic ray antinuclei, in: 38th ICRC, 2024, p. 1440. doi:10.22323/1.444.1440.
[189] F. Rogers, et al. (GAPS collaboration), Sensitivity of the GAPS experiment to low-energy cosmic-ray antiprotons, Astropart. Phys. 145 (2023) 102791. doi:10.1016/j.astropartphys.2022.102791. arXiv:2206.12991.
[190] K. Sakai, et al. (BESS collaboration), Search for Antideuterons of Cosmic Origin Using the BESS-Polar II Magnetic-Rigidity Spectrometer, Phys. Rev. Lett. 132 (2024) 131001. doi:10.1103/PhysRevLett.132.131001.
[191] A. Kounine (AMS collaboration), Latest AMS Results on Cosmic Light Antimatter Particles, PAW'24 Conference 107 (2023) 083031. URL: https://indico.cern.ch/event/1367212/timetable/#20240318.detailed.
[192] M. Aguilar, et al. (AMS collaboration), Towards Understanding the Origin of Cosmic-Ray Electrons, Phys. Rev. Lett. 122 (2019) 101101. doi:10.1103/PhysRevLett.122.101101.
[193] A. Kounine, et al. (AMS collaboration), Understanding the Origin of Cosmic-Ray Electrons, in: 38th ICRC, 2024, p. 65. doi:10.22323/1.444.0065.
[194] G. Ambrosi, et al. (DAMPE collaboration), Direct detection of a break in the teraelectronvolt cosmic-ray spectrum of electrons and positrons, Nature 552 (2017) 63–66. doi:10.1038/nature24475. arXiv:1711.10981.
[195] O. Adriani, et al. (CALET collaboration), Direct Measurement of the Spectral Structure of Cosmic-Ray Electrons+Positrons in the TeV Region with CALET on the International Space Station, Phys. Rev. Lett. 131 (2023) 191001. doi:10.1103/PhysRevLett.131.191001. arXiv:2311.05916.
[196] S. Thoudam, Origin of the break in the cosmic-ray electron plus positron spectrum at ~ 1 TeV, A&A 690 (2024) A351. doi:10.1051/0004-6361/202348607. arXiv:2409.05509.
[197] D. Droz, et al. (DAMPE collaboration), A neural network classifier for electron identification on the DAMPE experiment, JINST 16 (2021) P07036. doi:10.1088/1748-0221/16/07/P07036. arXiv:2102.05534.
[198] J. S. George, et al. (ACE-CRIS), Elemental Composition and Energy Spectra of Galactic Cosmic Rays During Solar Cycle 23, ApJ 698 (2009) 1666–1681. doi:10.1088/0004-637X/698/2/1666.
[199] K. A. Lave, et al. (ACE-CRIS), Galactic Cosmic-Ray Energy Spectra and Composition during the 2009-2010 Solar Minimum Period, ApJ 770 (2013) 117. doi:10.1088/0004-637X/770/2/117.
[200] M. Aguilar, et al. (AMS collaboration), Properties of Heavy Secondary Fluorine Cosmic Rays: Results from the Alpha Magnetic Spectrometer, Phys. Rev. Lett. 126 (2021) 081102. doi:10.1103/PhysRevLett.126.081102.
[201] M. Aguilar, et al. (AMS collaboration), Properties of a New Group of Cosmic Nuclei: Results from the Alpha Magnetic Spectrometer on Sodium, Aluminum, and Nitrogen, Phys. Rev. Lett. 127 (2021) 021101. doi:10.1103/PhysRevLett.127.021101.
[202] M. Aguilar, et al. (AMS collaboration), Observation of the Identical Rigidity Dependence of He, C, and O Cosmic Rays at High Rigidities by the Alpha Magnetic Spectrometer on the International Space Station, Phys. Rev. Lett. 119 (2017) 251101. doi:10.1103/PhysRevLett.119.251101.
[203] M. Aguilar, et al. (AMS collaboration), Properties of Neon, Magnesium, and Silicon Primary Cosmic Rays Results from the Alpha Magnetic Spectrometer, Phys. Rev. Lett. 124 (2020) 211102. doi:10.1103/PhysRevLett.124.211102.
[204] M. Aguilar, et al. (AMS collaboration), Observation of New Properties of Secondary Cosmic Rays Lithium, Beryllium, and Boron by the Alpha Magnetic Spectrometer on the International Space Station, Phys. Rev. Lett. 120 (2018) 021101. doi:10.1103/PhysRevLett.120.021101.
[205] M. J. Boschini, S. D. Torre, M. Gervasi, D. Grandi, G. Jóhannesson, G. L. Vacca, N. Masi, I. V. Moskalenko, et al., A Hint of a Low-energy Excess in Cosmic-Ray Fluorine, ApJ 925 (2022) 108. doi:10.3847/1538-4357/ac313d.
[206] M.-J. Zhao, X.-J. Bi, K. Fang, Can the production cross-section uncertainties explain the cosmic fluorine anomaly?, Phys. Rev. D 107 (2023) 063020. doi:10.1103/PhysRevD.107.063020. arXiv:2209.03799.
[207] Y. Génolini, D. Maurin, I. V. Moskalenko, M. Unger, Current status and desired precision of the isotopic production cross sections relevant to astrophysics of cosmic rays. II. Fluorine to silicon and updated results for Li, Be, and B, Phys. Rev. C 109 (2024) 064914. doi:10.1103/PhysRevC.109.064914. arXiv:2307.06798.
[208] O. Adriani, et al. (CALET collaboration), Cosmic-Ray Boron Flux Measured from 8.4 GeV/n to 3.8 TeV/n with the Calorimetric Electron Telescope on the International Space Station, Phys. Rev. Lett. 129 (2022) 251103. doi:10.1103/PhysRevLett.129.251103. arXiv:2212.07873.
[209] O. Adriani, et al. (CALET collaboration), Direct Measurement of the Cosmic-Ray Carbon and Oxygen Spectra from 10 GeV/n to 2.2 TeV/n with the Calorimetric Electron Telescope on the International Space Station, Phys. Rev. Lett. 125 (2020) 251102. doi:10.1103/PhysRevLett.125.251102. arXiv:2012.10319.
[210] F. Alemanno, et al. (DAMPE collaboration), Detection of spectral hardenings in cosmic-ray boron-to-carbon and boron-to-oxygen flux ratios with DAMPE, Sci. Bull. 67 (2022) 2162–2166. doi:10.1016/j.scib.2022.10.002. arXiv:2210.08833.
[211] M. Aguilar, et al. (AMS collaboration), Precision Measurement of the Proton Flux in Primary Cosmic Rays from Rigidity 1 GV to 1.8 TV with the Alpha Magnetic Spectrometer on the International Space Station, Phys. Rev. Lett. 114 (2015) 171103. doi:10.1103/PhysRevLett.114.171103.
[212] M. Aguilar, et al. (AMS collaboration), Precision Measurement of the Helium Flux in Primary Cosmic Rays of Rigidities 1.9 GV to 3 TV with the Alpha Magnetic Spectrometer on the International Space Station, Phys. Rev. Lett. 115 (2015) 211101. doi:10.1103/PhysRevLett.115.211101.
[213] O. Adriani, et al. (CALET collaboration), Measurement of the Iron Spectrum in Cosmic Rays from 10 GeV/n to 2.0 TeV/n with the Calorimetric Electron Telescope on the International Space Station, Phys. Rev. Lett. 126 (2021) 241101. doi:10.1103/PhysRevLett.126.241101. arXiv:2106.08036.
[214] O. Adriani, et al. (CALET collaboration), Direct Measurement of the Nickel Spectrum in Cosmic Rays in the Energy Range from 8.8 GeV/n to 240 GeV/n with CALET on the International Space Station, Phys. Rev. Lett. 128 (2022) 131103. doi:10.1103/PhysRevLett.128.131103.

[215] W. R. Binns, R. G. Bose, D. L. Braun, T. J. Brandt, W. M. Daniels, P. F. Dowkontt, S. P. Fitzsimmons, D. J. Hahne, et al., The SUPERTIGER Instrument: Measurement of Elemental Abundances of Ultra-Heavy Galactic Cosmic Rays, ApJ 788 (2014) 18. doi:10.1088/0004-637X/788/1/18.
[216] P. H. Fowler, R. N. F. Walker, M. R. W. Masheder, R. T. Moses, A. Worley, Ultra-heavy cosmic ray studies with Ariel VI, Nature 291 (1981) 45–47. doi:10.1038/291045a0.
[217] W. R. Binns, et al. (ACE-CRIS), The Isotopic Abundances of Galactic Cosmic Rays with Atomic Number $29 \leq Z \leq 38$, ApJ 936 (2022) 13. doi:10.3847/1538-4357/ac82e7.
[218] N. E. Walsh, Y. Akaike, W. R. Binns, R. G. Bose, T. J. Brandt, D. L. Braun, N. W. Cannady, P. F. Dowkontt, et al., SuperTIGER instrument abundances of galactic cosmic rays for the charge interval $41 \leq Z \leq 56$, Adv. Space Res. 70 (2022) 2666–2673. doi:10.1016/j.asr.2022.04.063.
[219] W. R. Binns, T. L. Garrard, P. S. Gibner, M. H. Israel, M. P. Kertzman, J. Klarmann, B. J. Newport, E. C. Stone, et al., Abundances of Ultraheavy Elements in the Cosmic Radiation: Results from HEAO 3, ApJ 346 (1989) 997. doi:10.1086/168082.
[220] E. K. Shirk, P. B. Price, Charge and energy spectra of cosmic rays with $Z > 60$: the Skylab experiment., ApJ 220 (1978) 719–733. doi:10.1086/155955.
[221] A. J. Westphal, P. B. Price, B. A. Weaver, V. G. Afanasiev, Evidence against stellar chromospheric origin of Galactic cosmic rays, Nature 396 (1998) 50–52. doi:10.1038/23887.
[222] A. B. Alexandrov, A. V. Bagulya, P. A. Babaev, M. M. Chernyavsky, A. A. Gippius, S. A. Gorbunov, V. M. Grachev, G. V. Kalinina, et al., Insight into History of GCR Heavy Nuclei Fluxes by Their Tracks in Meteorites, Physics of Atomic Nuclei 85 (2022) 446–458. doi:10.1134/S1063778822050039.
[223] O. Adriani, et al. (PAMELA collaboration), Measurements of Cosmic-Ray Hydrogen and Helium Isotopes with the PAMELA Experiment, ApJ 818 (2016) 68. doi:10.3847/0004-637X/818/1/68. arXiv:1512.06535.
[224] W. Menn, et al. (PAMELA collaboration), Lithium and Beryllium Isotopes with the PAMELA Experiment, ApJ 862 (2018) 141. doi:10.3847/1538-4357/aacf89. arXiv:1806.10948.
[225] F. Nozzoli, C. Cernetti, Beryllium Radioactive Isotopes as a Probe to Measure the Residence Time of Cosmic Rays in the Galaxy and Halo Thickness: A "Data-Driven" Approach, Universe 7 (2021) 183. doi:10.3390/universe7060183.
[226] E. A. Bogomolov, et al. (PAMELA collaboration), Lithium and Beryllium Isotopes in the PAMELA Experiment, Bull. Russ. Acad. Sci. Phys 87 (2023) 863–866. doi:10.3103/S1062873823702374.
[227] E. A. Bogomolov, G. I. Vasilyev, W. Menn, O. Adriani, G. A. Bazilevskaya, G. C. Barbarino, R. Bellotti, M. Boezio, et al., Boron Isotopes in the PAMELA Experiment, Physics of Atomic Nuclei 87 (2024) 71–76. doi:10.1134/S1063778824020108.
[228] S. Gabici, Cosmic-Ray Physics (Direct, CRD): Rapporteur Talk, in: 38th ICRC, 2024, p. 30. doi:10.22323/1.444.0030.
[229] N. E. Yanasak, M. E. Wiedenbeck, R. A. Mewaldt, A. J. Davis, A. C. Cummings, J. S. George, R. A. Leske, E. C. Stone, et al., Measurement of the Secondary Radionuclides ^{10}Be, ^{26}Al, ^{36}Cl, ^{54}Mn, and ^{14}C and Implications for the Galactic Cosmic-Ray Age, ApJ 563 (2001) 768–792. doi:10.1086/323842.
[230] J. J. Connell, Galactic Cosmic-Ray Confinement Time: Ulysses High Energy Telescope Measurements of the Secondary Radionuclide ^{10}Be, ApJ 501 (1998) L59–L62. doi:10.1086/311437.
[231] A. Lukasiak, Voyager Measurements of the Charge and Isotopic Composition of Cosmic Ray Li, Be and B Nuclei and Implications for Their Production in the Galaxy, in: 26th ICRC, volume 3, 1999, p. 41.
[232] T. Hams, et al. (ISOMAX), Measurement of the Abundance of Radioactive ^{10}Be and Other Light Isotopes in Cosmic Radiation up to 2 GeV/n with the Balloon-borne Instrument ISOMAX, ApJ 611 (2004) 892–905. doi:10.1086/422384.
[233] Maurin, D., Ferronato Bueno, E., Derome, L., A simple determination of the halo size from ^{10}Be/^{9}Be data, A&A 667 (2022) A25. doi:10.1051/0004-6361/202243546.
[234] M. E. Wiedenbeck, The abundance of the radioactive isotope ^{26}Al in galactic cosmic rays., in: 17th ICRC, volume 9, 1983, pp. 147–150.
[235] A. Lukasiak, F. B. McDonald, W. R. Webber, Voyager Measurements of the Isotopic Composition of Cosmic-Ray Aluminum and Implications for the Propagation of Cosmic Rays, ApJ 430 (1994) L69. doi:10.1086/187440.
[236] J. A. Simpson, J. J. Connell, Cosmic-Ray ^{26}Al and Its Decay in the Galaxy, ApJ 497 (1998) L85–L88. doi:10.1086/311290.
[237] M. E. Wiedenbeck, The Isotopic Composition of Cosmic Ray Chlorine, in: F. C. Jones (Ed.), 19th ICRC, volume 2, 1985, p. 84.
[238] J. J. Connell, M. A. DuVernois, J. A. Simpson, The Cosmic-Ray Radioactive Nuclide ^{36}Cl and Its Propagation in the Galaxy, ApJ 509 (1998) L97–L100. doi:10.1086/311773.
[239] M. E. Wiedenbeck, R. A. Leske, The isotopic composition of iron-group galactic cosmic rays., Adv. in Space Res. 15 (1995) 25. doi:10.1016/S0273-1177(99)80120-3.
[240] A. Hesse, B. S. Acharya, U. Heinbach, W. Heinrich, M. Henkel, B. Luzietti, M. Simon, E. R. Christian, et al., Isotopic composition of silicon and iron in the galactic cosmic radiation., A&A 314 (1996) 785–794. URL: https://ui.adsabs.harvard.edu/abs/1996A&A...314..785H.
[241] A. J. Westphal, V. G. Afanasyev, P. B. Price, M. Solarz, V. V. Akimov, V. G. Rodin, N. I. Shvets, Measurement of the Isotopic Composition of Manganese, Iron, and Nickel in the Galactic Cosmic Rays, ApJ 468 (1996) 679. doi:10.1086/177725.
[242] M. A. DuVernois, Galactic Cosmic-Ray Manganese: Ulysses High Energy Telescope Results, ApJ 481 (1997) 241–252. doi:10.1086/304032.
[243] A. Lukasiak, F. B. McDonald, W. R. Webber, Voyager Measurements of the Mass Composition of Cosmic-Ray Ca through Fe Nuclei, ApJ 488 (1997) 454–461. doi:10.1086/304677.
[244] R. A. Leske, The Elemental and Isotopic Composition of Galactic Cosmic-Ray Nuclei from Scandium through Nickel, ApJ 405 (1993) 567. doi:10.1086/172388.

[245] J. J. Connell, J. A. Simpson, Isotopic Abundances of Fe and Ni in Galactic Cosmic-Ray Sources, ApJ 475 (1997) L61–L64. doi:10.1086/310452.
[246] M. E. Wiedenbeck, W. R. Binns, E. R. Christian, A. C. Cummings, B. L. Dougherty, P. L. Hink, J. Klarmann, R. A. Leske, et al., Constraints on the Time Delay between Nucleosynthesis and Cosmic-Ray Acceleration from Observations of ^{59}Ni and ^{59}Co, ApJ 523 (1999) L61–L64. doi:10.1086/312242.
[247] W. R. Binns, et al. (ACE-CRIS), Observation of the ^{60}Fe nucleosynthesis-clock isotope in galactic cosmic rays, Science 352 (2016) 677–680. doi:10.1126/science.aad6004.
[248] J. J. Connell, J. A. Simpson, Ulysses HET Measurements of Electron-capture Secondary Isotopes: Testing the Role of Cosmic Ray Reacceleration, in: D. Kieda, M. Salamon, B. Dingus (Eds.), 26th ICRC, volume 3, 1999, p. 33.
[249] R. A. Mewaldt, J. D. Spalding, E. C. Stone, R. E. Vogt, High resolution measurements of galactic cosmic-ray neon, magnesium, and silicon isotopes, ApJ 235 (1980) L95–L99. doi:10.1086/183166.
[250] M. E. Wiedenbeck, D. E. Greiner, Isotopic Anomalies in the Galactic Cosmic-Ray Source, Phys. Rev. Lett. 46 (1981) 682–685. doi:10.1103/PhysRevLett.46.682.
[251] P. Ferrando, J. J. Engelmann, P. Goret, L. Koch-Miramond, N. Petrou, Measurement of the isotopic composition of cosmic-rays at 3 GeV/n using a new geomagnetic method, A&A 193 (1988) 69–80. URL: https://ui.adsabs.harvard.edu/abs/1988A&A...193...69F.
[252] M. A. Duvernois, M. Garcia-Munoz, K. R. Pyle, J. A. Simpson, M. R. Thayer, The Isotopic Composition of Galactic Cosmic-Ray Elements from Carbon to Silicon: The Combined Release and Radiation Effects Satellite Investigation, ApJ 466 (1996) 457. doi:10.1086/177524.
[253] J. Connell, High Resolution Measurements of the Isotopic Composition of Galactic Cosmic Ray C, N, O, Ne, Mg and Si from the Ulysses HET, in: 25th ICRC, volume 3, 1997, p. 381.
[254] W. R. Webber, A. Lukasiak, F. B. McDonald, Voyager Measurements of the Mass Composition of Cosmic-Ray Ne, Mg, Si and S Nuclei, ApJ 476 (1997) 766–770. doi:10.1086/303662.
[255] W. R. Binns, et al. (ACE-CRIS), Cosmic-Ray Neon, Wolf-Rayet Stars, and the Superbubble Origin of Galactic Cosmic Rays, ApJ 634 (2005) 351–364. doi:10.1086/496959. arXiv:astro-ph/0508398.
[256] M. E. Wiedenbeck, W. R. Binns, E. R. Christian, A. C. Cummings, A. J. Davis, J. S. George, P. L. Hink, M. H. Israel, et al., The isotopic source composition of cosmic-ray iron, cobalt, and nickel, Adv. in Space Res. 27 (2001) 773–778. doi:10.1016/S0273-1177(01)00120-X.
[257] M. E. Hill, R. C. Allen, P. C. Brandt, R. B. Decker, M. Gkioulidou, S. M. Krimigis, P. Kollmann, R. L. McNutt, Jr., P. Mostafavi, R. Nikoukar, et al., Cosmic Rays Measurements on an Interstellar Probe: A Bold Approach to Concluding the Second Century of Space Aged Science, in: Bulletin of the American Astronomical Society, volume 55, 2023, p. 169. doi:10.3847/25c2cfeb.d16c0c2f.
[258] T. Aramaki, et al. (GAPS collaboration), Antideuteron sensitivity for the GAPS experiment, Astropart. Phys. 74 (2016) 6–13. doi:10.1016/j.astropartphys.2015.09.001.
[259] N. Saffold, et al. (GAPS collaboration), Cosmic antihelium-3 nuclei sensitivity of the GAPS experiment, Astropart. Phys. 130 (2021) 102580. doi:10.1016/j.astropartphys.2021.102580. arXiv:2012.05834.
[260] T. Aramaki, P. Hansson Adrian, G. Karagiorgi, H. Odaka, Dual MeV Gamma-Ray and Dark Matter Observatory - GRAMS Project, Astropart. Phys. 114 (2020) 107–114. doi:10.1016/j.astropartphys.2019.07.002. arXiv:1901.03430.
[261] M. Iwasaki, S. N. Nakamura, K. Shigaki, Y. Shimizu, H. Tamura, T. Ishikawa, R. S. Hayano, E. Takada, et al., Discovery of antiproton trapping by long-lived metastable states in liquid helium, Phys. Rev. Lett. 67 (1991) 1246–1249. doi:10.1103/PhysRevLett.67.1246.
[262] S. N. Nakamura, M. Iwasaki, H. Outa, R. S. Hayano, Y. Watanabe, T. Nagae, T. Yamazaki, H. Tada, et al., Negative-pion trapping by a metastable state in liquid helium, Phys. Rev. A 45 (1992) 6202–6208. doi:10.1103/PhysRevA.45.6202.
[263] T. Yamazaki, M. Aoki, M. Iwasaki, R. S. Hayano, T. Ishikawa, H. Outa, E. Takada, H. Tamura, et al., Trapping of negative kaons by metastable states during the atomic cascade in liquid helium, Phys. Rev. Lett. 63 (1989) 1590–1592. doi:10.1103/PhysRevLett.63.1590.
[264] G. T. Condo, On the absorption of negative pions by liquid helium, Phys. Letters 9 (1964) 65–66. doi:10.1016/0031-9163(64)90216-1.
[265] J. E. Russell, Metastable States of $\alpha\pi^-e^-$, αK^-e^-, and $\alpha\bar{p}e^-$ Atoms, Phys. Rev. Lett. 23 (1969) 63–64. doi:10.1103/PhysRevLett.23.63.
[266] J. E. Russell, Interactions of an αK^-e^- Atom with a He Atom, Phys. Rev. 188 (1969) 187–197. doi:10.1103/PhysRev.188.187.
[267] D. E. Wright, J. E. Russell, Energies of Highly Excited Heliumlike Exotic Atoms, Phys. Rev. A 6 (1972) 2488–2492. doi:10.1103/PhysRevA.6.2488.
[268] E. Widmann, I. Sugai, T. Yamazaki, R. S. Hayano, M. Iwasaki, S. N. Nakamura, H. Tamura, T. M. Ito, et al., Phase and density dependence of the delayed annihilation of metastable antiprotonic helium atoms in gas, liquid, and solid helium, Phys. Rev. A 51 (1995) 2870–2880. doi:10.1103/PhysRevA.51.2870.
[269] F. Nozzoli, I. Rashevskaya, L. Ricci, F. Rossi, P. Spinnato, E. Verroi, P. Zuccon, G. Giovanazzi, Antideuteron Identification in Space with Helium Calorimeter, Instruments 8 (2024). doi:10.3390/instruments8010003.
[270] B. F. Rauch, W. V. Zober, R. F. Borda, R. G. Bose, D. L. Braun, J. Buckley, J. Calderon, N. W. Cannady, et al., The Trans-Iron Galactic Element Recorder for the International Space Station (TIGERISS), in: 38th ICRC, 2024, p. 171. doi:10.22323/1.444.0171.
[271] M. Sasaki, Overview and preliminary results of the SuperTIGER-2 flight, in: 43rd COSPAR Scientific Assembly. Held 28 January - 4 February, volume 43, 2021, p. 1335.
[272] B. Rauch, N. Walsh, W. Zober, Q. Abarr, Y. Akaike, W. Binns, T. Brandt, J. Buckley, et al., SuperTIGER Instrument

and Galactic Cosmic Ray Abundances from $_{10}$Ne to $_{56}$Ba, in: AAS/High Energy Astrophysics Division, volume 20 of *AAS/High Energy Astrophysics Division*, 2023, p. 303.05.

[273] V. Bulatov, et al. (NUCLEON-2 collaboration), NUCLEON-2 mission for the investigation of isotope and charge composition of cosmic ray ions, Advances in Space Research 64 (2019) 2610–2618. doi:10.1016/j.asr.2019.08.031.

[274] O. Vasiliev, et al. (NUCLEON-2 collaboration), Current Status of the NUCLEON-2 Mission, Phys. Part. Nucl. Lett. 18 (2021) 36–51. doi:10.1134/S154747712101012X.

[275] O. A. Vasil'ev, et al., Detector Part of the Station for the Research and Irradiation of Promising Products of Semiconductor Micro- and Nanoelectronics with High-Energy Ion Beams, Phys. Part. Nucl. Lett. 18 (2021) 217–221. doi:10.1134/S1547477121020205.

[276] A. Kurganov, et al., Fragmentation of Cosmic Ray Nuclei and Its Experimental Study, Phys. Part. Nucl. Lett. 20 (2023) 637–649. doi:10.1134/S1547477123040453.

[277] A. V. Butenko, et al., Status of NICA Complex, Phys. Part. Nucl. Lett. 21 (2024) 212–217. doi:10.1134/S154747712470002X.

[278] D. Kyratzis (HERD collaboration), Overview of the HERD space mission, Phys. Scr 97 (2022) 054010. doi:10.1088/1402-4896/ac63fc.

[279] O. Adriani, A. Agnesi, S. Albergo, M. Antonelli, L. Auditore, A. Basti, P. Betti, E. Berti, G. Bigongiari, L. Bonechi, et al., The CaloCube calorimeter for high-energy cosmic-ray measurements in space: Response of a large-scale prototype to protons, Nuclear Instruments and Methods in Physics Research A 1061 (2024) 169079. doi:10.1016/j.nima.2024.169079.

[280] D. Karmanov, A. Panov, D. Podorozhny, L. Tkachev, A. Turundaevskiy, The HERO (High Energy Ray Observatory) detector current status, Advances in Space Research 64 (2019) 2619–2626. doi:10.1016/j.asr.2019.04.025.

[281] D. M. Podorozhny, D. E. Karmanov, I. M. Kovalev, A. A. Kurganov, A. D. Panov, A. N. Turundaevsky, The HERO Project (High Energy Cosmic Ray Observatory): Objectives and Design Layout, Physics of Atomic Nuclei 87 (2024) 151–159. doi:10.1134/S1063778824700091.

[282] A. Kurganov, D. Karmanov, A. Panov, D. Podorozhny, L. Tkachev, A. Turundaevsky, HERO (High Energy Ray Observatory) optimization and current status, arXiv e-prints (2023) arXiv:2306.13406. doi:10.48550/arXiv.2306.13406. arXiv:2306.13406.

[283] R. Battiston, B. Bertucci, O. Adriani, G. Ambrosi, B. Baudouy, P. Blasi, M. Boezio, D. Campana, et al., High precision particle astrophysics as a new window on the universe with an Antimatter Large Acceptance Detector In Orbit (ALADInO), Exp. Astron. 51 (2021) 1299–1330. doi:10.1007/s10686-021-09708-w.

[284] O. Adriani, et al. (ALADInO collaboration), Design of an Antimatter Large Acceptance Detector In Orbit (ALADInO), Instruments 6 (2022) 19. doi:10.3390/instruments6020019.

[285] S. Schael, et al., AMS-100: The next generation magnetic spectrometer in space – An international science platform for physics and astrophysics at Lagrange point 2, Nucl. Instr. Meth. Phys. Res. A 944 (2019) 162561. doi:10.1016/j.nima.2019.162561. arXiv:1907.04168.

[286] A. W. Strong, I. V. Moskalenko, V. S. Ptuskin, Cosmic-ray propagation and interactions in the Galaxy, Ann. Rev. Nucl. Part. Sci. 57 (2007) 285–327. doi:10.1146/annurev.nucl.57.090506.123011. arXiv:astro-ph/0701517.

[287] P. D. Serpico, Cosmic ray interactions with matter and radiation, Proc. Int. Sch. Phys. Fermi 208 (2024) 1–40. doi:10.3254/ENFI240002. arXiv:2308.04361.

[288] G. M. Raisbeck, Nuclear Interactions during Cosmic Ray Propagation and their Implications, in: 16th ICRC, volume 14, 1979, p. 146.

[289] Y. Génolini, D. Maurin, I. V. Moskalenko, M. Unger, Current status and desired precision of the isotopic production cross sections relevant to astrophysics of cosmic rays: Li, Be, B, C, and N, Phys. Rev. C 98 (2018) 034611. doi:10.1103/PhysRevC.98.034611. arXiv:1803.04686.

[290] P. Ferrando, W. R. Webber, P. Goret, J. C. Kish, D. A. Schrier, A. Soutoul, O. Testard, Measurement of ^{12}C, ^{16}O, and ^{56}Fe charge changing cross sections in helium at high energy, comparison with cross sections in hydrogen, and application to cosmic-ray propagation, Phys. Rev. C 37 (1988) 1490–1501. doi:10.1103/PhysRevC.37.1490.

[291] W. R. Webber, D. A. Brautigam, Fragmentation of ^{56}Fe nuclei on CH2, carbon, and hydrogen targets - Individual charge changing and total cross sections, ApJ 260 (1982) 894–908. doi:10.1086/160308.

[292] W. R. Webber, J. C. Kish, D. A. Schrier, Total charge and mass changing cross sections of relativistic nuclei in hydrogen, helium, and carbon targets, Phys. Rev. C 41 (1990) 520–532. doi:10.1103/PhysRevC.41.520.

[293] W. R. Webber, J. C. Kish, D. A. Schrier, Individual charge changing fragmentation cross sections of relativistic nuclei in hydrogen, helium, and carbon targets, Phys. Rev. C 41 (1990) 533–546. doi:10.1103/PhysRevC.41.533.

[294] G. T. Guzik, C.-X. Chen, et al. (Transport collaboration), A Program for the Systematic Interpretation of Cosmic Ray Data, in: 21st ICRC, volume 3, 1990, p. 428.

[295] W. R. Webber, J. C. Kish, D. A. Schrier, Individual isotopic fragmentation cross sections of relativistic nuclei in hydrogen, helium, and carbon targets, Phys. Rev. C 41 (1990) 547–565. doi:10.1103/PhysRevC.41.547.

[296] W. R. Webber, J. C. Kish, D. A. Schrier, Formula for calculating partial cross sections for nuclear reactions of nuclei with E > 200 MeV/nucleon in hydrogen targets, Phys. Rev. C 41 (1990) 566–571. doi:10.1103/PhysRevC.41.566.

[297] C. N. Knott, S. Albergo, et al. (Transport collaboration), Interactions of relativistic neon to nickel projectiles in hydrogen, elemental production cross sections, Phys. Rev. C 53 (1996) 347–357. doi:10.1103/PhysRevC.53.347.

[298] C.-X. Chen, S. Albergo, et al. (Transport collaboration), Relativistic Interaction of ^{22}Ne and ^{26}Mg in Hydrogen and the Cosmic-Ray Implications, ApJ 479 (1997) 504–521. doi:10.1086/303881.

[299] C. N. Knott, S. Albergo, et al. (Transport collaboration), Interactions of relativistic ^{36}Ar and ^{40}Ar nuclei in hydrogen: Isotopic production cross sections, Phys. Rev. C 56 (1997) 398–406. doi:10.1103/PhysRevC.56.398.

[300] C.-X. Chen, S. Albergo, et al. (Transport collaboration), Systematics of isotopic production cross sections from interac-

tions of relativistic ^{40}Ca in hydrogen, Phys. Rev. C 56 (1997) 1536–1543. doi:10.1103/PhysRevC.56.1536.

[301] W. R. Webber, A. Soutoul, J. C. Kish, J. M. Rockstroh, Y. Cassagnou, R. Legrain, O. Testard, Measurement of charge changing and isotopic cross sections at ~600 MeV/nucleon from the interactions of ~30 separate beams of relativistic nuclei from ^{10}B to ^{55}Mn in a liquid hydrogen target, Phys. Rev. C 58 (1998) 3539–3552. doi:10.1103/PhysRevC.58.3539.

[302] W. R. Webber, J. C. Kish, J. M. Rockstroh, Y. Cassagnou, R. Legrain, A. Soutoul, O. Testard, C. Tull, Production Cross Sections of Fragments from Beams of 400-650 MeV per Nucleon ^{9}Be, ^{11}B, ^{12}C, ^{14}N, ^{15}N, ^{16}O, ^{20}Ne, ^{22}Ne, ^{56}Fe, and ^{58}Ni Nuclei Interacting in a Liquid Hydrogen Target. I. Charge Changing and Total Cross Sections, ApJ 508 (1998) 940–948. doi:10.1086/306445.

[303] W. R. Webber, J. C. Kish, J. M. Rockstroh, Y. Cassagnou, R. Legrain, A. Soutoul, O. Testard, C. Tull, Production Cross Sections of Fragments from Beams of 400-650 MeV per Nucleon ^{9}Be, ^{11}B, ^{12}C, ^{14}N, ^{15}N, ^{16}O, ^{20}Ne, ^{22}Ne, ^{56}Fe, and ^{58}Ni Nuclei Interacting in a Liquid Hydrogen Target. II. Isotopic Cross Sections of Fragments, ApJ 508 (1998) 949–958. doi:10.1086/306446.

[304] C. Zeitlin, L. Heilbronn, J. Miller, A. Fukumura, Y. Iwata, T. Murakami, J. MacGibbon, L. Pinsky, et al., Nuclear fragmentation cross sections for NASA database development, in: E. Norman, L. Schroeder, G. Wozniak (Eds.), Nuclear Physics in the 21st Century, volume 610 of *Am. Inst. Phys. Conf. Series*, 2002, pp. 285–289. doi:10.1063/1.1469936.

[305] F. A. Cucinotta, W. Schimmerling, J. W. Wilson, L. E. Peterson, P. B. Saganti, J. F. Dicello, Uncertainties in estimates of the risks of late effects from space radiation, Adv. in Space Res. 34 (2004) 1383–1389. doi:10.1016/j.asr.2003.10.053.

[306] C. Zeitlin, L. Heilbronn, J. Miller, S. E. Rademacher, T. Borak, T. R. Carter, K. A. Frankel, W. Schimmerling, et al., Heavy fragment production cross sections from 1.05 GeV/nucleon ^{56}Fe in C, Al, Cu, Pb, and CH_2 targets, Phys. Rev. C 56 (1997) 388–397. doi:10.1103/PhysRevC.56.388.

[307] C. Zeitlin, A. Fukumura, L. Heilbronn, Y. Iwata, J. Miller, T. Murakami, Fragmentation cross sections of 600 MeV/nucleon ^{20}Ne on elemental targets, Phys. Rev. C 64 (2001) 024902. doi:10.1103/PhysRevC.64.024902.

[308] C. Zeitlin, S. Guetersloh, L. Heilbronn, J. Miller, A. Fukumura, Y. Iwata, T. Murakami, Fragmentation cross sections of 290 and 400 MeV/nucleon ^{12}C beams on elemental targets, Phys. Rev. C 76 (2007) 014911. doi:10.1103/PhysRevC.76.014911.

[309] C. Zeitlin, S. Guetersloh, L. Heilbronn, J. Miller, A. Fukumura, Y. Iwata, T. Murakami, L. Sihver, et al., Fragmentation cross sections of medium-energy ^{35}Cl, ^{40}Ar, and ^{48}Ti beams on elemental targets, Phys. Rev. C 77 (2008) 034605. doi:10.1103/PhysRevC.77.034605.

[310] C. Zeitlin, J. Miller, S. Guetersloh, L. Heilbronn, A. Fukumura, Y. Iwata, T. Murakami, S. Blattnig, et al., Fragmentation of ^{14}N, ^{16}O, ^{20}Ne, and ^{24}Mg nuclei at 290 to 1000 MeV/nucleon, Phys. Rev. C 83 (2011) 034909. doi:10.1103/PhysRevC.83.034909. arXiv:1102.2848.

[311] J. M. Sisterson, Status of Production Cross Section Measurements Needed for Cosmic Ray Studies, in: Lunar and Planetary Science Conference, volume 29, 1998.

[312] R. C. Reedy, Cosmogenic-nuclide production rates: Reaction cross section update, Nucl. Instr. Meth. Phys. Res. B 294 (2013) 470–474. doi:10.1016/j.nimb.2011.08.034.

[313] R. Michel, B. Dittrich, U. Herpers, F. Peiffer, T. Schiffmann, P. Cloth, P. Dragovitsch, D. Filges, Proton-induced spallation at 600 MeV, The Analyst 114 (1989) 287. doi:10.1039/an9891400287.

[314] B. Dittrich, U. Herpers, H. J. Hofmann, W. Wölfli, R. Bodemann, M. Lüpke, R. Michel, P. Dragovitsch, et al., AMS measurements of thin-target cross sections for the production of ^{10}Be and ^{26}Al by high-energy protons, Nucl. Instr. Meth. Phys. Res. B 52 (1990) 588–594. doi:10.1016/0168-583X(90)90481-9.

[315] R. Bodemann, H.-J. Lange, I. Leya, R. Michel, T. Schiekel, R. Rösel, U. Herpers, H. J. Hofmann, et al., Production of residual nuclei by proton-induced reactions on C, N, O, Mg, AI and Si, Nucl. Instr. Meth. Phys. Res. B 82 (1993) 9–31. doi:10.1016/0168-583X(93)95077-I.

[316] R. Michel, M. Gloris, H.-J. Lange, I. Leya, M. Lüpke, U. Herpers, B. Dittrich-Hannen, R. Rösel, et al., Nuclide production by proton-induced reactions on elements ($6 \leq Z \leq 29$) in the energy range from 800 to 2600 MeV, Nucl. Instr. Meth. Phys. Res. B 103 (1995) 183–222. doi:10.1016/0168-583X(95)00566-8.

[317] T. Schiekel, F. Sudbrock, U. Herpers, M. Gloris, H.-J. Lange, I. Leya, R. Michel, B. Dittrich-Hannen, et al., Nuclide production by proton-induced reactions on elements ($6 \leq Z \leq 29$) in the energy range from 200 MeV to 400 MeV, Nucl. Instr. Meth. Phys. Res. B 114 (1996) 91–119. doi:10.1016/0168-583X(96)00145-0.

[318] R. Michel, R. Bodemann, H. Busemann, R. Daunke, M. Gloris, H.-J. Lange, B. Klug, A. Krins, et al., Cross sections for the production of residual nuclides by low- and medium-energy protons from the target elements C, N, O, Mg, Al, Si, Ca, Ti, V, Mn, Fe, Co, Ni, Cu, Sr, Y, Zr, Nb, Ba and Au, Nucl. Instr. Meth. Phys. Res. B 129 (1997) 153–193. doi:10.1016/S0168-583X(97)00213-9.

[319] I. Leya, H. Busemann, H. Baur, R. Wieler, M. Gloris, S. Neumann, R. Michel, F. Sudbrock, et al., Cross sections for the proton-induced production of He and Ne isotopes from magnesium, aluminum, and silicon, Nucl. Instr. Meth. Phys. Res. B 145 (1998) 449–458. doi:10.1016/S0168-583X(98)00528-X.

[320] I. Leya, R. Wieler, J.-C. David, S. Leray, L. Donadille, J. Cugnon, R. Michel, Production of noble gas isotopes by proton-induced reactions on lead, Nucl. Instr. Meth. Phys. Res. B 229 (2005) 1–23. doi:10.1016/j.nimb.2004.11.009.

[321] I. Leya, R. Wieler, J.-C. David, S. Leray, L. Donadille, J. Cugnon, R. Michel, Production of noble gas isotopes by proton-induced reactions on lead and bismuth, Nucl. Instr. Meth. Phys. Res. A 562 (2006) 760–763. doi:10.1016/j.nima.2006.02.049.

[322] K. Ammon, I. Leya, B. Lavielle, E. Gilabert, J.-C. David, U. Herpers, R. Michel, Cross sections for the production of helium, neon and argon isotopes by proton-induced reactions on iron and nickel, Nucl. Instr. Meth. Phys. Res. B 266 (2008) 2–12. doi:10.1016/j.nimb.2007.10.024.

[323] J. M. Sisterson, A. M. Koehler, A. J. T. Jull, D. J. Donahue, L. McHargue, R. C. Reedy, P. A. J. Englert, Cross Section

Measurements for the Production of ^{14}C and ^{10}Be: Improved Estimates for Cosmogenic Nuclide Production Rates, in: Lunar and Planetary Science Conference, volume 23, 1992.

[324] J. M. Sisterson, A. J. T. Jull, A. Beverding, A. M. Koehler, C. Castaneda, J. Vincent, D. J. Donahue, P. A. J. Englert, et al., Proton production cross sections for ^{14}C from silicon and oxygen: implications for cosmic-ray studies, Nucl. Instr. Meth. Phys. Res. B 92 (1994) 510–512. doi:10.1016/0168-583X(94)96064-X.

[325] J. M. Sisterson, K. Kim, A. Beverding, P. A. J. Englert, M. Caffee, A. J. T. Jull, D. J. Donahue, L. McHargue, et al., Measurement of proton production cross sections of ^{10}Be and ^{26}Al from elements found in lunar rocks, Nucl. Instr. Meth. Phys. Res. B 123 (1997) 324–329. doi:10.1016/S0168-583X(96)00409-0.

[326] J. M. Sisterson, M. W. Caffee, Neon Production from Al, Mg, SI and Fe: New Proton Production Cross Section Measurements, in: Lunar and Planetary Science Conference, volume 29, 1998.

[327] J. M. Sisterson, J. Vincent, D. T. L. Jones, P. J. Binns, K. Langen, I. S. Z. Buthelezi, F. D. Brooks, A. Buffler, et al., Production of Short-lived Radionuclides by Protons and Neutrons in Fe and Ni Targets: Cross Sections Needed for Cosmic Ray Studies, in: Lunar and Planetary Science Conference, volume 31, 2000.

[328] K. J. Kim, J. M. Sisterson, P. A. J. Englert, M. W. Caffee, R. C. Reedy, J. Vincent, C. Castaneda, Experimental cross-sections for the production of ^{10}Be from natural carbon targets with 40.6 to 500 MeV protons, Nucl. Instr. Meth. Phys. Res. B 196 (2002) 239–244. doi:10.1016/S0168-583X(02)01297-1.

[329] J. M. Sisterson, J. Vincent, Cross section measurements for proton-induced reactions in Fe and Ni producing relatively short-lived radionuclides at E_p = 140 and 500 MeV, Nucl. Instr. Meth. Phys. Res. B 251 (2006) 1–8. doi:10.1016/j.nimb.2006.05.015.

[330] C. Villagrasa-Canton, A. Boudard, J.-E. Ducret, et al., Spallation residues in the reaction ^{56}Fe+p at 0.3A, 0.5A, 0.75A, 1.0A, and 1.5A GeV, Phys. Rev. C 75 (2007) 044603. doi:10.1103/PhysRevC.75.044603. arXiv:nucl-ex/0612001.

[331] Y. E. Titarenko, V. F. Batyaev, A. Y. Titarenko, M. A. Butko, K. V. Pavlov, S. N. Florya, R. S. Tikhonov, S. G. Mashnik, et al., Cross sections for nuclide production in a ^{56}Fe target irradiated by 300, 500, 750, 1000, 1500, and 2600 MeV protons compared with data on a hydrogen target irradiated by 300, 500, 750, 1000, and 1500 MeV/nucleon ^{56}Fe ions, Phys. Rev. C 78 (2008) 034615. doi:10.1103/PhysRevC.78.034615. arXiv:0804.1260.

[332] G. Rudstam, Systematics of Spallation Yields, Z. Naturforsch. A 21 (1966) 1027–1041. doi:10.1515/zna-1966-0724.

[333] R. Silberberg, C. H. Tsao, Partial Cross-Sections in High-Energy Nuclear Reactions, and Astrophysical Applications. I. Targets With Z $\leq$ 28., ApJS 25 (1973) 315–333. doi:10.1086/190271.

[334] R. Silberberg, C. H. Tsao, Partial Cross-Sections in High-Energy Nuclear Reactions, and Astrophysical Applications. II. Targets Heavier than Nickel, ApJS 25 (1973) 335–367. URL: http://adsabs.harvard.edu/abs/1973ApJS...25..335S.

[335] J. R. Letaw, R. Silberberg, C. H. Tsao, Proton-nucleus total inelastic cross sections – an empirical formula for E greater than 10 MeV, ApJS 51 (1983) 271–275. doi:10.1086/190849.

[336] R. Silberberg, C. H. Tsao, J. R. Letaw, Improved cross section calculations for astrophysical applications, ApJS 58 (1985) 873–881. doi:10.1086/191058.

[337] R. Silberberg, C. H. Tsao, Spallation processes and nuclear interaction products of cosmic rays, Phys. Rep. 191 (1990) 351–408. doi:10.1016/0370-1573(90)90109-F.

[338] L. Sihver, C. H. Tsao, R. Silberberg, T. Kanai, A. F. Barghouty, Total reaction and partial cross section calculations in proton-nucleus ($Z_t \leq 26$) and nucleus-nucleus reactions (Z_p and $Z_t \leq 26$), Phys. Rev. C 47 (1993) 1225–1236. doi:10.1103/PhysRevC.47.1225.

[339] C. H. Tsao, R. Silberberg, A. F. Barghouty, L. Sihver, T. Kanai, Scaling algorithm to calculate heavy-ion spallation cross sections, Phys. Rev. C 47 (1993) 1257–1262. doi:10.1103/PhysRevC.47.1257.

[340] R. Silberberg, C. H. Tsao, A. F. Barghouty, Updated Partial Cross Sections of Proton-Nucleus Reactions, ApJ 501 (1998) 911–919. doi:10.1086/305862.

[341] C. H. Tsao, R. Silberberg, A. F. Barghouty, Partial Cross Sections of Nucleus-Nucleus Reactions, ApJ 501 (1998) 920–926. doi:10.1086/305863.

[342] W. R. Webber, A. Soutoul, J. C. Kish, J. M. Rockstroh, Updated Formula for Calculating Partial Cross Sections for Nuclear Reactions of Nuclei with Z $\leq$ 28 and E $>$ 150 MeV/n in Hydrogen Targets, ApJS 144 (2003) 153–167. doi:10.1086/344051.

[343] F. A. Cucinotta, S. Pak, Isotopic production cross sections in proton-^{16}O and proton-^{12}C interactions for energies from 10 MeV/u to 100 GeV/u, Nucl. Instr. Meth. Phys. Res. B 534 (2023) 26–34. doi:10.1016/j.nimb.2022.11.005. arXiv:2205.00290.

[344] J. C. David, I. Leya, Spallation, cosmic rays, meteorites, and planetology, Prog. Part. Nucl. Phys. 109 (2019) 103711. doi:10.1016/j.ppnp.2019.103711.

[345] H. J. Crawford, J. Engelage, F. C. Jones, T. G. Guzik, J. W. Mitchell, J. P. Wefel, C. J. Waddington, W. R. Webber, et al., A database of fragmentation cross section measurements applicable to cosmic ray propagation calculations, in: 21st ICRC, volume 3, 1990.

[346] T. A. Porter, G. Jóhannesson, I. V. Moskalenko, The GALPROP Cosmic-ray Propagation and Nonthermal Emissions Framework: Release v57, ApJS 262 (2022) 30. doi:10.3847/1538-4365/ac80f6. arXiv:2112.12745.

[347] I. V. Moskalenko, S. G. Mashnik, A. W. Strong, New calculation of radioactive secondaries in cosmic rays, in: 27th ICRC, volume 5, 2001, pp. 1836–1839. doi:https://arxiv.org/abs/astro-ph/0106502.

[348] I. V. Moskalenko, S. G. Mashnik, Evaluation of Production Cross Sections of Li, Be, B in CR, in: 28th ICRC, volume 4, 2003, p. 1969. doi:https://arxiv.org/abs/astro-ph/0306367.

[349] S. G. Mashnik, K. K. Gudima, I. V. Moskalenko, R. E. Prael, A. J. Sierk, CEM2K and LAQGSM codes as event generators for space-radiation-shielding and cosmic-ray-propagation applications, Adv. in Space Res. 34 (2004) 1288–1296. doi:10.1016/j.asr.2003.08.057. arXiv:nucl-th/0210065.

[350] I. V. Moskalenko, A. W. Strong, S. G. Mashnik, Propagation of Cosmic Rays: Nuclear Physics in Cosmic-Ray Studies, in: R. C. Haight, M. B. Chadwick, T. Kawano, P. Talou (Eds.), Int. Conf. on Nucl. Data for Science and Technology, volume 769 of *Am. Inst. Phys. Conf. Series*, 2005, pp. 1612–1617. doi:10.1063/1.1945315. arXiv:astro-ph/0411400.
[351] B. Coste, L. Derome, D. Maurin, A. Putze, Constraining Galactic cosmic-ray parameters with $Z \leq 2$ nuclei, A&A 539 (2012) A88. doi:10.1051/0004-6361/201117927. arXiv:1108.4349.
[352] A. Reinert, M. W. Winkler, A precision search for WIMPs with charged cosmic rays, J. Cosmology Astropart. Phys. 2018 (2018) 055. doi:10.1088/1475-7516/2018/01/055.
[353] C. Evoli, D. Gaggero, A. Vittino, M. Di Mauro, D. Grasso, M. N. Mazziotta, Cosmic-ray propagation with DRAGON2: II. Nuclear interactions with the interstellar gas, J. Cosmology Astropart. Phys. 2018 (2018) 006. doi:10.1088/1475-7516/2018/07/006.
[354] M. M. Block, F. Halzen, Experimental Confirmation that the Proton is Asymptotically a Black Disk, Phys. Rev. Lett. 107 (2011) 212002. doi:10.1103/PhysRevLett.107.212002. arXiv:1109.2041.
[355] M. M. Block, L. Durand, P. Ha, F. Halzen, Comprehensive fits to high energy data for σ, ρ, and B, and the asymptotic black-disk limit, Phys. Rev. D 92 (2015) 114021. doi:10.1103/PhysRevD.92.114021. arXiv:1511.02406.
[356] K. Sümmerer, W. Brüchle, D. J. Morrissey, M. Schädel, B. Szweryn, Y. Weifan, Target fragmentation of Au and Th by 2.6 GeV protons, Phys. Rev. C 42 (1990) 2546–2561. doi:10.1103/PhysRevC.42.2546.
[357] K. Sümmerer, B. Blank, Modified empirical parametrization of fragmentation cross sections, Phys. Rev. C 61 (2000) 034607. doi:10.1103/PhysRevC.61.034607. arXiv:nucl-ex/9911006.
[358] K. Sümmerer, Improved empirical parametrization of fragmentation cross sections, Phys. Rev. C 86 (2012) 014601. doi:10.1103/PhysRevC.86.014601. arXiv:1205.5436.
[359] C. Schmitt, K.-H. Schmidt, A. Kelić-Heil, SPACS: A semi-empirical parameterization for isotopic spallation cross sections, Phys. Rev. C 90 (2014) 064605. doi:10.1103/PhysRevC.90.064605.
[360] C. Schmitt, K.-H. Schmidt, A. Kelić-Heil, Erratum: SPACS: A semi-empirical parameterization for isotopic spallation cross sections [Phys. Rev. C 90, 064605 (2014)], Phys. Rev. C 94 (2016) 039901. doi:10.1103/PhysRevC.94.039901.
[361] B. Mei, Improved empirical parameterization for projectile fragmentation cross sections, Phys. Rev. C 95 (2017) 034608. doi:10.1103/PhysRevC.95.034608.
[362] J. W. Wilson, L. W. Townsend, F. F. Badavi, A semiempirical nuclear fragmentation model, Nucl. Instr. Meth. Phys. Res. B 18 (1986) 225–231. doi:10.1016/S0168-583X(86)80035-0.
[363] F. F. Badavi, L. W. Townsend, J. W. Wilson, J. W. Norbury, An algorithm for a semiempirical nuclear fragmentation model, Comput. Phys. Commun. 47 (1987) 281–294. doi:10.1016/0010-4655(87)90114-7.
[364] J. W. Wilson, J. L. Shinn, L. W. Townsend, R. K. Tripathi, F. F. Badavi, S. Y. Chun, NUCFRG2: A semiempirical nuclear fragmentation model, Nucl. Instr. Meth. Phys. Res. B 94 (1994) 95–102. doi:10.1016/0168-583X(94)95662-6.
[365] A. M. Adamczyk, R. B. Norman, S. I. Sriprisan, L. W. Townsend, J. W. Norbury, S. R. Blattnig, T. C. Slaba, NUCFRG3: Light ion improvements to the nuclear fragmentation model, Nucl. Instr. Meth. Phys. Res. A 678 (2012) 21–32. doi:10.1016/j.nima.2012.02.021.
[366] A. Koning, S. Hilaire, S. Goriely, TALYS: modeling of nuclear reactions, Eur. Phys. J. A 59 (2023) 131. doi:10.1140/epja/s10050-023-01034-3, [Erratum: Eur.Phys.J.A 59, 146 (2023)].
[367] G. Battistoni, F. Broggi, M. Brugger, others, M. Campanella, M. Carboni, A. Empl, A. Fassò, et al., Applications of FLUKA Monte Carlo code for nuclear and accelerator physics, Nucl. Instr. Meth. Phys. Res. B 269 (2011) 2850–2856. doi:10.1016/j.nimb.2011.04.028.
[368] S. G. Mashnik, Validation and verification of MCNP6 against intermediate and high-energy experimental data and results by other codes, Eur. Phys. J. Plus 126 (2011) 49. doi:10.1140/epjp/i2011-11049-1. arXiv:1011.4978.
[369] S. G. Mashnik, L. M. Kerby, MCNP6 fragmentation of light nuclei at intermediate energies, Nucl. Instr. Meth. Phys. Res. A 764 (2014) 59–81. doi:10.1016/j.nima.2014.07.016. arXiv:1404.7820.
[370] L. M. Kerby, S. G. Mashnik, Total reaction cross sections in CEM and MCNP6 at intermediate energies, Nucl. Instr. Meth. Phys. Res. B 356 (2015) 135–145. doi:10.1016/j.nimb.2015.04.057. arXiv:1505.00842.
[371] K. Niita, S. Chiba, T. Maruyama, T. Maruyama, H. Takada, T. Fukahori, Y. Nakahara, A. Iwamoto, Analysis of the (N,xN') reactions by quantum molecular dynamics plus statistical decay model, Phys. Rev. C 52 (1995) 2620–2635. doi:10.1103/PhysRevC.52.2620. arXiv:nucl-th/9508004.
[372] L. Sihver, T. Sato, K. Gustafsson, D. Mancusi, H. Iwase, K. Niita, H. Nakashima, Y. Sakamoto, et al., An update about recent developments of the PHITS code, Adv. in Space Res. 45 (2010) 892–899. doi:10.1016/j.asr.2010.01.002.
[373] L. Sihver, O. Ploc, T. Sato, K. Niita, S. Hashimoto, S. El-Jaby, The PHITS code for space applications: status and recent developments, in: 40th COSPAR Scientific Assembly, volume 40, 2014.
[374] M. Hultqvist, M. Lazzeroni, A. Botvina, I. Gudowska, N. Sobolevsky, A. Brahme, Evaluation of nuclear reaction cross-sections and fragment yields in carbon beams using the SHIELD-HIT Monte Carlo code. Comparison with experiments, Phys. Med. Biol. 57 (2012) 4369–4385. doi:10.1088/0031-9155/57/13/4369.
[375] I. Pshenichnov, A. Botvina, I. Mishustin, W. Greiner, Nuclear fragmentation reactions in extended media studied with Geant4 toolkit, Nucl. Instr. Meth. Phys. Res. B 268 (2010) 604–615. doi:10.1016/j.nimb.2009.12.023. arXiv:0911.2017.
[376] D. Maurin, USINE: Semi-analytical models for Galactic cosmic-ray propagation, Comput. Phys. Commun. 247 (2020) 106942. doi:10.1016/j.cpc.2019.106942. arXiv:1807.02968.
[377] E. Ferronato Bueno, L. Derome, Y. Génolini, D. Maurin, V. Tatischeff, M. Vecchi, Transport parameters from AMS-02 F/Si data and fluorine source abundance, A&A 688 (2024) A17. doi:10.1051/0004-6361/202244660. arXiv:2208.01337.
[378] Y. Wang, J. Wu, W.-C. Long, Testing the consistency of propagation between light and heavy cosmic ray nuclei, Chinese Phys. C 46 (2022) 095102. doi:10.1088/1674-1137/ac6ed4. arXiv:2108.03687.
[379] D. M. Gomez-Coral, C. Gerrity, R. Munini, P. von Doetinchem, Current status and new perspectives on cosmic ray

deuterons, Phys. Rev. D 107 (2023) 123008. doi:10.1103/PhysRevD.107.123008. arXiv:2303.09775.
[380] P. De La Torre Luque, M. N. Mazziotta, F. Loparco, F. Gargano, D. Serini, Implications of current nuclear cross sections on secondary cosmic rays with the upcoming DRAGON2 code, J. Cosmology Astropart. Phys. 2021 (2021) 099. doi:10.1088/1475-7516/2021/03/099.
[381] P. De La Torre Luque, M. N. Mazziotta, F. Loparco, F. Gargano, D. Serini, Markov chain Monte Carlo analyses of the flux ratios of B, Be and Li with the DRAGON2 code, J. Cosmology Astropart. Phys. 2021 (2021) 010. doi:10.1088/1475-7516/2021/07/010. arXiv:2102.13238.
[382] M. Korsmeier, A. Cuoco, Implications of lithium to oxygen AMS-02 spectra on our understanding of cosmic-ray diffusion, Phys. Rev. D 103 (2021) 103016. doi:10.1103/PhysRevD.103.103016.
[383] H. Jacobs, P. Mertsch, V. H. M. Phan, Unstable cosmic ray nuclei constrain low-diffusion zones in the Galactic disc, MNRAS 526 (2023) 160–174. doi:10.1093/mnras/stad2719. arXiv:2305.10337.
[384] P. De La Torre Luque, T. Linden, Galactic Gas Models Strongly Affect the Determination of the Diffusive Halo Height (2024). arXiv:2408.05179.
[385] N. Abgrall, et al. (NA61/SHINE collaboration), Measurements of $\pi^{\pm}$, $K^{\pm}$, K^0_S , Λ and proton production in proton–carbon interactions at 31 GeV/c with the NA61/SHINE spectrometer at the CERN SPS, Eur. Phys. J. C 76 (2016) 84. doi:10.1140/epjc/s10052-016-3898-y. arXiv:1510.02703.
[386] M. Unger, et al. (NA61/SHINE collaboration), New Results from the Cosmic-Ray Program of the NA61/SHINE facility at the CERN SPS (2019). arXiv:1909.07136.
[387] N. Amin, et al. (NA61/SHINE collaboration), Results from a Pilot Study on the Measurement of Nuclear Fragmentation with NA61/SHINE at the CERN SPS: 11C Production in C+p Interactions at 13.5A GeV/c, in: 37th ICRC, 2022, p. 102.
[388] J. R. Letaw, R. Silberberg, C. H. Tsao, Propagation of heavy cosmic-ray nuclei, ApJS 56 (1984) 369–391. doi:10.1086/190989.
[389] F. G. Kondev, M. Wang, W. J. Huang, S. Naimi, G. Audi, The NUBASE2020 evaluation of nuclear physics properties, Chinese Phys. C 45 (2021) 030001. doi:10.1088/1674-1137/abddae.
[390] W. J. Huang, M. Wang, F. G. Kondev, G. Audi, S. Naimi, The AME 2020 atomic mass evaluation (I). Evaluation of input data, and adjustment procedures, Chinese Phys. C 45 (2021) 030002. doi:10.1088/1674-1137/abddb0.
[391] M. Wang, W. J. Huang, F. G. Kondev, G. Audi, S. Naimi, The AME 2020 atomic mass evaluation (II). Tables, graphs and references, Chinese Phys. C 45 (2021) 030003. doi:10.1088/1674-1137/abddaf.
[392] M. Aguilar, et al. (AMS collaboration), Antiproton Flux, Antiproton-to-Proton Flux Ratio, and Properties of Elementary Particle Fluxes in Primary Cosmic Rays Measured with the Alpha Magnetic Spectrometer on the International Space Station, Phys. Rev. Lett. 117 (2016) 091103. doi:10.1103/PhysRevLett.117.091103.
[393] M. Di Mauro, F. Donato, N. Fornengo, R. Lineros, A. Vittino, Interpretation of AMS-02 electrons and positrons data, J. Cosmology Astropart. Phys. 04 (2014) 006. doi:10.1088/1475-7516/2014/04/006. arXiv:1402.0321.
[394] P. Mertsch, A. Vittino, S. Sarkar, Explaining cosmic ray antimatter with secondaries from old supernova remnants, Phys. Rev. D 104 (2021) 103029. doi:10.1103/physrevd.104.103029. arXiv:2012.12853.
[395] M. Di Mauro, F. Donato, N. Fornengo, A. Vittino, Dark matter vs. astrophysics in the interpretation of AMS-02 electron and positron data, J. Cosmology Astropart. Phys. 05 (2016) 031. doi:10.1088/1475-7516/2016/05/031. arXiv:1507.07001.
[396] M. Di Mauro, F. Donato, A. Goudelis, P. D. Serpico, New evaluation of the antiproton production cross section for cosmic ray studies, Phys. Rev. D 90 (2014) 085017. doi:10.1103/PhysRevD.90.085017. arXiv:1408.0288, [Erratum: Phys.Rev.D 98, 049901 (2018)].
[397] F. Donato, M. Korsmeier, M. Di Mauro, Prescriptions on antiproton cross section data for precise theoretical antiproton flux predictions, Phys. Rev. D 96 (2017) 043007. doi:10.1103/PhysRevD.96.043007. arXiv:1704.03663.
[398] M. Korsmeier, F. Donato, M. Di Mauro, Production cross sections of cosmic antiprotons in the light of new data from the NA61 and LHCb experiments, Phys. Rev. D 97 (2018). doi:10.1103/physrevd.97.103019.
[399] T. Anticic, et al. (NA49 collaboration), Inclusive production of protons, anti-protons and neutrons in p+p collisions at 158 GeV/c beam momentum, Eur. Phys. J. C 65 (2009). doi:10.1140/epjc/s10052-009-1172-2.
[400] A. Aduszkiewicz, et al. (NA61/SHINE collaboration), Measurements of $\pi^{\pm}$, $K^{\pm}$, p and $\overline{p}$ spectra in proton-proton interactions at 20, 31, 40, 80 and 158 GeV/c with the NA61/SHINE spectrometer at the CERN SPS, Eur. Phys. J. C 77 (2017) 671. doi:10.1140/epjc/s10052-017-5260-4. arXiv:1705.02467.
[401] D. Dekkers, J. A. Geibel, R. Mermod, G. Weber, T. R. Willitts, K. Winter, B. Jordan, M. Vivargent, et al., Experimental Study of Particle Production at Small Angles in Nucleon-Nucleon Collisions at 19 and 23 GeV/c, Phys. Rev. 137 (1965) B962–B978. doi:10.1103/PhysRev.137.B962.
[402] J. V. Allaby, F. G. Binon, A. N. Diddens, P. Duteil, A. Klovning, R. Meunier, High-energy particle spectra from proton interactions at 19.2 GeV/c, CERN-70-12 (1970). doi:10.17182/hepdata.1345.
[403] I. Arsene, et al. (BRAHMS collaboration), Production of mesons and baryons at high rapidity and high P_T in proton-proton collisions at $\sqrt{s}$ = 200 GeV, Phys. Rev. Lett. 98 (2007) 252001. doi:10.1103/PhysRevLett.98.252001. arXiv:hep-ex/0701041.
[404] R. Aaij, et al. (LHCb collaboration), Measurement of Antiproton Production in p–He Collisions at $\sqrt{s_{\rm NN}}$ = 110 GeV, Phys. Rev. Lett. 121 (2018) 222001. doi:10.1103/PhysRevLett.121.222001.
[405] B. Baatar, et al. (NA49 collaboration), Inclusive production of protons, anti-protons, neutrons, deuterons and tritons in p+C collisions at 158 GeV/c beam momentum, Eur. Phys. J. C 73 (2013) 2364. doi:10.1140/epjc/s10052-013-2364-3. arXiv:1207.6520.
[406] F. Donato, N. Fornengo, P. Salati, Antideuterons as a signature of supersymmetric dark matter, Phys. Rev. D 62 (2000).

doi:10.1103/physrevd.62.043003.
[407] F. Donato, N. Fornengo, D. Maurin, Antideuteron fluxes from dark matter annihilation in diffusion models, Phys. Rev. D 78 (2008) 043506. doi:10.1103/PhysRevD.78.043506. arXiv:0803.2640.
[408] M. Cirelli, N. Fornengo, M. Taoso, A. Vittino, Anti-helium from dark matter annihilations, J. High Energy Phys. 2014 (2014). doi:10.1007/jhep08(2014)009.
[409] J. I. Kapusta, Mechanisms for deuteron production in relativistic nuclear collisions, Phys. Rev. C 21 (1980) 1301–1310. doi:10.1103/PhysRevC.21.1301.
[410] S. T. Butler, C. A. Pearson, Deuterons from High-Energy Proton Bombardment of Matter, Phys. Rev. 129 (1963) 836–842. doi:10.1103/PhysRev.129.836.
[411] R. Scheibl, U. Heinz, Coalescence and flow in ultrarelativistic heavy ion collisions, Phys. Rev. C 59 (1999) 1585–1602. doi:10.1103/PhysRevC.59.1585.
[412] K. Blum, K. C. Y. Ng, R. Sato, M. Takimoto, Cosmic rays, antihelium, and an old navy spotlight, Phys. Rev. D 96 (2017) 103021. doi:10.1103/PhysRevD.96.103021. arXiv:1704.05431.
[413] F. Bellini, A. P. Kalweit, Testing production scenarios for (anti-)(hyper-)nuclei and exotica at energies available at the CERN Large Hadron Collider, Phys. Rev. C 99 (2019) 054905. doi:10.1103/PhysRevC.99.054905. arXiv:1807.05894.
[414] M. Kachelrieß, S. Ostapchenko, J. Tjemsland, Alternative coalescence model for deuteron, tritium, helium-3 and their antinuclei, Eur. Phys. J. A 56 (2020) 4. doi:10.1140/epja/s10050-019-00007-9. arXiv:1905.01192.
[415] M. Kachelrieß, S. Ostapchenko, J. Tjemsland, Revisiting cosmic ray antinuclei fluxes with a new coalescence model, J. Cosmology Astropart. Phys. 08 (2020) 048. doi:10.1088/1475-7516/2020/08/048. arXiv:2002.10481.
[416] F. Bellini, K. Blum, A. P. Kalweit, M. Puccio, Examination of coalescence as the origin of nuclei in hadronic collisions, Phys. Rev. C 103 (2021) 014907. doi:10.1103/PhysRevC.103.014907. arXiv:2007.01750.
[417] J. Adam, et al. (ALICE collaboration), Enhanced production of multi-strange hadrons in high-multiplicity proton-proton collisions, Nature Phys. 13 (2017) 535–539. doi:10.1038/nphys4111. arXiv:1606.07424.
[418] V. V. Abramov, et al., High p_T Deuteron and Anti-deuteron Production in pp and p a Collisions at 70-GeV, Sov. J. Nucl. Phys. 45 (1987) 845.
[419] M. Korsmeier, F. Donato, N. Fornengo, Prospects to verify a possible dark matter hint in cosmic antiprotons with antideuterons and antihelium, Phys. Rev. D 97 (2018) 103011. doi:10.1103/PhysRevD.97.103011. arXiv:1711.08465.
[420] A. Ibarra, S. Wild, Prospects of antideuteron detection from dark matter annihilations or decays at AMS-02 and GAPS, J. Cosmology Astropart. Phys. 02 (2013) 021. doi:10.1088/1475-7516/2013/02/021. arXiv:1209.5539.
[421] N. Fornengo, L. Maccione, A. Vittino, Dark matter searches with cosmic antideuterons: status and perspectives, J. Cosmology Astropart. Phys. 09 (2013) 031. doi:10.1088/1475-7516/2013/09/031. arXiv:1306.4171.
[422] D.-M. Gomez-Coral, A. Menchaca Rocha, V. Grabski, A. Datta, P. von Doetinchem, A. Shukla, Deuteron and antideuteron production simulation in cosmic-ray interactions, Phys. Rev. D 98 (2018) 023012. doi:10.1103/PhysRevD.98.023012.
[423] A. Shukla, A. Datta, P. von Doetinchem, D.-M. Gomez-Coral, C. Kanitz, Large-scale Simulations of Antihelium Production in Cosmic-ray Interactions, Phys. Rev. D 102 (2020) 063004. doi:10.1103/PhysRevD.102.063004. arXiv:2006.12707.
[424] M. W. Winkler, T. Linden, Dark Matter Annihilation Can Produce a Detectable Antihelium Flux through $\overline{\Lambda}_b$ Decays, Phys. Rev. Lett. 126 (2021) 101101. doi:10.1103/PhysRevLett.126.101101. arXiv:2006.16251.
[425] M. Kachelriess, S. Ostapchenko, J. Tjemsland, Comment on "Dark Matter Annihilation Can Produce a Detectable Antihelium Flux through $\bar{\Lambda}_b$ Decays" (2021). arXiv:2105.00799.
[426] M. W. Winkler, T. Linden, Response to Comment on "Dark Matter Annihilation Can Produce a Detectable Antihelium Flux through $\overline{\Lambda}_b$ Decays" (2021). arXiv:2106.00053.
[427] Antihelium production in $\overline{\Lambda}_b^0$ decays, Technical Report, CERN, Geneva, 2024. URL: https://cds.cern.ch/record/2905862.
[428] C. Alt, et al. (NA49 collaboration), Inclusive production of charged pions in p+p collisions at 158 GeV/c beam momentum, Eur. Phys. J. C 45 (2005) 343–381. doi:10.1140/epjc/s2005-02391-9.
[429] T. Anticic, et al. (NA49 collaboration), Inclusive production of charged kaons in p+p collisions at 158 GeV/c beam momentum and a new evaluation of the energy dependence of kaon production up to collider energies, Eur. Phys. J. C 68 (2010) 1–73. doi:10.1140/epjc/s10052-010-1328-0.
[430] A. Aduszkiewicz, et al. (NA61/SHINE collaboration), Production of Λ-hyperons in inelastic p+p interactions at 158 GeV/c, Eur. Phys. J. C 76 (2016) 198. doi:10.1140/epjc/s10052-016-4003-2. arXiv:1510.03720.
[431] K. Aamodt, et al. (ALICE collaboration), Production of pions, kaons and protons in pp collisions at $\sqrt{s} = 900$ GeV with ALICE at the LHC, Eur. Phys. J. C 71 (2011). doi:10.1140/epjc/s10052-011-1655-9.
[432] S. Chatrchyan, et al. (CMS collaboration), Study of the inclusive production of charged pions, kaons, and protons in pp collisions at $\sqrt{s} = 0.9, 2.76$, and 7 TeV, Eur. Phys. J. C 72 (2012). doi:10.1140/epjc/s10052-012-2164-1.
[433] A. Sirunyan, et al. (CMS collaboration), Measurement of charged pion, kaon, and proton production in proton-proton collisions at $\sqrt{s} = 13$ TeV, Phys. Rev. D 96 (2017). doi:10.1103/physrevd.96.112003.
[434] M. Antinucci, A. Bertin, P. Capiluppi, M. D'Agostino-Bruno, A. M. Rossi, G. Vannini, G. Giamcomelli, A. Bussière, Multiplicities of charged particles up to ISR energies, Nuovo Cimento Lett. 6 (1973) 121–128. doi:10.1007/BF02827250.
[435] C. Alt, et al. (NA49 collaboration), Inclusive production of charged pions in p+C collisions at 158 GeV/c beam momentum, Eur. Phys. J. C 49 (2007) 897–917. doi:10.1140/epjc/s10052-006-0165-7.
[436] S. Abdollahi, et al. (Fermi-LAT collaboration), Incremental Fermi Large Area Telescope Fourth Source Catalog, ApJS 260 (2022) 53. doi:10.3847/1538-4365/ac6751. arXiv:2201.11184.
[437] C. D. Dermer, Binary collision rates of relativistic thermal plasmas. II-Spectra, ApJ 307 (1986) 47–59.
[438] O. Adriani, et al. (LHCf collaboration), Measurements of longitudinal and transverse momentum distributions for neutral

pions in the forward-rapidity region with the LHCf detector, Phys. Rev. D 94 (2016) 032007. doi:10.1103/PhysRevD.94.032007. arXiv:1507.08764.

[439] J. Aleksić, et al. (MAGIC collaboration), The major upgrade of the MAGIC telescopes, Part II: A performance study using observations of the Crab Nebula, Astropart. Phys. 72 (2016) 76–94. doi:10.1016/j.astropartphys.2015.02.005. arXiv:1409.5594.

[440] M. De Naurois (H.E.S.S. collaboration), The H.E.S.S. experiment : current status and future prospects, in: 36th ICRC, 2019, p. 656. doi:10.22323/1.358.0656.

[441] A. Albert, et al. (HAWC collaboration), 3HWC: The Third HAWC Catalog of Very-High-Energy Gamma-ray Sources, ApJ 905 (2020) 76. doi:10.3847/1538-4357/abc2d8. arXiv:2007.08582.

[442] A. Addazi, et al. (LHAASO collaboration), The Large High Altitude Air Shower Observatory (LHAASO) Science Book (2021 Edition), Chinese Phys. C 46 (2022) 035001–035007. arXiv:1905.02773.

[443] B. S. Acharya, et al. (CTA Consortium), Introducing the CTA concept, Astropart. Phys. 43 (2013) 3–18. doi:10.1016/j.astropartphys.2013.01.007.

[444] S. Mariani, Fixed-target physics with the LHCb experiment at CERN, Ph.D. thesis, Universita degli studi di Firenze, 2021. URL: https://cds.cern.ch/record/2806641, presented 08 Apr 2022.

[445] O. B. Garcia, G. Bregliozzi, D. Calegari, V. Carassiti, G. Ciullo, V. Coco, P. Collins, P. C. Pinto, et al., High-density gas target at the LHCb experiment, Phys. Rev. Accel. Beams 27 (2024) 111001. doi:10.1103/PhysRevAccelBeams.27.111001.

[446] S. R. Kelner, F. A. Aharonian, Energy spectra of gamma-rays, electrons and neutrinos produced at interactions of relativistic protons with low energy radiation, Phys. Rev. D 78 (2008) 034013. doi:10.1103/PhysRevD.82.099901. arXiv:0803.0688, [Erratum: Phys.Rev.D 82, 099901 (2010)].

[447] P. de la Torre Luque, M. N. Mazziotta, A. Ferrari, F. Loparco, P. Sala, D. Serini, FLUKA cross sections for cosmic-ray interactions with the DRAGON2 code, J. Cosmology Astropart. Phys. 07 (2022) 008. doi:10.1088/1475-7516/2022/07/008. arXiv:2202.03559.

[448] T. Kamae, N. Karlsson, T. Mizuno, T. Abe, T. Koi, Parameterization of Gamma, $e^{\pm}$ and Neutrino Spectra Produced by p-p Interaction in Astronomical Environment, ApJ 647 (2006) 692–708. doi:10.1086/513602. arXiv:astro-ph/0605581, [Erratum: Astrophys.J. 662, 779 (2007)].

[449] M. Kachelrieß, I. V. Moskalenko, S. Ostapchenko, AAfrag: Interpolation routines for Monte Carlo results on secondary production in proton-proton, proton-nucleus and nucleus-nucleus interactions, Comput. Phys. Commun. 245 (2019) 106846. doi:10.1016/j.cpc.2019.08.001. arXiv:1904.05129.

[450] S. Ostapchenko, Monte Carlo treatment of hadronic interactions in enhanced Pomeron scheme: I. QGSJET-II model, Phys. Rev. D 83 (2011) 014018. doi:10.1103/PhysRevD.83.014018. arXiv:1010.1869.

[451] E. Kafexhiu, F. Aharonian, A. M. Taylor, G. S. Vila, Parametrization of gamma-ray production cross-sections for pp interactions in a broad proton energy range from the kinematic threshold to PeV energies, Phys. Rev. D 90 (2014) 123014. doi:10.1103/PhysRevD.90.123014. arXiv:1406.7369.

[452] M. Bhatt, I. Sushch, M. Pohl, A. Fedynitch, S. Das, R. Brose, P. Plotko, D. M. A. Meyer, Production of secondary particles in heavy nuclei interactions in supernova remnants, Astropart. Phys. (2020). doi:10.1016/j.astropartphys.2020.102490. arXiv:2006.07018.

[453] A. Aduszkiewicz, et al. (NA61/SHINE collaboration), Measurements of production and inelastic cross sections for p+C, p+Be , and p+Al at 60 GeV/c and p+C and p+Be at 120 GeV/c, Phys. Rev. D 100 (2019) 112001. doi:10.1103/PhysRevD.100.112001. arXiv:1909.03351.

[454] A. Esmaeili, A. Esmaili, P. D. Serpico, Closer scrutiny of cosmic ray proton energy losses, Phys. Rev. D 109 (2024) 123024. doi:10.1103/PhysRevD.109.123024. arXiv:2403.18012.

[455] H. L. Bradt, B. Peters, The Heavy Nuclei of the Primary Cosmic Radiation, Phys. Rev. 77 (1950) 54–70. doi:10.1103/PhysRev.77.54.

[456] W.-Q. Shen, B. Wang, J. Feng, W.-L. Zhan, Y.-T. Zhu, E.-P. Feng, Total reaction cross section for heavy-ion collisions and its relation to the neutron excess degree of freedom, Nucl. Phys. A 491 (1989) 130–146. doi:10.1016/0375-9474(89)90209-1.

[457] S. Barshay, C. B. Dover, J. P. Vary, The validity of the factorization hypothesis for nucleus-nucleus cross sections at high energies, Phys. Lett. B 51 (1974) 5–8. doi:10.1016/0370-2693(74)90136-1.

[458] S. Barshay, C. B. Dover, J. P. Vary, Nucleus-nucleus cross sections and the validity of the factorization hypothesis at intermediate and high energies, Phys. Rev. C 11 (1975) 360–369. doi:10.1103/PhysRevC.11.360.

[459] V. S. Barashenkov, A. Polanski, Electronic guide for nuclear cross-sections: version 1994, Technical Report, Joint Inst. Nucl. Res., Dubna, 1994. URL: https://cds.cern.ch/record/278901.

[460] H. P. Wellisch, D. Axen, Total reaction cross section calculations in proton-nucleus scattering, Phys. Rev. C 54 (1996) 1329–1332. doi:10.1103/PhysRevC.54.1329.

[461] R. K. Tripathi, F. A. Cucinotta, J. W. Wilson, Accurate universal parameterization of absorption cross sections, Nucl. Instr. Meth. Phys. Res. B 117 (1996) 347–349. doi:10.1016/0168-583X(96)00331-X.

[462] R. K. Tripathi, F. A. Cucinotta, J. W. Wilson, Accurate universal parameterization of absorption cross sections III - light systems, Nucl. Instr. Meth. Phys. Res. B 155 (1999) 349–356. doi:10.1016/S0168-583X(99)00479-6.

[463] A. Ingemarsson, M. Lantz, Geometrical aspects of reaction cross sections for ^{3}He, ^{4}He, and ^{12}C projectiles, Phys. Rev. C 67 (2003) 064605. doi:10.1103/PhysRevC.67.064605.

[464] K. Iida, A. Kohama, K. Oyamatsu, Formula for Proton-Nucleus Reaction Cross Section at Intermediate Energies and Its Application, J. Phys. Soc. Jpn. 76 (2007) 044201. doi:10.1143/JPSJ.76.044201. arXiv:nucl-th/0601039.

[465] L. Sihver, D. Mancusi, Present status and validation of HIBRAC, Radiat. Meas. 44 (2009) 38–46. doi:10.1016/j.radmeas.2008.11.004.

[466] L. Sihver, M. Lantz, A. Kohama, Improved parametrization of the transparency parameter in Kox and Shen models of total reaction cross sections, Phys. Rev. C 89 (2014) 067602. doi:10.1103/PhysRevC.89.067602.

[467] L. Sihver, A. Kohama, K. Iida, K. Oyamatsu, S. Hashimoto, H. Iwase, K. Niita, Current status of the "Hybrid Kurotama model" for total reaction cross sections, Nucl. Instr. Meth. Phys. Res. B 334 (2014) 34–39. doi:10.1016/j.nimb.2014.04.021.

[468] S. Y. Shmakov, V. V. Uzhinskii, A. M. Zadorozhny, DIAGEN — Generator of inelastic nucleus-nucleus interaction diagrams, Comput. Phys. Commun. 54 (1989) 125–135. doi:10.1016/0010-4655(89)90038-6.

[469] P. Shukla, Glauber model and the heavy ion reaction cross section, Phys. Rev. C 67 (2003) 054607. doi:10.1103/PhysRevC.67.054607. arXiv:nucl-th/0302030.

[470] M. Takechi, M. Fukuda, M. Mihara, K. Tanaka, T. Chinda, T. Matsumasa, M. Nishimoto, R. Matsumiya, et al., Reaction cross sections at intermediate energies and Fermi-motion effect, Phys. Rev. C 79 (2009) 061601. doi:10.1103/PhysRevC.79.061601.

[471] M. Y. H. Farag, E. H. Esmael, I. A. M. Abdul-Magead, S. S. Mousa, New empirical formulae for the in-medium nucleon-nucleon cross-section, Nucl. Phys. A 989 (2019) 21–39. doi:10.1016/j.nuclphysa.2019.05.011.

[472] V. Andersen, F. Ballarini, G. Battistoni, M. Campanella, M. Carboni, F. Cerutti, A. Empl, A. Fassò, et al., The FLUKA code for space applications: recent developments, Adv. in Space Res. 34 (2004) 1302–1310. doi:10.1016/j.asr.2003.03.045.

[473] J. L. Rodríguez-Sánchez, J.-C. David, D. Mancusi, A. Boudard, J. Cugnon, S. Leray, Improvement of one-nucleon removal and total reaction cross sections in the Liège intranuclear-cascade model using Hartree-Fock-Bogoliubov calculations, Phys. Rev. C 96 (2017) 054602. doi:10.1103/PhysRevC.96.054602.

[474] L. Sihver, M. Lantz, M. Takechi, A. Kohama, A. Ferrari, F. Cerutti, T. Sato, A comparison of total reaction cross section models used in particle and heavy ion transport codes, Adv. in Space Res. 49 (2012) 812–819. doi:10.1016/j.asr.2011.11.029.

[475] F. Luoni, F. Horst, C. A. Reidel, A. Quarz, L. Bagnale, L. Sihver, U. Weber, R. B. Norman, et al., Total nuclear reaction cross-section database for radiation protection in space and heavy-ion therapy applications, New J. Phys. 23 (2021) 101201. doi:10.1088/1367-2630/ac27e1. arXiv:2105.11981.

[476] V. V. Zerkin, B. Pritychenko, J. Totans, L. Vrapcenjak, A. Rodionov, G. I. Shulyak, EXFOR-NSR PDF database: a system for nuclear knowledge preservation and data curation, JINST 17 (2022) P03012. doi:10.1088/1748-0221/17/03/P03012. arXiv:2202.12807.

[477] N. Otuka, E. Dupont, V. Semkova, B. Pritychenko, A. I. Blokhin, M. Aikawa, S. Babykina, M. Bossant, et al., Towards a More Complete and Accurate Experimental Nuclear Reaction Data Library (EXFOR): International collaboration Between Nuclear Reaction Data Centres (NRDC), Nuclear Data Sheets 120 (2014) 272–276. doi:10.1016/j.nds.2014.07.065. arXiv:2002.07114.

[478] V. V. Zerkin, B. Pritychenko, The experimental nuclear reaction data (EXFOR): Extended computer database and Web retrieval system, Nucl. Instr. Meth. Phys. Res. A 888 (2018) 31–43. doi:10.1016/j.nima.2018.01.045. arXiv:1802.05714.

[479] W. Bauhoff, Tables of reaction and total cross sections for proton-nucleus scattering below 1 GeV, Atom. Data Nucl. Data Tabl. 35 (1986) 429–447. doi:10.1016/0092-640X(86)90016-1.

[480] R. F. Carlson, Proton-Nucleus Total Reaction Cross Sections and Total Cross Sections Up to 1 GeV, Atom. Data Nucl. Data Tabl. 63 (1996) 93–116. doi:10.1006/adnd.1996.0010.

[481] F. F. Chen, C. P. Leavitt, A. M. Shapiro, Total p-p and p-n Cross Sections at Cosmotron Energies, Phys. Rev. 103 (1956) 211–225. doi:10.1103/PhysRev.103.211.

[482] D. V. Bugg, D. C. Salter, G. H. Stafford, R. F. George, K. F. Riley, R. J. Tapper, Nucleon-Nucleon Total Cross Sections from 1.1 to 8 GeV/c, Phys. Rev. 146 (1966) 980–992. doi:10.1103/PhysRev.146.980.

[483] J. Jaros, et al., Nucleus-Nucleus Total Cross-Sections for Light Nuclei at 1.55 GeV/nucleon and 2.89 GeV/nucleon, Phys. Rev. C 18 (1978) 2273–2292. doi:10.1103/PhysRevC.18.2273.

[484] F. S. Dietrich, et al., Proton Reaction Cross Sections Measured in the BNL/AGS E943 Experiment, J. Nucl. Sci. Tech. 39 (2002) 269–271. doi:10.1080/00223131.2002.10875091.

[485] B. M. Bobchenko, et al., Measurement of total inelastic cross-sections from proton interactions with nuclei in the momentum range from 5 GeV/c to 9 GeV/c and π^- mesons with nuclei in the momentum range from 1.75 GeV/c TO 6.5 GeV/c, Sov. J. Nucl. Phys. 30 (1979) 805.

[486] A. Ashmore, G. Cocconi, A. N. Diddens, A. M. Wetherell, Total Cross Sections of Protons with Momentum Between 10 and 28 Gev/c, Phys. Rev. Lett. 5 (1960) 576–578. doi:10.1103/PhysRevLett.5.576.

[487] G. Bellettini, G. Cocconi, A. N. Diddens, E. Lillethun, G. Matthiae, J. P. Scanlon, A. M. Wetherell, Proton-nuclei cross sections at 20 GeV, Nucl. Phys. 79 (1966) 609–624. doi:10.1016/0029-5582(66)90267-7.

[488] G. J. Igo, J. L. Friedes, H. Palevsky, R. Sutter, G. Bennett, W. D. Simpson, D. M. Corley, R. L. Stearns, Measurements of 1 GeV proton total scattering cross section on H, He, ^{6}Li, C, O and Pb targets, Nucl. Phys. B 3 (1967) 181–187. doi:10.1016/0550-3213(67)90168-X.

[489] S. P. Denisov, S. V. Donskov, Y. P. Gorin, A. I. Petrukhin, Y. D. Prokoshkin, D. A. Soyanova, J. V. Allaby, G. Giacomelli, Total cross-sections of π^+, K^+ and p on protons and deuterons in the momentum range 15 GeV/c to 60 GeV/c, Phys. Lett. B 36 (1971) 415–421. doi:10.1016/0370-2693(71)90739-8.

[490] S. N. Ganguli, R. Raghavan, A. Subramanian, Analysis of proton-Carbon inelastic cross-sections measured in satellite experiment and upper limit on primary cosmic-ray deuteron flux in the energy range 20 GeV to 600 GeV, Pramana 2 (1974) 341. doi:10.1007/BF02847248.

[491] S. P. Denisov, S. V. Donskov, Y. P. Gorin, R. N. Krasnokutsky, A. I. Petrukhin, Y. D. Prokoshkin, D. A. Stoyanova, Absorption cross-sections for pions, kaons, protons and anti-protons on complex nuclei in the 6 GeV/c to 60 GeV/c

momentum range, Nucl. Phys. B 61 (1973) 62–76. doi:10.1016/0550-3213(73)90351-9.
[492] A. S. Carroll, et al., Absorption Cross-Sections of $\pi^{\pm}$, $K^{\pm}$, p and $\overline{\mathrm{p}}$ on Nuclei Between 60 GeV/c and 280 GeV/c, Phys. Lett. B 80 (1979) 319–322. doi:10.1016/0370-2693(79)90226-0.
[493] F. Fumuro, R. Ihara, T. Ogata, A-Dependence in Proton Nucleus Interactions at 400 GeV, Nucl. Phys. B 152 (1979) 376–389. doi:10.1016/0550-3213(79)90088-9.
[494] S. A. Azimov, et al., Multiplicity of Secondary Particles in Inelastic Proton - Neon Interactions at 300-GeV/c, Phys. Rev. D 23 (1981) 2512. doi:10.1103/PhysRevD.23.2512.
[495] V. E. Dudkin, E. E. Kovalev, N. A. Nefedov, V. A. Antonchik, S. D. Bogdanov, V. F. Kosmach, A. Y. Likhachev, J. Hassan, E. V. Benton, H. J. Crawford, Multiplicities of secondaries in nuclear interactions, induced by ^{20}Ne, ^{40}Ar, and ^{56}Fe nuclei at 0.1 GeV/nucleon to 0.5 GeV/nucleon, Nucl. Phys. A 568 (1994) 906–916. doi:10.1016/0375-9474(94)90366-2.
[496] U. Dersch, et al. (SELEX), Total Cross Section Measurements with π^-, Σ^- and Protons on Nuclei and Nucleons around 600 GeV/c, Nucl. Phys. B 579 (2000) 277–312. doi:10.1016/S0550-3213(00)00204-2. arXiv:hep-ex/9910052.
[497] J. Carvalho, Compilation of cross sections for proton nucleus interactions at the HERA energy, Nucl. Phys. A 725 (2003) 269–275. doi:10.1016/S0375-9474(03)01597-5.
[498] M. Giacomelli, L. Sihver, J. Skvarč, N. Yasuda, R. Ilić, Projectile like fragment emission angles in fragmentation reactions of light heavy ionsin the energy region $<$ 200 MeV/nucleon : Modeling and simulations, Phys. Rev. C 69 (2004) 064601. doi:10.1103/PhysRevC.69.064601.
[499] S. Momota, T. Ohtsubo, A. Honma, A. Kitagawa, S. Sato, Anisotropic momentum distribution of ^{11}B and ^{11}C produced from ^{12}C beam at 100 MeV/nucleon, Phys. Scr 98 (2023) 085301. doi:10.1088/1402-4896/acdf93.
[500] C. H. Tsao, R. Silberberg, A. F. Barghouty, L. Sihver, Energy Degradation in Cosmic-Ray Nuclear Spallation Reactions: Relaxing the Straight-ahead Approximation, ApJ 451 (1995) 275. doi:10.1086/176217.
[501] J. P. Kneller, J. R. Phillips, T. P. Walker, Testing Two Nuclear Physics Approximations Used in the Standard Leaky-Box Model for the Spallogenic Production of LiBeB, ApJ 589 (2003) 217–224. doi:10.1086/374592. arXiv:astro-ph/0302069.
[502] J. R. Letaw, J. H. Adams, Jr., R. Silberberg, C. H. Tsao, Electron capture decay of cosmic rays., Ap&SS 114 (1985) 365–379. doi:10.1007/BF00653983.
[503] L. W. Wilson, The Nuclear and Atomic Physics Governing Changes in the Composition of Relativistic Cosmic Rays., Ph.D. thesis, University of California, Berkeley, 1978.
[504] H. J. Crawford, Single Electron Attachment and Stripping Cross-Sections for Relativistic Heavy Ions., Ph.D. thesis, University of California, Berkeley, 1979.
[505] D. Benyamin, N. J. Shaviv, T. Piran, Electron-capture Isotopes Could Constrain Cosmic-Ray Propagation Models, ApJ 851 (2017) 109. doi:10.3847/1538-4357/aa9935. arXiv:1709.01585.
[506] M. Borchiellini, D. Maurin, M. Vecchi, The role of electron capture decay in the precision era of Galactic cosmic-ray data, in: 38th ICRC, 2024, p. 66.
[507] R. Duperray, B. Baret, D. Maurin, G. Boudoul, A. Barrau, L. Derome, K. Protasov, M. Buénerd, Flux of light antimatter nuclei near Earth, induced by cosmic rays in the Galaxy and in the atmosphere, Phys. Rev. D 71 (2005) 083013. doi:10.1103/PhysRevD.71.083013. arXiv:astro-ph/0503544.
[508] R. P. Duperray, K. V. Protasov, A. Y. Voronin, Antideuteron production in proton-proton and proton-nucleus collisions, Eur. Phys. J. A 16 (2003) 27–34. doi:10.1140/epja/i2002-10074-0. arXiv:nucl-th/0209078.
[509] R. P. Duperray, C. Y. Huang, K. V. Protasov, M. Buénerd, Parametrization of the antiproton inclusive production cross section on nuclei, Phys. Rev. D 68 (2003) 094017. doi:10.1103/PhysRevD.68.094017. arXiv:astro-ph/0305274.
[510] R. P. Duperray, K. V. Protasov, L. Derome, M. Buénerd, A model for A = 3 antinuclei production in proton-nucleus collisions, Eur. Phys. J. A 18 (2003) 597–604. doi:10.1140/epja/i2003-10099-9. arXiv:nucl-th/0301103.
[511] A. A. Moiseev, J. F. Ormes, Inelastic cross section for antihelium on nuclei: an empirical formula for use in the experiments to search for cosmic antimatter, Astropart. Phys. 6 (1997) 379–386. doi:10.1016/S0927-6505(96)00071-0.
[512] V. Uzhinsky, J. Apostolakis, A. Galoyan, G. Folger, V. M. Grichine, V. N. Ivanchenko, D. H. Wright, Antinucleus-nucleus cross sections implemented in Geant4, Phys. Lett. B 705 (2011) 235–239. doi:10.1016/j.physletb.2011.10.010.
[513] M. C. Lemaire, Elastic and inelastic scattering of antiprotons, Lecture Notes in Physics, Springer, Berlin, Heidelberg, 1985, pp. 285–309. doi:10.1007/3-540-16054-x_176.
[514] D. V. Bugg, J. Hall, A. S. Clough, R. L. Shypit, K. Bos, J. C. Kluyver, R. A. Kunne, L. Linssen, et al., $\overline{\mathrm{p}}$p total cross sections below 420 MeV/c, Phys. Lett. B 194 (1987) 563–567. doi:10.1016/0370-2693(87)90235-8.
[515] G. Carboni, G. Kantardjian, D. Lloyd Owen, M. Ambrosio, G. Anzivino, G. Barbarino, G. Paternoster, S. Patricelli, et al., Measurement of the antiproton-proton total cross section and elastic scattering at the CERN intersecting storage rings, Phys. Lett. B 108 (1982) 145–150. doi:10.1016/0370-2693(82)91161-3.
[516] D. L. Owen, Antiproton-Proton Total and Elastic Cross-Sections at the CERN ISR and the SPS Collider, AIP Conference Proceedings 98 (1983) 293–311. doi:10.1063/1.2947550.
[517] U. Amaldi, T. Fazzini, G. Fidecaro, C. Ghesquière, M. Legros, H. Steiner, Antiproton-proton total cross-sections between 0.575 and 5.35 GeV/c, Nuovo Cimento 34 (1964) 825–853. doi:10.1007/bf02812514.
[518] G. Arnison, A. Astbury, B. Aubert, C. Bacci, G. Bauer, A. Bézaguet, R. Böck, R. Bossart, et al., Elastic and total cross section measurement at the CERN proton-antiproton collider, Phys. Lett. B 128 (1983) 336–342. doi:10.1016/0370-2693(83)90271-x.
[519] M. Bozzo, P. L. Braccini, F. Carbonara, R. Castaldi, F. Cervelli, G. Chiefari, E. Drago, M. Haguenauer, et al., Measurement of the proton-antiproton total and elastic cross sections at the CERN SPS collider, Phys. Lett. B 147 (1984) 392–398. doi:10.1016/0370-2693(84)90139-4.
[520] G. J. Alner, R. E. Ansorge, B. Asman, C. N. Booth, L. Burow, P. Carlson, C. DeClercq, R. S. DeWolf, et al., Antiproton-proton cross sections at 200 and 900 GeV c.m. energy, Z. Physik C 32 (1986) 153–161. doi:10.1007/bf01552491.

[521] A. S. Carroll, I. H. Chiang, T. F. Kycia, K. K. Li, P. O. Mazur, P. M. Mockett, D. C. Rahm, W. F. Baker, et al., Total cross sections of $\pi^{\pm}$, $K^{\pm}$, p and $\overline{\mathrm{p}}$ on protons and deuterons between 23 and 280 GeV/c, Phys. Lett. B 61 (1976) 303–308. doi:10.1016/0370-2693(76)90155-6.

[522] A. S. Carroll, I. H. Chiang, T. F. Kycia, K. K. Li, M. D. Marx, D. C. Rahm, W. F. Baker, D. P. Eartly, et al., Total cross sections of $\pi^{\pm}$, $K^{\pm}$, p and $\overline{p}$ on protons and deuterons between 200 and 370 GeV/c, Phys. Lett. B 80 (1979) 423–427. doi:10.1016/0370-2693(79)91205-x.

[523] F. Abe, M. Albrow, D. Amidei, C. Anway-Wiese, G. Apollinari, M. Atac, P. Auchincloss, P. Azzi, et al., Measurement of the antiproton-proton total cross section at $\sqrt{s} = 546$ and 1800 GeV, Phys. Rev. D 50 (1994) 5550–5561. doi:10.1103/physrevd.50.5550.

[524] C. Avila, W. F. Baker, R. DeSalvo, D. P. Eartly, C. Guss, H. Jostlein, M. R. Mondardini, J. Orear, et al., A measurement of the proton-antiproton total cross section at $\sqrt{s} = 1.8$ TeV, Phys. Lett. B 445 (1999) 419–422. doi:10.1016/s0370-2693(98)01421-x.

[525] C. A. Coombes, B. Cork, W. Galbraith, G. R. Lambertson, W. A. Wenzel, Antiproton-Proton Cross Sections at 133, 197, 265, and 333 Mev, Phys. Rev. 112 (1958) 1303–1310. doi:10.1103/PhysRev.112.1303.

[526] T. Elioff, L. Agnew, O. Chamberlain, H. Steiner, C. Wiegand, T. Ypsilantis, $\overline{p}$-p Cross Sections from 534 to 1068 Mev, Phys. Rev. Lett. 3 (1959) 285–288. doi:10.1103/PhysRevLett.3.285.

[527] B. Cork, O. I. Dahl, D. H. Miller, A. G. Tenner, C. L. Wang, Antiproton-proton interaction cross-sections at 45, 90, 145, and 245 MeV, Nuovo Cimento 25 (1962) 497–508. doi:10.1007/bf02733689.

[528] T. Elioff, L. Agnew, O. Chamberlain, H. M. Steiner, C. Wiegand, T. Ypsilantis, Antiproton-Nucleon Cross Sections from 0.5 to 1.0 BeV, Phys. Rev. 128 (1962) 869–884. doi:10.1103/PhysRev.128.869.

[529] S. J. Lindenbaum, W. A. Love, J. A. Niederer, S. Ozaki, J. J. Russell, L. C. L. Yuan, Antiproton-Proton and Proton-Proton Total Cross Sections from 4 to 20 Bev/c, Phys. Rev. Lett. 7 (1961) 185–188. doi:10.1103/PhysRevLett.7.185.

[530] W. Galbraith, E. W. Jenkins, T. F. Kycia, B. A. Leontic, R. H. Phillips, A. L. Read, R. Rubinstein, Total Cross Sections of Protons, Antiprotons, and π and K Mesons on Hydrogen and Deuterium in the Momentum Range 6-22 GeV/c, Phys. Rev. 138 (1965) B913–B920. doi:10.1103/PhysRev.138.B913.

[531] R. J. Abrams, R. L. Cool, G. Giacomelli, T. F. Kycia, B. A. Leontic, K. K. Li, D. N. Michael, Total Cross Sections of $\mathrm{K}^{\pm}$ Mesons and Antiprotons on Nucleons up to 3.3 GeV/c, Phys. Rev. D 1 (1970) 1917–1935. doi:10.1103/PhysRevD.1.1917.

[532] J. V. Allaby, Y. B. Bushnin, S. P. Denisov, A. N. Diddens, R. W. Dobinson, S. V. Donskov, G. Giacomelli, Y. P. Gorin, et al., Total cross-sections of π^-, K^-, and $\overline{\mathrm{p}}$ on protons and deuterons in the momentum range 20–65 GeV/c, Phys. Lett. B 30 (1969) 500–505. doi:10.1016/0370-2693(69)90184-1.

[533] S. P. Denisov, S. V. Donskov, Y. P. Gorin, V. A. Kachanov, V. M. Kutjin, A. I. Petrukhin, Y. D. Prokoshkin, E. A. Razuvaev, et al., Measurements of antideuteron absorption and stripping cross sections at the momentum 13.3 GeV/c, Nucl. Phys. B 31 (1971) 253–260. doi:10.1016/0550-3213(71)90229-x.

[534] R. L. Workman, et al. (Particle Data Group), Review of Particle Physics, PTEP 2022 (2022) 083C01. doi:10.1093/ptep/ptac097.

[535] F. Balestra, S. Bossolasco, M. P. Bussa, L. Bussa, L. Ferrero, D. Panzieri, G. Piragino, F. Tosello, et al., Inelastic interaction of antiprotons with 4He nuclei between 200 and 600 MeV/c, Phys. Lett. B 165 (1985) 265–269. doi:10.1016/0370-2693(85)91227-4.

[536] F. Balestra, R. Barbieri, Y. A. Batusov, G. Bendiscioli, F. O. Breivik, S. Bossolasco, M. P. Bussa, L. Busso, et al., $\overline{p}$-^{3}He reaction cross section at 200 MeV/c, Phys. Lett. B 215 (1988) 247–250. doi:10.1016/0370-2693(88)91428-1.

[537] B. Cork, G. R. Lambertson, O. Piccioni, W. A. Wenzel, Cross Sections for Antiprotons in Hydrogen, Beryllium, Carbon, and Lead, Phys. Rev. 107 (1957) 248–256. doi:10.1103/PhysRev.107.248.

[538] H. Aihara, J. Chiba, H. Fujii, T. Fujii, H. Iwasaki, T. Kamae, K. Nakamura, T. Sumiyoshi, et al., Absorption cross sections for antiprotons on carbon, aluminum and copper at 485 and 597 MeV/c, Nucl. Phys. A 360 (1981) 291–296. doi:10.1016/0375-9474(81)90147-0.

[539] L. E. Agnew, O. Chamberlain, D. V. Keller, R. Mermod, E. H. Rogers, H. M. Steiner, C. Wiegand, Experiments on Antiprotons: Cross Sections of Complex Nuclei, Phys. Rev. 108 (1957) 1545–1553. doi:10.1103/PhysRev.108.1545.

[540] S. Acharya, et al. (ALICE collaboration), Measurement of the Low-Energy Antideuteron Inelastic Cross Section, Phys. Rev. Lett. 125 (2020) 162001. doi:10.1103/PhysRevLett.125.162001.

[541] F. Binon, S. P. Denisov, S. V. Donskov, P. Duteil, G. Giacomelli, Y. P. Gorin, V. A. Kachanov, V. M. Kutyin, et al., Absorption cross-sections of 25 GeV/c antideuterons in Li, C, Al, Cu and Pb, Phys. Lett. B 31 (1970) 230–232. doi:10.1016/0370-2693(70)90112-7.

[542] S. P. Denisov, Y. P. Dmitrevski, S. V. Donskov, Y. P. Gorin, Y. M. Melnik, A. I. Petrukhin, Y. D. Prokoshkin, V. S. Seleznev, et al., Energy dependence of total cross-sections on protons in the momentum range up to 65 GeV/c, Phys. Lett. B 36 (1971) 528–532. doi:10.1016/0370-2693(71)90548-x.

[543] S. Acharya, et al. (ALICE collaboration), Measurement of the low-energy antitriton inelastic cross section, Phys. Lett. B 848 (2024). doi:10.1016/j.physletb.2023.138337.

[544] F. Alemanno, et al. (DAMPE collaboration), Observation of a spectral hardening in cosmic ray boron spectrum with the DAMPE space mission (2024). arXiv:2412.11460.

[545] O. Adriani, et al. (PAMELA collaboration), Measurement of Boron and Carbon Fluxes in Cosmic Rays with the PAMELA Experiment, ApJ 791 (2014) 93. doi:10.1088/0004-637X/791/2/93. arXiv:1407.1657.

[546] D. Mueller, S. P. Swordy, P. Meyer, J. L'Heureux, J. M. Grunsfeld, Energy Spectra and Composition of Primary Cosmic Rays, ApJ 374 (1991) 356. doi:10.1086/170125.

[547] H. S. Ahn, et al. (CREAM), Energy Spectra of Cosmic-ray Nuclei at High Energies, ApJ 707 (2009) 593–603. doi:10.1088/0004-637X/707/1/593. arXiv:0911.1889.

[548] S. Agostinelli, J. Allison, K. Amako, J. Apostolakis, H. Araujo, P. Arce, M. Asai, D. Axen, et al., Geant4—a simulation toolkit, Nucl. Instr. Meth. Phys. Res. A 506 (2003) 250–303. doi:10.1016/s0168-9002(03)01368-8.

[549] G. Battistoni, T. Boehlen, F. Cerutti, P. W. Chin, L. S. Esposito, A. Fassò, A. Ferrari, A. Lechner, et al., Overview of the FLUKA code, Ann. Nucl. Energy 82 (2015) 10–18. doi:10.1016/j.anucene.2014.11.007.

[550] C. Ahdida, D. Bozzato, D. Calzolari, F. Cerutti, N. Charitonidis, A. Cimmino, A. Coronetti, G. L. D'Alessandro, et al., New Capabilities of the FLUKA Multi-Purpose Code, Front. Phys. 9 (2022). doi:10.3389/fphy.2021.788253.

[551] Q. Yan, V. Choutko, A. Oliva, M. Paniccia, Measurements of nuclear interaction cross sections with the Alpha Magnetic Spectrometer on the International Space Station, Nucl. Phys. A 996 (2020) 121712. doi:10.1016/j.nuclphysa.2020.121712.

[552] F. Alemanno, et al. (DAMPE collaboration), Hadronic cross section measurements with the DAMPE space mission using 20 GeV-10 TeV cosmic-ray protons and ^{4}He, Phys. Rev. D 111 (2025) 012002. doi:10.1103/PhysRevD.111.012002.

[553] M. Doser, M. Botlo, S. Ahmad, C. Amsler, R. Armenteros, E. G. Auld, D. A. Axen, D. Bailey, et al., Annihilation into $\pi^+\pi^-$ and K^+K^- from atomic p states, Nucl. Phys. A 486 (1988) 493–511. doi:10.1016/0375-9474(88)90159-5.

[554] C. Amsler, H. Breuker, M. Bumbar, M. Cerwenka, G. Costantini, R. Ferragut, M. Fleck, M. Giammarchi, et al., Antiproton annihilation at rest in thin solid targets and comparison with Monte Carlo simulations, Eur. Phys. J. A 60 (2024) 225. doi:10.1140/epja/s10050-024-01428-x.

[555] L. E. Agnew, T. Elioff, W. B. Fowler, R. L. Lander, W. M. Powell, E. Segrè, H. M. Steiner, H. S. White, et al., Antiproton Interactions in Hydrogen and Carbon below 200 Mev, Phys. Rev. 118 (1960) 1371–1391. doi:10.1103/PhysRev.118.1371.

[556] J. G. Loken, M. Derrick, Some low energy proton-antiproton cross sections, Phys. Letters 3 (1963) 334–335. doi:10.1016/0031-9163(63)90179-3.

[557] K. Böckmann, B. Nellen, E. Paul, B. Wagini, I. Borecka, J. Diaz, U. Heeren, U. Liebermeister, et al., Elastic scattering, pion production, and annihilation into pions in antiproton-proton interactions at 5.7 GeV/c, Nuovo Cimento A 42 (1966) 954–996. doi:10.1007/bf02720569.

[558] D. Cline, J. English, D. D. Reeder, Measurement of the Proton-Antiproton Total Annihilation Cross Section at Low Energy, Phys. Rev. Lett. 27 (1971) 71–74. doi:10.1103/PhysRevLett.27.71.

[559] W. Brückner, B. Cujec, H. Döbbeling, K. Dworschak, F. Güttner, H. Kneis, S. Majewski, M. Nomachi, et al., Measurements of the antiproton-proton annihilation cross-section in the beam momentum range between 180 and 600 MeV/c, Z. Physik A 335 (1990) 217–229. doi:10.1007/bf01294477.

[560] O. Chamberlain, G. Goldhaber, L. Jauneau, T. Kalogeropoulos, E. Segrè, R. Silberberg, Antiproton-Nucleon Annihilation Process. II, Phys. Rev. 113 (1959) 1615–1634. doi:10.1103/PhysRev.113.1615.

[561] P. L. McGaughey, K. D. Bol, M. R. Clover, R. M. DeVries, N. J. DiGiacomo, J. S. Kapustinsky, W. E. Sondheim, G. R. Smith, et al., Dynamics of low-energy antiproton annihilation in nuclei as inferred from inclusive proton and pion measurements, Phys. Rev. Lett. 56 (1986) 2156–2159. doi:10.1103/PhysRevLett.56.2156.

[562] W. Markiel, H. Daniel, T. Von Egidy, F. J. Hartmann, P. Hofmann, W. Kanert, H. S. Plendl, K. Ziock, et al., Emission of helium ions after antiproton annihilation in nuclei, Nucl. Phys. A 485 (1988) 445–460. doi:10.1016/0375-9474(88)90547-7.

[563] J. Cugnon, J. Vandermeulen, Antiproton-nucleus interaction, Annales de Physique 14 (1989) 49–87. doi:10.1051/anphys:019890040104900.

[564] J. Riedlberger, C. Amsler, M. Doser, U. Straumann, P. Truol, D. Bailey, S. Barlag, U. Gastaldi, et al., Antiproton annihilation at rest in nitrogen and deuterium gas, Phys. Rev. C 40 (1989) 2717–2731. doi:10.1103/physrevc.40.2717.

[565] A. S. Sudov, A. S. Botvina, A. S. Iljinov, Y. S. Golubeva, V. G. Nedorezov, H. Daniel, T. von Egidy, F. J. Hartmann, et al., Production of light particles after antiproton-nucleus annihilation and their interpretation with statistical models, Nucl. Phys. A 554 (1993) 223–245. doi:10.1016/0375-9474(93)90340-4.

[566] S. Ahmad, B. E. Bonner, J. A. Buchanan, C. S. Chan, J. M. Clement, S. E. Eiseman, A. Empi, A. Etkin, et al., Antiproton-nucleus interactions at 5 to 9 GeV/c, Nucl. Phys. A 558 (1993) 393–403. doi:10.1016/0375-9474(93)90408-p.

[567] D. Zharenov, Interaction of antiprotons with nuclear matter within the INCL model, Ph.D. thesis, Université Paris-Saclay, 2023.

[568] A. Wrońska, H. Aghai–Khozani, M. Corradini, R. Hayano, M. Hori, M. Leali, E. Lodi–Rizzini, V. Mascagna, et al., New results of the antiproton-carbon annihilation cross section measurement at low energies, Eur. Phys. J. Conferences 130 (2016). doi:10.1051/epjconf/201613007014.

[569] H. Aghai-Khozani, A. Bianconi, M. Corradini, R. Hayano, M. Hori, M. Leali, E. Lodi Rizzini, V. Mascagna, et al., Measurement of the antiproton–nucleus annihilation cross-section at low energy, Nucl. Phys. A 970 (2018) 366–378. doi:10.1016/j.nuclphysa.2018.01.001.

[570] V. F. Andreyev, P. S. Baranov, S. V. Levonyan, Y. S. Pol, L. V. Fil'koy, Y. S. Golubeva, A. S. Iljinov, Multiplicities and correlations of secondary charged particles in the interactions of antineutrons and antideuterons with a momentum of 6.1 GeV/c per nucleon with tantalum nuclei, Nuovo Cimento A 103 (1990) 1163–1176. doi:10.1007/bf02820545.

[571] B. Gunderson, J. Learned, J. Mapp, D. D. Reeder, Measurement of the antineutron-proton cross section at low energy, Phys. Rev. D 23 (1981) 587–594. doi:10.1103/PhysRevD.23.587.

[572] T. Armstrong, C. Chu a, J. Clement b, C. Elinon c, M. Furic a, K. Hartman b, A. Hicks a, E. Hungerford a, et al., Measurement of antineutron-proton total and annihilation cross sections from 100 to 500 MeV/c, Phys. Rev. D 36 (1987) 659–673. doi:10.1103/physrevd.36.659.

[573] F. Iazzi, A. Feliciello, M. Agnello, M. Astrua, E. Botta, T. Bressani, D. Calvo, S. Costa, et al., Antineutron–proton total cross section from 50 to 400 MeV/c, Phys. Lett. B 475 (2000) 378–385. doi:10.1016/s0370-2693(00)00086-1.

[574] M. Astrua, E. Botta, T. Bressani, D. Calvo, C. Casalegno, A. Feliciello, A. Filippi, S. Marcello, et al., Antineutron–nucleus annihilation cross sections below 400 MeV/c, Nucl. Phys. A 697 (2002) 209–224. doi:10.1016/s0375-9474(01)01252-0.

[575] S. Gori, et al., ACE (Accelerator Complex Evolution) Science Workshop Report, 2024. arXiv:2403.02422.
[576] K. Ammigan, et al., HEP High Power Targetry Roadmap – Workshop Report, 2025. arXiv:2502.03305.
[577] P. Capiluppi, A. Bertin, A. Bussière, R. J. Ellis, G. Giacomelli, A. M. Rossi, G. Vannini, Charged particle production in proton-proton inclusive reaction at very high energies, Nucl. Phys. B 79 (1974) 189–258. doi:10.1016/0550-3213(74)90484-2.
[578] B. Alper, H. Böggild, P. Booth, F. Bulos, L. J. Carolll, G. Damgaard, G. Von Dardel, B. Duff, et al., Production spectra of $\pi^{\pm}$, K $^{\pm}$, p $^{\pm}$ at large angles in proton-proton collisions in the CERN intersecting storage rings, Nucl. Phys. B 100 (1975) 237–290. doi:10.1016/0550-3213(75)90618-5.
[579] Y. M. Antipov, S. P. Denisov, S. V. Donskov, Y. P. Gorin, V. A. Kachanov, V. P. Khromov, V. M. Kutyin, L. G. Landsberg, et al., Observation of antihelium-3, Nucl. Phys. B 31 (1971) 235–252. doi:10.1016/0550-3213(71)90228-8.
[580] W. Bozzoli, A. Bussiere, G. Giacomelli, E. Lesquoy, R. Meunier, L. Moscoso, A. Muller, F. Rimondi, et al., Production of d, T, ^{3}He, $\overline{d}$, $\overline{t}$ and $\overline{^3\mathrm{He}}$ by 200 GeV Protons, Nucl. Phys. B 144 (1978) 317–328. doi:10.1016/0550-3213(78)90373-5.
[581] A. A. Alves Jr., et al. (LHCb collaboration), The LHCb detector at the LHC, JINST 3 (2008) S08005. doi:10.1088/1748-0221/3/08/S08005.
[582] C. Barschel, Precision luminosity measurement at LHCb with beam-gas imaging, Ph.D. thesis, RWTH Aachen U., 2014. URL: https://cds.cern.ch/record/1693671, presented 05 Mar 2014.
[583] R. Aaij, et al. (LHCb collaboration), The LHCb Upgrade I, JINST 19 (2024) P05065. doi:10.1088/1748-0221/19/05/P05065. arXiv:2305.10515.
[584] R. Aaij, et al. (LHCb collaboration), Measurement of antiproton production from antihyperon decays in pHe collisions at $\sqrt{s_{\mathrm{NN}}} = 110$ GeV, Eur. Phys. J. C 83 (2023). doi:10.1140/epjc/s10052-023-11673-x.
[585] A. Bursche, et al. (LHCb collaboration), Physics opportunities with the fixed-target program of the LHCb experiment using an unpolarized gas target, Technical Report, CERN, Geneva, 2018. URL: https://cds.cern.ch/record/2649878.
[586] Light nuclei reconstruction and identification with time of flight measurement (LHCb collaboration), 2023. URL: https://cds.cern.ch/record/2868172.
[587] C. Lucarelli, Extending the physics reach of the fixed-target programme at the LHCb experiment, Ph.D. thesis, Florence U., 2024. URL: https://cds.cern.ch/record/2889345, presented 24 Jan 2024.
[588] R. Aaij, , et al. (LHCb collaboration), Helium identification with LHCb, JINST 19 (2024) P02010. doi:10.1088/1748-0221/19/02/P02010.
[589] Observation of antihypertriton in pp collisions with LHCb (LHCb collaboration), Technical Report, CERN, Geneva, 2024. URL: https://cds.cern.ch/record/2868251?ln=it.
[590] J. Baptista Leite, et al. (LHCb collaboration), LHCb Framework TDR for the LHCb Upgrade II Opportunities in flavour physics, and beyond, in the HL-LHC era, Technical Report CERN-LHCC-2021-012, CERN, Geneva, 2022. URL: https://cds.cern.ch/record/2776420?ln=en.
[591] LHCb Upgrade II Scoping Document (LHCb collaboration), Technical Report CERN-LHCC-2024-010, CERN, Geneva, 2024. URL: https://cds.cern.ch/record/2903094?ln=en, under LHCC review.
[592] K. Aamodt, et al. (ALICE collaboration), The ALICE experiment at the CERN LHC, JINST 3 (2008) S08002. doi:10.1088/1748-0221/3/08/S08002.
[593] K. Aamodt, et al. (ALICE collaboration), Midrapidity antiproton-to-proton ratio in pp collisions at $\sqrt{s} = 0.9$ and 7 TeV measured by the ALICE experiment, Phys. Rev. Lett. 105 (2010) 072002. doi:10.1103/PhysRevLett.105.072002. arXiv:1006.5432.
[594] J. Adam, et al. (ALICE collaboration), Multiplicity dependence of charged pion, kaon, and (anti)proton production at large transverse momentum in p-Pb collisions at $\sqrt{s_{\mathrm{NN}}} = 5.02$ TeV, Phys. Lett. B 760 (2016) 720–735. doi:10.1016/j.physletb.2016.07.050. arXiv:1601.03658.
[595] S. Acharya, D. Adamová, S. P. Adhya, A. Adler, J. Adolfsson, M. M. Aggarwal, G. Aglieri Rinella, M. Agnello, et al. (ALICE collaboration), Production of charged pions, kaons, and (anti-)protons in Pb-Pb and inelastic pp collisions at $\sqrt{s_{NN}} = 5.02$ TeV, Phys. Rev. C 101 (2020) 044907. doi:10.1103/PhysRevC.101.044907.
[596] S. Acharya, et al. (ALICE collaboration), Production of pions, kaons, (anti-)protons and ϕ mesons in Xe–Xe collisions at $\sqrt{s_{\mathrm{NN}}} = 5.44$ TeV, Eur. Phys. J. C 81 (2021) 584. doi:10.1140/epjc/s10052-021-09304-4. arXiv:2101.03100.
[597] S. Acharya, et al. (ALICE collaboration), Measurement of the production and elliptic flow of (anti)nuclei in Xe-Xe collisions at $\sqrt{s_{\mathrm{NN}}}$ =5.44 TeV, Phys. Rev. C 110 (2024) 064901. doi:10.1103/PhysRevC.110.064901. arXiv:2405.19826.
[598] S. Acharya, et al. (ALICE collaboration), Multiplicity dependence of light (anti-)nuclei production in p-Pb collisions at $\sqrt{s_{\mathrm{NN}}} = 5.02$ TeV, Phys. Lett. B 800 (2020) 135043. doi:10.1016/j.physletb.2019.135043. arXiv:1906.03136.
[599] S. Acharya, et al. (ALICE collaboration), Measurement of the production of (anti)nuclei in p–Pb collisions at $\sqrt{s_{\mathrm{NN}}}$ =8.16TeV, Phys. Lett. B 846 (2023) 137795. doi:10.1016/j.physletb.2023.137795. arXiv:2212.04777.
[600] M. Rasà (ALICE collaboration), Light (anti)nuclei production with the ALICE experiment at the LHC, Nuovo Cimento C 47 (2024) 82. doi:10.1393/ncc/i2024-24082-3.
[601] E. Bartsch (ALICE collaboration), Results on light (anti)hypernuclei production with ALICE at the LHC, J. Phys. Conf. Series 2586 (2023) 012014. doi:10.1088/1742-6596/2586/1/012014.
[602] S. Acharya, et al. (ALICE collaboration), Search for a common baryon source in high-multiplicity pp collisions at the LHC, Phys. Lett. B 811 (2020) 135849. doi:10.1016/j.physletb.2020.135849. arXiv:2004.08018.
[603] S. Acharya, et al. (ALICE collaboration), Common femtoscopic hadron-emission source in pp collisions at the LHC (2023). arXiv:2311.14527.
[604] S. Acharya, et al. (ALICE collaboration), Investigating the p-$\pi^{\pm}$ and p-p-$\pi^{\pm}$ dynamics with femtoscopy in pp collisions at $\sqrt{s} = 13$ TeV (2025). arXiv:2502.20200.
[605] L. Fabbietti, V. Mantovani Sarti, O. Vazquez Doce, Study of the Strong Interaction Among Hadrons with Correlations at

the LHC, Ann. Rev. Nucl. Part. Sci. 71 (2021) 377–402. doi:10.1146/annurev-nucl-102419-034438. arXiv:2012.09806.
[606] S. Acharya, et al. (ALICE collaboration), Towards the understanding of the genuine three-body interaction for p–p–p and p–p–Λ, Eur. Phys. J. A 59 (2023) 145. doi:10.1140/epja/s10050-023-00998-6. arXiv:2206.03344.
[607] D. L. Mihaylov, J. Haidenbauer, V. M. Sarti, Constraining the pΛ interaction from a combined analysis of scattering data and correlation functions, Phys. Lett. B 850 (2024) 138550. doi:10.1016/j.physletb.2024.138550. arXiv:2312.16970.
[608] Letter of intent for ALICE 3: A next-generation heavy-ion experiment at the LHC (ALICE collaboration) (2022). arXiv:2211.02491.
[609] O. Adriani, et al. (LHCf collaboration), The LHCf detector at the CERN Large Hadron Collider, JINST 3 (2008) S08006. doi:10.1088/1748-0221/3/08/S08006.
[610] O. Adriani, et al. (LHCf collaboration), Measurement of inclusive forward neutron production cross section in proton-proton collisions at $\sqrt{s}$ = 13 TeV with the LHCf Arm2 detector, J. High Energy Phys. 11 (2018) 073. doi:10.1007/JHEP11(2018)073. arXiv:1808.09877.
[611] O. Adriani, et al. (LHCf collaboration), Measurement of energy flow, cross section and average inelasticity of forward neutrons produced in $\sqrt{s}$ = 13 TeV proton-proton collisions with the LHCf Arm2 detector, J. High Energy Phys. 07 (2020) 016. doi:10.1007/JHEP07(2020)016. arXiv:2003.02192.
[612] O. Adriani, et al. (LHCf collaboration), Measurement of forward photon production cross-section in proton–proton collisions at $\sqrt{s}$ = 13 TeV with the LHCf detector, Phys. Lett. B 780 (2018) 233–239. doi:10.1016/j.physletb.2017.12.050. arXiv:1703.07678.
[613] G. Piparo, et al. (LHCf collaboration), Measurement of the forward η meson production rate in p-p collisions at $\sqrt{s}$ = 13 TeV with the LHCf-Arm2 detector, J. High Energy Phys. 10 (2023) 169. doi:10.1007/JHEP10(2023)169. arXiv:2305.06633.
[614] M. Buenerd, I. Efthymiopoulos, A High Energy Secondary Beam of Ion Fragments for Instrumental Tests at CERN, Technical Report CERN-AB-2003-052-ATB, CERN, 2003. doi:https://cds.cern.ch/record/622246.
[615] H. Strobele, I. Efthymiopoulos, Light work with heavy ions, CERN Cour. 52N4 (2012) 33–35. doi:http://cerncourier.com/cws/article/cern/49354.
[616] H. Adhikary, et al. (NA61/SHINE collaboration), Measurement of the mass-changing, charge-changing and production cross sections of ^{11}C, ^{11}B and ^{10}B nuclei in ^{12}C+p interactions at 13.5 GeV/c per nucleon (2024). arXiv:2410.18273.
[617] B. Adams, et al. (COMPASS++/AMBER proto-collaboration), COMPASS++/AMBER: Proposal for Measurements at the M2 beam line of the CERN SPS Phase-1: 2022-2024, Technical Report, CERN, Geneva, 2019. URL: https://cds.cern.ch/record/2676885, the collaboration has not yet constituted itself, thus instead of a Spokesperson currently the nominated Contact Person is acting in place.
[618] M. Zemko, V. Frolov, S. Huber, V. Jary, I. Konorov, A. Kveton, D. Levit, J. Novy, et al., Free-running data acquisition system for the AMBER experiment, Eur. Phys. J. Conferences 251 (2021) 04028. doi:10.1051/epjconf/202125104028.
[619] N. Abgrall, et al. (NA61/SHINE collaboration), NA61/SHINE facility at the CERN SPS: beams and detector system, JINST 9 (2014) 6005P. doi:10.1088/1748-0221/9/06/P06005. arXiv:1401.4699.
[620] M. Gazdzicki (NA61/SHINE collaboration), Report from the NA61/SHINE experiment at the CERN SPS, Technical Report, CERN, Geneva, 2019. doi:10.17181/CERN.E3JY.7Z6E.
[621] L. Fields, P. Podlaski (NA61/SHINE collaboration), Report from the NA61/SHINE experiment at the CERN SPS, Technical Report, CERN, Geneva, 2020. URL: http://cds.cern.ch/record/2739340.
[622] A. Aduszkiewicz, et al. (NA61/SHINE collaboration), Measurement of meson resonance production in π^- + C interactions at SPS energies, Eur. Phys. J. C 77 (2017) 626. doi:10.1140/epjc/s10052-017-5184-z. arXiv:1705.08206.
[623] H. Adhikary, et al. (NA61/SHINE collaboration), Measurement of hadron production in π–C interactions at 158 and 350 GeV/c with NA61/SHINE at the CERN SPS, Phys. Rev. D 107 (2023) 062004. doi:10.1103/PhysRevD.107.062004. arXiv:2209.10561.
[624] T. Anticic, et al. (NA49 collaboration), Antideuteron and deuteron production in midcentral Pb+Pb collisions at 158A GeV, Phys. Rev. C 85 (2012) 044913. doi:10.1103/PhysRevC.85.044913. arXiv:1111.2588.
[625] T. Anticic, et al. (NA49 collaboration), Production of deuterium, tritium, and ^{3}He in central Pb+Pb collisions at 20A, 30A, 40A, 80A, and 158A GeV at the CERN Super Proton Synchrotron, Phys. Rev. C 94 (2016) 044906. doi:10.1103/PhysRevC.94.044906. arXiv:1606.04234.
[626] The neutron Time-Of-Flight facility at CERN: Technical Description (n_TOF collaboration), 2013. URL: https://cds.cern.ch/record/1514680.
[627] M. Barbagallo, et al. (n_TOF collaboration), (n,cp) reactions study at the n_TOF facility at CERN: results for the Cosmological Lithium problem, CERN Proc. 1 (2019) 259–264.
[628] O. Kester, P. Spiller, H. Stoecker, FAIR at GSI, Challenges and Goals for Accelerators in the XXI Century (2016). doi:10.1142/9789814436403_0032.
[629] S. Rossi, The National Centre for Oncological Hadrontherapy (CNAO): Status and perspectives, Physica Medica 31 (2015) 333–351. doi:https://doi.org/10.1016/j.ejmp.2015.03.001.
[630] W. Fischer, The Relativistic Heavy Ion Collider, in: S. Myers, O. Bruning (Eds.), Challenges and Goals for Accelerators in the XXI Century, 2016, pp. 351–369. doi:10.1142/9789814436403_0021.
[631] W. Schimmerling, Genesis of the NASA Space Radiation Laboratory, Life Sciences in Space Research 9 (2016) 2–11. doi:10.1016/j.lssr.2016.03.001.
[632] P. N. Peplowski, Cross sections for the production of radionuclides via ^{nat}Cu(p,X) spallation reactions for proton energies from 250 MeV to 2 GeV, Nucl. Phys. A 1006 (2021) 122067. doi:https://doi.org/10.1016/j.nuclphysa.2020.122067.
[633] H. Geissel, P. Armbruster, K. Behr, A. Brünle, K. Burkard, M. Chen, H. Folger, B. Franczak, et al., The GSI projectile fragment separator (FRS): a versatile magnetic system for relativistic heavy ions, Nucl. Instr. Meth. Phys. Res. B 70

(1992) 286–297. doi:10.1016/0168-583X(92)95944-M.
[634] C. Paradela, L. Tassan-Got, J. Benlliure, J. L. Rodríguez-Sánchez, L. Audouin, A. Boudard, E. Casarejos, T. Enqvist, et al., Isotopic production cross sections of residual nuclei in the spallation reaction ^{136}Xe+p at 200A MeV, Phys. Rev. C 95 (2017) 044606. doi:10.1103/PhysRevC.95.044606.
[635] P. Napolitani, K.-H. Schmidt, L. Tassan-Got, P. Armbruster, T. Enqvist, A. Heinz, V. Henzl, D. Henzlova, et al., Measurement of the complete nuclide production and kinetic energies of the system ^{136}Xe+H at 1 GeV per nucleon, Phys. Rev. C 76 (2007) 064609. doi:10.1103/PhysRevC.76.064609.
[636] F. Rejmund, B. Mustapha, P. Armbruster, J. Benlliure, M. Bernas, A. Boudard, J. Dufour, T. Enqvist, et al., Measurement of isotopic cross sections of spallation residues in 800A MeV ^{197}Au+p collisions, Nucl. Phys. A 683 (2001) 540–565. doi:10.1016/S0375-9474(00)00468-1.
[637] L. Audouin, L. Tassan-Got, P. Armbruster, J. Benlliure, M. Bernas, A. Boudard, E. Casarejos, S. Czajkowski, et al., Evaporation residues produced in spallation of ^{208}Pb by protons at 500A MeV, Nucl. Phys. A 768 (2006) 1–21. doi:10.1016/j.nuclphysa.2006.01.006.
[638] T. Enqvist, W. Wlazło, P. Armbruster, J. Benlliure, M. Bernas, A. Boudard, S. Czajkowski, R. Legrain, et al., Isotopic yields and kinetic energies of primary residues in 1A GeV ^{208}Pb+p reactions, Nucl. Phys. A 686 (2001) 481–524. doi:https://doi.org/10.1016/S0375-9474(00)00563-7.
[639] J. Taïeb, K.-H. Schmidt, L. Tassan-Got, P. Armbruster, J. Benlliure, M. Bernas, A. Boudard, E. Casarejos, et al., Evaporation residues produced in the spallation reaction ^{238}U+p at 1A GeV, Nucl. Phys. A 724 (2003) 413–430. doi:10.1016/S0375-9474(03)01517-3.
[640] E. Le Gentil, T. Aumann, C. O. Bacri, J. Benlliure, S. Bianchin, M. Böhmer, A. Boudard, J. Brzychczyk, et al., Coincidence Measurement of Residues and Light Particles in the Reaction ^{56}Fe+p at 1 GeV per Nucleon with the Spallation Reactions Setup SPALADIN, Phys. Rev. Lett. 100 (2008) 022701. doi:10.1103/PhysRevLett.100.022701.
[641] T. Yordanov, O. Ducret, et al., Study of the reaction mechanisms of ^{136}Xe+p and ^{136}Xe+^{12}C at 1A GeV with inverse kinematics and large-acceptance detectors, Eur. Phys. J. A 55 (2019) 11. doi:10.1140/epja/i2019-12683-8.
[642] P. Spiller, R. Balss, P. Bartolome, J. Blaurock, U. Blell, O. Boine-Frankenheim, L. Bozyk, M. Chorowski, et al., The FAIR Heavy Ion Synchrotron SIS100, JINST 15 (2020) T12013–T12013. doi:10.1088/1748-0221/15/12/T12013.
[643] H. Geissel, H. Weick, M. Winkler, G. Münzenberg, V. Chichkine, M. Yavor, T. Aumann, K. Behr, et al., The Super-FRS project at GSI, Nucl. Instr. Meth. Phys. Res. B 204 (2003) 71–85. doi:10.1016/S0168-583X(02)01893-1, 14th International Conference on Electromagnetic Isotope Separators and Techniques Related to their Applications.
[644] J. W. Xia, et al., The heavy ion cooler-storage-ring project (HIRFL-CSR) at Lanzhou, Nucl. Instr. Meth. Phys. Res. A 488 (2002) 11–25. doi:10.1016/S0168-9002(02)00475-8.
[645] X. Zhou, J. Yang (HIAF project team), Status of the high-intensity heavy-ion accelerator facility in China, AAPPS Bull. 32 (2022) 35. doi:10.1007/s43673-022-00064-1.
[646] L. N. Sheng, et al., Ion-optical updates and performance analysis of High energy FRagment Separator (HFRS) at HIAF, Nucl. Instr. Meth. Phys. Res. B 547 (2024) 165214. doi:10.1016/j.nimb.2023.165214.
[647] B. Mei, et al., Isotopic cross sections in fragmentation reactions of ^{12,14}C, ^{14,16}N, and ^{16}O projectiles on a carbon target, Phys. Rev. C 108 (2023) 034602. doi:10.1103/PhysRevC.108.034602.
[648] R. J. Glauber, Cross Sections in Deuterium at High Energies, Phys. Rev. 100 (1955) 242–248. doi:10.1103/PhysRev.100.242.
[649] R. J. Glauber, High-energy collision theory, in: W. E. Brittin, et al. (Eds.), Lectures in Theoretical Physics, volume I, Interscience, New York, 1959, p. 315.
[650] V. N. Gribov, Glauber Corrections and the Interaction between High-energy Hadrons and Nuclei, Sov. Phys. JETP 29 (1969) 483. URL: https://ui.adsabs.harvard.edu/abs/1969JETP...29..483G.
[651] V. N. Gribov, A Reggeon Diagram Technique, Sov. Phys. JETP 26 (1968) 414–423.
[652] D. Kyratzis, Latest advancements of the HERD space mission, Nucl. Instr. Meth. Phys. Res. A 1048 (2023) 167970. doi:10.1016/j.nima.2022.167970.
[653] R. M. Baltrusaitis, G. L. Cassiday, J. W. Elbert, P. R. Gerhardy, S. Ko, E. C. Loh, Y. Mizumoto, P. Sokolsky, et al., Total Proton-Proton Cross Section at $\sqrt{s} = 30$ TeV, Phys. Rev. Lett. 52 (1984) 1380–1383. doi:10.1103/PhysRevLett.52.1380.
[654] M. Aglietta, et al., Measurement of the proton-air inelastic cross section at $\sqrt{s} \approx 2$ TeV from the EAS-TOP experiment, Phys. Rev. D 79 (2009) 032004. doi:10.1103/PhysRevD.79.032004.
[655] S. P. Knurenko, V. R. Sleptsova, I. E. Sleptsov, N. N. Kalmykov, S. S. Ostapchenko, Longitudinal EAS development at E(0) = 10^{18} eV to 3×10^{19} eV and the QGSJET model, in: 26th ICRC, 1999.
[656] S. Knurenko, Fluctuations of the depth of maximum in extensive air showers and cross-section of p-air inelastic collision for energy range $10^{15} - 10^{17}$ eV, in: 32nd ICRC, 2011, p. 185. doi:10.7529/ICRC2011/V01/0181.
[657] M. Honda, M. Nagano, S. Tonwar, K. Kasahara, T. Hara, N. Hayashida, Y. Matsubara, M. Teshima, et al., Inelastic cross section for p-air collisions from air shower experiments and total cross section for p-p collisions up to $\sqrt{s} = 24$ TeV, Phys. Rev. Lett. 70 (1993) 525–528. doi:10.1103/PhysRevLett.70.525.
[658] N. Nesterova, Tien Shan experimental results on the inelastic proton-air cross section at 0.5 – 5 PeV, J. Phys. Conf. Series 409 (2013) 012066. doi:10.1088/1742-6596/409/1/012066.
[659] P. Abreu, et al. (Pierre Auger collaboration), Measurement of the Proton-Air Cross Section at $\sqrt{s} = 57$ TeV with the Pierre Auger Observatory, Phys. Rev. Lett. 109 (2012) 062002. doi:10.1103/PhysRevLett.109.062002. arXiv:1208.1520.
[660] R. M. Ulrich (Pierre Auger collaboration), Extension of the measurement of the proton-air cross section with the Pierre Auger Observatory, in: 34th ICRC, 2016, p. 401. doi:10.22323/1.236.0401.
[661] R. U. Abbasi, et al., Measurement of the proton-air cross section with Telescope Array's Black Rock Mesa and Long Ridge fluorescence detectors, and surface array in hybrid mode, Phys. Rev. D 102 (2020) 062004. doi:10.1103/PhysRevD.

102.062004.
[662] G. Aielli, et al., Proton-air cross section measurement with the ARGO-YBJ cosmic ray experiment, Phys. Rev. D 80 (2009) 092004. doi:10.1103/PhysRevD.80.092004.
[663] H. H. Mielke, H. Foller, J. Engler, J. Knapp, Cosmic ray hadron flux at sea level up to 15 TeV, J. Phys. G Nucl. Phys.. 20 (1994) 637. doi:10.1088/0954-3899/20/4/010.
[664] K. Werner, The hadronic interaction model EPOS, Nucl. Phys. BProc. Suppl. 175-176 (2008) 81–87. doi:10.1016/j.nuclphysbps.2007.10.012.
[665] T. Pierog, I. Karpenko, J. M. Katzy, E. Yatsenko, K. Werner, EPOS LHC: Test of collective hadronization with data measured at the CERN Large Hadron Collider, Phys. Rev. C 92 (2015) 034906. doi:10.1103/PhysRevC.92.034906.
[666] R. Engel, Photoproduction within the two component dual parton model. 1. Amplitudes and cross-sections, Z. Physik C 66 (1995) 203–214. doi:10.1007/BF01496594.
[667] S. Roesler, R. Engel, J. Ranft, The Monte Carlo event generator DPMJET-III, in: Int. Conf. Adv. Monte Carlo Radiat. Phys. Part. Transp. Simul. Appl., 2000, pp. 1033–1038. doi:10.1007/978-3-642-18211-2_166.
[668] A. Fedynitch, Cascade equations and hadronic interactions at very high energies, Ph.D. thesis, KIT, Karlsruhe, Dept. Phys., 2015. doi:10.5445/IR/1000055433.
[669] P. Bożek, W. Broniowski, M. Rybczyński, G. Stefanek, GLISSANDO 3: GLauber Initial-State Simulation AND mOre, ver. 3, Comput. Phys. Commun. 245 (2019) 106850. doi:10.1016/j.cpc.2019.07.014.
[670] V. G. Ableev, V. A. Bodyagin, R. Dymarz, Alpha-nucleus differential cross section at 445 GeV/c per nucleon, Acta Phys. Pol. B 16 (1985) 913–929.
[671] I. Tanihata, et al., Measurements of interaction cross sections and radii of He isotopes, Phys. Lett. B 160 (1985) 380–384. doi:10.1016/0370-2693(85)90005-X.
[672] T. H. Prettyman, J. S. Hendricks, R. C. Reedy, Effects of Meteoroid Shape on Cosmogenic Nuclide Production, in: L. E. Board (Ed.), 77th Annual Meeting of the Meteoritical Society, volume 77 of *LPI Contributions*, 2014, p. 5407.
[673] H. Palme, A. Jones, Solar System Abundances of the Elements, Treatise on Geochemistry 1 (2003) 711. doi:10.1016/B0-08-043751-6/01060-4.
[674] C. Geppert, P. Müller, K. Wendt, C. Schnabel, H. A. Synal, U. Herpers, S. Merchel, Intercomparison measurements between accelerator and laser based mass spectrometry for ultra-trace determination of ^{41}Ca in the $10^{-11}-10^{-10}$ isotopic range, Nucl. Instr. Meth. Phys. Res. B 229 (2005) 519–526. doi:10.1016/j.nimb.2004.12.122.
[675] S. Merchel, W. Bremser, V. Alfimov, M. Arnold, G. Aumaitre, L. Benedetti, D. D. Bourles, M. Caffee, et al., Ultra-trace analysis of ^{36}Cl by accelerator mass spectrometry: an interlaboratory study, Anal. Bioanal. Chem. 400 (2011) 3125–3132. doi:10.1007/s00216-011-4979-2.
[676] M. Christl, C. Vockenhuber, P. W. Kubik, L. Wacker, J. Lachner, V. Alfimov, H. A. Synal, The ETH Zurich AMS facilities: Performance parameters and reference materials, Nucl. Instr. Meth. Phys. Res. B 294 (2013) 29–38. doi:10.1016/j.nimb.2012.03.004.
[677] I. Leya, J. Hirtz, J.-C. David, Galactic Cosmic Rays, Cosmic-Ray Variations, and Cosmogenic Nuclides in Meteorites, ApJ 910 (2021) 136. doi:10.3847/1538-4357/abe52f.
[678] G. Korschinek, A. Bergmaier, T. Faestermann, U. C. Gerstmann, K. Knie, G. Rugel, A. Wallner, I. Dillmann, et al., A new value for the half-life of ^{10}Be by Heavy-Ion Elastic Recoil Detection and liquid scintillation counting, Nucl. Instr. Meth. Phys. Res. B 268 (2010) 187–191. doi:10.1016/j.nimb.2009.09.020.
[679] G. Jörg, Y. Amelin, K. Kossert, C. Lierse v. Gostomski, Precise and direct determination of the half-life of ^{41}Ca, Geochim. Cosmochim. Acta 88 (2012) 51–65. doi:10.1016/j.gca.2012.03.036.
[680] M. U. Sliz, B. A. Hofmann, I. Leya, S. Szidat, C. Espic, J. Gattacceca, R. Braucher, D. Borschneck, et al., Terrestrial ages of seven meteorite strewn fields and two single unpaired meteorites from the Sultanate of Oman determined using ^{14}C and ^{10}Be, Meteorit. Planet. Sci. 57 (2022) 2170–2191. doi:10.1111/maps.13922.
[681] M. Tauseef, I. Leya, J. Gattacceca, B. Hofmann, S. Szidat, R. Braucher, ^{14}C and ^{14}C–^{10}Be terrestrial age dating system for meteorites - New data for four recently fallen meteorites, Meteorit. Planet. Sci. 59 (2024) 1219–1235. doi:10.1111/maps.14144.
[682] R. Michel, On the Unification of Thin Target and Thick Target Approaches to the Interpretation of Cosmogenic Nuclides in Meteorites, Meteoritics 20 (1985) 711.
[683] R. Michel, F. Peiffer, S. Theis, F. Begemann, H. Weber, P. Signer, R. Wieler, P. Cloth, et al., Production of stable and radioactive nuclides in thick stony targets (R = 15 and 25 cm) isotropically irradiated with 600 MeV protons and simulation of the production of cosmogenic nuclides in meteorites, Nucl. Instr. Meth. Phys. Res. B 42 (1989) 76–100. doi:10.1016/0168-583X(89)90013-X.
[684] R. Michel, C. J. Allegre, J. Audouze, F. Begemann, J. L. Birck, P. Cloth, B. Dittrich-Hannen, D. Filges, et al., Simulation of the Interaction of Galactic Protons with Meteoroids: Isotropic Irradiation of an Artificial Iron Meteoroid with 1.6 GeV Protons, Meteoritics 28 (1993) 399. URL: https://ui.adsabs.harvard.edu/abs/1993Metic..28R.399M.
[685] R. Michel, H. J. Lange, I. Leya, U. Herpers, B. Meltzow, B. Dittrich-Hannen, M. Suter, P. W. Kubik, Thick-Target Simulation Experiments as a Basis for Consistent Modeling of Cosmogenic Nuclide Production in Extraterrestrial Matter, Meteoritics 30 (1995) 548.
[686] U. Herpers, R. Rösel, R. Michel, M. Lüpke, D. Filges, P. Dragovitsch, W. Wölfli, B. Dittrich, et al., Simulation of the interaction of galactic protons with meteoroids: On the production of ^{7}Be, ^{10}Be and ^{22}Na in an artifical meteoroid irradiated isotropically with 1.6 GeV protons, Meteoritics 26 (1991) 344. URL: https://ui.adsabs.harvard.edu/abs/1991Metic..26S.344H.
[687] I. Leya, H. J. Lange, M. Lüpke, U. Neupert, R. Daunke, O. Fanenbruck, R. Michel, R. Rösel, et al., Simulation of the interaction of GCR protons with meteoroids: On the production of radionuclides in thick gabbro and iron targets

irradiated isotropically with 1.6 GeV protons, Meteorit. Planet. Sci. 35 (2000) 287–318. doi:10.1111/j.1945-5100.2000.tb01776.x.

[688] I. Leya, R. Michel, Cross sections for neutron-induced reactions up to 1.6 GeV for target elements relevant for cosmochemical, geochemical, and technological applications, Nucl. Instr. Meth. Phys. Res. B 269 (2011) 2487–2503. doi:10.1016/j.nimb.2011.07.011.

[689] J. M. Sisterson, K. J. Kim, R. C. Reedy, Revised Production Rates for ^{22}Na and ^{54}Mn in Meteorites Using Cross Sections Measured for Neutron-induced Reactions, in: S. Mackwell, E. Stansbery (Eds.), Lunar and Planetary Science Conference, Lunar and Planetary Science Conference, 2004, p. 1354. URL: https://ui.adsabs.harvard.edu/abs/2004LPI....35.1354S.

[690] J. M. Sisterson, Cross section measurements for neutron-induced reactions off C, Al, SiO_2, Si and Au producing relatively short-lived radionuclides at neutron energies between 70 and 160 MeV, Nucl. Instr. Meth. Phys. Res. B 261 (2007) 993–995. doi:10.1016/j.nimb.2007.03.030.

[691] Y. Li, X. Zhang, W. Dong, Z. Ren, T. Dong, A. Xu, Simulation of the production rates of cosmogenic nuclides on the Moon based on Geant4, J. Geophys. Res. 122 (2017) 1473–1486. doi:10.1002/2016JA023308.

[692] P. Čechvala, R. Breier, J. Masarik, Production rates of cosmogenic nuclides in extraterrestrial material using GEANT4 software, J. Radioanal. Nucl. Chem. 332 (2023) 4403–4411. doi:10.1007/s10967-023-09135-5.

[693] O. Lyod Pinto, J. Miikael Tiit, Mapping Water on the Moon and Mars using a Muon Tomograph (2023). arXiv:2310.08174.

[694] B. Heisinger, D. Lal, A. J. T. Jull, P. Kubik, S. Ivy-Ochs, S. Neumaier, K. Knie, V. Lazarev, et al., Production of selected cosmogenic radionuclides by muons. 1. Fast muons, Earth Planet. Sci. Lett. 200 (2002) 345–355. doi:10.1016/S0012-821X(02)00640-4.

[695] B. Heisinger, D. Lal, A. J. T. Jull, P. Kubik, S. Ivy-Ochs, K. Knie, E. Nolte, Production of selected cosmogenic radionuclides by muons: 2. Capture of negative muons, Earth Planet. Sci. Lett. 200 (2002) 357–369. doi:10.1016/S0012-821X(02)00641-6.

[696] T. Graf, P. Signer, R. Wieler, U. Herpers, R. Sarafin, Cosmogenic nuclides and nuclear tracks in the chondrite Knyahinya, Geochim. Cosmochim. Acta 54 (1990) 2521–2534. doi:10.1016/0016-7037(90)90239-H.

[697] L. Walsh, U. Schneider, A. Fogtman, C. Kausch, S. McKenna-Lawlor, L. Narici, J. Ngo-Anh, G. Reitz, et al., Research plans in Europe for radiation health hazard assessment in exploratory space missions, Life Sci. Space Res. 21 (2019) 73–82. doi:10.1016/j.lssr.2019.04.002.

[698] National Academies of Sciences, Engineering, and Medicine, Space Radiation and Astronaut Health: Managing and Communicating Cancer Risks, The National Academies Press, Washington, DC, 2021. doi:10.17226/26155.

[699] S. Freese, A. P. Reddy, K. Lehnhardt, Radiation impacts on human health during spaceflight beyond Low Earth Orbit, REACH 2-4 (2016) 1–7. doi:10.1016/j.reach.2016.11.002.

[700] J. Chancellor, G. Scott, J. Sutton, Space Radiation: The Number One Risk to Astronaut Health beyond Low Earth Orbit, Life 4 (2014) 491–510. doi:10.3390/life4030491.

[701] J. G. Roederer, H. Zhang, Dynamics of Magnetically Trapped Particles: Foundations of the Physics of Radiation Belts and Space Plasmas, Astrophysics and Space Science Library, 2 ed., Springer, Berlin, Heidelberg, 2014. doi:10.1007/978-3-642-41530-2.

[702] D. V. Reames, Solar Energetic Particles, Lecture Notes in Physics, 2nd ed., Springer, Cham, 2021. doi:10.1007/978-3-030-66402-2.

[703] J. Wilson, J. Shinn, R. Tripathi, R. Singleterry, M. Clowdsley, S. Thibeault, F. Cheatwood, W. Schimmerling, et al., Issues in deep space radiation protection, Acta Astronautica 49 (2001) 289–312. doi:10.1016/S0094-5765(01)00107-2.

[704] C. Zeitlin, C. La Tessa, The Role of Nuclear Fragmentation in Particle Therapy and Space Radiation Protection, Frontiers in Oncology 6 (2016) 1–13. doi:10.3389/fonc.2016.00065.

[705] C. Zeitlin, Space Radiation Shielding, Springer, Cham, 2021, pp. 353–375. doi:10.1007/978-3-319-12191-8_28.

[706] M. I. Dobynde, Y. Y. Shprits, Radiation environment created with GCRs inside a spacecraft, Life Sci. Space Res. 24 (2020) 116–121. doi:10.1016/j.lssr.2019.09.001.

[707] F. A. Cucinotta, I. Plante, A. L. Ponomarev, M. H. Kim, Nuclear interactions in heavy ion transport and event-based risk models, Radiat. Prot. Dosimetry 143 (2011) 384–90. doi:10.1093/rpd/ncq512.

[708] F. Horst, D. Boscolo, M. Durante, F. Luoni, C. Schuy, U. Weber, Thick shielding against galactic cosmic radiation: A Monte Carlo study with focus on the role of secondary neutrons, Life Sci. Space Res. 33 (2022) 58–68. doi:10.1016/j.lssr.2022.03.003.

[709] L. H. Heilbronn, T. B. Borak, L. W. Townsend, P. E. Tsai, C. A. Burnham, R. A. McBeth, Neutron yields and effective doses produced by Galactic Cosmic Ray interactions in shielded environments in space, Life Sci. Space Res. 7 (2015) 90–9. doi:10.1016/j.lssr.2015.10.005.

[710] T. C. Slaba, S. R. Blattnig, M. S. Clowdsley, Variation in lunar neutron dose estimates, Radiation Research 176 (2011) 827–41. doi:10.1667/rr2616.1.

[711] J. M. DeWitt, E. R. Benton, Secondary proton buildup in space radiation shielding, Life Sci. Space Res. 41 (2024) 119–126. doi:10.1016/j.lssr.2024.02.005.

[712] M. C. Vozenin, Y. Alaghband, O. G. G. Drayson, F. Piaget, R. Leavitt, B. D. Allen, N. L. Doan, T. Rostomyan, et al., More May Not be Better: Enhanced Spacecraft Shielding May Exacerbate Cognitive Decrements by Increasing Pion Exposures during Deep Space Exploration, Radiation Research 201 (2024) 93–103. doi:10.1667/RADE-23-00241.1.S1.

[713] S. L. Koontz, P. A. Boeder, C. Pankop, B. Reddell, The ionizing radiation environment on the International Space Station: performance vs. expectations for avionics and materials, in: IEEE Radiation Effects Data Workshop, IEEE, Seattle, WA, 2005, pp. 110–116. doi:10.1109/redw.2005.1532675.

[714] L. W. Townsend, J. H. Adams, S. R. Blattnig, M. S. Clowdsley, D. J. Fry, I. Jun, C. D. McLeod, J. I. Minow, et al., Solar particle event storm shelter requirements for missions beyond low Earth orbit, Life Sci. Space Res. 17 (2018) 32–39. doi:10.1016/j.lssr.2018.02.002.

[715] M. I. Dobynde, Y. Y. Shprits, A. Y. Drozdov, J. Hoffman, J. Li, Beating 1 Sievert: Optimal Radiation Shielding of Astronauts on a Mission to Mars, Space Weather 19 (2021). doi:10.1029/2021sw002749.

[716] Y. Akisheva, Y. Gourinat, Utilisation of Moon Regolith for Radiation Protection and Thermal Insulation in Permanent Lunar Habitats, Appl. Sci. 11 (2021). doi:10.3390/app11093853.

[717] J. Allison, K. Amako, J. Apostolakis, P. Arce, M. Asai, T. Aso, E. Bagli, A. Bagulya, et al., Recent developments in Geant4, Nucl. Instr. Meth. Phys. Res. A 835 (2016) 186–225. doi:10.1016/j.nima.2016.06.125.

[718] J. W. Wilson, T. C. Slaba, F. F. Badavi, B. D. Reddell, A. A. Bahadori, Advances in NASA radiation transport research: 3DHZETRN, Life Sci. Space Res. 2 (2014) 6–22. doi:10.1016/j.lssr.2014.05.003.

[719] J. W. Wilson, T. C. Slaba, F. F. Badavi, B. D. Reddell, A. A. Bahadori, 3DHZETRN: Shielded ICRU spherical phantom, Life Sci. Space Res. 4 (2015) 46–61. doi:10.1016/j.lssr.2015.01.002.

[720] J. W. Wilson, T. C. Slaba, F. F. Badavi, B. D. Reddell, A. A. Bahadori, 3DHZETRN: Neutron leakage in finite objects, Life Sci. Space Res. 7 (2015) 27–38. doi:10.1016/j.lssr.2015.09.003.

[721] J. W. Wilson, T. C. Slaba, F. F. Badavi, B. D. Reddell, A. A. Bahadori, Solar proton exposure of an ICRU sphere within a complex structure Part I: Combinatorial geometry, Life Sci. Space Res. 9 (2016) 69–76. doi:10.1016/j.lssr.2016.05.002.

[722] J. W. Norbury, Double-Differential FRaGmentation (DDFRG) models for proton and light ion production in high energy nuclear collisions, Nucl. Instr. Meth. Phys. Res. A 986 (2021). doi:10.1016/j.nima.2020.164681.

[723] J. W. Norbury, DDFRG2: Double-Differential FRaGmentation model for pion production in high energy nuclear collisions, Nucl. Instr. Meth. Phys. Res. A 1053 (2023). doi:10.1016/j.nima.2023.168336.

[724] S. R. Blattnig, S. R. Swaminathan, A. T. Kruger, M. Ngom, J. W. Norbury, Parametrizations of inclusive cross sections for pion production in proton-proton collisions, Phys. Rev. D 62 (2000). doi:10.1103/PhysRevD.62.094030.

[725] T. Sato, Y. Iwamoto, S. Hashimoto, T. Ogawa, T. Furuta, S.-I. Abe, T. Kai, Y. Matsuya, et al., Recent improvements of the particle and heavy ion transport code system – PHITS version 3.33, J. Nucl. Sci. Techn. 61 (2023) 127–135. doi:10.1080/00223131.2023.2275736.

[726] Y. Iwamoto, S. Hashimoto, T. Sato, N. Matsuda, S. Kunieda, Y. Çelik, N. Furutachi, K. Niita, Benchmark study of particle and heavy-ion transport code system using shielding integral benchmark archive and database for accelerator-shielding experiments, Journal of Nuclear Science and Technology 59 (2021) 665–675. doi:10.1080/00223131.2021.1993372.

[727] M. E. Rising, J. C. Armstrong, S. R. Bolding, F. B. Brown, J. S. Bull, T. P. Burke, A. R. Clark, D. A. Dixon, et al., MCNP Code Version 6.3.0 Release Notes, Technical Report LA-UR-22-33103, Rev. 1, Los Alamos National Laboratory, Los Alamos, NM, USA, 2023. doi:10.2172/1909545.

[728] M. H. Kim, J. W. Wilson, F. A. Cucinotta, Description of transport codes for space radiation shielding, Health Phys 103 (2012) 621–39. doi:10.1097/HP.0b013e318266732f.

[729] T. Nakamura, L. Heilbronn, Handbook on Secondary Particle Production and Transport by High-Energy Heavy Ions, World Scientific, Singapore, 2005. doi:10.1142/5973.

[730] D. Satoh, D. Moriguchi, T. Kajimoto, H. Uehara, N. Shigyo, M. Ueyama, M. Yoshioka, Y. Uozumi, et al., Measurement of neutron-production double-differential cross-sections on carbon bombarded with 290 MeV/nucleon carbon and oxygen ions, Nucl. Instr. Meth. Phys. Res. A 644 (2011) 59–67. doi:10.1016/j.nima.2011.04.054.

[731] Y. Itashiki, Y. Imahayashi, N. Shigyo, Y. Uozumi, D. Satoh, T. Kajimoto, T. Sanami, Y. Koba, et al., Measurement of Neutron Production Double-differential Cross-sections on Carbon Bombarded with 430 MeV/Nucleon Carbon Ions, J. Radiat. Prot. Res. 41 (2016) 344–349. doi:10.14407/jrpr.2016.41.4.344.

[732] D. L. Stricklin, J. VanHorne-Sealy, C. I. Rios, L. A. Scott Carnell, L. P. Taliaferro, Neutron Radiobiology and Dosimetry, Radiation Research 195 (2021) 480–496. doi:10.1667/RADE-20-00213.1.

[733] W. G. Lynch, Nuclear Fragmentation in Proton- and Heavy-Ion-Induced Reactions, Ann. Rev. Nucl. Part. Sci. 37 (1987) 493–535. doi:10.1146/annurev.ns.37.120187.002425.

[734] A. Luehr, D. C. Hansen, R. Teiwes, N. Sobolevsky, O. Jaekel, N. Bassler, The impact of modeling nuclear fragmentation on delivered dose and radiobiology in ion therapy, Phys. Med. Biol. 57 (2012) 5169. doi:10.1088/0031-9155/57/16/5169.

[735] J. Krimmer, M. Chevallier, J. Constanzo, D. Dauvergne, M. D. Rydt, G. Dedes, N. Freud, P. Henriquet, et al., Collimated prompt gamma TOF measurements with multi-slit multi-detector configurations, JINST 10 (2015) P01011. doi:10.1088/1748-0221/10/01/P01011.

[736] S. Marcatili, J. Collot, S. Curtoni, D. Dauvergne, J.-Y. Hostachy, C. Koumeir, J. M. Létang, J. Livingstone, et al., Ultra-fast prompt gamma detection in single proton counting regime for range monitoring in particle therapy, Phys. Med. Biol. 65 (2020) 245033. doi:10.1088/1361-6560/ab7a6c.

[737] K. Parodi, W. Enghardt, T. Haberer, In-beam PET measurements of β^+ radioactivity induced by proton beams, Phys. Med. Biol. 47 (2001) 21. doi:10.1088/0031-9155/47/1/302.

[738] W. Enghardt, P. Crespo, F. Fiedler, R. Hinz, K. Parodi, J. Pawelke, F. Pönisch, Charged hadron tumour therapy monitoring by means of PET, Nucl. Instr. Meth. Phys. Res. A 525 (2004) 284–288. doi:10.1016/j.nima.2004.03.128, proceedings of the International Conference on Imaging Techniques in Subatomic Physics, Astrophysics, Medicine, Biology and Industry.

[739] C. Finck, Y. Karakaya, V. Reithinger, R. Rescigno, J. Baudot, J. Constanzo, D. Juliani, J. Krimmer, et al., Study for online range monitoring with the interaction vertex imaging method, Phys. Med. Biol. 62 (2017) 9220. doi:10.1088/1361-6560/aa954e.

[740] R. Félix-Bautista, L. Ghesquière-Diérickx, L. Marek, C. Granja, P. Soukup, D. Turecek, L. Kelleter, S. Brons, et al.,

Quality assurance method for monitoring of lateral pencil beam positions in scanned carbon-ion radiotherapy using tracking of secondary ions, Medical Physics 48 (2021) 4411–4424. doi:10.1002/mp.15018.

[741] J. Dudouet, D. Cussol, D. Durand, M. Labalme, Benchmarking Geant4 nuclear models for hadron therapy with 95 MeV/nucleon carbon ions, Phys. Rev. C 89 (2014) 054616. doi:10.1103/PhysRevC.89.054616.

[742] M. Vanstalle, I. Mattei, A. Sarti, F. Bellini, F. Bini, F. Collamati, E. D. Lucia, M. Durante, et al., Benchmarking Geant4 hadronic models for prompt-γ monitoring in carbon ion therapy, Medical Physics 44 (2017) 4276–4286. doi:10.1002/mp.12348.

[743] E. Haettner, H. Iwase, M. Krämer, G. Kraft, D. Schardt, Experimental study of nuclear fragmentation of 200 and 400 MeV/u 12C ions in water for applications in particle therapy, Phys. Med. Biol. 58 (2013) 8265. doi:10.1088/0031-9155/58/23/8265.

[744] F. Horst, G. Aricò, K.-T. Brinkmann, S. Brons, A. Ferrari, T. Haberer, A. Mairani, K. Parodi, et al., Measurement of ^{4}He charge- and mass-changing cross sections on H, C, O, and Si targets in the energy range 70–220 MeV/u for radiation transport calculations in ion-beam therapy, Phys. Rev. C 99 (2019) 014603. doi:10.1103/PhysRevC.99.014603.

[745] C. Divay, J. Colin, D. Cussol, C. Finck, Y. Karakaya, M. Labalme, M. Rousseau, S. Salvador, et al., Differential cross section measurements for hadron therapy: 50 MeV/nucleon ^{12}C reactions on H, C, O, Al, and $^{\text{nat}}$Ti targets, Phys. Rev. C 95 (2017) 044602. doi:10.1103/PhysRevC.95.044602.

[746] I. Mattei, A. Alexandrov, L. Alunni Solestizi, G. Ambrosi, S. Argirò, N. Bartosik, G. Battistoni, N. Belcari, et al., Measurement of ^{12}C Fragmentation Cross Sections on C, O, and H in the Energy Range of Interest for Particle Therapy Applications, IEEE Transactions on Radiation and Plasma Medical Sciences 4 (2020) 269–282. doi:10.1109/TRPMS.2020.2972197.

[747] D. Boscolo, D. Scognamiglio, F. Horst, U. Weber, C. Schuy, M. Durante, C. L. Tessa, E. Kozlova, et al., Characterization of the Secondary Neutron Field Produced in a Thick Aluminum Shield by 1 GeV/u ^{56}Fe Ions Using TLD-Based Ambient Dosimeters, Front. Phys. 8 (2020) 365. doi:10.3389/fphy.2020.00365.

[748] S. Biondi, et al., The FragmentatiOn Of Target (FOOT) Experiment and Its DAQ System, IEEE Trans. Nucl. Sci. 68 (2021) 2464–2471. doi:10.1109/TNS.2021.3084309. arXiv:2010.16251.

[749] M. Toppi, et al. (FOOT collaboration), Elemental fragmentation cross sections for a ^{16}O beam of 400 MeV/u kinetic energy interacting with a graphite target using the FOOT ΔE-TOF detectors, Front. Phys. 10 (2022) 979229. doi:10.3389/fphy.2022.979229.

[750] R. Ridolfi, et al. (FOOT collaboration), Angular differential and elemental fragmentation cross sections of a 400 MeV/nucleon ^{16}O beam on a graphite target with the FOOT experiment, 2024. arXiv:2501.00553.

[751] F. Tommasino, E. Scifoni, M. Durante, New Ions for Therapy, Int. J. Part. Therapy 2 (2015) 428–438. doi:10.14338/IJPT-15-00027.1.

[752] T. Tessonnier, A. Mairani, S. Brons, T. Haberer, J. Debus, K. Parodi, Experimental dosimetric comparison of ^{1}H, ^{4}He, ^{12}C and ^{16}O scanned ion beams, Phys. Med. Biol. 62 (2017) 3958. doi:10.1088/1361-6560/aa6516.

[753] International Commission on Radiation Units and Measurements, Prescribing, Recording, and Reporting Photon Beam Therapy (Report 62), ICRU, Bethesda, MD, 1999. URL: https://www.icru.org/report/prescribing-recording-and-reporting-photon-beam-therapy-report-62/, iCRU Report 62.

[754] R. Ulrich, R. Engel, M. Unger, Hadronic Multiparticle Production at Ultra-High Energies and Extensive Air Showers, Phys. Rev. D 83 (2011) 054026. doi:10.1103/PhysRevD.83.054026. arXiv:1010.4310.

[755] E. Waxman, J. Bahcall, High Energy Neutrinos from Cosmological Gamma-Ray Burst Fireballs, Phys. Rev. Lett. 78 (1997) 2292–2295. doi:10.1103/PhysRevLett.78.2292. arXiv:astro-ph/9701231.

[756] R. Alves Batista, D. Boncioli, A. di Matteo, A. van Vliet, D. Walz, Effects of uncertainties in simulations of extragalactic UHECR propagation, using CRPropa and SimProp, J. Cosmology Astropart. Phys. 10 (2015) 063. doi:10.1088/1475-7516/2015/10/063. arXiv:1508.01824.

[757] D. Boncioli, Cosmic-ray propagation in extragalactic space and secondary messengers, Proc. Int. Sch. Phys. Fermi 208 (2024) 315–351. doi:10.3254/ENFI240009. arXiv:2309.12743.

[758] D. Biehl, D. Boncioli, A. Fedynitch, W. Winter, Cosmic ray and neutrino emission from gamma-ray bursts with a nuclear cascade, A&A 611 (2018) A101. doi:10.1051/0004-6361/201731337. arXiv:1705.08909.

[759] D. Boncioli, A. Fedynitch, W. Winter, Nuclear Physics Meets the Sources of the Ultra-High Energy Cosmic Rays, Sci. Rep. 7 (2017) 4882. doi:10.1038/s41598-017-05120-7. arXiv:1607.07989.

[760] S. Aerdker, et al., CRPropa 3.2: a public framework for high-energy astroparticle simulations, in: 38th ICRC, 2023, p. 1471. doi:10.22323/1.444.1471. arXiv:2308.09532.

[761] R. Aloisio, D. Boncioli, A. Di Matteo, A. F. Grillo, S. Petrera, F. Salamida, SimProp v2r4: Monte Carlo simulation code for UHECR propagation, J. Cosmology Astropart. Phys. 11 (2017) 009. doi:10.1088/1475-7516/2017/11/009. arXiv:1705.03729.

[762] S. Rossoni, D. Boncioli, G. Sigl, Investigating binary-neutron-star mergers as production sites of high-energy neutrinos, JCAP 01 (2025) 009. doi:10.1088/1475-7516/2025/01/009. arXiv:2407.19957.

[763] E. Kido, T. Inakura, M. Kimura, N. Kobayashi, S. Nagataki, N. Shimizu, A. Tamii, Y. Utsuno, Evaluations of uncertainties in simulations of propagation of ultrahigh-energy cosmic-ray nuclei derived from microscopic nuclear models, Astropart. Phys. 152 (2023) 102866. doi:10.1016/j.astropartphys.2023.102866. arXiv:2206.03447.

[764] A. Tamii, et al. (PANDORA collaboration), PANDORA Project for the study of photonuclear reactions below $A = 60$, Eur. Phys. J. A 59 (2023) 208. doi:10.1140/epja/s10050-023-01081-w. arXiv:2211.03986.

[765] L. Tolos, L. Fabbietti, Strangeness in Nuclei and Neutron Stars, Prog. Part. Nucl. Phys. 112 (2020) 103770. doi:10.1016/j.ppnp.2020.103770. arXiv:2002.09223.

[766] S. Acharya, et al. (ALICE collaboration), Investigation of the p–Σ_0 interaction via femtoscopy in pp collisions, Phys.

Lett. B 805 (2020) 135419. doi:10.1016/j.physletb.2020.135419. arXiv:1910.14407.
[767] S. Acharya, et al. (ALICE collaboration), Unveiling the strong interaction among hadrons at the LHC, Nature 588 (2020) 232–238. doi:10.1038/s41586-020-3001-6. arXiv:2005.11495, [Erratum: Nature 590, E13 (2021)].
[768] S. Acharya, et al. (ALICE collaboration), p-p, p-Λ, and Λ − Λ correlations studied via femtoscopy in pp reactions at $\sqrt{s} = 7$ TeV, Phys. Rev. C 99 (2019) 024001. doi:10.1103/PhysRevC.99.024001.
[769] S. Acharya, et al. (ALICE collaboration), Exploring the NΛ–NΣ coupled system with high precision correlation techniques at the LHC, Phys. Lett. B 833 (2022) 137272. doi:10.1016/j.physletb.2022.137272. arXiv:2104.04427.
[770] S. Acharya, et al. (ALICE collaboration), Towards the understanding of the genuine three-body interaction for p–p–p and p–p–Λ, Eur. Phys. J. A 59 (2023) 145. doi:10.1140/epja/s10050-023-00998-6. arXiv:2206.03344.
[771] A. Kievsky, E. Garrido, M. Viviani, L. E. Marcucci, L. Serksnyte, R. Del Grande, nnn and ppp correlation functions, Phys. Rev. C 109 (2024) 034006. doi:10.1103/PhysRevC.109.034006. arXiv:2310.10428.
[772] H.-W. Hammer, A. Nogga, A. Schwenk, Colloquium: Three-body forces: From cold atoms to nuclei, Rev. Mod. Phys. 85 (2013) 197–217. doi:10.1103/RevModPhys.85.197.
[773] D. Gerstung, N. Kaiser, W. Weise, Hyperon–nucleon three-body forces and strangeness in neutron stars, Eur. Phys. J. A 56 (2020) 175. doi:10.1140/epja/s10050-020-00180-2. arXiv:2001.10563.
[774] L. Fabbietti, A. Kalweit, T. Linden, P. Von Doetinchem (organizing committee), JENAA2024: Joint ECFA-NuPECC-APPEC Activities, https://indico.cern.ch/event/1400721/, 2024.